Diss. ETH no. 26220

Optimization and Feedback Control of the Size and Shape Evolution of Elongated Crystals in Suspension

A thesis submitted to attain the degree of

DOCTOR OF SCIENCES of ETH ZURICH

(Dr. sc. ETH Zurich)

presented by

Stefan Bötschi

MSc ETH ME, ETH Zurich

born on 24.12.1989

citizen of
Zürich, Switzerland

accepted on the recommendation of

Prof. Dr. Marco Mazzotti (ETH Zurich), examiner
Prof. em. Dr. Manfred Morari (ETH Zurich), co-examiner
Prof. Dr. Kai Sundmacher (Otto von Guericke University Magdeburg),
co-examiner

2019

Acknowledgments

First and foremost, I would like to express my gratitude to my supervisors, Prof. Marco Mazzotti and Prof. Manfred Morari, for welcoming me as a doctoral student and for their constant support and guidance. Working in their groups over the past few years has been a very rewarding experience, both from a professional and from a personal point of view. I deeply admire their impressively sharp minds, their ability to provide constructive criticism any time, their continuous strive for clarity, and their constant encouragement "to keep it simple".

I also thank Prof. Kai Sundmacher for his interest in my work and for generously acting as a co-examiner of this thesis.

I feel privileged to have received outstanding public education at ETH Zurich over many years, and I gratefully acknowledge the funding of the Swiss National Science Foundation for carrying out my doctoral studies in the scope of the "CrystOCAM 2.0" research project (project number 155971). At this point, I also thank the Swiss Confederation for generously funding these two institutions, thereby providing great opportunities for many people; students and staff alike.

Special thanks go to David Ochsenbein, who, as an experienced doctoral candidate and later as a postdoctoral researcher, patiently introduced me to the world of crystallization and who provided a direction and a purpose for my first efforts in the field. Special thanks also go to my fellow doctoral student and "project buddy" Ashwin Kumar Rajagopalan. Ashwin's tireless efforts enabled the experimental campaigns conducted during "CrystOCAM 2.0". I have experienced our close collaboration as exceptionally fruitful and beneficial for the outcome of the project. I highly value Ashwin's extraordinary skills as an engineer, his diligence, his devotion to his work, and also his humorous nature. I

I

Abstract

The purification and the solidification of substances is of interest in a large number of applications in the fine chemical, pharmaceutical, and food industries. Batch crystallization from solution is often applied to fulfill this task. The macroscopic shapes of the crystals obtained in this way are governed by the principles of crystallography, and thus they exhibit a compound-specific diversity. Still, the shape and also the size of these solids can be influenced by the choice of the process operating conditions, for instance, by varying the driving force or by applying mechanical action. Since the particle size and shape distribution (PSSD) is widely accepted to be a central attribute of the obtained solid powder, the ability to engineer crystalline particles to a desirable size and shape is of great interest regardless of the application.

The main purpose of this thesis is to develop, to implement, and to evaluate—both in simulation and in experiments—optimization and feedback control algorithms aimed at the manipulation of particle size and shape during batch crystallization processes. The presented methodologies are mainly concerned with elongated (or needle-like) crystals, since particles of this type often cause problems in the pharmaceutical industry. The main challenges encountered during the development of these methodologies are their high requirements with respect to online size and shape monitoring abilities, the limited predictive capabilities of currently available crystal shape evolution models, and the often encountered lack of physical actuators to alter the crystal shape.

In particular, the following results have been achieved:

- Model-based path planning methodologies have been developed for studying computationally the possible size and shape transitions

of single crystals undergoing temperature cycling.

- Feedback control laws for driving the average particle dimensions of ensembles of elongated crystals to target regions during growth-dominated batch cooling crystallization have been conceived and successfully validated.

- A feedback controller for the targeted length reduction of elongated particles using wet milling has been designed and tested.

- A multidimensional kinetic model for the dissolution of an elongated organic compound has been identified from experimental data. Furthermore, a simple feedback law for the controlled operation of dissolution stages has been implemented.

- The feedback controllers developed for wet milling and dissolution have been integrated and combined with a simple controlled growth stage to operate a multistage process for the systematic PSSD modification in a fully automated, controlled, and thus robust manner. In particular, a significant and repeatable shape transformation from elongated to more equant particles has been realized in lab-scale experiments.

From a control systems engineering point of view, the results collected in this thesis simply represent yet another example of the potential of feedback control. From a crystallization perspective, however, the developed control and operating strategies represent a novel and robust approach to crystallizing compounds that form elongated particles. The key benefits of these strategies are that most of them do not require kinetic models to operate the process and that they can mitigate considerably undesirable batch-to-batch variations in terms of selected properties of the product PSSD.

Zusammenfassung

Das Reinigen und das Verfestigen von Substanzen ist in vielen Anwendungen in der chemischen, pharmazeutischen und Nahrungsmittelindustrie von Interesse. Zur Erfüllung dieser Aufgabe wird oftmals Batch-Kristallisation aus der Lösung verwendet. Die makroskopischen Formen der Kristalle, die auf diese Weise entstehen, sind durch die Prinzipien der Kristallografie gegeben und weisen deswegen eine stoffspezifische Diversität auf. Dennoch können die Form und auch die Grösse dieser Festkörper durch die Wahl der Prozessbedingungen beeinflusst werden, zum Beispiel durch das Variieren der chemischen Antriebskraft oder durch mechanische Einflussnahme. Weil die Grössen- und Formverteilung der Partikel eine weitläufig akzeptierte zentrale Eigenschaft des erhaltenen Pulvers ist, ist die Fähigkeit, kristalline Partikel in eine wünschenswerte Grösse und Form zu bringen unabhängig von der Anwendung von grossem Interesse.

Das Hauptziel dieser Arbeit ist das Entwickeln, das Implementieren und das Beurteilen von Optimierungs- und Regelungsalgorithmen zur Manipulation von Partikelgrösse und -form während Batch-Kristallisationsprozessen, sowohl mittels Simulation als auch mittels Experimenten. Die vorgestellten Methoden beziehen sich hauptsächlich auf längsförmige (oder nadelförmige) Kristalle, weil Partikel dieser Art oftmals Probleme in der pharmazeutischen Industrie verursachen. Die grössten Herausforderungen, die während der Entwicklung dieser Methoden angetroffen wurden, sind deren hohe Anforderungen an die Echtzeitüberwachung von Grösse und Form, die begrenzten prädiktiven Fähigkeiten von zurzeit verfügbaren Modellen für die Kristallformentwicklung, sowie auch der oftmals angetroffene Mangel an physischen Aktuatoren zur Änderung der Kristallform.

Insbesondere wurden die folgenden Resultate erzielt:

- Modellbasierte Methoden zur Planung von Trajektorien wurden entwickelt, um computergestützt die möglichen Grössen- und Formveränderungen von Einzelkristallen mittels Temperaturzyklen zu untersuchen.

- Regelalgorithmen, um die durchschnittlichen Partikelabmessungen von Populationen längsförmiger Kristalle während wachstumsdominierten Batch-Kühlkristallisationsprozessen zu Zielregionen hin zu steuern, wurden konzipiert und erfolgreich validiert.

- Ein Regelalgorithmus zur gezielten Reduktion der Länge von längsförmigen Partikeln mittels Nassmahlen wurde entwickelt und getestet.

- Ein mehrdimensionales kinetisches Modell für die Auflösung eines längsförmigen organischen Stoffes wurde aus experimentellen Daten abgeleitet. Weiter wurde ein simpler Regelalgorithmus für den kontrollierten Betrieb von Auflösungsstufen implementiert.

- Die Regelalgorithmen, die für das Nassmahlen und die Auflösungsphase entwickelt wurden, wurden mit einer einfachen geregelten Wachstumsphase kombiniert, um einen Mehrphasenprozess für die systematische Veränderung der Grössen- und Formverteilung der Partikel in einer vollständig automatisierten, geregelten, und deshalb robusten Art und Weise zu betreiben. Insbesondere wurde in Laborexperimenten eine bedeutende und wiederholbare Formveränderung von längsförmigen hin zu kompakteren Partikeln realisiert.

Von einem regelungstechnischen Standpunkt aus gesehen stellen die in dieser Arbeit gesammelten Resultate einfach ein weiteres Beispiel des Potenzials der Rückkopplungsregelung dar. Aus der Perspektive der Kristallisation hingegen entsprechen die entwickelten Regel- und Steuerungsstrategien einem neuartigen und robusten Ansatz, um Stoffe zu kristallisieren, die längsförmige Partikel bilden. Die Hauptvorteile dieser Strategien sind, dass die meisten von ihnen keine kinetischen Modelle benötigen, um den Prozess durchzuführen und dass sie unerwünschte Batch-zu-Batch-Abweichungen von ausgewählten Eigenschaften der Grössen- und Formverteilung des Produktes bedeutend abschwächen können.

Contents

List of Figures

List of Tables

Chapter 1

Introduction

Compounds of interest need to be purified and solidified in a large number of applications in the fine chemical, pharmaceutical, and food industries. Crystallization from solution is one of the most widespread techniques to fulfill this task. The physical principle of this unit operation is to generate and to maintain a chemical potential difference that acts as a driving force for the compound in solution to undergo a transition into the solid, crystalline state. For reasons of simplicity and flexibility, this process is often carried out in a stirred tank, called the batch crystallizer, and the supersaturated state can, for instance, be achieved by cooling the solution, evaporating the solvent, or adding antisolvent. Due to the highly regular and ordered nature of the crystal lattice, the resulting solid particles exhibit excellent purity. The macroscopic shapes of the crystals or particles obtained during crystallization steps are generally diverse.[1] They are compound-specific and governed by the principles of crystallography. Still, the size and the shape of the particles can be influenced by exploiting a variety of factors such as polymorphic transformations,[2,3] the choice of solvent,[4,5] the presence of impurities or additives,[5,6] and the supersaturation.[7,8]

The particle size and shape distribution (PSSD) of the crystallized solids is of high importance for two main reasons. First, since crystallization usually takes place early in the production chain, it impacts the performance of downstream unit operations. Second, important quality attributes of the product are also affected by particle size and shape.[9–11]

For instance, the size and the shape of the particles consisting of the active pharmaceutical ingredient (API) affect the dissolution rate and thus the uptake into a patient's body.[12,13] Another example is that elongated particles cause serious difficulties in downstream processing steps such as filtration[14] and powder flow.[15,16] Particle size and shape can also influence catalytic activity[17] or simply the physical appearance of a powder.[18]

Regardless of the application, the ability to engineer crystalline particles to a desirable size and shape is of great interest. Accordingly, methodologies to "manipulate crystal size and shape in a predictable manner" were seen as potentially revolutionary in a widely cited perspectives article about API product and process design that was published about a decade ago.[19] In the same article, achieving the desired product purity, crystal form, PSSD, yield, and productivity were listed as the main goals for any API crystallization process.[19] This thesis is mainly concerned with the third of these goals.

The purpose of this thesis is to develop, to implement, and to evaluate optimization and feedback control algorithms aimed at the manipulation of particle size and shape during batch crystallization processes. In this context, it needs to be emphasized that considering both the size and the shape of the particles is far from being established in the crystallization literature, not to mention in industry. On top of that, experimental validations of such concepts are very rare (see, e.g., refs 20 and 21). The methodologies presented in this thesis are mainly concerned with elongated crystals, since particles of this type are encountered often in the pharmaceutical industry and because their shape can often be described using no more than two dimensions. Note that in this thesis, for reasons of simplicity, the term needle-like is used as an umbrella term to refer to any type of elongated particle (i.e., to refer to particles with an aspect ratio above one, where the aspect ratio is the ratio of the particle length and width). While suitable process models are required to perform process optimization, online monitoring tools enable the application of feedback control. Thus, in the following sections of this introductory chapter, particle size and shape modeling concepts are summarized and an online monitoring tool is introduced. Reviewing these techniques provides the basis for the work reported in this thesis.

1.1 Modeling Particle Size and Shape

Ideal crystals are faceted, symmetrical bodies whose appearance is a direct consequence of the regular arrangement of the constituting molecules or ions in the crystal lattice.[9] Convex polytopes are a means to mathematically characterize such a body. Due to symmetry, both the size and the shape of a crystal can usually be described by a relatively small number of characteristic dimensions. This is done by grouping all the crystal facets with identical properties and assigning one characteristic dimension to each of the obtained facet groups. Such a characteristic dimension usually quantifies the normal distance of one of the facets in the group to the center of the crystal body.[22] An example with two characteristic dimensions is described in Section 2.5.1.

In crystallization processes, many particles do not exhibit the geometrically ideal shape of a convex polytope, be it because of defects in the crystal lattice or simply because of collisions that induce attrition or breakage. Even if most of the crystals were ideal, it is extremely difficult to monitor the characteristic dimensions of a large number of these faceted bodies reliably and quickly enough for process control purposes. Thus, generic particle shape models are often adopted, where the true shape of a particle is approximated by a simple geometric body such as a sphere, a cube, a cuboid, a rod, or a cylinder. Usually, these generic shapes can be fully characterized using between one and three characteristic dimensions that are all perpendicular to each other, which implies—contrary to the more general description of the convex polytopes mentioned above— that none of the faces of the body can appear or disappear when it grows or dissolves.[23] An illustrative example, where a cylinder is used to approximate an elongated crystal, is given in Section 2.5.2.

Regardless of the employed crystal shape model (convex polytope or generic), the characteristic dimensions can be grouped into a vector $\boldsymbol{L}$. A population (i.e., a set of crystalline particles) can then be described as a set of points in the particle size and shape space spanned by the dimensions of $\boldsymbol{L}$. As the number of particles in a population becomes larger and larger, the population can be characterized by a continuous density function. Within the widely used population balance framework,[24] this function is often called the number density function $f(t, \boldsymbol{L})$ (or PSSD). In the general case $\boldsymbol{L} \in \mathbb{R}^n$, the quantity $f(t, \boldsymbol{L}) \, \mathrm{d}V_{\boldsymbol{L}}$ corresponds to the

number of particles (usually per mass of solvent) contained in the infinitesimal volume $dV_{\boldsymbol{L}} = dL_1 \, dL_2 \ldots dL_n$ around $\boldsymbol{L}$ in the particle size and shape space. In this thesis, the special case $\boldsymbol{L} = [L_1 \ L_2]^{\mathrm{T}} \in \mathbb{R}^2$ is considered. Thus, the number density function $f(t, L_1, L_2)$ can conveniently by visualized as a contour plot. A detailed discussion of how to visualize two-dimensional PSSDs, especially experimentally acquired ones, can be found in Section 5.4.1. Returning to the general case of n characteristic dimensions, in a batch crystallizer under the assumption of perfect mixing, the evolution of the PSSD $f(t, \boldsymbol{L})$ over time is modeled by the partial differential equation

$$\frac{\partial f(t, \boldsymbol{L})}{\partial t} + \nabla_{\boldsymbol{L}} \cdot \big(\boldsymbol{X}(t, \boldsymbol{L}, \boldsymbol{y}) f(t, \boldsymbol{L}) \big) = B(t, \boldsymbol{L}, \boldsymbol{y}) - H(t, \boldsymbol{L}, \boldsymbol{y}) \quad (1.1)$$

where $\boldsymbol{X}$ is a vector of positive growth rates or negative dissolution rates, $\boldsymbol{y}$ is a vector of properties of the liquid phase with entries such as the solute concentration, the temperature, or the supersaturation, and B and H are source and sink terms modeling the birth and the death of particles, respectively. Apart from a few simple problems, obtaining an analytical solution to eq 1.1, which is called the population balance equation (or PBE), is generally infeasible. Thus, a variety of numerical solution techniques have been developed. [24–29]

The reader interested in an in-depth treatment of the modeling of crystal size and shape is kindly referred to the dissertations by Christian Borchert [30] and David R. Ochsenbein. [31]

1.2 Monitoring Particle Size and Shape Distributions

In order to model or to control a crystallization process, the ability to quantitatively monitor both the solid phase (suspended particles) and the liquid phase (solute dissolved in the solvent) is indispensable. For process control, online monitoring is required, which means that the sampling time of the monitoring device has to be much shorter than the characteristic time constant of the observed process dynamics. In this section, one possibility to monitor online the evolution of the solid phase (i.e., the PSSD) is summarized, while monitoring of the liquid phase (i.e., of the solute concentration) is addressed in Section 1.3.

Often, commercially available solid phase characterization tools condense shape related information of crystals into a single characteristic length.[34] Hence, a one dimensional particle size distribution (PSD) is obtained, leaving out the shape information of the crystals. However, due to the variety of shapes exhibited by crystals, a multidimensional PSSD is required to accurately quantify the population of crystals. For instance, applying one-dimensional solid characterization techniques to elongated particles was shown to yield misleading PSDs if the shape of the particles evolves over time.[35] As a remedy, multiprojection imaging systems were proposed,[23,36–39] as they are able to tackle shape-related issues rather satisfactorily. The stereoscopic imaging setup reported previously,[39] henceforth referred to as the flow through cell (FTC), used a dual-projection technique capable of merging particle size information provided by two cameras into PSSDs. The major drawback of the FTC was its bulky mechanical design ($126 \times 126 \times 90$ cm), making it vulnerable to vibrations during image acquisition. Moreover, the employed Xenon flashes required additional optics to provide collimated light. Also, a square flow channel assembled by gluing four sapphire glass windows

---

The material presented in Section 1.2 has been adapted from ref 32 (Rajagopalan, A. K.; Schneeberger, J.; Salvatori, F.; Bötschi, S.; Ochsenbein, D. R.; Oswald, M. R.; Pollefeys, M.; Mazzotti, M. A comprehensive shape analysis pipeline for stereoscopic measurements of particulate populations in suspension. *Powder Technol.* **2017**, *321*, 479–493. DOI: 10.1016/j.powtec.2017.08.044). A complete presentation of this material appears in Ashwin Kumar Rajagopalan's dissertation.[33]

held by a brass holder was used, making maintenance of the device cumbersome.

Based on the issues described above, a more compact version of the optomechanical setup ($80 \times 74 \times 42$ cm) was developed with the goal of overcoming the problems associated with the FTC. The smaller setup, henceforth referred to as dual imaging system for crystallization observation (µ-DISCO), fits into a standard laboratory hood and is less vibration-susceptible during operation. A schematic of this setup is shown in Figure 1.1; it consists of two monochrome CMOS cameras in an orthogonal configuration with telecentric optics resulting in an orthographic projection with very low spatial distortions. The camera-lens system provides a field of view of 2.41×2.02 mm and the image resolution of both cameras is 2448×2048 pixels. Thus, one pixel of the camera corresponds to about $1 \, \mu m^2$ in the focal plane. The suspension is sampled from the crystallizer using a peristaltic pump and flows through a quartz square channel embedded in a sampling loop. The cross section of the custom designed, one-piece flow channel is 2×2 mm and incorporates the two transitions between the circular tubing and the square channel at both ends. Two high-power, telecentric LED illuminators that emit collimated light rays parallel to the optical axis produce high-contrast silhouettes of particles passing through the flow channel. The whole setup is mounted on an optical rail construction. Manual translation stages that allow high precision alignment of the two cameras, and rotation stages that allow orienting the parallel illumination beams, are used. The cameras are connected to high-speed USB 3.0 ports and controlled with custom drivers.

The introduction of the new cameras allows to operate the µ-DISCO either in a standard mode with a constant low frame rate (1–7 Hz) or in a so-called burst mode. In the burst mode, after triggering a burst, a predefined number of image pairs is acquired as quickly as possible (with a theoretical maximum frame rate of 75 Hz). This mode of operation is particularly useful for capturing processes with fast dynamics, such as the dissolution of crystals. In both modes, the µ-DISCO can be operated either online, i.e., the image processing is performed on the fly, or offline, where the image processing is performed after the image acquisition for the entire measurement period. In the scope of this thesis, the µ-DISCO was exclusively operated in the burst mode. Image acquisition
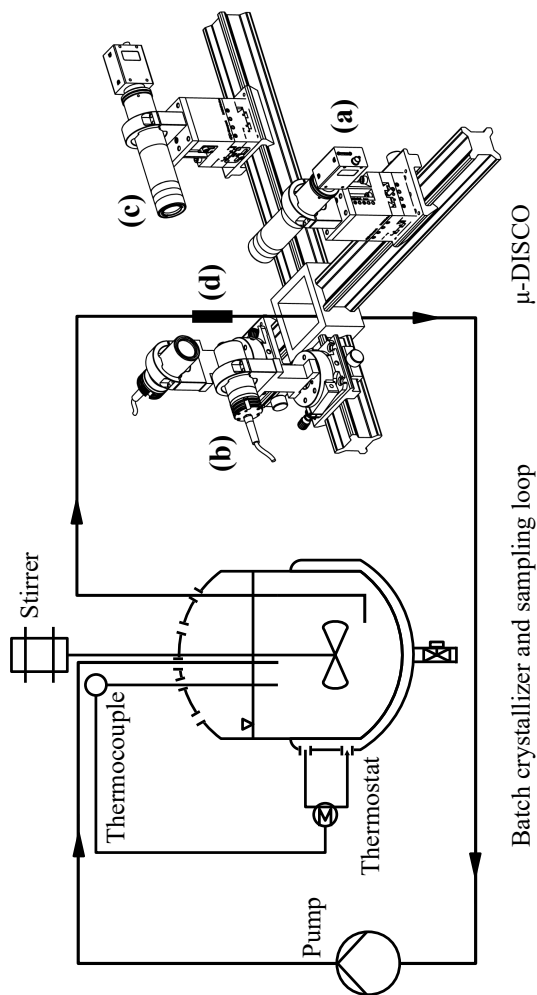
Figure 1.1: Schematic of the dual imaging system for crystallization observation (μ-DISCO) connected to a batch crystallizer by means of a sampling loop. The suspension is pumped from the batch crystallizer through the flow channel (**d**) and backlight illuminated using two telecentric illuminators (**b**). The suspension is photographed using two digital cameras (**a**) with telecentric optics (**c**). The two cameras, lenses, and illuminators are mounted orthogonally on an optical rail construction.

bursts were performed at equally spaced points in time. The sampling intervals were 2 min for offline image processing and 5 min for online processing. In the online case, the image processing delay is about 2 min. After this delay, a number of signals (e.g., PSSDs, particle counts, total particle volume) become available and can be used in feedback control algorithms.

Apart from the hardware and the improved image acquisition protocol (burst mode), the main innovation of the μ-DISCO with respect to the FTC is its image analysis pipeline. It features a stereoscopic camera calibration model to compensate for mechanical misalignment of the cameras, adaptive background subtraction to exclude dust or scratches on the flow channel from the analysis, improved particle contour matching between two simultaneously acquired images, and volumetric 3D reconstruction of the detected particles. The reconstructed crystals are subjected to a supervised shape classification strategy, which categorizes each detected crystal into five shape classes (sphere, needle, quasi-equant, platelet, and non-convex). Afterwards, the characteristic dimensions of the classified particles are determined, allowing for the reconstruction of a PSSD for each shape class by applying a binning protocol. The sequence of image processing steps from image acquisition to PSSD reconstruction is illustrated in Figure 1.2. A more detailed explanation of the single steps can be found elsewhere.[32]

1.3   Monitoring the Solute Concentration

One of the most commonly available and extensively used techniques for online solute concentration estimation in crystallization processes is the attenuated total reflectance Fourier transform infrared (ATR-FTIR) spectroscopy. It has been applied to obtain solubility curves,[41–43] to study fundamental phenomena in a batch crystallization process,[3,37,43–47]
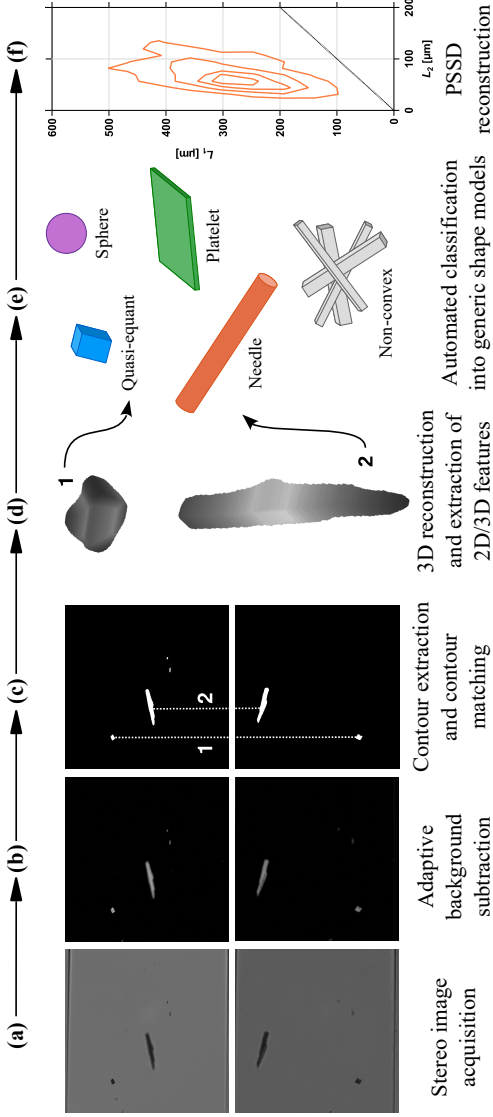
Figure 1.2: Illustration of the image processing pipeline. Apart from the camera calibration model (not illustrated), it features **(a)** the image acquisition, **(b)** an adaptive background subtraction, **(c)** a contour extraction step and a contour matching algorithm, **(d)** volumetric shape reconstruction, and **(e)** the automated shape classification of reconstructed particles. At the end of the pipeline, a PSSD for each generic particle shape model is obtained. Here, the PSSD of the needle class **(f)** is illustrated.

and to apply feedback control to crystallization processes.[21,48] Calibration methods exist to relate the IR absorbance to the solute concentration.[42,49] Irrespective of the calibration method used, there are systems which are often difficult to characterize using the ATR-FTIR, e.g, systems with low solubility, with low peak sensitivity of the compound in the mid-IR region, with low absolute change in the solute concentration during the crystallization process, or with a combination of these features.[49,50] Unfortunately, these unfavorable experimental conditions occur when working with low seed loadings of β L-glutamic acid (BLGA) in water, which is the system primarily used in this thesis. These conditions prohibited the use of commercially available spectroscopic techniques to accurately observe the evolution of the solute concentration.

Fortunately, in a seeded batch crystallization process where no reactions occur, the presence of solid particles and their change over time inherently contains information regarding the liquid phase through the mass conservation constraint, i.e., an increase in the mass of the crystals is reflected as a decrease in the solute concentration, and vice-versa. This basic principle can be exploited by means of multiprojection imaging devices, such as the µ-DISCO,[32] that provide time-resolved measurements. Apart from characterizing the population of crystals, the image analysis routines of the µ-DISCO provide an estimate of the visual hull[51] of the particles observed in the channel. The volume of a specific visual hull can be seen as an approximation to the volume of the corresponding particle. A schematic of this particle volume approximation procedure is visualized in Figure 1.3. Below, the quantity obtained by estimating and summing up the visual hull volumes of all the particles imaged within a short period of time, i.e., between the time instants t and $t + \Delta t$ (where Δt can be the duration of a µ-DISCO burst), will be referred to as the total visual hull volume $\hat{V}(t)$ at time t.

In order to estimate the change in the solute concentration based on the observed change in the total visual hull volume, the material balance

$$\hat{c}(t) = c_0 - \rho_{\mathrm{c}}\big(\phi_{\mathrm{v}}\hat{V}(t) - V_{\mathrm{seed}}\big) \tag{1.2}$$
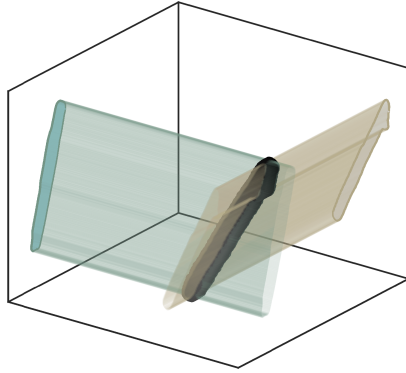
Figure 1.3: Schematic of the visual hull approximation procedure for the silhouettes of a needle-like particle observed by the two cameras of a stereoscopic imaging device such as the μ-DISCO.[32] The two silhouettes (green and gray areas on the vertical planes) are projected into and intersected in space, yielding the visual hull (dark body) of the particle.

is employed, where $\hat{c}$ and c_0 are the estimated solute concentration at time t and the known initial solute concentration, respectively, both on a per mass of solvent basis. ρ_c is the crystal density, ϕ_v is a scaling factor explained below, $\hat{V}$ is the total visual hull volume observed at time t, and V_seed is the volume of seeds added per mass of solvent. The latter quantity is defined as

$$V_\mathrm{seed} = \frac{m_\mathrm{seed}}{m_\mathrm{solvent}\rho_\mathrm{c}} \tag{1.3}$$

where m_seed is the mass of seeds and m_solvent is the mass of the pure solvent. Since a measurement approach that is based on sampling particles from a crystallizer is considered, a scaling factor ϕ_v has to be introduced to account for the difference in the volume of particles observed by the device $\hat{V}$ in the time interval between t and $t + \Delta t$ and the total volume of particles in the crystallizer. At the time instant t_0 (i.e., when the

seeding takes place), the total volume of the solids in the crystallizer is given by the known volume of the seeds. Thus, the scaling factor can initially be taken to be the ratio of the volume of the seeds (which, for convenience, is normalized by the solvent mass) and $\hat{V}(t_0)$. Under the assumption that the ratio of the total solid volume in the crystallizer to the sampled solid volume remains constant over the course of the batch experiment, the same scaling factor can be applied at all sampling instants with $t > t_0$. Thus, the scaling factor in eq 1.2 is defined to be the constant

$$\phi_{\mathrm{v}} = \frac{V_{\mathrm{seed}}}{\hat{V}(t_0)} \tag{1.4}$$

The method proposed here to estimate the solute concentration has a certain error associated with it. First, the visual hull volume overestimates the true volume of the observed crystals.[32] Second, to use the information provided by sampling devices in a quantitative way, the sampling from the crystallizer needs to be unbiased and consistent over time, which may or may not be the case. One way of assessing the impact of these errors, and thus the accuracy of the method, is to compare the solute concentration estimates obtained from eq 1.2 with independent measurements. To this end, a series of batch experiments was carried out with the aim of obtaining the solubility curve of BLGA in water using the proposed method and of comparing this curve to solubility data available in the literature. Saturated solutions of BLGA in water were prepared in a lab-scale batch crystallizer at multiple temperatures. Subsequently, the clear solutions were cooled to a relative supersaturation level of 1.01, where the relative supersaturation is defined as the ratio of the solute concentration to the solubility. Afterward, small amounts of seed crystals were suspended in the solutions, where these amounts had to be chosen so as there was only a small number of overlapping particles[39] in the images taken by the μ-DISCO. After an initial steady state phase, the suspensions were heated slowly using predefined temperature profiles to drive them to slightly undersaturated conditions. Then, the suspensions were kept at the chosen final temperatures for several hours

to let them equilibrate. This procedure should lead to the dissolution of solids and an associated change in the solute concentration, which could be visualized in the phase diagram. During all the experiments and all the experimental phases, the evolution of the solid phase was characterized using the µ-DISCO. A detailed description of the materials and methods, of the experimental setup, and of the employed experimental protocol is outside the scope of this section and can be found elsewhere.[40] Also note that a second experimental campaign applying the proposed solute concentration estimation method to the system vanillin in water can be found in the same reference. In a postprocessing step, eq 1.2 was applied to estimate the evolution of the solute concentration over time for each experiment. It is important to note that online estimation is possible as well. By combining the solute concentration estimates for the multiple experiments obtained in this way, a certain range of the solubility curve of BLGA in water could be covered. The independently measured solubility curve used for comparison is reported in the literature.[3,52] This solubility curve was also used to obtain the value of c_0 in eq 1.2 at the corresponding saturation temperatures of the experiments.

A total of five experiments was performed using BLGA and according to the procedure outlined above, each covering a different part of the temperature range from 25.0 °C to 30.6 °C. Below, these five experiments will be referred to as experiments α through ϵ. The corresponding results are visualized in Figure 1.4. From Figure 1.4a,b, it is clear that the concentration estimate increased in accordance with the process temperature profile, thereby slowly reaching plateaus while the temperature was kept constant as well. In Figure 1.4c, it can be seen that the concentration versus temperature evolution of the five experiments stayed close to the solubility of BLGA in water reported in the literature[3,52] and approached it during the intermediate and final temperature plateaus. A comparison with concentration estimates obtained from ATR-FTIR is also shown in Figure 1.4c, where it can be seen that the ATR-FTIR data are more noisy than those obtained from the µ-DISCO. The relevance of this comparison and the details thereof are discussed in ref 40.

In addition to the BLGA solubility measurements summarized above, an elementary error analysis of eq 1.2 was performed using a simulation study that mimics the conditions of experiment α. This study is explained in ref 40. Two different errors, namely, the random error that
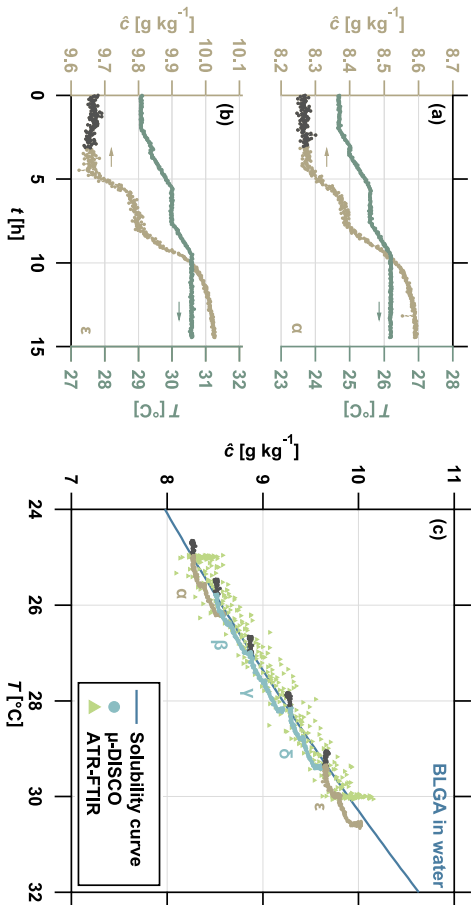
Figure 1.4: Evolution of the solute concentration estimate (dark gray and brown solid markers) and the temperature (dark green solid markers) for BLGA experiment (a) α and (b) ϵ. (c) Phase diagram (concentration versus temperature) containing the solubility of BLGA in water reported in the literature[3,52] (solid blue line), the experiments α through ϵ (dark gray, light blue, and brown solid markers), and concentration estimates obtained from ATR-FTIR (light green solid markers). The brown and light blue markers correspond to data points where the temperature was above the initial saturation temperature for each experiment, whereas the dark gray markers highlight the data points where it was below.

stems from the fluctuation in the obtained total visual hull volume and the systematic error resulting from the overestimation of the total particle volume by the total visual hull volume were evaluated. The random and the systematic error committed on the concentration estimate were $0.01\,\mathrm{g\,kg^{-1}}$ and $0.08\,\mathrm{g\,kg^{-1}}$, respectively.

To summarize, even though the presented method is approximate in nature, estimating the solute concentration by observing the solid phase is promising, as the solubility measurements obtained show good agreement with literature data. The method is useful in situations where employing commercially available standard solute concentration monitoring tools is challenging, which was the case for most of the experimental campaigns performed to validate the concepts presented in this thesis. Additionally, in the development phase of fine chemical production processes, both the solid and the liquid phase could be characterized using the same device. In such a scenario, this approach would eliminate the need to develop calibration models for characterizing the liquid phase, which is beneficial since only small amounts of the compound may be available.

1.4 Optimization and Control of Crystal Size and Shape

There are multiple challenges associated with optimizing and controlling the evolution of the size and the shape of crystals in suspension. In this work, we distinguish control strategies that rely on kinetic models (e.g., growth or dissolution rates) from those that solely require thermodynamic knowledge (i.e., solubility data) or do not require any prior knowledge at all. The former control schemes will be referred to as model-based approaches, whereas the latter will be called model-free. In terms of optimization strategies for the crystal size and shape evolution, it lies in their nature that they are model-based. Also note that in this thesis, the term control always refers to techniques from the field of automatic control or control systems engineering.

A recurring theme in this thesis is the trade-off between the model-based and the model-free operation of crystal size and shape modification processes. Multidimensional kinetic models of the crystal size and shape evolution allow to study the process through simulation, be it for the

purpose of gaining an increased understanding of the process itself or of optimizing it. However, kinetic process models are always compound-specific, their development has proven to be a challenging and tedious task (see, e.g., refs 46,53–56 and Chapter 5 of this thesis), and the resulting model predictions are still uncertain from a quantitative point of view. In light of the last point, feedback control is essential to operate the process robustly.[48,57–59] Another challenge is the fact that the optimization and model-based control problems that arise when trying to systematically modify particle size and shape are very complex, already in the single crystal case (see Chapter 2). The process dynamics are highly nonlinear[58] and the batch process is inherently transient in nature, i.e., it is not operated at steady state.[60] The optimization and control problems get even more involved when moving to the industrially relevant case of particle ensembles. An alternative approach presents itself in the combination of advanced online monitoring techniques and simple, potentially model-free feedback control strategies. By definition, kinetic models are not required for operating them,[59] but such models can still be useful in the design phase. In fact, the availability of only one such model (capturing the dynamics of the process at least qualitatively) enables the development and initial testing of suitable model-free feedback control algorithms through simulation. Afterward, these control laws can be validated experimentally and potentially also be applied to systems (i.e., compounds and solvents) that are different from that the controller has originally been developed for.

Regardless of the chosen process operating strategy, crystallization from solution usually suffers from severe underactuation,[61] i.e., the lack of potent physical actuators to influence the particle size and shape evolution during the process. This aspect of the problem is certainly among the most challenging ones, which makes it the second recurring theme in this thesis. As demonstrated previously (and also in Chapter 6 of this thesis), one way of mitigating the problem of underactuation is by combining several unit operations such as growth, dissolution, and milling to a cyclic size and shape modification process.[21,62–64]

1.5 Structure of this Thesis

This thesis consists of original work that has been published in a number of peer-reviewed journal contributions [32,40,52,65–68] or that has been accepted for publication. [69] A significant part of the work, namely, the experimental studies, was conducted in close collaboration with a fellow doctoral student, Ashwin Kumar Rajagopalan. In this thesis, an effort is made to rearrange and to combine the material reported in the articles mentioned above into chapters that have a well-defined theme, thereby thoroughly covering—both from a conceptual and from an experimental point of view—the optimization and control aspects of the research conducted within the SNSF-funded "CrystOCAM 2.0" project. The chapters of this thesis are independent in the sense that they contain all the required definitions. The overlap with the journal publications is indicated as footnotes at the beginning of each chapter or section.

In Chapter 2, optimization methodologies are developed to assess temperature cycling, i.e., consecutive cycles of growth and dissolution, as a process to systematically modify the size and the shape of single crystals growing in a batch process. For a given two-dimensional kinetic model, the trade-off between the required path time and the required number of switches between growth and dissolution to achieve a desired size and shape transition is quantified. The material reported in Chapter 2 has been published in ref 52.

The computational tools presented in Chapter 2 are not directly applicable to the case of polydisperse particle ensembles and they do not take into account uncertainties in the process model. One can address these issues by simplifying the initial problem, for instance by considering average characteristics instead of an entire particle population and by first addressing single unit operations (i.e., growth and dissolution stages) instead of the complete cyclic process. These unit operations can then be operated robustly by employing a combination of online monitoring and feedback control. In Chapter 3, two control strategies to operate a growth stage for a population of needle-like seed crystals are presented. One of these controllers is inherently model-based, while the other can also be operated without any kinetic model. Both controllers aim at directing the average length and width of the crystals in the population toward a desired target by acting on the process temperature. The model-

free control strategy was successfully validated experimentally and parts of the results of this campaign are presented in Chapter 3. The material reported in Chapter 3 has been published in refs 65 and 66.

In Chapter 4, a feedback control approach for the systematic reduction of the average length (and thus of the average aspect ratio) of a population of needle-like crystals is introduced. This controller makes use of wet milling as a potent physical actuator to modify particle size and shape. An excerpt of the results of a dedicated experimental campaign are presented, demonstrating the effectiveness of the control strategy. The material reported in Chapter 4 has been published in ref 67.

In Chapter 5, due to the lack of multidimensional dissolution rate models in the literature, a study on two-dimensional population balance modeling of the dissolution of BLGA in water is presented. One of the obtained models is used to discuss the potential of temperature cycling for particle size and shape manipulation for this compound. Furthermore, a feedback controller aimed at robustly operating dissolution stages within cyclic size and shape modification processes is presented. Finally, results from an experimental campaign that validate the performance of the control algorithm are presented and discussed. The material reported in Chapter 5 has been published in ref 68.

In Chapter 6, the control strategies for wet milling and dissolution (see Chapters 4 and 5, respectively) are combined with a simple controlled growth stage to form a controlled multistage process with the purpose of particle size and shape modification. This process is operated in a fully automated manner, without the need of kinetic process models, and it has the capability to significantly reduce the aspect ratio of needle-like seed particles. The results of an experimental campaign using two different compounds prove additionally that the controlled operation of this process introduces considerable robustness with respect to variations in the initial conditions of the batch, thereby mitigating batch-to-batch variations. The material reported in Chapter 6 has been accepted for publication; see ref 69.

Finally, in Chapter 7 conclusions drawn from the contributions collected in this thesis are made from a high-level perspective. Accordingly, possible directions for future work in the field of optimizing and controlling the size and shape evolution of crystals in suspension are suggested.

Nomenclature

Acronyms

API	active pharmaceutical ingredient
ATR-FTIR	attenuated total reflectance Fourier transform infrared
BLGA	β L-glutamic acid
DISCO	dual imaging system for crystallization observation
FTC	flow through cell
IR	infrared
PBE	population balance equation
PS(S)D	particle size (and shape) distribution
SNSF	Swiss National Science Foundation

Roman symbols

B	source term of a PBE $[\mu m^{-n}\,kg^{-1}\,s^{-1}]$
c	solute concentration (per mass of solvent basis) $[g\,kg^{-1}]$
f	number density function (PSSD) $[\mu m^{-n}\,kg^{-1}]$
H	sink term of a PBE $[\mu m^{-n}\,kg^{-1}\,s^{-1}]$
$\boldsymbol{L}$	vector of characteristic particle dimensions $[\mu m]$
m_{seed}	seed mass $[g]$
m_{solvent}	solvent mass $[kg]$
n	# dimensions of the particle size and shape space $[–]$
T	temperature $[°C]$
t	time, unit varies
$\mathrm{d}V_{\boldsymbol{L}}$	infinitesimal volume around $\boldsymbol{L}$ $[\mu m^{n}]$
$\hat{V}$	total visual hull volume $[\mu m^{3}]$
V_{seed}	volume of seeds added per solvent mass $[\mu m^{3}\,kg^{-1}]$
$\boldsymbol{X}$	vector of growth or dissolution rates $[\mu m\,s^{-1}]$
$\boldsymbol{y}$	vector of properties of the liquid phase, unit varies

Greek symbols

$\alpha, \ldots, \epsilon$	experiment labels
ρ_{c}	crystal density $[g\,\mu m^{-3}]$

ϕ_v scaling factor for particle volume $[\mathrm{kg}^{-1}]$

Superscripts and subscripts

0   initial value (at seed addition)
ˆ   measurement or estimate

Chapter 2

Single Crystal Temperature Cycling

2.1 Introduction

During crystallization from solution, the application of consecutive cycles of growth and dissolution is a technique with the potential to systematically modify the size and shape of the resulting particles.[21,55,62,70–73] In this thesis, this type of process operation is referred to as temperature cycling.

Particle size is often described by one characteristic particle dimension. Several studies in the literature apply model expressions for the growth and the dissolution rate of the particle size with the goal of optimizing the final particle size distribution of a batch crystallization process.[74–76] Approaches to temperature cycling that do not rely on kinetic models, but purely on feedback of measurements provided by process analytical technology, were shown to be capable of increasing the average crystal size.[77–79] It was also demonstrated that programmed temperature cycles can enhance crystal purity.[80] If the crystal shape is to be

---

taken into account as well, it is necessary to use at least two independent particle dimensions and thus to work with particle size and shape distributions (PSSDs). Imaging devices capable of quantifying the evolution of particle shape characteristics over time have been reported [20,23,32,39,81] (see also Section 1.2). The data obtained from these and similar tools can be applied, among other things, to estimate the parameters of model expressions for the growth and the dissolution rates of independent crystal dimensions. [46,53,54,56]

From a process design point of view, the ability to assess the potential of particle size and shape modification via temperature cycling, given the kinetic model of a specific compound, is desirable. For single crystals, contributions from Doherty's group [70,71,82,83] provide a methodology to predict the shape evolution of faceted crystals during growth, dissolution, and cycles of growth and dissolution under the assumption of constant relative facet growth and dissolution rates; corresponding experimental studies were presented as well. [71,84] Bajcinca and co-workers [62,72,73] derived analytical results enabling the computation of supersaturation and undersaturation trajectories that cause a time-optimal size and shape change of both single crystals and PSSDs. These results hinge on the assumption that the growth and dissolution rates are modeled as simple power laws of supersaturation and undersaturation. One of these results was applied in an experimental context, but without studying the influence of the explicit temperature dependence of the employed kinetic models on the result of the optimization problem. [21]

In this chapter, the temperature cycling problem is addressed in the case of complex model expressions for the growth and dissolution rates of the independent crystal dimensions that depend on temperature explicitly. The focus lies on the computation of temperature trajectories that result in desired size and shape changes with short path time and a given maximum number of switches between supersaturated and undersaturated states of the solution. For the sake of obtaining a simple operating protocol, it is desirable to keep the number of switches low. On the other hand, allowing more switches for a desired transition in the crystal size and shape space corresponds to accessing more degrees of freedom for constructing time-optimal paths, which may change the evolution of the crystal size and shape significantly. In more general terms, it is anticipated that the path time and the number of switches

may represent a trade-off in the sense of conflicting objectives, which will be explored in this chapter. The discussion of this problem is restricted to single crystals whose size and shape can be described or reasonably well approximated by two independent dimensions. A derivative-free path planning methodology that enables the assessment of the potential for modifying the size and shape of such crystals is suggested. Additionally, such methodology is an effective tool for analyzing the trade-off between the minimum required process time and the maximum allowed number of switches. The results obtained with this methodology are compared with those produced by an alternative, gradient-based approach to the path planning problem.

This chapter is organized as follows. First, the single crystal temperature cycling problem is stated in Section 2.2. Second, a derivative-free methodology for approximating the solution of the temperature cycling problem aimed at minimum process time is introduced in Section 2.3. Moreover, an extension to this methodology is described that enables the quantification of the trade-off introduced above. In Section 2.4, an alternative, gradient-based path planning approach is presented. Finally, in Section 2.5, case studies based on both approaches, using two different model compounds, are presented and discussed.

2.2 Problem Statement

The basic setting is the batch crystallization of single crystals of a solute from its solution in a specific solvent. Crystals whose size and shape can be described or well approximated by the same two independent dimensions L_1 and L_2 at any time of the process are considered. This assumption is consistent with previous work involving generic particle models,[23,39,54,56] and also with crystals modeled as convex polyhedra as long as the borders of the morphology cone[30] are not crossed (see, e.g., Eisenschmidt and co-workers[21,46]). Macroscopic models of the growth rates $G_i(S, T, \boldsymbol{L})$ and of the dissolution rates $D_i(S, T, \boldsymbol{L})$ along the two characteristic dimensions ($i = 1, 2$) as explicit functions of relative supersaturation or undersaturation S, temperature T, and the particle dimensions $\boldsymbol{L} = [L_1 \ L_2]^{\mathrm{T}}$ are assumed to be available. The relative su-

persaturation or undersaturation is defined as

$$S = \frac{c}{c^*(T)} \tag{2.1}$$

where c is the solute concentration in the given solvent, and $c^*(T)$ represents the solute solubility in the solvent as a function of temperature T. Equation 2.1 is substituted for the dependence on S of the growth and dissolution rates. Thus, in the absence of nucleation and breakage, the evolution of the ith crystal dimension is governed by the growth rate $G_i(c(t), T(t), \boldsymbol{L}(t)) \geq 0$ $(i = 1, 2)$ in the supersaturated case $S > 1$, and by the dissolution rate $D_i(c(t), T(t), \boldsymbol{L}(t)) \leq 0$ $(i = 1, 2)$ in the undersaturated case $S < 1$. Note that in the saturated case $S = 1$, the crystal dimensions $\boldsymbol{L}(t)$ remain constant $(G_i = D_i = 0, \ i = 1, 2)$. The solute concentration c in the batch crystallizer is a dependent variable that evolves according to the material balance

$$c(t) = c_0 + \frac{\rho_c}{m_s} \left(V_0 - V\big(\boldsymbol{L}(t)\big) \right) \tag{2.2}$$

where c_0 is the initial solute concentration, V_0 the initial crystal volume, $V\big(\boldsymbol{L}(t)\big)$ the current crystal volume, ρ_c the crystal density, and m_s the solvent mass.

For consecutive cycles of growth and dissolution, the switched, generally nonlinear system of differential algebraic equations (DAEs)

$$\frac{\mathrm{d}\boldsymbol{L}(t)}{\mathrm{d}t} = \begin{cases} \boldsymbol{G}\big(c(t), T(t), \boldsymbol{L}(t)\big) & \text{if } S(t) \geq 1 \\ \boldsymbol{D}\big(c(t), T(t), \boldsymbol{L}(t)\big) & \text{if } S(t) < 1 \end{cases} \tag{2.3}$$
$$c(t) = c_0 + \frac{\rho_c}{m_s} \left(V_0 - V\big(\boldsymbol{L}(t)\big) \right)$$

is obtained, with the growth and dissolution rate vectors $\boldsymbol{G}(c, T, \boldsymbol{L}) =$

$\left[G_1(c,T,\boldsymbol{L})\ G_2(c,T,\boldsymbol{L})\right]^{\mathrm{T}}$ and $\boldsymbol{D}(c,T,\boldsymbol{L}) = \left[D_1(c,T,\boldsymbol{L})\ D_2(c,T,\boldsymbol{L})\right]^{\mathrm{T}}$, respectively, and the given initial conditions $\boldsymbol{L}(0) = \boldsymbol{L}_0$, and $c(0) = c_0$. Notice that the time dependence of the variables in the equations is omitted in some cases to enhance readability. Also note that the temperature is not a state of the system model, i.e., it is assumed that it can be adjusted instantaneously. This assumption is often justifiable, because the thermal dynamics of a small batch crystallizer for single crystals are usually considerably faster than the dynamics of crystal growth and dissolution. Thus, the control input of the system model given in eq 2.3 is defined to be directly the temperature $T(t)$.

The basic problem considered in this chapter is the computation of a temperature trajectory $T(t)$ that causes a size and shape change of a single crystal from given initial dimensions $\boldsymbol{L}_0 = [L_{10}\ L_{20}]^{\mathrm{T}}$ and from a given initial solute concentration c_0 to desired target crystal dimensions $\boldsymbol{L}_{\mathrm{t}} = [L_{1\mathrm{t}}\ L_{2\mathrm{t}}]^{\mathrm{T}}$ in the smallest possible time t_{f} and with an upper limit on the number of switches from a supersaturated to an undersaturated state, and back. In a first step, the minimum-time problem is stated without any restriction concerning the number of switches. This problem can be formulated as the optimal control problem

$$
\begin{aligned}
&\underset{T(t),\ t_{\mathrm{f}}}{\text{minimize}} && t_{\mathrm{f}} \\[4pt]
&\text{subject to} && \text{eq 2.3} \qquad t \in [0, t_{\mathrm{f}}] \\
&&& T_{\min} \le T(t) \le T_{\max} \\
&&& S(t) \in \left\{ \left[S_{\mathrm{D,min}},\, S_{\mathrm{D,max}}\right] \cup \left[S_{\mathrm{G,min}},\, S_{\mathrm{G,max}}\right] \right\} \qquad (2.4)\\
&&& V_{\min} \le V\big(\boldsymbol{L}(t)\big) \\
&&& \boldsymbol{L}(0) = \boldsymbol{L}_0 \\
&&& c(0) = c_0 \\
&&& \boldsymbol{L}(t_{\mathrm{f}}) = \boldsymbol{L}_{\mathrm{t}}
\end{aligned}
$$

The decision variables are the temperature profile $T(t)$ and the process time t_{f}. Constraints on the temperature, the supersaturation, and the undersaturation are introduced, because models for the growth and

dissolution rates are usually only valid within certain ranges of these quantities (see, e.g., refs 54 and 46). Note that the constraint on $S(t)$ consists of the union of the two ranges $S_{\mathrm{D,min}} \leq S(t) \leq S_{\mathrm{D,max}} \leq 1$ and $1 \leq S_{\mathrm{G,min}} \leq S(t) \leq S_{\mathrm{G,max}}$, which are disjoint in the general case. Additionally, the crystal volume is constrained to lie above a minimum volume V_{min} in order to prevent complete dissolution of the crystal. Note that in any numerical and also practical context, the strict equality constraint on the final size and shape vector $\boldsymbol{L}(t_{\mathrm{f}})$ in fact corresponds to a small, finite target region.

In general, the optimal control problem stated in eq 2.4 is nonlinear and also nonconvex, which makes it challenging to solve. A derivative-free methodology for computing an approximate solution to eq 2.4 is introduced in Section 2.3, including an extension of this methodology that yields a solution in the case of an additional constraint on the maximum allowed number of switches between supersaturation and undersaturation.

2.3 Derivative-free Path Planning Approach

The switched dynamics of eq 2.3 and the constraint on $S(t)$ in eq 2.4 determine the nonsmooth nature of the optimal control problem stated in Section 2.2. Therefore, in this section, a derivate-free methodology for computing an approximate solution to this problem is suggested.

2.3.1 Attainable Regions for Crystal Size and Shape

The growth and dissolution rate vectors $\boldsymbol{G}(c, T, \boldsymbol{L})$ and $\boldsymbol{D}(c, T, \boldsymbol{L})$, respectively, are restricted to certain subspaces.[72,73] Thus, in a first step, the concept of attainable regions for crystal size and shape via a single growth or dissolution stage is introduced. A vector $\begin{bmatrix} \boldsymbol{L}^{\mathrm{T}} & c \end{bmatrix}^{\mathrm{T}}$ can be assigned to every point $\boldsymbol{L}$ in the crystal size and shape space, where the solute concentration c at that point is given by eq 2.2. For any such vector, a growth rate vector with maximum possible slope $\boldsymbol{G}_{\mathrm{max}}(c, \boldsymbol{L})$ (called growth maximum vector) and a growth rate vector with minimum possible slope $\boldsymbol{G}_{\mathrm{min}}(c, \boldsymbol{L})$ (called growth minimum vector) exist, as illustrated in Figure 2.1a. The direction and the magnitude of these vectors are determined by both the model expressions for the growth and dissolution rates and the constraints imposed on temperature, su-

persaturation, and undersaturation. During an infinitesimally small time step, growth trajectories starting at $\begin{bmatrix} \boldsymbol{L}^{\mathrm{T}} & c \end{bmatrix}^{\mathrm{T}}$ cannot leave the cone defined by the growth maximum and minimum vectors, irrespective of the applied (feasible) temperature level. As the values of $\boldsymbol{L}$ and c progress in time, the growth maximum and minimum vectors change as well. The dissolution maximum and minimum vectors $\boldsymbol{D}_{\max}(c, \boldsymbol{L})$ and $\boldsymbol{D}_{\min}(c, \boldsymbol{L})$, respectively, are defined likewise. The two boundary curves of the crystal size and shape region attainable from a specific initial vector $\begin{bmatrix} \boldsymbol{L}^{\mathrm{T}} & c \end{bmatrix}^{\mathrm{T}}$ by growth (dissolution) can be identified by integrating eq 2.3 once with the temperature trajectory $T(t)$ chosen such that the growth (dissolution) maximum vector is followed at every point in time, and once such that the growth (dissolution) minimum vector is followed.

A related concept is that of constant temperature attainable regions. In contrast to the more general attainable regions introduced above, a constant temperature attainable region consists of the set of all constant temperature trajectories that violate neither the constraints on temperature nor those on supersaturation and undersaturation when starting from a specific initial vector $\begin{bmatrix} \boldsymbol{L}^{\mathrm{T}} & c \end{bmatrix}^{\mathrm{T}}$. Such a constant temperature attainable region is always a subset of the more general attainable region from the same initial state. An illustrative example of the two different types of attainable regions is shown in Figure 2.1b.

In many cases, the region attainable by a single growth or dissolution stage can be significantly enlarged by temperature cycling, i.e., by appending consecutive cycles of dissolution and growth to the initial stage.[72,73] As described in the next section, the concept of constant temperature attainable regions allows a conceptually simple approach to the temperature cycling problem of eq 2.4. Note that a similar approach based on the more general attainable regions would also be feasible.

2.3.2 Shortest Path Approach

The optimal control problem of eq 2.4 can be approximated by considering a directed graph obtained by performing the sequence of steps listed below. This approach is motivated by the observation that constant temperature attainable regions are often small compared with a region of interest in the crystal size and shape space (see Figure 2.1b), which leads to the computationally desirable case of a sparse graph.
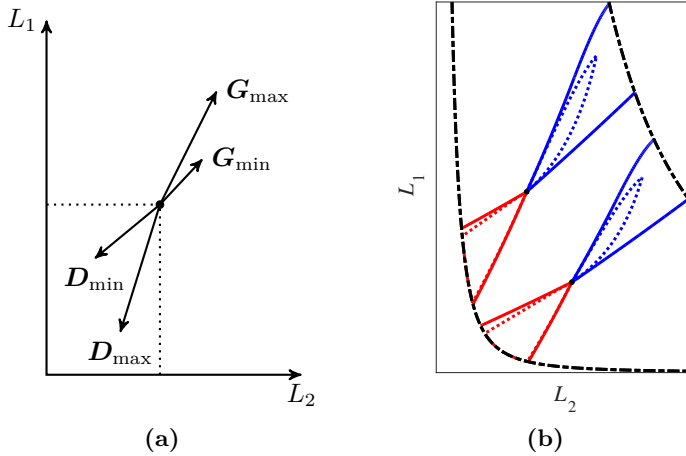
Figure 2.1: **(a)** Qualitative illustration of the growth maximum vector $\boldsymbol{G}_{\max}(c, \boldsymbol{L})$, the growth minimum vector $\boldsymbol{G}_{\min}(c, \boldsymbol{L})$, the dissolution maximum vector $\boldsymbol{D}_{\max}(c, \boldsymbol{L})$, and the dissolution minimum vector $\boldsymbol{D}_{\min}(c, \boldsymbol{L})$. **(b)** Attainable regions of two different initial vectors $\left[\boldsymbol{L}^{\mathrm{T}} \, c\right]^{\mathrm{T}}$ for a cylindrical particle (length L_1 and width L_2) with growth and dissolution rates chosen for the sake of clarity of representation. The attainable regions (growth in blue, dissolution in red) are bounded by solid lines, whereas the dashed black lines represent the minimum allowed and the maximum achievable particle volume, the latter being defined by the concentration at which $T = T_{\min}$ achieves $S = S_{\mathrm{G,min}}$. The corresponding constant temperature attainable regions have dotted lines as boundaries.

1. The crystal size and shape space is discretized using a grid within the ranges $L_{1,\min} \leq L_1 \leq L_{1,\max}$ and $L_{2,\min} \leq L_2 \leq L_{2,\max}$ or within any other region of interest. This discretization yields a finite set of grid points $\mathcal{P} = \{\boldsymbol{L}_1, \ldots, \boldsymbol{L}_{N_{\mathcal{P}}}\}$ with cardinality $N_{\mathcal{P}}$. Again, note that the solute concentration c_j at each grid point $\boldsymbol{L}_j \in \mathcal{P}$ is defined by eq 2.2.

2. Constant temperature attainable regions are computed for each grid point $\boldsymbol{L}_j \in \mathcal{P}$, separately for both growth and dissolution. The computation consists of repeated forward integrations of eq 2.3 using the elements of a discrete, finite set of constant temperature values that covers the whole range of feasible initial temperatures at $\left[\boldsymbol{L}_j^{\mathrm{T}}\ c_j\right]^{\mathrm{T}}$. The set of growth and dissolution trajectories obtained in this way constitutes the constant temperature attainable region of a certain grid point $\boldsymbol{L}_j$. Let the set of grid points that lie within this region be $\mathcal{R}_j = \{\boldsymbol{L}_k \in \mathcal{P} \mid \boldsymbol{L}_k \text{ reachable from } \boldsymbol{L}_j \text{ with } T(t) = \text{const.}\}$ with cardinality $N_{\mathcal{R}_j}$; this set is a discrete representation of the constant temperature attainable region of the grid point $\boldsymbol{L}_j$.

3. Constant temperature levels T_{jk} and trajectory times t_{jk} that connect the base points $\boldsymbol{L}_j \in \mathcal{P}$ with all the grid points $\boldsymbol{L}_k \in \mathcal{R}_j$ of the corresponding constant temperature attainable regions are computed. If the growth and dissolution trajectories that constitute the constant temperature attainable region of $\boldsymbol{L}_j$ (see previous step) do not intersect in the crystal size and shape space, the mappings $\boldsymbol{L}_k \to T_{jk}$ and $\boldsymbol{L}_k \to t_{jk}$ are unique, and T_{jk} and t_{jk} can be well approximated by interpolation.

The assumption of non-intersecting constant temperature trajectories (see step 3 above) is reasonable from a physical point of view, and it therefore imposes only a mild restriction on the model expressions for the growth and dissolution rates. Still, note that if this assumption should not be satisfied, finding an approximate solution to eq 2.4 becomes significantly more challenging, except in the trivial cases $G_1(c, T, \boldsymbol{L}) = G_2(c, T, \boldsymbol{L})$ and $D_1(c, T, \boldsymbol{L}) = D_2(c, T, \boldsymbol{L})$, the latter of the two being addressed in Section 2.5.1.

The three steps above yield a sparse directed graph $\mathcal{H} = (\mathcal{V}, \mathcal{A})$ whose finite set of nodes $\mathcal{V}$ corresponds to the set of grid points $\mathcal{P}$ of the

spatial discretization. The finite set of arcs $\mathcal{A}$ consists of the constant temperature trajectories that connect the grid points $\boldsymbol{L}_j \in \mathcal{P}$, and the nonnegative arc weights are defined by the associated path times t_{jk}. Shortest paths between arbitrary nodes of this directed graph can be found efficiently using Dijkstra's algorithm.[85] Provided that the initial node $I \in \mathcal{V}$ and the target node $F \in \mathcal{V}$ correspond to the grid points $\boldsymbol{L}_0$ and $\boldsymbol{L}_{\mathrm{t}}$, respectively, such a shortest path represents an approximate solution of the optimal control problem stated in eq 2.4. The corresponding temperature profile $T(t)$ is piecewise constant and consists of the sequence of pairs (T_{jk}, t_{jk}) that is associated with the arc sequence of the shortest path.

The accuracy of the shortest path (SP) approach described above is governed by the extent and the resolution of the spatial discretization. Note that once the directed graph $\mathcal{H}$ has been constructed for a fixed set of initial conditions $\boldsymbol{L}(0) = \boldsymbol{L}_0$ and $c(0) = c_0$, an approximate solution of the optimal control problem of eq 2.4 can efficiently be obtained for a large number of targets $\boldsymbol{L}_{\mathrm{t}}$.

It is worth noting that the SP approach presented in this section has similarities to dynamic programming (DP). In fact, general shortest path problems and deterministic DP problems with a finite set of states are closely related.[86] In our case, this means that once the directed graph $\mathcal{H}$ is available, the shortest path between any two nodes can also be found using standard DP approaches. One could also try to formulate eq 2.4 directly as a DP problem, i.e., without constructing first the directed graph $\mathcal{H}$. However, at least two complications would arise. First, the process time t_{f} in eq 2.4 is subject to optimization, and consequently, time would have to be introduced as an additional state variable in the DP problem. Second, addressing the final state constraint in eq 2.4 would require the computation of backward reachable sets.[87] The SP approach introduced in this section is believed to be more intuitive, especially because it is based on the concept of attainable regions (see Section 2.3.1).

2.3.3 Shortest Path Approach with a Limited Number of Switches

In this section, the SP approach introduced in Section 2.3.2 is extended to the case where the temperature cycling problem posed in eq 2.4 is to

be solved with the additional constraint of a maximum allowed number of switches between growth and dissolution. The basic idea is to modify the directed graph $\mathcal{H} = (\mathcal{V}, \mathcal{A})$ that was constructed for a specific problem, as suggested by Zenklusen.[88] The methodology is exemplified by means of the simple directed graph $\mathcal{H}$ shown in Figure 2.2a. In fact, this directed graph can be viewed as consisting of three elements: the set of nodes, among which the initial node I and the final node F; the set of growth arcs (solid blue arrows); and the set of dissolution arcs (dotted red arrows); each arc has its own weight, indicating the time needed to move along the arc. Then, one can define two subgraphs, $\mathcal{H}_g$ and $\mathcal{H}_d$, constituted only of the growth and the dissolution arcs, respectively, and of the nodes connected to their heads and tails, with the exception of the initial node I and the arcs connected to it (see Figure 2.2c,d). Likewise, one can define two reduced forms of the original directed graph $\mathcal{H}$, namely, one without the dissolution arcs (called $\mathcal{H}_G$, see Figure 2.2c) and one without the growth arcs (called $\mathcal{H}_D$, see Figure 2.2d). These four building blocks, namely, the directed graphs $\mathcal{H}_G$, $\mathcal{H}_D$, $\mathcal{H}_g$, and $\mathcal{H}_d$, can be combined to form two alternating sequences $\mathcal{H}_G$-$\mathcal{H}_d$-$\mathcal{H}_g$-$\mathcal{H}_d$-... and $\mathcal{H}_D$-$\mathcal{H}_g$-$\mathcal{H}_d$-$\mathcal{H}_g$-..., with a total number of $n_{\max} + 1$ building blocks each, where $n_{\max} \in \{0, 1, 2, \ldots\}$ defines an upper limit for the range of the number of switches between growth and dissolution arcs that is to be investigated. Whenever two copies of the same node are present in two adjacent building blocks, these are connected with a new unidirectional auxiliary arc (representing an instantaneous switch between growth and dissolution) with an associated weight of 0. To the two resulting extended graphs $\mathcal{K}_G$ and $\mathcal{K}_D$ (see Figure 2.2e for an example of an extended graph $\mathcal{K}_G$ with $n_{\max} = 2$) Dijkstra's algorithm[85] can be applied, thus yielding a set of shortest paths connecting the initial node I with the final node $F_0 = F$ and all its copies F_n ($n \in \{1, \ldots, n_{\max}\}$), starting with either a growth step or a dissolution step, depending which of the two extended graphs is used. Note that this set of paths covers the whole range of allowed switches from 0 to $n_{\max}$, and thus quantifies the trade-off between the required path time and the maximum allowed number of switches between growth and dissolution to reach the target node F. A postprocessing step produces a Pareto front, as explained below.

A more formal description of the algorithm to construct an extended graph $\mathcal{K}_G$ is given in Table A.1 in Appendix A; the algorithm to construct

$\mathcal{K}_\mathrm{D}$ proceeds analogously.

Concerning our simple example for $n_{\max} = 2$, the Pareto front corresponding to the directed graph $\mathcal{H}$ of Figure 2.2a is shown in Figure 2.2b. By inspection of the extended graph $\mathcal{K}_\mathrm{G}$ shown in Figure 2.2e, the shortest paths from I to F_1 and F_2 are identified as I–3–6–$6'$–F_1 (path time 9.2) and I–3–$3'$–$4'$–$4''$–F_2 (path time 8.5), respectively. Notice that there is no path from I to F_0, i.e., a path without any switches does not exist. In this simple example, the Pareto front can be confirmed by directly inspecting the original directed graph $\mathcal{H}$ in Figure 2.2a. Namely, the shortest path from I to F with 1 switch is identified as I–3–6–F (path time 9.2), and that with 2 switches as I–3–4–F (path time 8.5).

Two important remarks regarding the procedure described in this section have to be made:

- The overall trade-off is constructed by taking the pointwise minimum between the two trade-offs obtained from the two extended graphs $\mathcal{K}_\mathrm{G}$ (enforcing the first arc in the shortest path to be a growth arc) and $\mathcal{K}_\mathrm{D}$ (enforcing the first arc to be a dissolution arc).

- Artifacts in the trade-offs can appear when multiple switches between copies of the same node $v \in \mathcal{V}$ occur, e.g., when zero-weight arcs between copies of the target node F are followed. Then, the resulting trade-off contains points that have equal process time, but a different number of switches. The points with too many switches are artifacts and thus not part of the corresponding Pareto front, which is defined here in the strict sense of the term. However, such artifacts can readily be detected during a postprocessing step. In the results of the case studies presented in Section 2.5, points that are optimal in the Pareto sense and thus not artifacts are highlighted. Fronts that have not been postprocessed in this way are called Pareto-like fronts. The term trade-off is used whenever it is not necessary to distinguish between the Pareto front and the Pareto-like front, or when both concepts are addressed simultaneously.

(a) $\mathcal{H}$

(b) Pareto front

(c) $\mathcal{H}_{\mathrm{G}}$ and $\mathcal{H}_{\mathrm{g}}$

(d) $\mathcal{H}_{\mathrm{D}}$ and $\mathcal{H}_{\mathrm{d}}$

(e) Extended graph $\mathcal{K}_{\mathrm{G}}$ for $n_{\max} = 2$. To increase clarity, unique labels are assigned to node copies.
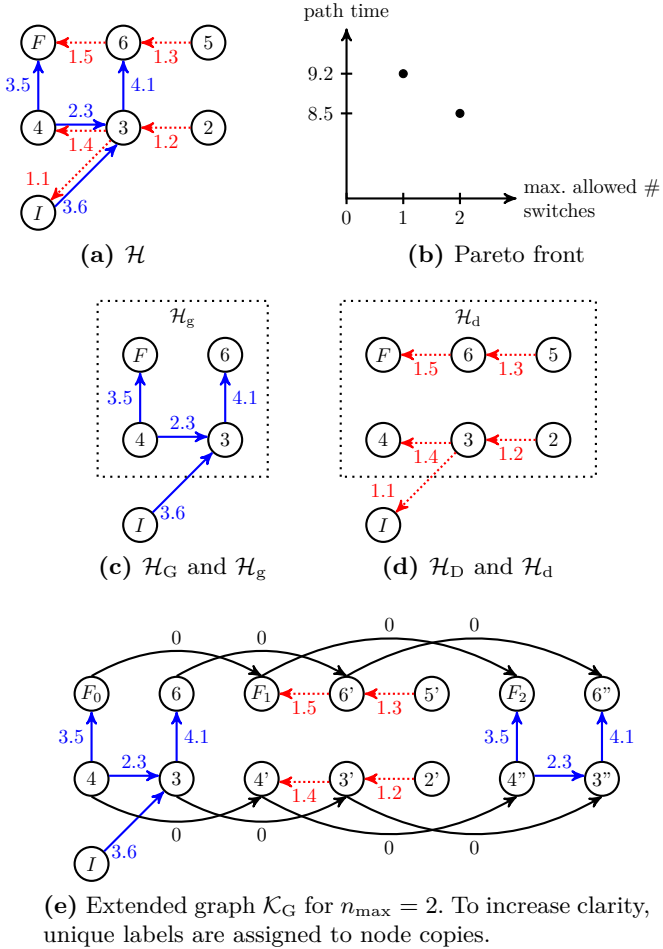
Figure 2.2: Example of constructing an extended graph $\mathcal{K}_{\mathrm{G}}$.

2.4 Gradient-based Path Planning Approach

An alternative way of approaching the temperature cycling problem stated in eq 2.4 is to cast it into a multistage optimal control problem by fixing the number of stages M and the nature of the first stage, which can be either growth or dissolution. To this end, let $\mathcal{M} = \{1, 2, \ldots, M\} = \mathcal{M}_G \cup \mathcal{M}_D$ be the set of stages. If the first stage is a growth stage, the set of growth stages is $\mathcal{M}_G = \{1, 3, 5, \ldots\}$, otherwise it is $\mathcal{M}_G = \{2, 4, 6, \ldots\}$. In both cases, the set of dissolution stages is $\mathcal{M}_D = \mathcal{M} \setminus \mathcal{M}_G$. Let $l \in \mathcal{M}$ enumerate the alternating sequence of growth and dissolution stages. The multistage optimal control problem is

$$
\begin{aligned}
\underset{T^l(t),\ t_{\mathrm{f}}^l\ l=1,\ldots,M}{\text{minimize}} \quad & \sum_{l=1}^{M} t_{\mathrm{f}}^l \\
\text{subject to} \quad & \frac{\mathrm{d}\boldsymbol{L}^l(t)}{\mathrm{d}t} = \begin{cases} \boldsymbol{G}\big(c^l(t), T^l(t), \boldsymbol{L}^l(t)\big) & \text{if } l \in \mathcal{M}_G \\ \boldsymbol{D}\big(c^l(t), T^l(t), \boldsymbol{L}^l(t)\big) & \text{otherwise} \end{cases} \\
& c^l(t) = c_0 + \frac{\rho_{\mathrm{c}}}{m_{\mathrm{s}}}\left(V_0 - V\big(\boldsymbol{L}^l(t)\big)\right) \\
& \boldsymbol{L}^l(0) = \boldsymbol{L}^{l-1}(t_{\mathrm{f}}^{l-1}) \\
& c^l(0) = c^{l-1}(t_{\mathrm{f}}^{l-1}) \\
& T_{\min} \leq T^l(t) \leq T_{\max} \\
& S^l(t) \in \begin{cases} \big[S_{G,\min},\ S_{G,\max}\big] & \text{if } l \in \mathcal{M}_G \\ \big[S_{D,\min},\ S_{D,\max}\big] & \text{otherwise} \end{cases} \\
& V_{\min} \leq V\big(\boldsymbol{L}^l(t)\big) \\
& 0 \leq t_{\mathrm{f}}^l, \qquad\qquad t \in [0,\ t_{\mathrm{f}}^l], \quad l \in \mathcal{M} \\
& \boldsymbol{L}^M(t_{\mathrm{f}}^M) = \boldsymbol{L}_{\mathrm{t}}
\end{aligned}
\tag{2.5}
$$

where $t_{\mathrm{f}}^0 = 0$, $\boldsymbol{L}^0(0) = \boldsymbol{L}_0$, and $c^0(0) = c_0$.

The multistage optimal control problem posed in eq 2.5 can be transcribed into a nonlinear program (NLP) by using the technique of mul-

tiple shooting over multiple stages.[89] In order to do so, the duration t_{f}^{l} of each of the M stages is defined to be a decision variable of the NLP. Note that the lower bound on each stage duration t_{f}^{l} is set to zero, so as the NLP solver is free to effectively skip certain stages. Second, N_{int} shooting intervals per stage are introduced, and an unknown constant temperature, i.e., the control input, is introduced for each shooting interval. These control inputs represent another $M \cdot N_{\mathrm{int}}$ decision variables. Third, the continuous-time ODE that represents the first constraint in eq 2.5 is discretized in time. The second and fourth constraint in eq 2.5, which represent the material balance, can be implicitly satisfied by substituting the algebraic constraint on $c^{l}(t)$ in the right-hand side of the ODE constraint. Finally, the $M \cdot N_{\mathrm{int}}$ end states of each shooting interval are introduced as decision variables, which enables ensuring the continuity of the crystal size and shape vector $\boldsymbol{L}(t)$ across the boundaries of both the shooting intervals and the stages. If the resulting NLP is feasible, a stationary point can be computed using a dedicated solver.

In the following, the methodology described above is referred to as the multistage (MS) approach. Compared with the SP approach, the MS approach to the temperature cycling problem has the advantage that the crystal size and shape space does not need to be discretized using a fixed, finite grid. However, because this approach relies on gradient-based optimization of a nonconvex problem, convergence to a satisfactory stationary point cannot be guaranteed, not even if reasonable initial guesses for all the decision variables are available. In particular, note that the number of stages effectively used by the obtained solution may often be smaller than M. Finally, to determine an appropriate number of stages and nature of the first stage, a series of NLPs has to be solved for each target crystal size and shape $\boldsymbol{L}_{\mathrm{t}}$.

2.5 Case Studies

In this section, models of the growth rates, the dissolution rates, and the solubilities of the two systems potassium dihydrogen phosphate (KDP) in water and β L-glutamic acid (BLGA) in water are introduced. Then, three case studies that illustrate the methodologies described in Sections 2.3 and 2.4 are presented; two based on KDP, and one on BLGA.

The implementation of the SP approach relied on the MATLAB[90]
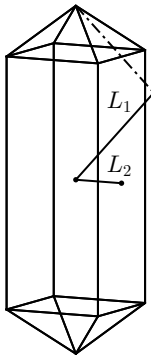
Figure 2.3: Ideal potassium dihydrogen phosphate crystal with $\frac{L_1}{L_2} = \frac{5}{2}$; visualized using the multi-parametric toolbox (MPT3)[93]

(v8.6) routines `shortestpath` for Dijkstra's algorithm[85] and `ode23` for the integration of eq 2.3, where the algebraic part of this system of equations was differentiated once with respect to time to obtain a system of ODEs. The construction of the directed graph $\mathcal{H}$ (see Section 2.3.2) was parallelized and carried out on a multiprocessor system with 32 CPU cores.

In the MS approach, the direct transcription steps listed in Section 2.4 were performed using the software CasADi[91] (v3.1) interfaced from MATLAB[90] (v8.6). The number of shooting intervals per stage of eq 2.5 was set to 30, and the continuous-time dynamics on each shooting interval were discretized using five steps of the standard fourth-order Runge-Kutta scheme. The resulting NLP was solved by IPOPT[92] (v3.12).

2.5.1 Potassium Dihydrogen Phosphate (KDP)

KDP crystals grown in water have two independent facet families.[8] Their corresponding dimensions L_1 and L_2 are shown in Figure 2.3, whereas the required geometrical information can be found elsewhere.[30] Eisenschmidt et al.[46] measured the solubility of KDP in water and provided a model of the facet growth and dissolution rates. The solubility

is

$$c^*(T) = 4.6479 \times 10^{-5}\, T^2 - 2.2596 \times 10^{-2}\, T + 2.8535 \qquad (2.6)$$

and the expressions for the growth and the dissolution rates are

$$G_i = k_{g,i}\, \exp\left(-\frac{E_{A,g,i}}{RT}\right)(S - 1 - s_{1,i}\theta^2 - s_{2,i}\theta - s_{3,i}) \qquad (2.7)$$

$$D_i = k_{d,i}\, \exp\left(-\frac{E_{A,d,i}}{RT}\right)(S - 1) \qquad (2.8)$$

where $i = 1, 2$, T is the temperature in Kelvin, and $\theta = T - 273.15$ is the temperature in degrees Celsius. The parameters associated with the growth rates G_i in eq 2.7 are listed in Table 2.1. Note that if $S - 1 - s_{1,i}\theta^2 - s_{2,i}\theta - s_{3,i} < 0$, G_i has to be set to 0 to prevent the unphysical situation of a negative growth rate. As the dissolution rates D_1 and D_2 observed by Eisenschmidt et al.[46] are practically equal, it is assumed here—for the sake of simplicity—that both facet families dissolve with equal rates. Note that this assumption simplifies the computation of the constant temperature attainable regions and the temperature levels T_{jk} (see Section 2.3.2) in the dissolution case. In fact, T_{jk} are the temperatures that correspond to an initial undersaturation of $S = S_{D,\min}$ (implying fast dissolution), and they can always be obtained by inverting eq 2.1. The values for the parameters of eq 2.8 are listed in Table 2.1 as well.

The parameters for the constraints in eqs 2.4 and 2.5 were fixed at $T_{\min} = 298.15\,\text{K}$, $T_{\max} = 318.15\,\text{K}$, $S_{G,\min} = 1.08$, $S_{G,\max} = 1.12$, $S_{D,\min} = 0.95$, and $S_{D,\max} = 0.99$. The prismatic, rectangular facets (associated with the dimension L_2) are present in the crystals as long as the condition $L_1 > 0.68265 L_2$ is satisfied and the corresponding crystal

Table 2.1: Parameter values for the growth rates G_i and the dissolution rates D_i of KDP. (Adapted with permission from ref 46. Copyright 2015 American Chemical Society.)

Parameter	Unit	$i = 1$	$i = 2$
$k_{\mathrm{g},i}$	$\mu\mathrm{m\,s}^{-1}$	1.370×10^7	6.010×10^6
$E_{\mathrm{A,g},i}$	$\mathrm{J\,mol}^{-1}$	3.910×10^4	3.710×10^4
$s_{1,i}$	$^\circ\mathrm{C}^{-2}$	5.906×10^{-6}	1.706×10^{-5}
$s_{2,i}$	$^\circ\mathrm{C}^{-1}$	-1.079×10^{-3}	-1.913×10^{-3}
$s_{3,i}$	$-$	6.585×10^{-2}	9.732×10^{-2}
$k_{\mathrm{d},i}$	$\mu\mathrm{m\,s}^{-1}$	5.450×10^5	5.450×10^5
$E_{\mathrm{A,d},i}$	$\mathrm{J\,mol}^{-1}$	2.825×10^4	2.825×10^4

volume is[30]

$$V(\boldsymbol{L}) = 10.9479 L_2^2 L_1 - 4.9825 L_2^3 \tag{2.9}$$

The density of KDP crystals is $\rho_{\mathrm{c}} = 2.34\,\mathrm{g\,cm}^{-3}$.[94] The parameters m_{s}, c_0, $\boldsymbol{L}_0$, $\boldsymbol{L}_{\mathrm{t}}$, and $V_{\min}$ (see eqs 2.3, 2.4, and 2.5) are specific to the case studies presented in Sections 2.5.3 and 2.5.4.

2.5.2 β L-Glutamic Acid (BLGA)

The crystal morphology of the β polymorph of L-glutamic acid is determined by the interplay of three independent facet families.[54,95] However, because the shape of these crystals is generally needle-like, it can be approximated by cylinders of suitable length L_1 and width L_2,[54] as shown in Figure 2.4. The corresponding approximate particle volume is given by

$$V(\boldsymbol{L}) = \frac{\pi}{4} L_2^2 L_1 \tag{2.10}$$
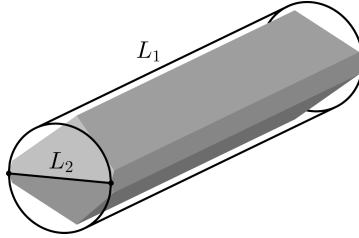
Figure 2.4: Ideal β L-glutamic acid crystal approximated by a cylinder with $\frac{L_1}{L_2} = \frac{50}{9}$; visualized using the multi-parametric toolbox (MPT3)[93]

The solubility of BLGA in water was measured by Schöll et al.[3] An exponential fit to these data yields

$$c^*(T) = 3.3652 \times 10^{-3} \exp\left(3.59 \times 10^{-2}\,\theta\right) \tag{2.11}$$

The growth rate model of BLGA in the L_1 and L_2 directions used in this chapter consists of the empirical expression

$$G_i = k_{g,i,1}(S-1)^{k_{g,i,2}} \exp\left(-\frac{k_{g,i,3}}{T}\right) \qquad i = 1,2 \tag{2.12}$$

where T is the temperature in Kelvin. The parameters were fitted according to Ochsenbein et al.,[54] but using the mean crystal length and width (as illustrated in Figure 2.4) as measured outputs and considering only desupersaturation experiments where both mean length and width increased over time. The resulting parameter values are listed in Table 2.2. The constraints on temperature and supersaturation were set to $T_{\min} = 298.15\,\mathrm{K}$, $T_{\max} = 314.15\,\mathrm{K}$ and $S_{\mathrm{G,min}} = 1.10$, $S_{\mathrm{G,max}} = 1.25$,

Table 2.2: Parameter values for the growth rates and the dissolution rates of BLGA.

Parameter	Unit	$i = 1$	$i = 2$
$k_{\mathrm{g},i,1}$	$\mathrm{\mu m\,s^{-1}}$	2.403×10^3	5.812×10^1
$k_{\mathrm{g},i,2}$	–	3.665	2.477
$k_{\mathrm{g},i,3}$	K	2.434×10^3	2.422×10^3
$k_{\mathrm{d},i,1}$	$\mathrm{\mu m\,s^{-1}}$	2.0	1.0
$k_{\mathrm{d},i,2}$	–	1.6	1.8

respectively. For BLGA, a fictitious dissolution rate model of the form

$$D_i = -k_{\mathrm{d},i,1}(1 - S)^{k_{\mathrm{d},i,2}} \qquad i = 1, 2 \tag{2.13}$$

was used, where the corresponding parameter values are also listed in Table 2.2. The temperature limits were the same as those for growth. The undersaturation limits were set to $S_{\mathrm{D,min}} = 0.9$ and $S_{\mathrm{D,max}} = 0.99$. The density of BLGA crystals is $\rho_{\mathrm{c}} = 1.59\,\mathrm{g\,cm^{-3}}$.[96] Analogous to KDP, the parameters m_{s}, c_0, $\boldsymbol{L}_0$, $\boldsymbol{L}_{\mathrm{t}}$, and V_{min} (see eqs 2.3, 2.4, and 2.5) are case-specific.

2.5.3 Case study 1: KDP

The first case study is based on the KDP model introduced in Section 2.5.1. For the SP approach, the region of interest in the crystal size and shape space was defined to be the rectangle bounded by $L_{1,\mathrm{min}} = 95\,\mathrm{\mu m}$, $L_{1,\mathrm{max}} = 560\,\mathrm{\mu m}$, $L_{2,\mathrm{min}} = 35\,\mathrm{\mu m}$, and $L_{2,\mathrm{max}} = 465\,\mathrm{\mu m}$. This region was discretized using a regular grid spacing of $\Delta L = 3.75\,\mathrm{\mu m}$. The parameters m_{s}, c_0, $\boldsymbol{L}_0$, $\boldsymbol{L}_{\mathrm{t}}$, and V_{min} were set to the values reported in Table 2.3. Note that the rather small value of the solvent mass m_{s} was chosen to achieve a significant variation of the solute concentration during the growth and dissolution stages, which in turn facilitates comparing the characteristics of the SP and the MS approach.

In a first step, the trade-off between the path time (from $\boldsymbol{L}_0$ to $\boldsymbol{L}_{\mathrm{t}}$)

Table 2.3: Parameter values for case study 1 (KDP).

Parameter	Unit	Value
m_s	g	0.0400
c_0	$g\,g^{-1}$	0.3325
$\boldsymbol{L}_0$	µm	$[200\ 200]^T$
$\boldsymbol{L}_t$	µm	$[320\ 200]^T$
V_{min}	µm^3	$V\big([140\ 120]^T\big) \approx 1.3 \times 10^7$

and the maximum allowed number of switches between growth and dissolution was quantified. For the SP approach, the methodologies described in Sections 2.3.2 and 2.3.3 were applied while setting $n_{max} = 15$. For the MS approach, eq 2.5 was solved repeatedly for the sequence of maximum allowed number of stages from $M = 1$ (no switch) to $M = 16$ (fifteen switches). For each number of stages, the problem was solved twice: once starting with a growth stage, and once starting with a dissolution stage. In all cases, the initial guesses for the decision variables were set to $500\,s$, $[200\ 200]^T$ µm, and $308.15\,K$ for the stage duration, the crystal dimensions, and the temperatures, respectively. The trade-offs obtained in this way are illustrated in Figure 2.5a. For the SP approach, the path with thirteen switches corresponds to the overall shortest path in the associated directed graph $\mathcal{H}$ (see Section 2.3.2). That is, given the space discretization $\Delta L = 3.75\,$µm, there exists no shorter path. Compared with the solutions of the SP approach, those of the MS approach correspond to path times that are up to $5.7\,\%$ smaller (one switch). This difference is attributed to the fact that the trajectories of the MS approach are not restricted to move between the nodes of a fixed grid in the crystal size and shape space. For both approaches, Figure 2.5a shows that at least one switch is required to reach the desired target $\boldsymbol{L}_t$. Furthermore, the decrease in the path time is $10.2\,\%$ (MS) and $14.2\,\%$ (SP) when choosing the path with fifteen and thirteen switches, respectively, instead of that with only one switch.

Figure 2.5a suggests that the paths with two or three switches are a good compromise between keeping the path time and the number

Figure 2.5: **(a)** Trade-off between the path time and the maximum allowed number of switches between growth and dissolution for both the SP (circles) and the MS (diamonds) approach in the first case study (Section 2.5.3). Points that are optimal in the Pareto sense are highlighted with filled markers. **(b)** Paths in the crystal size and shape space corresponding to the colored elements of the Pareto front obtained from the SP approach in Figure 2.5a. The gray dots represent the chosen space discretization. The dash-dotted line indicates the minimum allowed crystal volume $V_{\min}$. The gray shaded region excludes KDP morphologies for which one of the two facet families would be absent.

of switches low. The trajectories associated with two allowed switches are shown in Figure 2.6 for both approaches. Note that the piecewise-constant temperature profiles shown in Figure 2.6b are the actual results of the optimization. The trajectories of the crystal dimensions L (Figure 2.6a), the supersaturation S (Figure 2.6c), and the solute concentration c (Figure 2.6d) were obtained in a postprocessing step by conducting forward simulations of eq 2.3 using the computed temperature profiles. It can be seen in Figure 2.6a that the trajectories obtained with both the SP and the MS approach hit the target point L_t. Both approaches try to operate close to the constraints $S_{G,min}$ and $S_{D,min}$ (see Figure 2.6c). This behavior can be explained with the employed growth and dissolution rates for the KDP facets (see eqs 2.7 and 2.8): since $D_1 = D_2$ is assumed, there is no spatial degree of freedom during the dissolution stages, and keeping the undersaturation at $S_{D,min}$ thus corresponds to the fastest possible operating policy. For a fixed value of the solute concentration c, the ratio of G_1 and G_2 decreases monotonically with increasing supersaturation, i.e., growing at $S_{G,min}$ leads to the largest progress toward the target L_t measured in spatial coordinates.

If a maximum of thirteen instead of two switches is allowed, the SP and the MS approach yield the piecewise constant temperature profiles shown in Figure 2.7b. The other trajectories (see Figures 2.7a,c-d) were again obtained by forward simulation. The MS approach converged to a solution that makes use of only seven out of the allowed thirteen switches. An important observation is that both approaches lead to paths in the crystal size and shape space that cycle along the minimum volume line (see Figure 2.7a), while trying to stay as close as possible to the supersaturation and undersaturation constraints $S_{G,min}$ and $S_{D,min}$, respectively (see Figure 2.7c). The former behavior is a consequence of the explicit temperature dependence of the employed growth and dissolution rates (see eqs 2.7 and 2.8). In fact, a smaller crystal volume (i.e., closer to the minimum volume line) corresponds to a higher solute concentration in the closed system, and thus higher temperatures are required to achieve specific supersaturation or undersaturation levels (e.g., $S_{G,min}$ or $S_{D,min}$). These higher temperatures then increase the growth or dissolution rates. Therefore, for both approaches, larger allowed numbers of switches correspond to paths that cycle along the minimum allowed crystal volume line. For the SP approach, this behavior can be observed

in Figure 2.5b. In this way, the overall path time for reaching the target L_t can be reduced, and the characteristic shape of the trade-offs shown in Figure 2.5a follows. In an experimental context, the presence of thermal inertia would prevent an accurate implementation of the very short dissolution stages (see Figure 2.7b). However, note that the presented path planning methodologies provide a variety of Pareto-optimal trajectories, enabling the selection of the most suitable solution for the specific system.

Compared with the MS approach, the SP approach offers the possibility to quantify the trade-off between the path time and the maximum allowed number of switches for a large number of target points L_t. The directed graph $\mathcal{H}$ and the extended graphs $\mathcal{K}_G$ and $\mathcal{K}_D$ (see Sections 2.3.2 and 2.3.3) are independent of the target point L_t, i.e., they have to be constructed only once. The construction of $\mathcal{H}$, which is clearly the most computationally intensive step, required about 3000 s for this case study, using the parallel setup mentioned above. Having $\mathcal{K}_G$ and $\mathcal{K}_D$ available as well, the Pareto-like front for reaching a given target point L_t can be computed in the order of 1 s on an off-the-shelf notebook, whereas the MS approach requires in the order of 1000 s to 2000 s for each L_t.

In the context of this case study, the trade-off was quantified for each of the grid points used as target points. For each of these target points L_t, both the path with the minimum path time and the path corresponding to the minimum possible number of switches were computed. These solutions correspond to the two extreme points of the Pareto front of each target point. The results are illustrated in Figure 2.8. It can be seen in Figure 2.8b that a single dissolution stage decreases the initial crystal size, but the ratio $\frac{L_1}{L_2}$ remains constant since we have $L_1(0) = L_2(0)$ and $D_1 = D_2$. On the contrary, a single growth stage does increase the ratio $\frac{L_1}{L_2}$. In summary, based on the KDP model and the initial crystal dimensions considered in this case study, temperature cycling can only produce more elongated KDP crystal shapes. Whether this finding is desirable or not from a process design point of view depends on the specific target application of the solid product. In any case, it is recommended to model the growth and the dissolution rates for ranges of allowed supersaturation and undersaturation, respectively, as large as possible, since Figures 2.6c and 2.7c indicate that the corresponding constraints are a limiting factor.

Figure 2.6: Trajectories associated with two allowed switches for both the SP and the MS approach in the first case study (Section 2.5.3). SP growth and dissolution stages are colored in navy blue and dark red, respectively; MS stages in light blue and pink. **(a)** Paths in the crystal size and shape space. The gray dots represent the space discretization chosen for the SP approach. The dash-dotted line indicates the minimum allowed crystal volume $V_{\min}$. The gray shaded region excludes KDP morphologies for which one of the two facet families would be absent. **(b)** Temperature profiles; **(c)** supersaturation and undersaturation profiles; **(d)** solute concentration profiles.

Figure 2.7: Trajectories associated with thirteen allowed switches for both the SP and the MS approach in the first case study (Section 2.5.3). SP growth and dissolution stages are colored in navy blue and dark red, respectively; MS stages in light blue and pink. **(a)** Paths in the crystal size and shape space. The gray dots represent the space discretization chosen for the SP approach. The dash-dotted line indicates the minimum allowed crystal volume $V_{\min}$. The gray shaded region excludes KDP morphologies for which one of the two facet families would be absent. **(b)** Temperature profiles; **(c)** supersaturation and undersaturation profiles; **(d)** solute concentration profiles.
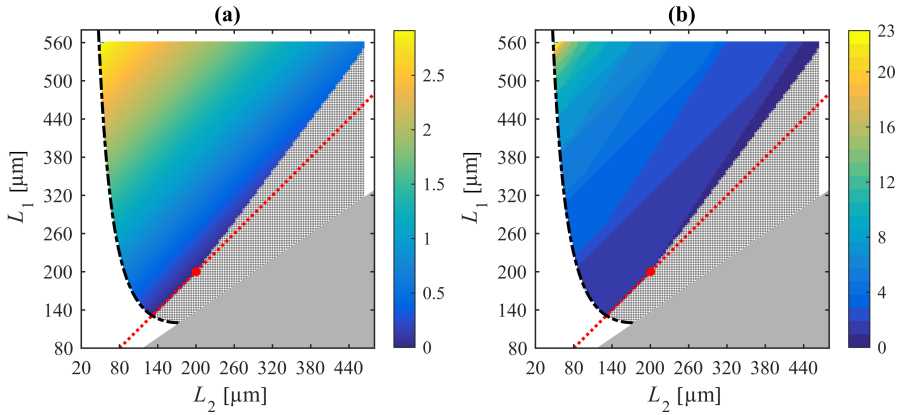
Figure 2.8: **(a)** Map that visualizes the minimum path time required to reach each grid point in the first case study (SP approach). The path time (in hours) is encoded in the color bar. **(b)** Map that shows the minimum number of switches required to reach each grid point in the first case study (SP approach). The red dot represents the initial crystal dimensions $\boldsymbol{L}_0$, and the red dotted line is the diagonal. The dash-dotted line indicates the minimum allowed crystal volume $V_{\min}$. The gray shaded region excludes KDP morphologies for which one of the two facet families would be absent. Gray dots represent grid points that cannot be reached from $\boldsymbol{L}_0$.

2.5.4 Case study 2: KDP with Different Amounts of Solvent

The purpose of the second case study is to investigate the effect of changing the solvent mass m_s in eqs 2.3 and 2.5 on the trade-off between the path time and the maximum allowed number of switches. For a given change in size and shape of the single crystal during growth or dissolution, different amounts of solvent lead to faster or slower variation of the solute concentration. In an experimental context, for a fixed initial solute concentration c_0 and fixed initial crystal dimensions $\boldsymbol{L}_0$, varying the solvent mass would correspond to changing the size of a small batch crystallizer containing the single crystal. A different interpretation presents itself in the form of the following thought experiment: assume that instead of a single crystal, a certain number of crystals was initially suspended in a small batch crystallizer, all of them with identical dimensions, and behaving identically during the subsequent growth and dissolution stages. Within the framework of eq 2.3, this situation could be modeled by simply dividing the solvent mass m_s by the number of crystals. Thus, solving the temperature cycling problem for small solvent masses can be seen as a step toward investigating the behavior of monodisperse crystal populations. In any case, more pronounced changes in the solute concentration are expected to amplify the influence of the explicit temperature dependence of the crystal growth and dissolution rates on the solution of the temperature cycling problem.

In this case study, the parameters listed in Sections 2.5.1 and 2.5.3 remained unaltered—apart from the solvent mass m_s. The MS approach was used to compute the trade-offs between the path time and the maximum allowed number of switches for the series of solvent masses $m_s = \{0.4\,\text{g}, 0.1\,\text{g}, 0.07\,\text{g}, 0.04\,\text{g}\}$. The resulting Pareto-like fronts are illustrated in Figure 2.9. Notice that the Pareto-like front for $m_s = 0.04\,\text{g}$ is the same as the corresponding MS front shown in Figure 2.5a in the first case study. As expected, the trade-off between the two objectives is most pronounced for the case with the smallest solvent mass $m_s = 0.04\,\text{g}$. Figure 2.9 also reveals that the solvent mass has the biggest impact on the path time for the paths with only one and two allowed switches. As can be seen from the trajectories shown in the previous case study (see Section 2.5.3), low numbers of switches correspond to paths that are
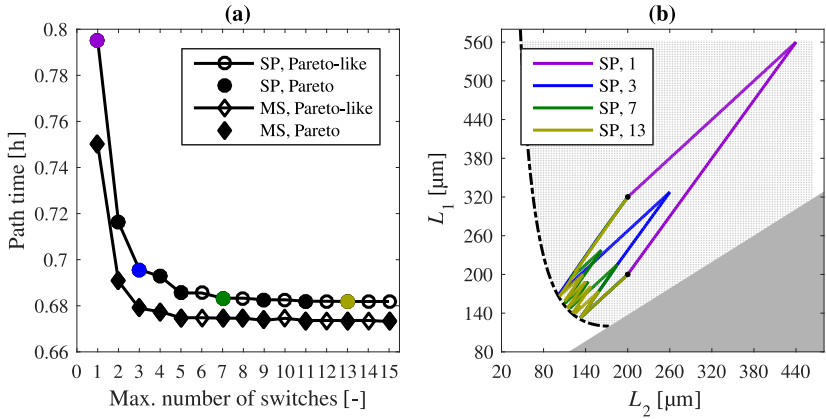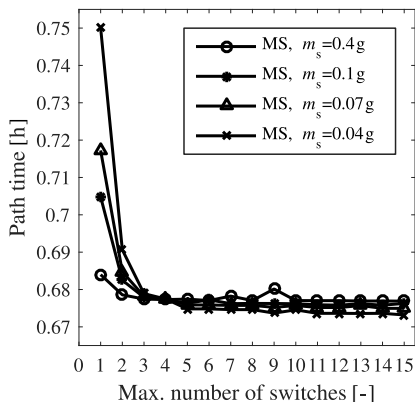
Figure 2.9: Pareto-like fronts between the path time and the maximum allowed number of switches between growth and dissolution for the compound KDP and a series of solvent masses m_s (Section 2.5.4). All fronts were computed using the MS approach.

forced to move far away from the minimum volume line, thus having to operate at relatively low solute concentrations for a long time span, and not being able to exploit the accelerating effect of the explicit temperature dependence of the growth and dissolution rates. On the other hand, if the solvent mass is high (and, consequently, the suspension density is low), this effect is negligible, and the process can be run using the lowest possible number of switches without a significant process time penalty.

In the case of $m_s = 0.4\,g$, the front shown in Figure 2.9 exhibits a comparatively longer path time at nine allowed switches. The reason is that the numerical solver converged to an unfavorable local optimum of eq 2.5 in this case, making use of only two out of the nine allowed switches. Note that this behavior could be partially mitigated by changing the details of the numerical implementation, e.g., the initial guess for the decision variables, the number of shooting intervals, the integrator scheme for the differential equations, or the NLP solver.

2.5.5 Case study 3: BLGA

In the context of the third case study, the SP approach was applied to the BLGA model introduced in Section 2.5.2. The rectangular region of the crystal size and shape space bounded by $L_{1,\min} = 20\,\mu\text{m}$, $L_{1,\max} = 350\,\mu\text{m}$, $L_{2,\min} = 16\,\mu\text{m}$, and $L_{2,\max} = 120\,\mu\text{m}$ was discretized with a resolution of $\Delta L_1 = 2.5\,\mu\text{m}$ and $\Delta L_2 = 2\,\mu\text{m}$. Keeping in mind the cylindrical particle shape model employed for BLGA (see Figure 2.4), a lower limit of $\frac{L_1}{L_2} = 1.5$ was imposed on the crystal aspect ratio. As BLGA crystals grow slowly, the constant temperature attainable regions (see Section 2.3.1) were restricted to contain only grid points that can be reached within a time span of three days for each growth and dissolution stage. The values of the parameters m_s, c_0, $\boldsymbol{L}_0$, $\boldsymbol{L}_t$, and $V_{\min}$ (see eqs 2.3, 2.4, and 2.5) are reported in Table 2.4. The value for $\boldsymbol{L}_t$ was chosen since the transition from $\boldsymbol{L}_0$ to $\boldsymbol{L}_t$ represents a reduction of the crystal aspect ratio $\frac{L_1}{L_2}$ from 3 to 2. The trade-off between the required path time and the allowed number of switches to achieve this transition is plotted in Figure 2.10. This figure shows that the desired change in crystal size and shape is feasible if at least one switch between growth and dissolution is made along the path. On the basis of the SP approach with the given space discretization, the path consisting of nine switches represents the overall shortest path in the associated directed graph $\mathcal{H}$ (see Section 2.3.2). However, the reduction in path time when choosing this solution instead of that with just one switch is only $1\,\%$. The reason for this is that the change of solute concentration along the paths is virtually negligible in this case study. In this context, note that compared with the initial KDP crystal in the previous two case studies (see Sections 2.5.3 and 2.5.4), the initial volume of the BLGA crystal considered here is about 300 times smaller.

The piecewise constant temperature profile that defines the path with two switches is illustrated in Figure 2.11b. A forward simulation of eq 2.3 with this temperature profile produced the trajectories shown in Figures 2.11a,c-d. It can be seen in Figure 2.11c that the desired reduction of the crystal aspect ratio requires operating close to the supersaturation and undersaturation limits $S_{\text{G,min}}$ and $S_{\text{D,max}}$, because these values correspond to low and high ratios of $\frac{G_1}{G_2}$ and $\frac{D_1}{D_2}$, respectively. A consequence of this is the long path time of $191\,\text{h}$ to achieve the requested size

Table 2.4: Parameter values for the BLGA case study.

Parameter	Unit	Value
m_{s}	g	0.0300
c_0	$\mathrm{g\,g^{-1}}$	0.0105
$\boldsymbol{L}_0$	µm	$[120\ 40]^{\mathrm{T}}$
$\boldsymbol{L}_{\mathrm{t}}$	µm	$[120\ 60]^{\mathrm{T}}$
$V_{\min}$	$\mathrm{µm}^3$	$V\big([50\ 40]^{\mathrm{T}}\big) \approx 6.3 \times 10^4$
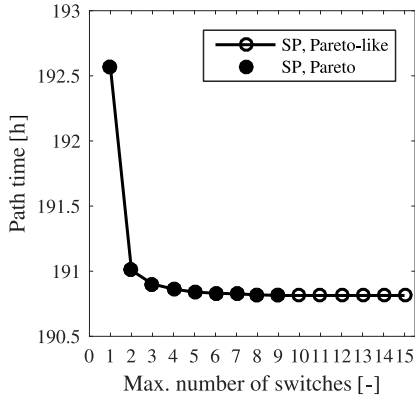
Figure 2.10: Trade-off between the path time and the maximum allowed number of switches between growth and dissolution for the SP approach in the third case study (Section 2.5.5). Points that are optimal in the Pareto sense are highlighted with filled markers.

and shape change.

Taking all the grid points in the discretized size and shape space as target points, the path corresponding to the minimum process time and that comprising the smallest possible number of switches was computed for each of them. The results are illustrated in Figure 2.12. These plots confirm that based on the BLGA model introduced in Section 2.5.2, the aspect ratio $\frac{L_1}{L_2}$ of the chosen initial crystal with dimensions $\boldsymbol{L}_0$ can be reduced by temperature cycling. However, the required process time is very high, i.e., in the order of a few hundred hours, which may make the implementation of this process unreasonable in many cases.

2.6 Conclusions

In this chapter, the systematic modification of single crystal size and shape via temperature cycling was treated for the case where crystal size and shape can be described by two independent dimensions. To this end, a derivative-free path planning methodology (SP) to compute a temperature profile that induces a desired size and shape change of a single crystal in a batch crystallization framework was proposed. This methodology is able to quantify the trade-off between the required process time and the allowed number of growth and dissolution stages. The results obtained by employing this methodology were compared with those obtained from an alternative, gradient-based approach (MS) in the form of a case study for the compound KDP.

A potential application of the SP approach lies within a model predictive control (MPC) framework. The methodology can be used to efficiently plan paths online, since efficient implementations of Dijkstra's algorithm[85] are widely available and the required directed graphs (see Section 2.3) can be constructed off-line. In this way, feedback of size and shape measurements can help to counteract the undesired influences of modeling errors, process disturbances, and the thermal inertia of the crystallizer. The key drawback of the SP approach is that it is based on a fixed, finite discretization of the crystal size and shape space. Furthermore, it cannot be easily extended to higher dimensional crystal shape models, mainly because the computational time for constructing the directed graphs may grow exponentially with the number of crystal dimensions.
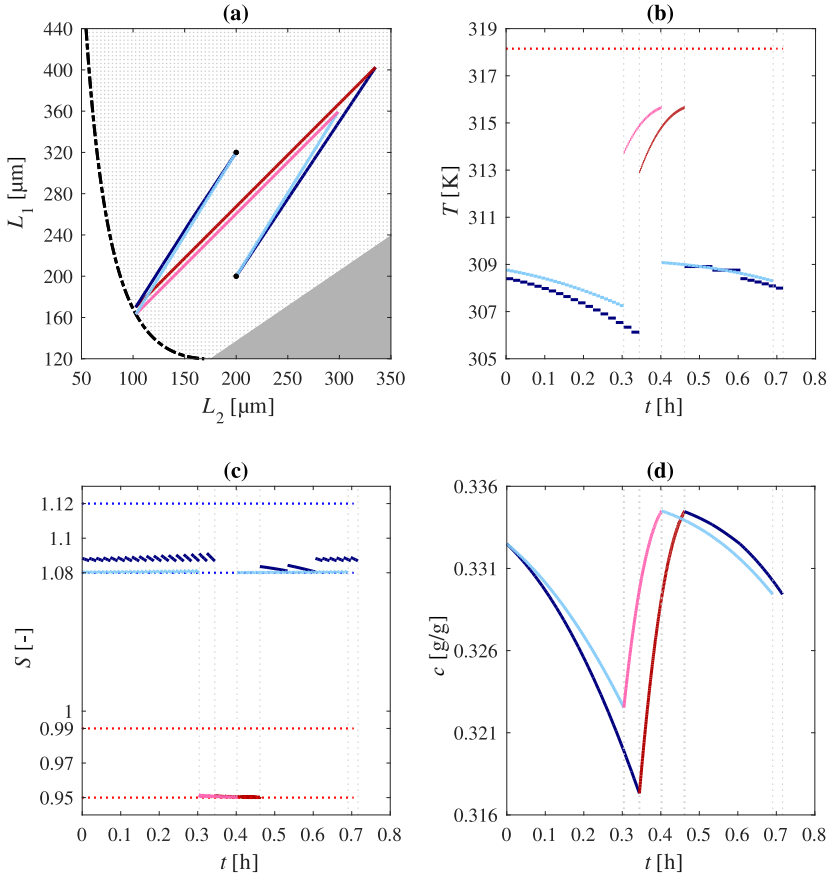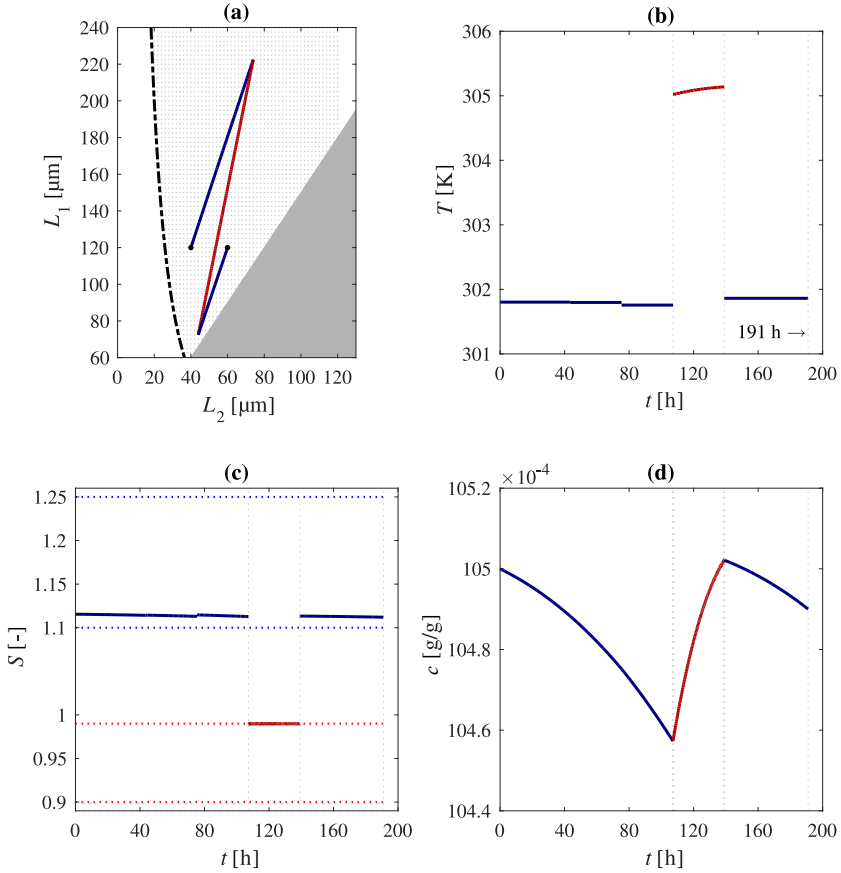
Figure 2.11: Trajectories associated with two allowed switches for the SP approach in the BLGA case study (Section 2.5.5). Growth and dissolution stages are colored in navy blue and dark red, respectively. **(a)** Paths in the crystal size and shape space. The gray dots represent the chosen space discretization. The dash-dotted line indicates the minimum allowed crystal volume $V_{\min}$. The gray shaded region designates a lower limit imposed on the aspect ratio of the BLGA crystal. **(b)** Temperature profiles; **(c)** supersaturation and undersaturation profiles; **(d)** solute concentration profiles.
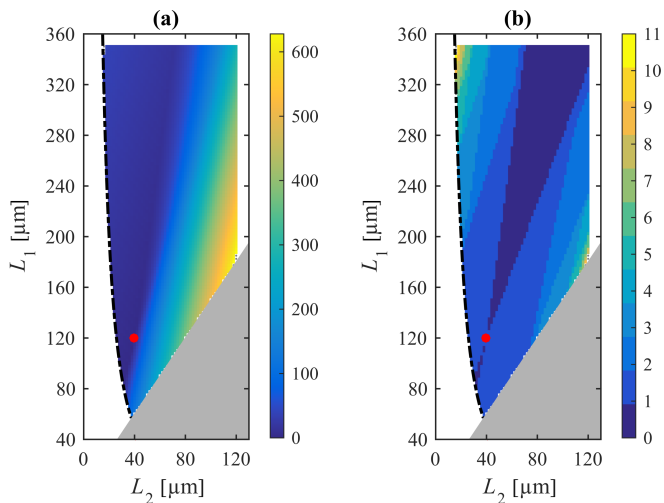
Figure 2.12: **(a)** Map that visualizes the minimum path time required to reach each grid point in the third case study (SP approach). The path time (in hours) is encoded in the color bar. **(b)** Map that shows the minimum number of switches required to reach each grid point in the third case study (SP approach). The red dot represents the initial crystal dimensions $\boldsymbol{L}_0$. The dash-dotted line indicates the minimum allowed crystal volume $V_{\min}$. The gray shaded region designates a lower limit imposed on the aspect ratio of the BLGA crystal. Gray dots represent grid points that cannot be reached from $\boldsymbol{L}_0$.

The MS approach does not require discretization of the size and shape space and it can be straightforwardly implemented for higher dimensional crystal shapes. Also, the general concept of multistage optimization can be applied to more complex situations, and to the corresponding models, involving populations of crystals undergoing temperature cycles. However, convergence to a satisfactory stationary point of the underlying nonconvex optimization problem cannot be guaranteed, which would make the MS approach a potentially poor choice in the context of MPC.

The results obtained from applying both path planning approaches within the case studies show that in the case of an explicit temperature dependence of the growth and dissolution rates, performing a large number of temperature cycles while keeping the crystal volume small can be favorable in terms of process time. However, such a strategy would correspond to a complicated operating protocol, and realizing the associated rapid sequence of temperature changes might not be feasible. Also, the uncertainties associated with the employed kinetic model have to be kept in mind, for instance concerning parametric uncertainty or model validity in the ranges of temperature, supersaturation, undersaturation, and crystal dimensions considered. A key strength of both path planning methodologies lies in their ability to provide not only one, but a variety of solutions to the temperature cycling problem, enabling the selection of a suitable path on a case-by-case basis by taking into account the above considerations.

The results of the presented case studies also illustrate the limitations of the temperature cycling process in terms of achieving a desired change in crystal size and shape. Namely, besides the possibility that the growth and dissolution rates of a certain compound may make such change entirely impossible, it might also be that the required process time is unacceptably high. The availability of both accurate kinetic models—valid within wide ranges of operating conditions—and suitable computational methodologies substantially facilitates the identification of such limitations.

Nomenclature

Acronyms

BLGA	β L-glutamic acid
DP	dynamic programming
KDP	potassium dihydrogen phosphate
MPC	model predictive control
MS	multistage
NLP	nonlinear program
ODE	ordinary differential equation
PS(S)D	particle size (and shape) distribution
SP	shortest path

Roman symbols

c	solute concentration (per mass of solvent basis) $[\mathrm{g\,g^{-1}}]$
c^*	solubility (per mass of solvent basis) $[\mathrm{g\,g^{-1}}]$
$\boldsymbol{D}$	dissolution rate vector $[\mathrm{\mu m\,s^{-1}}]$
D_i	dissolution rate along ith particle dimension $[\mathrm{\mu m\,s^{-1}}]$
E_A	activation energy $[\mathrm{J\,mol^{-1}}]$
F	final node of a path in a directed graph
$\boldsymbol{G}$	growth rate vector $[\mathrm{\mu m\,s^{-1}}]$
G_i	growth rate along ith particle dimension $[\mathrm{\mu m\,s^{-1}}]$
I	initial node of a path in a directed graph
k	growth or dissolution rate parameter, unit varies
$\boldsymbol{L}$	particle dimension vector $[\mathrm{\mu m}]$
L_i	ith particle dimension $[\mathrm{\mu m}]$
M	number of growth and dissolution stages $[-]$
m_s	solvent mass $[\mathrm{g}]$
n	number of switches between growth and dissolution $[-]$
$N_\mathcal{P}$	cardinality of a set of grid points $[-]$
$N_\mathcal{R}$	cardinality of a set of grid points within an attainable region $[-]$
R	ideal gas constant $[\mathrm{J\,mol^{-1}\,K^{-1}}]$
S	relative supersaturation or undersaturation, c/c^* $[-]$
s	growth rate parameter (see eq 2.7), unit varies

T	temperature [K]
t	time, unit varies
t_{f}	process time, unit varies
V	crystal volume [µm³]
v	node in a directed graph

Calligraphic symbols

$\mathcal{A}$	finite set of arcs in a directed graph
$\mathcal{B}$	finite set of arcs in an extended directed graph
$\mathcal{H}$	directed graph
$\mathcal{K}$	extended directed graph
$\mathcal{M}$	set of growth and dissolution stages
$\mathcal{P}$	finite set of grid points
$\mathcal{R}$	finite set of grid points within an attainable region
$\mathcal{V}$	finite set of nodes in a directed graph
$\mathcal{W}$	finite set of nodes in an extended directed graph

Greek symbols

θ	temperature, $\theta = T - 273.15$ [°C]
ρ_{c}	crystal density [g µm⁻³]

Superscripts and subscripts

0	initial value or condition
D	dissolution
d	dissolution
G	growth
g	growth
l	stage index
max	maximum or upper limit
min	minimum or lower limit
t	target

Chapter 3

Feedback Control for Growth Processes

3.1 Introduction

Due to the impact of the particle size and shape distribution (PSSD) obtained from a crystallization step on the efficiency of downstream operations as well as on product quality,[9,10] there is an incentive to manipulate particle size and shape already during the crystallization step. In batch crystallization, the variation of supersaturation lends itself to this task, since this quantity can readily be altered using physical actuators such as, e.g., the crystallizer jacket temperature. Consequently, considerable research efforts have been devoted to the calculation of temperature or supersaturation profiles that are, given a process model, optimal with respect to some performance measure. Such a mea-

sure can comprise quantities related to the one-dimensional particle size distribution (PSD) [75,97,98] or quantities related to the multidimensional PSSD. [62,99–103] However, it is well-known that the performance of crystallization processes relying on predefined operating policies is prone to deteriorate as a consequence of uncertainties in the model, entirely unmodeled phenomena, and unexpected disturbances. Feedback control is a promising approach to mitigate these undesirable effects, but its successful implementation requires online monitoring tools. [48,57–59,104] Imaging devices for monitoring particle size and shape have undergone significant progress within the last two decades. [105] Various contributions in the field of crystallization were reported in the literature. [20,23,32,38,39,53,81,106] For instance, the µ-DISCO is a stereoscopic imaging device tailored to provide statistically relevant PSSD measurements online (see also Section 1.2). [32]

Assuming or possessing online monitoring capabilities to track the evolution of the PSD or the PSSD, control schemes involving feedback of related quantities can be developed. Control strategies that take into account only the size of the particles but not their shape (i.e., measurements of the PSD or related quantities only) are relatively common in the literature. Several of these studies implement some form of model predictive control (MPC) and can thus be classified as model-based. [61,74,107–110] Approaches comprising model-free elements seem to appear less frequently. [111,112] The number of control schemes discussed in the literature that make use of measurements related to the PSSD (i.e., multiple characteristic particle dimensions) is yet limited. An early contribution relied on image analysis to control the shape of sodium chlorate crystals. [20] A proportional controller (i.e., model-free) for reaching a target average aspect ratio of potassium dihydrogen phosphate (KDP) crystals by manipulating the concentration of a tailor-made additive was also suggested. [113] Furthermore, computationally efficient nonlinear model predictive control (NMPC) schemes for the mean length and the mean aspect ratio of KDP crystals, including a discussion on the state estimation problem and the effect of uncertainties in the model, were presented. [114,115] Also, it was demonstrated experimentally that the average dimensions of a population of KDP crystals can be controlled using temperature cycling based on a pragmatic model predictive approach. [21] It is also worth noting that in the field of protein crystallization, a MPC

methodology that is concerned with crystal shape but avoids feedback of the latter by relying on growth rate models derived from extensive kinetic Monte Carlo simulations was suggested.[116,117]

In this chapter, a seeded batch cooling crystallization process where growth is the dominant phenomenon is considered. It is assumed that a multidimensional growth rate model and online PSSD monitoring capabilities are available to design feedback control strategies, where the accuracy of both the model and the monitoring is limited. A path following control (PFC) approach with the aim of driving the average dimensions of a population of needle-like seed crystals into a target region by varying the process temperature is proposed. Both a model-based and a model-free implementation of this control strategy are possible. A considerably more complex NMPC scheme is presented as well. First, simulation studies to assess and compare the effectiveness of these control strategies with respect to achieving the process goal are conducted. Since obtaining multidimensional growth rate models necessitates substantial efforts,[46,53–55] the requirements regarding the availability and accuracy of such models to make the feedback control approach effective are discussed. Obviously, these requirements go hand in hand with the complexity of the corresponding control strategy. Second, an experimental validation of the simplest of the proposed controllers, the model-free PFC, is presented using the system β L-glutamic acid (BLGA) in water.

This chapter is organized as follows. First, the problem to be investigated is stated in Section 3.2. Second, the path following control approach and the nonlinear model predictive controller are introduced in Sections 3.3 and 3.4, respectively. The process simulation framework, into which the feedback controllers were integrated, is described in Section 3.5. The simulation studies using both control strategies are presented in Section 3.6. Finally, the experimental campaign, where the model-free PFC scheme was applied, is described in Section 3.7.

3.2   Problem Statement

In this chapter, seeded batch cooling crystallization is considered. Growth of ensembles of needle-like particles whose size and shape can be approximated well by two independent dimensions is investigated. To obtain this approximation, generic particle models, such as that of a cylinder with

length L_1 and width L_2, are often employed, because imaging devices can measure the corresponding characteristic particle dimensions rapidly and robustly. [23,32,39] The supersaturation and the temperature of the process are constrained to regions where nucleation and agglomeration are negligible. Also, breakage is assumed to be negligible. These conditions enable the seed population to remain unimodal throughout the batch. Therefore, the control strategies presented in Sections 3.3 and 3.4 focus on the size and shape evolution of the seed crystals without addressing additional objectives concerning, e.g., nucleated crystals. Note that in this chapter, the term PSSD refers to a population of particles where each particle is characterized by two internal coordinates.

The goal for the controlled process is to drive an average measure of the size and shape of the particles in the seed population into a certain target region in the two-dimensional size and shape space. For instance, this space can be spanned by the number-weighted average dimensions

$$
\begin{aligned}
\bar{L}_{1,\mathrm{n}}(t) &= \frac{\mu_{10}(t)}{\mu_{00}(t)} \\
\bar{L}_{2,\mathrm{n}}(t) &= \frac{\mu_{01}(t)}{\mu_{00}(t)}
\end{aligned}
\tag{3.1}
$$

or by their volume-weighted counterparts

$$
\begin{aligned}
\bar{L}_{1,\mathrm{v}}(t) &= \frac{\mu_{22}(t)}{\mu_{12}(t)} \\
\bar{L}_{2,\mathrm{v}}(t) &= \frac{\mu_{13}(t)}{\mu_{12}(t)}
\end{aligned}
\tag{3.2}
$$

where

$$
\mu_{ij}(t) = \int\limits_{0}^{\infty} \int\limits_{0}^{\infty} L_1^i L_2^j f\big(t, L_1, L_2\big) \, \mathrm{d}L_1 \, \mathrm{d}L_2
\tag{3.3}
$$

represents the ij-cross moment of the number density function $f(t, L_1, L_2)$ (i.e., the PSSD) at time t. Note that until Section 3.6, the number density function is defined with respect to the solvent mass, i.e., f has units of $\mu m^{-2} \, kg^{-1}$. In the experimental parts of this chapter (Section 3.7 and the corresponding Appendix B), this is not the case and the number density has units of μm^{-2}. Obviously, according to eq 3.3, this change of units also applies to the cross moments. It is also worth mentioning that for a pure growth process with size-independent growth rates, a given seed PSSD $f_0(L_1, L_2)$ undergoes a rigid shift in the plane spanned by the two internal coordinates L_1 and L_2. In this case, the selection of target number-weighted average dimensions also specifies the target yield of the process.

The underlying assumption for controlling the process is that for a given solute concentration, for a given population, and within certain bounds for the temperature and the supersaturation, the ratio of the rate of change of the two average dimensions $\frac{\mathrm{d}\bar{L}_1}{\mathrm{d}t}/\frac{\mathrm{d}\bar{L}_2}{\mathrm{d}t}$ is a monotonic function of the process temperature. In this way, the evolution of the average shape can be influenced by varying the temperature and thus the supersaturation level. Note that this assumption is motivated by the strong and monotonic supersaturation dependence of a number of available multidimensional crystal growth rate models.[46,53,54] Still, it is important to keep in mind that it is generally not possible to achieve arbitrary ratios of the aforementioned rate of change. This fact leads to the concept of attainable regions for particle size and shape (see also Section 2.3.1).[21,52,62] It will be demonstrated that the feedback control approaches introduced in the following two sections can also be applied to automatically determine the boundaries of such attainable regions for a given seed population. In the case of the suggested model-free controller, this is possible without any prior knowledge of the multidimensional growth rate.

3.3 Path Following Control

The concept of path following control is known from robotics where, e.g., wheeled robots are made to follow a predefined path on a plane.[118,119] The basic idea of path following can be applied to the evolution of the average dimensions of a growing population of crystals. A schematic of
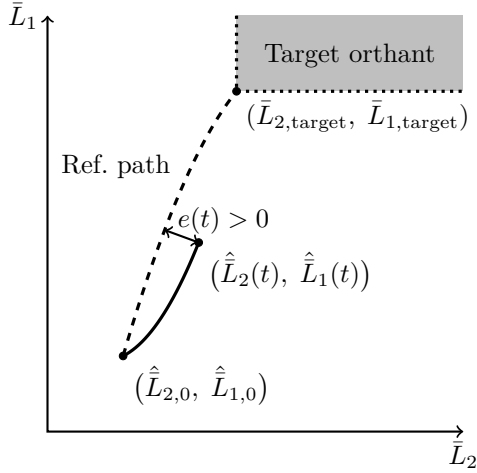
Figure 3.1: Schematic of the path following control approach.

this approach is shown in Figure 3.1. Given the measured average dimensions $[\hat{\bar{L}}_{1,0} \ \hat{\bar{L}}_{2,0}]^{\mathrm{T}}$ of the seed population and desired target average dimensions $[\bar{L}_{1,\text{target}} \ \bar{L}_{2,\text{target}}]^{\mathrm{T}}$, the evolution of the measured average dimensions $[\hat{\bar{L}}_1(t) \ \hat{\bar{L}}_2(t)]^{\mathrm{T}}$ is required to stay close to a predefined reference path that connects the two points. Note that, unlike in the case of robotics, in this application staying close to the reference path is not an objective per se, but merely a means toward the objective of reaching the target point. To this end, the lateral deviation of $[\hat{\bar{L}}_1(t) \ \hat{\bar{L}}_2(t)]^{\mathrm{T}}$ from the reference path in the two-dimensional crystal size and shape space is defined to be the control error $e(t)$, i.e.,

$$e(t) = \frac{\left(R_2'(t) - R_2(t)\right)\left(\hat{\bar{L}}_1(t) - R_1'(t)\right) + \left(R_1(t) - R_1'(t)\right)\left(\hat{\bar{L}}_2(t) - R_2'(t)\right)}{\sqrt{\left(R_2(t) - R_2'(t)\right)^2 + \left(R_1(t) - R_1'(t)\right)^2}}$$

(3.4)

where $[R_1(t)\ R_2(t)]^{\mathrm{T}}$ and $[R'_1(t)\ R'_2(t)]^{\mathrm{T}}$ are the two points of a discrete representation of the reference path that are closest to $[\hat{\bar{L}}_1(t)\ \hat{\bar{L}}_2(t)]^{\mathrm{T}}$ at time t, with the former point having a distance from the origin larger than the latter. This definition implies that $e(t) > 0$ if $[\hat{\bar{L}}_1(t)\ \hat{\bar{L}}_2(t)]^{\mathrm{T}}$ lies below the reference path, and vice versa (see Figure 3.1). A simple proportional-integral (PI) controller is chosen to keep $e(t)$ as close as possible to zero. This controller produces a feedback contribution

$$\Delta T_{\mathrm{fb}}(t) = k_{\mathrm{p}}\Big(e(t) + \frac{1}{\tau_{\mathrm{I}}} \int_{t_0}^{t} e(s)\ \mathrm{d}s\Big) \tag{3.5}$$

where k_{p} and τ_{I} are tuning parameters and t_0 is the seed addition time. This feedback contribution is added to a feedforward signal $T_{\mathrm{ff}}(t)$ (see Section 3.3.3) to obtain the set point for the process temperature

$$T_{\mathrm{set}}(t) = T_{\mathrm{ff}}(t) + \Delta T_{\mathrm{fb}}(t) \tag{3.6}$$

The set point $T_{\mathrm{set}}(t)$ and the corresponding relative supersaturation $S_{\mathrm{set}}(t) = c(t)/c^*\big(T_{\mathrm{set}}(t)\big)$ are constrained as follows: $T_{\min} \leq T_{\mathrm{set}}(t) \leq T_{\max}$ and $S_{\min} \leq S_{\mathrm{set}}(t) \leq S_{\max}$, respectively. Furthermore, integrator wind-up is limited by pausing the integration in eq 3.5 whenever one of the constraints on $T_{\mathrm{set}}(t)$ or $S_{\mathrm{set}}(t)$ is active.

By assigning a set point temperature that corresponds to a desired final supersaturation S_{final}, auxiliary functionality of the controller ends the batch as soon as the measured average dimensions have reached the target orthant, where the lower left corner of this orthant is given by the target point in Figure 3.1. Consequently, the batch time is not known a priori.

The steps listed below are necessary to design the PFC for a specific system.

1. Define the temperature and supersaturation limits $T_{\min}$, $T_{\max}$, $S_{\min}$, and $S_{\max}$, as well as the final supersaturation level S_{final}.

2. Given the seed PSSD with $[\hat{\bar{L}}_{1,0} \ \hat{\bar{L}}_{2,0}]^{\mathrm{T}}$, choose the desired target point $[\bar{L}_{1,\mathrm{target}} \ \bar{L}_{2,\mathrm{target}}]^{\mathrm{T}}$.

3. Choose the reference path and the feedforward signal $T_{\mathrm{ff}}(t)$.

4. Define the PI parameters k_{p} and τ_{I}.

Suggestions for carrying out these steps are given in the following subsections.

3.3.1 Temperature and Supersaturation Limits

The lower limit on the supersaturation $S_{\min}$ ensures significant growth, i.e., progress along the path, while the upper limit $S_{\max}$ prevents notable nucleation and agglomeration. The temperature bounds $T_{\min}$ and $T_{\max}$ can be imposed, e.g., by operational constraints of the equipment or by limited knowledge of the solubility. All these values should be selected according to prior experimental insight into the system that is to be controlled. The final supersaturation level S_{final} can be selected slightly above saturation in order to prevent unwanted dissolution of the product crystals due to uncertainty in the solubility data.

3.3.2 Target Selection

The evolution of the two average dimensions cannot be controlled independently; i.e., manipulating the process temperature T does not suffice to drive them to an arbitrary target point $[\bar{L}_{1,\mathrm{target}} \ \bar{L}_{2,\mathrm{target}}]^{\mathrm{T}}$. Changing the process temperature will influence the ratio $\frac{\mathrm{d}\bar{L}_1}{\mathrm{d}t}/\frac{\mathrm{d}\bar{L}_2}{\mathrm{d}t}$ according to the assumption made in Section 3.2, but it will also affect the overall growth speed by altering the supersaturation. If estimates of the attainable region [21,52,62] for the considered system are available, these can guide the selection of the target. If not, the target can be selected purely based on the desired final average size and shape. In this case, the process will probably not reach the target point, but the PFC will constantly take action and try to stay close to the reference path, only terminating the batch when the target orthant (see Figure 3.1) is reached.

3.3.3 Reference Path and Feedforward Signal

If a multidimensional growth rate model is available, the reference path and the feedforward signal $T_{\mathrm{ff}}(t)$ can be determined simultaneously by

running a dynamic optimization prior to starting the process. A suitable objective is to minimize the batch time subject to the dynamics of the process, and subject to reaching the interior of a given box around the target point. Further constraints are the bounds described in Section 3.3.1 and a realistic upper limit for the rate of temperature change. The decision variables are the batch time t_f and a parametrized version of the set point temperature profile $T_{\text{set}}(t)$. After performing this optimization, the optimized set point profile can directly be assigned to the feedforward temperature signal, i.e., $T_{\text{ff}}(t) = T_{\text{set,opt}}(t)$.

A considerably simpler alternative is to choose the reference path to be a line connecting $[\hat{\bar{L}}_{1,0} \ \hat{\bar{L}}_{2,0}]^{\text{T}}$ and $[\bar{L}_{1,\text{target}} \ \bar{L}_{2,\text{target}}]^{\text{T}}$ whose shape is consistent with the shape of an experimental estimate of the attainable region, or if the attainable region is unknown, to choose the straight line connecting the two points. The feedforward temperature signal $T_{\text{ff}}(t)$ can be chosen to be constant or, alternatively, some simple cooling profile. In this way, the PFC becomes a model-free approach relying solely on solubility data and on online monitoring to obtain measurements of the average dimensions. Below, this alternative approach will be referred to as model-free PFC, whereas the version featuring the optimization-based determination of the reference path is referred to as model-based PFC.

3.3.4 PI Parameters

Assigning the correct sign to the proportional gain k_p in eq 3.5 is crucial. This is best achieved by performing a small number of experimental batch runs in order to detect if the ratio $\frac{\mathrm{d}\bar{L}_1}{\mathrm{d}t} / \frac{\mathrm{d}\bar{L}_2}{\mathrm{d}t}$ increases or decreases with the process temperature. One possible way of doing so, which combines this task with the estimation of the attainable regions, is described in Section 3.6.1. Because of the meaning the two tuning parameters k_p and τ_I have in the PI control law (see eq 3.5), reasonable values can initially be selected according to physical insight. For instance, k_p can be chosen in the sense of a proportional band, i.e., based on a fraction of the span of the temperature interval defined by the constraints T_{min}, T_{max}, S_{min}, and S_{max} for a given initial solute concentration. As to the integrator time constant τ_I, a single-digit percentage of a rough estimate of the total batch time can be taken. If necessary, the values obtained in this way can subsequently be tuned according to the outcome of batches controlled by the PFC.

3.4 Nonlinear Model Predictive Control

NMPC is a considerably more sophisticated control strategy than the PFC approach introduced in Section 3.3. The basic idea is to repeatedly solve a dynamic optimization problem (similar to the one suggested in Section 3.3.3) at fixed sampling instants. The initial conditions of these optimization runs are measurements or estimates of the current process states. After an optimization run triggered at a sampling instant has terminated, only the first value in the obtained optimal control input profile is implemented. The procedure is then repeated at the next sampling instant.

In this chapter, the goal of the dynamic optimization runs performed at each sampling instant $t_k = t_0 + k t_{\text{samp}}$ $(k = 0, 1, 2, \dots)$ is to find the process temperature profile $T(t)$ and the batch time t_{f} that minimize the deviation of the final average crystal dimensions from the target point. To favor short batches, the batch time is penalized as well in the objective function. The process temperature, rate of temperature change, and the supersaturation are constrained, and the final average dimensions have to lie within the target orthant (see Figure 3.1). The mathematical formulation of this problem is

$$
\begin{aligned}
& \underset{T(t),\ t_{\text{f}}}{\text{minimize}} && q_{\bar{L}_1}\left(\bar{L}_1(t_k + t_{\text{f}}) - \bar{L}_{1,\text{target}}\right)^2 + \\
& && q_{\bar{L}_2}\left(\bar{L}_2(t_k + t_{\text{f}}) - \bar{L}_{2,\text{target}}\right)^2 + \frac{t_{\text{f}}}{t_{\text{f},0}} \\
& \text{subject to} && \frac{\mathrm{d}\mu_{00}(t)}{\mathrm{d}t} = 0 \\
& && \frac{\mathrm{d}\mu_{ij}(t)}{\mathrm{d}t} = iG_1\mu_{(i-1)j}(t) + jG_2\mu_{i(j-1)}(t), \\
& && ij \in \{10, 01, 11, 20, 02, 21, 12, 22, 03, 13\} \\
& && \frac{\mathrm{d}c(t)}{\mathrm{d}t} = -\rho_{\text{c}}k_{\text{v}}\frac{\mathrm{d}\mu_{12}(t)}{\mathrm{d}t} \\
& && S(t) = \frac{c(t)}{c^*\!\left(T(t)\right)}
\end{aligned}
\tag{3.7}
$$

$$T_{\min} \leq T(t) \leq T_{\max}$$
$$\left| \frac{\mathrm{d}T(t)}{\mathrm{d}t} \right| \leq \dot{T}_{\max}$$
$$S_{\min} \leq S(t) \leq S_{\max}, \qquad t \in [t_k, \ t_k + t_{\mathrm{f}}]$$
$$t_{\mathrm{samp}} \leq t_{\mathrm{f}}$$
$$T(t_k) = \hat{T}(t_k)$$
$$c(t_k) = \hat{c}(t_k)$$
$$\mu_{ij}(t_k) = \hat{\mu}_{ij}(t_k)$$
$$\bar{L}_{1,\mathrm{target}} \leq \bar{L}_1(t_k + t_{\mathrm{f}})$$
$$\bar{L}_{2,\mathrm{target}} \leq \bar{L}_2(t_k + t_{\mathrm{f}})$$

where $q_{\bar{L}_i}$ $(i = 1, 2)$ are weighting factors for penalizing the target deviation in the objective function, $t_{\mathrm{f},0}$ is an initial guess for the batch time t_{f}, $G_i = G_i\big(S(t), T(t)\big)$ $(i = 1, 2)$ are the size-independent growth rates along the two particle dimensions, ρ_{c} is the crystal density, k_{v} is the volume shape factor ($\pi/4$ for cylindrical particles), $\dot{T}_{\max}$ is an upper limit on the rate of temperature change, and t_{samp} is the sampling time of the controller. The dynamics of the process are given by the method of moments [25] and the material balance for the solute. The set of cross moments μ_{ij} with $ij \in \{00, 10, 01, 11, 20, 02, 21, 12, 22, 03, 13\}$ is considered to be able to handle both the number-weighted ($\bar{L}_i = \bar{L}_{i,\mathrm{n}}$, $i = 1, 2$) and the volume-weighted ($\bar{L}_i = \bar{L}_{i,\mathrm{v}}$, $i = 1, 2$) average dimensions. The state estimates at time t_k, and the measured process temperature at the same instant of time, are $\hat{c}(t_k)$ and $\hat{\mu}_{ij}(t_k)$, and $\hat{T}(t_k)$, respectively. It is well-known that obtaining accurate state estimates is a nontrivial task in general, which motivated dedicated research also in the field of batch crystallization.[120] In this chapter, a simplified approach to the state estimation problem is pursued. This approach is described in Section 3.5.5.

The optimization problem posed in eq 3.7 is a DAE-constrained optimal control problem, where the solute concentration $c(t)$ and the cross moments $\mu_{ij}(t)$ represent the differential states of the DAE system and the relative supersaturation $S(t)$ corresponds to its algebraic state. One

approach to obtaining a numerical solution to such a problem is direct transcription, where the problem is transformed into a large scale non-linear program (NLP) by simultaneously discretizing in time both the continuous control profile $T(t)$ and the states of the DAE system. [89] For the implementation in this chapter, a piecewise linear discretization with K intervals was chosen for the profile $T(t)$. The state evolution of the DAE system in each of these intervals was discretized using M steps of the implicit Euler scheme. These direct transcription steps were implemented using the software CasADi (v3.3). [91] A stationary point of the resulting NLP was computed using IPOPT (v3.12). [92] If the solver reported termination in a local minimum, the optimized piecewise linear temperature profile was defined to be the current $T_{\text{set,opt}}$ and the value $T_{\text{set,opt}}(t_k + t_{\text{samp}})$ was implemented as the current process temperature set point $T_{\text{set}}(t_k)$. Otherwise, the previous value was kept, i.e., $T_{\text{set}}(t_k) = T_{\text{set}}(t_{k-1})$. As in the PFC strategy, the batch was considered to be complete when the measurement of the average dimensions reached the target orthant. In this case, the temperature corresponding to S_{final} was chosen to be the set point temperature.

Since the NLP introduced above is inherently nonconvex, there is no guarantee of finding the global optimum. For improving the closed-loop behavior of the NMPC, i.e., for promoting convergence to similar control strategies of subsequent optimization runs, it was helpful to initialize the decision variables with the solution obtained at the previous sampling instant. Note that a discussion of recursive feasibility and stability of the considered NMPC problem lies outside the scope of this work. Still, in the scope of the simulation studies presented in Section 3.6, it can be said that neither feasibility nor stability issues were observed with the chosen discretization parameters K and M.

3.5 Process Simulation Framework

The performance of the control strategies introduced in Sections 3.3 and 3.4 was analyzed and compared using a custom process simulation framework that is illustrated schematically in Figure 3.2. This framework features a population balance model (PBM) with a dedicated numerical solver, initialization of this model with experimentally acquired seed PSSDs, a thermal model for a 2 L jacketed batch crystallizer connected
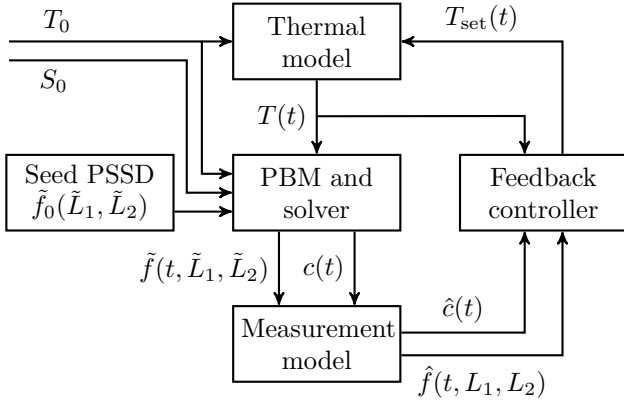
Figure 3.2: Schematic of the process simulation framework.

to a thermostat, and measurement models for the crystal population (and its cross moments $\hat{\mu}_{ij}(t)$) as well as for the solute concentration. The measurements are modeled and provided to the chosen feedback controller at the sampling instants $t_k = t_0 + kt_{\mathrm{samp}}$ $(k = 0, 1, 2, \dots)$. On the basis of this information, the controller decides about the new process temperature set point $T_{\mathrm{set}}(t_k)$.

A key feature of the framework is the combination of a morphological population balance model with a detailed measurement model for the PSSD. The framework simulates the process by solving a morphological population balance model (MPBM) that is based on faceted crystals modeled as convex polyhedra. On the other hand, the measurement model for the PSSD is based on a simpler, generic particle model, since it emulates the capabilities of an imaging-based online monitoring device for the particle size and shape evolution. [23,32,39]

In the following subsections, the constituent parts of this framework are explained in more detail.

3.5.1 Population Balance Model and Solver

A morphological population balance equation for the compound BLGA was used to simulate the crystallization of needle-like particles. The

approach applied in the preliminary virtual experiments presented in ref 54 was followed. In this approach, the BLGA crystals are modeled as convex polyhedra according to the three characteristic facet families $\{101\}$, $\{010\}$, and $\{021\}$.[37] The aspect ratio between the two facet families $\{010\}$ and $\{021\}$ is fixed to 1, which excludes the possibility of virtual facets and leads to a two-dimensional population $\tilde{f}(t, \tilde{L}_1, \tilde{L}_2)$, where the tilde superscript is used to explicitly distinguish the polyhedral particle description from the generic, cylindrical particle model. The two corresponding particle dimensions are defined as $\tilde{L}_1 = L_{\{101\}}$ and $\tilde{L}_2 = L_{\{010\}} = L_{\{021\}}$, where $L_{\{101\}}$ and $L_{\{010\}} = L_{\{021\}}$ are the perpendicular distances of the facets to the center of the crystal. In this case, and under the assumption of a perfectly mixed reactor, the MPBM for the growth process is

$$\frac{\partial \tilde{f}}{\partial t} + \frac{\partial \left(\tilde{G}_1 \tilde{f}\right)}{\partial \tilde{L}_1} + \frac{\partial \left(\tilde{G}_2 \tilde{f}\right)}{\partial \tilde{L}_2} = 0 \tag{3.8}$$

where $\tilde{G}_i$ $(i = 1, 2)$ are the facet growth rates. In this chapter, these facet growth rates were obtained by transforming the BLGA growth rates

$$G_i = k_{g,i,1}(S - 1)^{k_{g,i,2}} \exp\left(-\frac{k_{g,i,3}}{T}\right) \qquad i = 1, 2 \tag{3.9}$$

where the temperature T is in Kelvin here. These growth rates were reported elsewhere (see also Section 2.5.2)[52] and they are valid for the cylindrical particle model. The corresponding parameters are listed in Table 3.1. The transformation was performed according to

$$\tilde{G}_1 = \frac{1}{2} \cos(36.6°) G_1 \tag{3.10}$$
$$\tilde{G}_2 = \frac{1}{2} G_2$$

Table 3.1: Parameter values for the growth rates in eq 3.9.

Parameter	Unit	$i = 1$	$i = 2$
$k_{\mathrm{g},i,1}$	$\mu\mathrm{m\,s}^{-1}$	2.403×10^3	5.812×10^1
$k_{\mathrm{g},i,2}$	$-$	3.665	2.477
$k_{\mathrm{g},i,3}$	K	2.434×10^3	2.422×10^3

where the first relation relies on the detailed crystal geometry,[54] and the second relation represents an assumption that was made because it is exceedingly difficult to separate the influences of the two facet families $\{010\}$ and $\{021\}$ on G_2, the growth rate in the width direction.

To model also the evolution of the solute concentration $c(t)$, it is necessary to couple eq 3.8 with the material balance

$$\frac{\mathrm{d}c}{\mathrm{d}t} = -\rho_{\mathrm{c}} \frac{\mathrm{d}}{\mathrm{d}t} \int\limits_0^\infty \int\limits_0^\infty V_{\mathrm{c}}(\tilde{L}_1, \tilde{L}_2) \tilde{f}\big(t, \tilde{L}_1, \tilde{L}_2\big) \,\mathrm{d}\tilde{L}_1 \,\mathrm{d}\tilde{L}_2 \tag{3.11}$$

where $V_{\mathrm{c}}(\tilde{L}_1, \tilde{L}_2)$ is the volume of a polyhedral crystal with given facet distances $\tilde{L}_1$ and $\tilde{L}_2$.

The initial and boundary conditions

$$\tilde{f}(t_0, \tilde{L}_1, \tilde{L}_2) = \tilde{f}_0(\tilde{L}_1, \tilde{L}_2) \tag{3.12}$$
$$\tilde{f}(t, 0, \tilde{L}_2) = 0$$
$$\tilde{f}(t, \tilde{L}_1, 0) = 0$$
$$c(t_0) = c_0 = S_0 c^*(T_0)$$

were employed to solve eqs 3.8 and 3.11. The numerical solution was obtained using a fully discrete variant of a high resolution finite volume scheme relying on the van Leer flux limiter.[121] In this study, the compu-

tational grid was chosen to span the ranges $\tilde{L}_1 \in [0, \; 400\cos(36.6°)]$ µm and $\tilde{L}_2 \in [0, \; 100]$ µm with a resolution of 640 and 480 grid points, respectively. The polyhedral particle volume $V_c(\tilde{L}_1, \tilde{L}_2)$ used in eq 3.11 was precomputed numerically for each point $[\tilde{L}_1 \; \tilde{L}_2]^\mathrm{T}$ in this grid using the Multi-Parametric Toolbox.[93]

3.5.2 Seed PSSD

The seed population $\tilde{f}_0(\tilde{L}_1, \tilde{L}_2)$ in eq 3.12 was obtained from a sampled population of needle-like crystals measured earlier.[54] Since this measurement was performed on the basis of a cylindrical particle model with particle length L_1 and width L_2, these dimensions were transformed into the corresponding polyhedral facet distances $\tilde{L}_i$ ($i = 1, 2$) by applying the same transformation as given in eq 3.10. Subsequently, the sampled and transformed number density function was scaled to match the desired seed mass m_seed, resulting in the seed PSSD $\tilde{f}_0(\tilde{L}_1, \tilde{L}_2)$.

3.5.3 Thermal Model

A black-box modeling approach was applied to dynamically relate the process temperature set point $T_\mathrm{set}(t)$ to the actual process temperature $T(t)$ (see Figure 3.2). To this end, step response data were collected from a 2 L jacketed batch crystallizer that was filled with 2 kg of deionized and filtered water, stirred at 300 rpm, and connected to a CC240wl-CC3 thermostat (Huber, Offenburg, Germany) with fixed internal controller parameters (P-cascade = 1000, I-cascade = 1000, D-cascade = 0). The second-order model

$$\frac{\mathrm{d}^2 T(t)}{\mathrm{d}t^2} + 2\Gamma\omega_0 \frac{\mathrm{d}T(t)}{\mathrm{d}t} + \omega_0^2 T(t) = \omega_0^2 T_\mathrm{set}(t) \tag{3.13}$$

was fitted to these data, which yielded the two model parameters $\Gamma = 4.1 \times 10^{-1}$ and $\omega_0 = 3.7 \times 10^{-3}\,\mathrm{s}^{-1}$.

The differential equation given in eq 3.13 will subsequently be used as a simple model for the dynamic transition of the current process temperature $T(t)$ to the set point temperature $T_\mathrm{set}(t)$ issued by the feedback controller, also when the actual mass in the crystallizer is not exactly 2 kg, but in the order of this value.

3.5.4 Measurement Model

Measurements of the crystal population at each sampling instant were emulated using the virtual test bench (VTB) introduced previously.[39] The basic principle is uniform sampling of particles from the current morphological population, random placement and orientation of subsets of the corresponding convex polyhedra in a virtual flow cell, followed by stereoscopic projection, image analysis, and PSSD reconstruction. The VTB was adapted to match the characteristics of the µ-DISCO,[32] especially concerning the flow cell dimensions, the camera resolution and magnification, and the stereoscopic contour matching. The following pipeline describes the sequence of steps leading to a measurement of the PSSD at a sampling instant t_k:

1. Uniform sampling of N_s particles from the number density function $\tilde{f}(t_k, \tilde{L}_1, \tilde{L}_2)$.

2. Placement of a subset of N_p of the corresponding convex polyhedra (which were generated with the Multi-Parametric Toolbox[93]) in the virtual flow cell, using random particle positions and orientations, but excluding the possibility of intersecting particles or particles overlapping the borders of the cell.

3. Generation of two two-dimensional projections in order to emulate stereoscopic imaging.

4. Conversion to binary images and particle contour extraction.

5. Stereoscopic contour matching as described previously.[32]

6. Characterization of the dimensions L_1 and L_2 of the particles by imposing the generic, cylindrical particle model.[23]

7. Repetition of steps 2 through 6 until all the N_s sampled particles have been placed in the cell.

8. Application of a binning protocol to obtain the sampled PSSD $\hat{f}(t_k, L_1, L_2)$ from the characterized particle dimensions.[23]

In this study, the VTB parameters introduced above were fixed at $N_s = 4000$ and $N_p = 25$. These values were chosen to be on the conservative
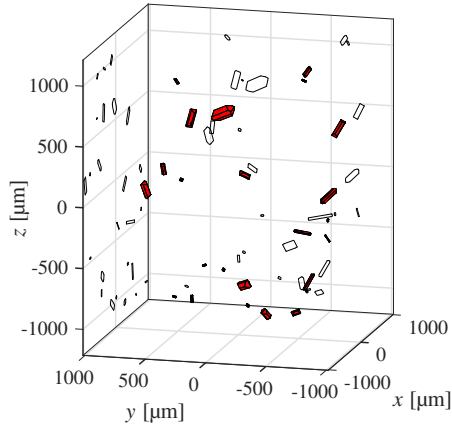
Figure 3.3: Arbitrary state of the virtual flow cell, containing 25 BLGA crystals shown as red convex polyhedra. The black solid lines on the xz- and on the yz-plane are the corresponding projections of the particle contours; i.e., these two planes and the contours form the virtual images to be analyzed subsequently.

side concerning the accuracy of the imaging method in the simulation, since typically around 10 000 particles per sampling instant are analyzed in a real experiment, and given the total number of particles in the seed population, one would expect about N_p particles to be present in the flow cell at each time instant. The chosen values of N_s and N_p lead to 160 different flow cell states and corresponding pairs of virtual images to be analyzed at each sampling instant. An example of such a state is shown in Figure 3.3. Using these parameters, typically about 90 % of the N_s particle contours could be matched and the corresponding particles characterized.

The measurements of the solute concentration were emulated by sampling from the Gaussian distribution

$$\hat{c}(t_k) \ \sim \ \mathcal{N}\big(a_{\hat{c}}c(t_k),\, b_{\hat{c}}^2\big) \tag{3.14}$$

where $a_{\hat{c}}$ and $b_{\hat{c}}$ are parameters needed to define the mean of the Gaussian and its standard deviation, respectively. In this study, the parameters $a_{\hat{c}}$ and $b_{\hat{c}}$ were fixed at the values 1.0 and $0.2\,\mathrm{g\,kg^{-1}}$, respectively (see also Table 3.2). This choice leads to measurement noise levels that are similar, but slightly larger in magnitude than those observed in ATR-FTIR data obtained experimentally from the studied system (BLGA in water).

Finally, it was assumed that the feedback controllers have access to perfect measurements of the process temperature $T(t)$, i.e., $\hat{T}(t_k) = T(t_k)$.

3.5.5 Interface to the Feedback Controllers

The measurements of the PSSD, of the solute concentration, and of the temperature obtained at each sampling instant need to be made available to the feedback controllers. Note that the former two measurements are noisy.

The PFC strategy requires measurements of the average particle dimensions, the solute concentration, and the process temperature. The noisy solute concentration measurements $\hat{c}(t_k)$ were low-pass filtered by the discretized version of a first-order element with a corner frequency of $1/30$ of the sampling frequency. Regarding the size and shape measurements, the number-weighted average dimensions of the sampled PSSD $\hat{f}(t_k, L_1, L_2)$ (see the last step of the sequence listed in Section 3.5.4) were calculated according to eq 3.1. These two average dimensions were then low-pass filtered individually by a second-order Butterworth filter designed using the MATLAB command `butter`,[122] where the cutoff frequency was chosen to be $1/10$ of the sampling frequency. The control error $e(t)$ was computed according to eq 3.4 using these filtered values. Note that, unlike in the case of the solute concentration, no artificial noise was added to the average dimensions calculated from the sampled PSSDs. Still, random sampling of N_s particles from the true morphological population and the characteristics of the measurement model (i.e., the VTB) already introduce noise and thus uncertainty into these signals.

The NMPC approach requires measurements of all the cross moments $\mu_{ij}(t_k)$ listed in Section 3.4, of the solute concentration, and of the process temperature. The solute concentration was low-pass filtered

making use of the same filter element as in the PFC strategy. Before calculating the cross moments of the sampled PSSD and using them as initial state estimates for the current NMPC iteration, the sampled PSSD $\hat{f}(t_k, L_1, L_2)$ was scaled according to

$$\hat{f}_{\text{scaled}}(t_k, L_1, L_2) = \hat{f}(t_k, L_1, L_2) \frac{c_0 - \hat{c}_{\text{filt}}(t_k) + \frac{m_{\text{seed}}}{m_{\text{solvent}}}}{k_{\text{v}} \rho_{\text{c}} \hat{\mu}_{12}(t_k)} \tag{3.15}$$

where $\hat{\mu}_{12}(t_k)$ was computed from $\hat{f}(t_k, L_1, L_2)$ and $\hat{c}_{\text{filt}}(t_k)$ is the low-pass filtered $\hat{c}(t_k)$. Note that the numerator of the scaling factor in eq 3.15 represents an estimate of the mass of solids per mass of solvent currently in the crystallizer, whereas the denominator is the sampled mass of solids per mass of solvent. Together with the low-pass filtering of $\hat{c}(t_k)$, this scaling and the subsequent calculation of the cross moments according to eq 3.3 can be seen as a state estimation approach, albeit it largely lacks the filtering capabilities of more sophisticated concepts. In the scope of this study, the NMPC was found to perform well using this approach.

3.6   Simulation Studies

The performance of the feedback controllers introduced in Sections 3.3 and 3.4 was assessed by coupling them with the process simulation framework presented in Section 3.5. The PFC approach was compared with the NMPC strategy. For both these control strategies, the number-weighted average dimensions, as defined in eq 3.1, were taken as the quantities to be controlled. It is emphasized here that the process model based on the polytopic particle shape model (see eqs 3.8, 3.10, 3.11, and 3.12) was not known to either of the presented feedback controllers, but merely served to simulate a virtual crystallization process.

Due to the elaborate measurement model for the PSSD presented in Section 3.5.4, the ratio between simulated batch time and required computational time was about 10 to 1 using all the four cores of an Intel Xeon E5-1630 v3 @ 3.70 GHz machine equipped with 32.0 GB of RAM in parallel. The time required for the numerical solution of the optimization problem posed in eq 3.7 was in the order of 2 s and thus it had a small impact on the overall computational time.

3.6.1 Path Following Control

In a first step, the model-free PFC (see Section 3.3) was used to obtain an estimate of the attainable region for the number-weighted average dimensions when starting from a given seed PSSD. To this end, two simulations were run using the parameter values listed in Table 3.2. The goal of the first closed-loop run was to automatically estimate the upper boundary of the attainable region. Therefore, an extreme target corresponding to substantial growth along L_1 and almost no growth along L_2 was chosen, i.e., $[\bar{L}_{1,\text{target}} \ \bar{L}_{2,\text{target}}]^{\text{T}} = [150 \ 30]^{\text{T}}$ µm. The second run was intended to estimate the lower boundary of the attainable region; i.e., the target $[\bar{L}_{1,\text{target}} \ \bar{L}_{2,\text{target}}]^{\text{T}} = [100 \ 60]^{\text{T}}$ µm was chosen, which corresponds to substantial growth along L_2. In order to plan the model-free reference paths (see Section 3.3.3), the first measurement $[\hat{\bar{L}}_{1,\text{n}}(t_0) \ \hat{\bar{L}}_{2,\text{n}}(t_0)]^{\text{T}}$ of each run (which was in the neighborhood of $[74.5 \ 27.5]^{\text{T}}$ µm for both runs) was taken as the initial point and connected with the target point using a straight line, i.e., the path was planned online during the first controller step. Furthermore, a constant feedforward temperature profile $T_{\text{ff}}(t) = T_0$ was assigned. The results of these two runs are illustrated in Figure 3.4, where the first run and the second run are referred to as run α and β, respectively. As expected, it can be seen that both runs failed to reach their target points. Run β did not even reach its target orthant, because the process time was restricted to 50 h. Still, the slopes of the evolutions of the measured average dimensions seem to be fairly constant over the course of both runs, thus enabling a linear extrapolation indicated by the dotted green lines in Figure 3.4a. The cone-like area in between these lines can be seen as an estimate of the attainable region. Note that the fairly constant slopes of the boundaries of the attainable region are a direct consequence of the growth rate model given in eqs 3.9 and 3.10, since the ratio $\tilde{G}_1/\tilde{G}_2$, which determines these slopes in the case of pure growth using number-weighted average dimensions, is effectively determined by the supersaturation level. However, the model-free PFC is not aware of this fact. It does not rely on any specific structure of the growth rates, as long as the basic assumption in Section 3.2 is satisfied.

The time series of the temperature, the concentration, the supersaturation, and the control error of the two runs are plotted in Figure 3.4b.

Table 3.2: List of parameter values used in the simulation studies.

Parameter	Unit	Value
General		
k_{v}	–	$\pi/4$
ρ_{c}	$\mathrm{g\,\mu m^{-3}}$	1.59×10^{-12}
m_{seed}	g	0.80
m_{solvent}	kg	1.75
T_0	°C	31.45
T_{min}	°C	20.00
T_{max}	°C	41.00
$c^{*\,3,52}$	$\mathrm{g\,kg^{-1}}$	$3.37\,\mathrm{e}^{(3.59\,\times\,10^{-2}\,T)}$
S_0	–	1.12
S_{min}	–	1.10
S_{max}	–	1.25
S_{final}	–	1.05
t_0	s	0.00
t_{samp}	s	300.00
$a_{\hat{c}}$	–	1.00
$b_{\hat{c}}$	$\mathrm{g\,kg^{-1}}$	0.20
N_{s}	–	4000
N_{p}	–	25
PFC		
k_{p}	$\mathrm{°C\,\mu m^{-1}}$	-1
τ_{I}	s	5000
NMPC		
K	–	40
M	–	3
$q_{\bar{L}_1}$	$\mathrm{\mu m^{-2}}$	1
$q_{\bar{L}_2}$	$\mathrm{\mu m^{-2}}$	10
$\dot{T}_{\mathrm{max}}$	$\mathrm{°C\,s^{-1}}$	0.05/60
$t_{\mathrm{f},0}$	s	3.60×10^4

Figure 3.4: Estimate of the attainable region for the number-weighted average dimensions obtained from the model-free PFC approach. **(a)** Size and shape space representation where L_1 and L_2 are the characteristic dimensions of the generic, cylindrical particle model. The thin blue lines represent the contour levels at 5 %, 25 %, 45 %, 65 %, 85 %, and 95 % of the maximum of the seed number density function based on the cylindrical particle model (i.e., prior to the transformation step described in Section 3.5.2). The black dashed lines indicate the reference paths for the two runs, the upper one for the first run (referred to as α), and the lower one for the second run (referred to as β). The two target orthants are given by the gray areas. The thick solid lines correspond to the measured and low-pass filtered evolutions of the number-weighted average dimensions and the dotted green lines represent linear fits to these data. **(b)** Evolution of the temperature, the concentration, the supersaturation, and the control error over time. The dark solid lines represent the simulated process conditions, the black dotted lines indicate constraints, and the gray dotted lines highlight the end of the profiles.

Due to the significantly different supersaturation levels, the progress in the size and shape plane (see Figure 3.4a) and the batch times vary strongly between the two runs. Combining the information obtained from Figure 3.4a and Figure 3.4b reveals that the upper boundary of the attainable region corresponds to the upper limit of the supersaturation $S_{\max}$ (run α) and that the lower limit was achieved by operating at $S_{\min}$ (run β). Since the first run (α) produced the upper boundary of the attainable region and the second run (β) produced the lower one (as intended by the prior selection of the target points), the sign of the controller parameter k_{p} (see Table 3.2) was correct. Note that it is not necessary to know the correct sign of k_{p} before performing these two runs for estimating the boundaries of the attainable region. If the sign was wrong during the two runs, it would just mean that the two boundaries are identified in reverse order. Subsequently, comparing the results of the two runs will enable the identification of the correct sign of k_{p}.

Having an estimate of the attainable region for a given seed population is of value in its own right. It also enables the selection of a reasonable target point in the size and shape space for subsequent controlled batch runs with the goal of repeatedly ending those batches at the same average dimensions and with comparable yield. In this study, the two targets $[\bar{L}_{1,\mathrm{target}} \ \bar{L}_{2,\mathrm{target}}]^{\mathrm{T}} = [200 \ 60]^{\mathrm{T}}$ µm and $[\bar{L}_{1,\mathrm{target}} \ \bar{L}_{2,\mathrm{target}}]^{\mathrm{T}} = [170 \ 70]^{\mathrm{T}}$ µm were chosen to assess if the model-free PFC approach is able to hit arbitrary target points within the attainable region. Two corresponding closed-loop runs, using again the parameter values listed in Table 3.2, were performed. The results are illustrated in Figure 3.5. Since the attainable region was estimated a priori to be cone-like with practically straight lines as boundaries (see Figure 3.4), the model-free reference paths were again chosen to be straight lines (with $T_{\mathrm{ff}}(t) = T_0$ as the feedforward temperature profile). Results obtained from the model-based PFC are not shown. In fact, the model-based PFC performed similarly to its model-free counterpart when applied to the studied system BLGA in water, since time-optimal reference paths to target points are almost straight lines in this case. Note that this is not necessarily the case for any system, i.e., using an available growth rate model to obtain sensible reference paths might lead to increased performance in terms of reaching the target and also to shorter batch times.

It is evident from Figure 3.5a that the model-free controller succeeded
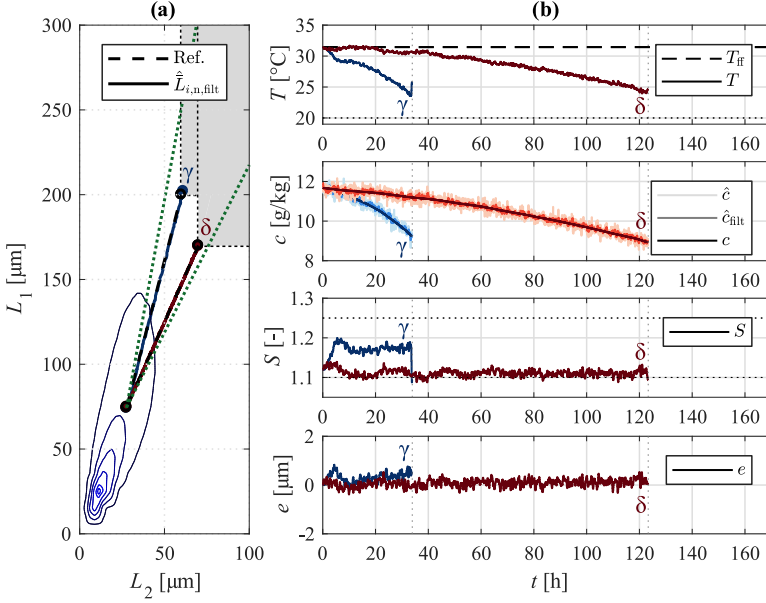
Figure 3.5: Closed-loop simulation runs using the model-free PFC scheme with the two targets $[\bar{L}_{1,\mathrm{target}} \quad \bar{L}_{2,\mathrm{target}}]^{\mathrm{T}} = [200 \quad 60]^{\mathrm{T}}$ µm (run γ) and $[\bar{L}_{1,\mathrm{target}} \quad \bar{L}_{2,\mathrm{target}}]^{\mathrm{T}} = [170 \quad 70]^{\mathrm{T}}$ µm (run δ). **(a)** Size and shape space representation where L_1 and L_2 are the characteristic dimensions of the generic, cylindrical particle model. The thin blue lines represent the contour levels at 5 %, 25 %, 45 %, 65 %, 85 %, and 95 % of the maximum of the seed number density function based on the cylindrical particle model (i.e., prior to the transformation step described in Section 3.5.2). The black dashed lines indicate the reference paths for the runs. The target orthants are given by the gray areas. The thick solid lines correspond to the measured and low-pass filtered evolutions of the number-weighted average dimensions, whereas the dotted green lines represent the estimate of the attainable region taken from Figure 3.4. **(b)** Evolution of the temperature, the concentration, the supersaturation, and the control error over time. The dark solid lines represent the simulated process conditions, the black dotted lines indicate constraints, and the gray dotted lines highlight the end of the profiles.

in its task: both batches ended close to their assigned target points, which was enabled by good tracking of the reference paths. As can be seen in Figure 3.5b, the batch time was close to 35 h for the first run with the target $[\bar{L}_{1,\text{target}} \ \bar{L}_{2,\text{target}}]^{\text{T}} = [200 \ 60]^{\text{T}}$ µm (referred to as run γ). It becomes clear from the corresponding time series plots of the control error and the supersaturation that the controller had to increase the supersaturation from the initial value of $S_0 = 1.12$ to a level of about 1.17 in order to be able to follow the path. The target of the second run δ, i.e., $[\bar{L}_{1,\text{target}} \ \bar{L}_{2,\text{target}}]^{\text{T}} = [170 \ 70]^{\text{T}}$ µm, was close to the lower boundary of the attainable region. As a consequence, the controller chose to operate at a comparatively low supersaturation level of about 1.11, which enabled it to follow the reference path and to reach the target point after about 123 h.

3.6.2 Nonlinear Model Predictive Control

The same problems considered in Section 3.6.1 using the model-free PFC were tackled using the NMPC scheme presented in Section 3.4. Here, it must be kept in mind that the model used in the controller is based on the generic, cylindrical particle model (where the growth rate model is defined in eq 3.9), which is in line with the capabilities of state-of-the art online PSSD monitoring tools. [23,32,39] Since the simulated process relies on a more accurate particle model in the form of a convex polyhedron, it is clear that there is a certain model/plant mismatch. Furthermore, the controller only has access to information collected from a sampled subset of all the particles in the population while relying on stereoscopic imaging, which impedes the accuracy of the state estimate required for solving the optimization problem posed in eq 3.7. The objective of the simulation studies is thus to check if the feedback mechanism can mitigate these negative effects to a satisfactory degree.

The results obtained from the simulation runs aimed at estimating the attainable region are shown in Figure 3.6. It is worth recalling that the reference path in the size and shape space, the feedforward temperature profile, and the control error are not defined for the NMPC strategy, hence they cannot be plotted in Figure 3.6. Moreover, the evolution of the measured average dimensions is not low-pass filtered in the case of NMPC (see Section 3.5.5). Still, when comparing Figure 3.6 to Figure 3.4, it can be seen that NMPC and PFC lead to very similar

batch runs and boundaries of the attainable region.

The results of the two NMPC runs aimed at the two separate targets $[\bar{L}_{1,\text{target}} \ \bar{L}_{2,\text{target}}]^{\text{T}} = [200 \ 60]^{\text{T}}$ µm (run γ) and $[\bar{L}_{1,\text{target}} \ \bar{L}_{2,\text{target}}]^{\text{T}} = [170 \ 70]^{\text{T}}$ µm (run δ) are visualized in Figure 3.7. It can be seen in Figure 3.7b that run γ ended after a batch time of about 39 h, because the NMPC operated the batch at a relatively low supersaturation for a long period of time, only realizing toward the end of the batch that it had to lower the temperature, i.e., to increase the supersaturation, in order to end up close to the target point. This observation is in line with the curved evolution of the measured average dimensions shown in Figure 3.7a. Qualitatively speaking, the same behavior can be observed for the second run δ. The average supersaturation level for this run was lower, since the target point was close to the lower boundary of the attainable region. Therefore, the batch time of about 134 h was significantly longer than for run γ. The behavior of increasing the supersaturation toward the end of the batch is caused by a mismatch between the predictions obtained from the population balance model used in the controller and the evolution of the measurements taken from the morphological population in the simulation framework. To be more precise, the two models differ in terms both of the employed particle shape model (generic versus polytopic) and of the growth rates (see eqs 3.9 and 3.10). The impact that these differences have on the model predictions was indirectly confirmed by running additional simulations (not shown here for the sake of brevity) where the same generic, cylindrical particle model was used both in the NMPC and in the simulation framework, with the same growth rates. Thus, in those simulations, the NMPC had access to a perfect process model. Those closed-loop runs led to a straight evolution of the path toward the target using an almost constant supersaturation level, similar to the behavior of the PFC discussed in Section 3.6.1. More direct evidence of the impact of the model/plant mismatch is provided by the dashed lines in Figure 3.7b, which represent the solution of the optimization run (see eq 3.7) performed at the first sampling instant t_0 of the corresponding batch run. Relying on the model and the initial state estimates, the NMPC predicts to be able to reach the desired target orthants for run γ and δ within about 58 h and 180 h, respectively, using practically constant supersaturation levels of about 1.14 and 1.10. Obviously, these predictions are wrong for both runs. Despite these con-
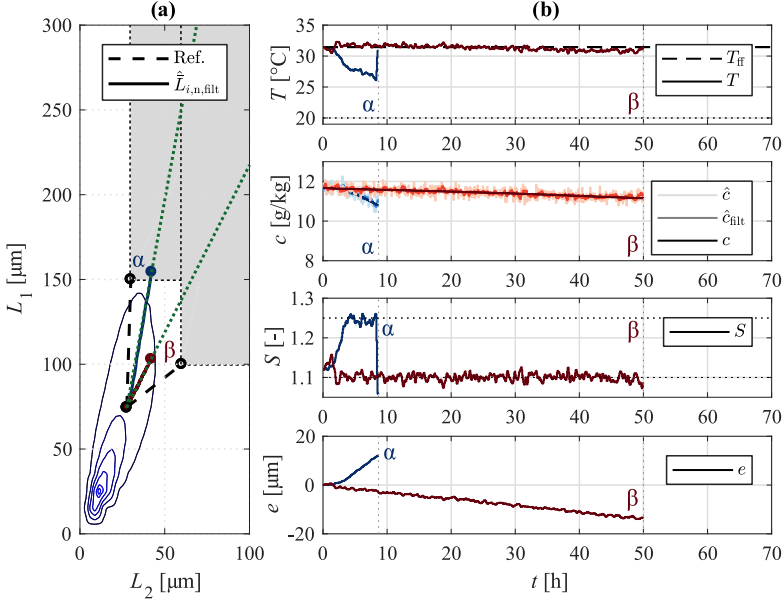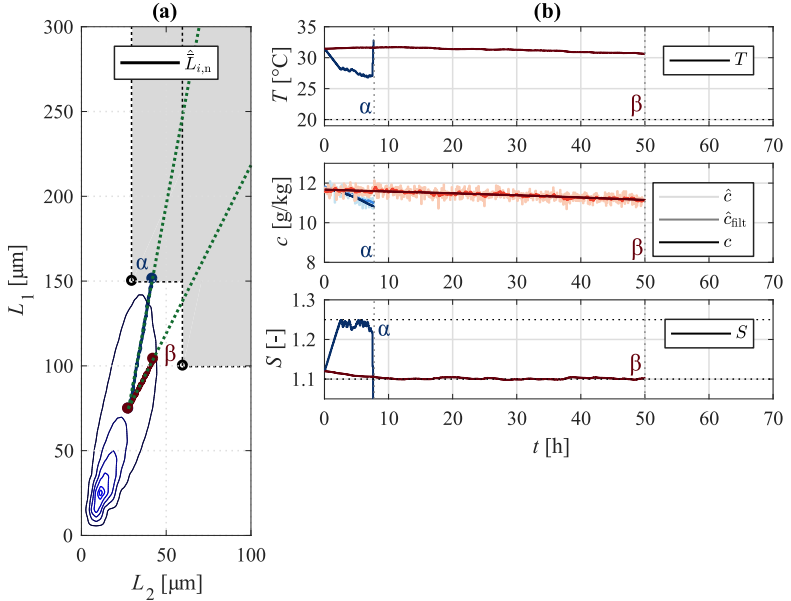
Figure 3.6: Estimate of the attainable region for the number-weighted average dimensions obtained from the NMPC strategy. **(a)** Size and shape space representation where L_1 and L_2 are the characteristic dimensions of the generic, cylindrical particle model. The thin blue lines represent the contour levels at 5 %, 25 %, 45 %, 65 %, 85 %, and 95 % of the maximum of the seed number density function based on the cylindrical particle model (i.e., prior to the transformation step described in Section 3.5.2). The two target orthants are given by the gray areas, the upper one for the first run (referred to as α), and the lower one for the second run (referred to as β). The thick solid lines correspond to the measured evolutions of the number-weighted average dimensions and the dotted green lines represent linear fits to these data. **(b)** Evolution of the temperature, the concentration, and the supersaturation over time. The dark solid lines represent the simulated process conditions, the black dotted lines indicate constraints, and the gray dotted lines highlight the end of the profiles.

siderations, it must be emphasized that the presence of the feedback mechanism clearly enables the controller to fulfill its task and to terminate close to the desired target points (see Figure 3.7a).

3.6.3 Robustness with Respect to Varying Growth Rates

The product quality obtained from consecutive batch cooling crystallization runs is known to vary in practice. It seems likely that this phenomenon is caused by disturbances acting on the process such as, for instance, residues from a previous batch resulting from improper cleaning or impurities in general. One possible effect of impurities (or additives) is that they may hinder the growth of certain crystal facets.[5,6] In the case of a batch run operated using a predefined cooling profile and without any size and shape feedback control, it is evident that a different final PSSD will result, even if the same seeds are used. Therefore, in this section, the robustness of the model-free PFC scheme with respect to variations in the growth rates in terms of achieving the same final average particle dimensions is investigated by means of a parametric sensitivity study. To this end, multiple closed-loop runs using the model-free PFC were performed, each of which using a different exponent $k_{g,1,2}$ for the relative supersaturation term in $\tilde{G}_1$, the growth rate along the {101} facet family of the BLGA crystals (see eqs 3.9 and 3.10). To be more precise, multipliers for the nominal value of $k_{g,1,2}$ were chosen in the range from 0.925 to 1.075. All these runs had the same target point, namely, $[\bar{L}_{1,\text{target}}\ \bar{L}_{2,\text{target}}]^{\text{T}} = [150\ 50]^{\text{T}}$ μm and they were performed using the parameters listed in Table 3.2. A summary of the results obtained in this way is illustrated in Figure 3.8. It is clear from Figure 3.8a that all the runs except the one with a multiplier for $k_{g,1,2}$ of 0.925 successfully reached the target point. The reason why this specific run missed the target point can be seen in Figure 3.8c: the PFC operated the batch at the lower boundary of the allowed supersaturation range ($S_{\text{min}} = 1.10$). Since the target point was missed, this means that an even lower supersaturation and thus an even higher batch time (see Figure 3.8b) would have been necessary to hit the target point in this run. For the remaining runs, it can be seen in Figure 3.8b,c that the higher the average supersaturation chosen by the PFC, the lower the batch time. More generally speaking, altering the exponent of the supersaturation term in one of the
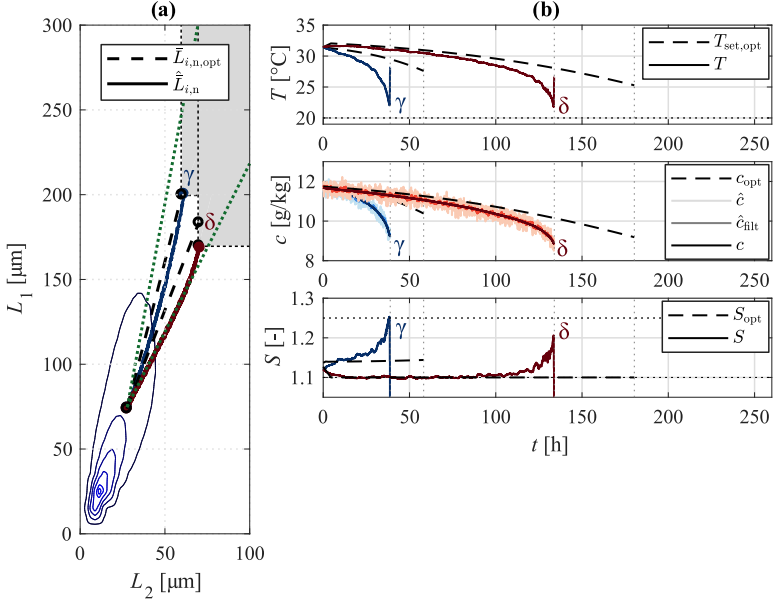
Figure 3.7: Closed-loop simulation runs using the NMPC strategy with the two targets $[\bar{L}_{1,\text{target}}\ \bar{L}_{2,\text{target}}]^{\text{T}} = [200\ 60]^{\text{T}}$ µm (run γ) and $[\bar{L}_{1,\text{target}}\ \bar{L}_{2,\text{target}}]^{\text{T}} = [170\ 70]^{\text{T}}$ µm (run δ). **(a)** Size and shape space representation where L_1 and L_2 are the characteristic dimensions of the generic, cylindrical particle model. The thin blue lines represent the contour levels at 5 %, 25 %, 45 %, 65 %, 85 %, and 95 % of the maximum of the seed number density function based on the cylindrical particle model (i.e., prior to the transformation step described in Section 3.5.2). The black dashed lines indicate the optimal paths obtained from solving the optimization problem given by eq 3.7 at time t_0, i.e., at the first sampling instant. The target orthants are given by the gray areas. The thick solid lines correspond to the measured evolutions of the number-weighted average dimensions, whereas the dotted green lines represent the estimate of the attainable region taken from Figure 3.6. **(b)** Evolution of the temperature, the concentration, and the supersaturation over time. The dark solid lines represent the simulated process conditions, the black dotted lines indicate constraints, and the gray dotted lines highlight the end of the profiles. Again, the black dashed lines indicate the optimal profiles obtained from solving the optimization problem at time t_0.
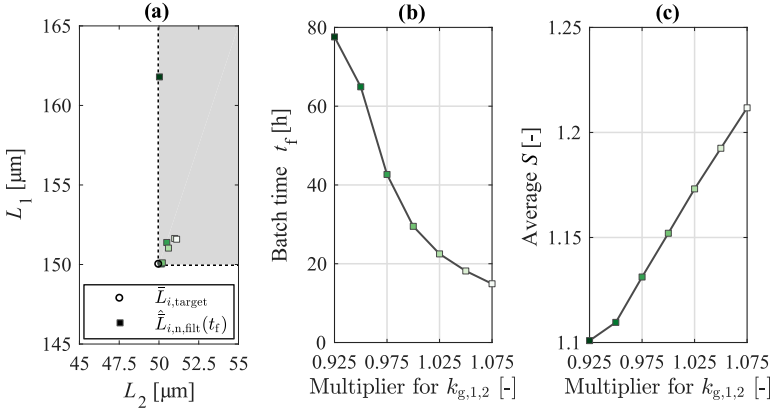
Figure 3.8: Summary of the results obtained from several closed-loop runs using the model-free PFC strategy, all aimed at the target point $[\bar{L}_{1,\text{target}} \ \bar{L}_{2,\text{target}}]^{\mathrm{T}} = [150 \ 50]^{\mathrm{T}}$ µm, but using different exponents $k_{\mathrm{g},1,2}$ for the supersaturation term in the growth rate $\tilde{G}_1$. **(a)** Size and shape space representation of the measured final average dimensions where L_1 and L_2 are the characteristic dimensions of the generic, cylindrical particle model. **(b)** Batch times in hours. **(c)** Average relative supersaturation levels. The dark gray lines are guides for the eye.

growth rates corresponds to changing the attainable region in the size and shape space. In conclusion, if the change in the attainable region as a function of the variation in the growth rates is not too pronounced, the robustness provided by the model-free PFC scheme allows the average particle dimensions of multiple batch runs to reach the same target point.

The same parametric sensitivity study was also conducted using the NMPC. The results are similar to those obtained from the model-free PFC, but they are not shown here for the sake of brevity.

3.7 Experiments

In this section, the experimental validation of the model-free PFC scheme introduced above is presented using the system BLGA in water. Note

that within this experimental section, the term PFC will always refer to the model-free implementation of the controller. It was decided to experimentally apply this specific controller, because it is the most simple strategy among those presented in this chapter.

In a first step, a seed population was prepared. Afterward, a supersaturation interval was identified experimentally in which the considered process is growth-dominated. Then, the underlying assumption for the operation of the PFC was verified for the case where volume-weighted average dimensions are considered (see Section 3.2); i.e., it was verified that the ratio of the rate of change of these two average dimensions is monotonic in the process temperature. To this end, a constant supersaturation control (CSC)[123,124] strategy was applied, which also allows to experimentally estimate the attainable region for the average sizes and shapes of a given seed population. Finally, multiple batch crystallization runs controlled by the PFC were performed for the considered seed population with the goal of repeatedly reaching target average dimensions within its attainable region.

To present the results concisely, the materials and methods applied to perform the experimental campaign are explained in Appendix B. More specifically, the materials are listed in Appendix B.1, the experimental setup is described in Appendix B.2, and the applied solid phase characterization technique is explained in Appendix B.3. In the same section, an explanation is given for using the volume-weighted rather than the number-weighted average dimensions in the experiments. Furthermore, the seed preparation protocol is given in Appendix B.4, the chosen limits for the operating conditions are listed in Appendix B.5, the experimental protocol is explained in Appendix B.6, and the technique applied to estimate the solute concentration is summarized in Appendix B.7.

3.7.1 Constant Supersaturation Control

To select sensible target average particle dimensions for batches controlled by the PFC, it is beneficial to estimate the attainable region for crystal size and shape corresponding to a given seed population. Recall from above that the attainable region is defined as a region in the space with the two average dimensions as coordinates, which under the given operating constraints is fully accessible to the seed population. In this experimental section, additionally the a priori experimental confirmation

of the monotonicity assumption introduced in Section 3.2 is required. After confirming this assumption, it is clear that the attainable region for a given seed population and for the chosen supersaturation limits is bounded by the two trajectories obtained with the supersaturation kept constant at its two extremal values. To this aim, CSC experiments were performed using the prepared seed population at four constant supersaturation levels, all of them within the supersaturation limits given in Table 3.3. For the sake of brevity, most of the parameters listed in this table are explained in Appendix B. The four constant supersaturation levels explored are referred to as ε, ζ, η, and θ, with values of 1.18, 1.14, 1.12, and 1.10, respectively.

Under supersaturated conditions, the solute concentration decreases as the solute mass is taken up from the liquid phase onto the solid phase. Hence, to maintain the supersaturation constant over time, the temperature of the process must be lowered.[123,124] To determine the appropriate process temperature set point, the equation

$$\hat{S}(t) = \frac{\hat{c}_{\mathrm{filt}}(t)}{c^*\big(T(t)\big)} \tag{3.16}$$

was solved for the temperature at each sampling instant of the controller using the desired constant value of the supersaturation. The procedure for obtaining the low-pass filtered solute concentration estimate $\hat{c}_{\mathrm{filt}}(t)$ is described in Appendix B.7.

The results of the CSC experiments also enable the selection of the correct sign of k_{p} in eq 3.5 for subsequent PFC experiments: a negative k_{p} results if the ratio $\frac{\mathrm{d}\bar{L}_{1,\mathrm{v}}}{\mathrm{d}t}\big/\frac{\mathrm{d}\bar{L}_{2,\mathrm{v}}}{\mathrm{d}t}$ decreases with temperature (increases with supersaturation) and a positive k_{p} is required in the opposite case.

The evolution of the low-pass filtered volume-weighted average dimensions in the crystal size and shape space of the seed population is shown in Figure 3.9a for the four different supersaturation levels. As expected for the needle-like BLGA in water, the population grows preferentially along the L_1 direction. A cone-like area can be observed in this plot, with the trajectory corresponding to experiment ε ($S = 1.18$) as the upper boundary and that of experiment θ ($S = 1.10$) as the lower

Table 3.3: List of parameter values used in the CSC and PFC experiments.[a]

Parameter	Unit	Value
Experimental		
ρ_c	$g\,\mu m^{-3}$	1.59×10^{-12}
$c^{*\,3,52}$	$g\,kg^{-1}$	$3.37\,e^{(3.59 \times 10^{-2}\,T)}$
c_0	$g\,kg^{-1}$	9.86
m_{seed}	g	0.35
T^*	°C	29.90
T_{min}	°C	20.00
T_{max}	°C	41.00
S_{min}	–	1.10
S_{max}	–	1.18
S_{final}	–	1.05
Controller		
t_{samp}	min	5
$t_{initial}$	min	5 (CSC)
		30 (PFC)
t_{max}	min	3000
t_{final}	min	70
n_{grid}	–	500 (L_1)
	–	150 (L_2)
k_p	$°C\,\mu m^{-1}$	-0.5
τ_I	s	5000

[a] Unless stated otherwise in the main text, the parameters given in this table were used for all the experiments.
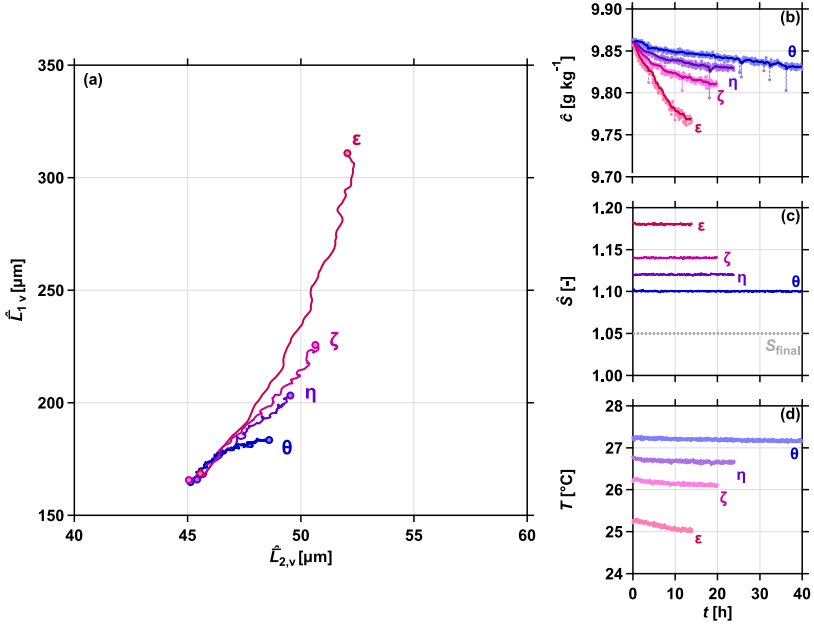
Figure 3.9: CSC experiments to estimate the attainable region of the seed population. **(a)** Evolution of the low-pass filtered volume-weighted average dimensions in the crystal size and shape space for crystals grown at $S = 1.10$ (θ), 1.12 (η), 1.14 (ζ), and 1.18 (ε). **(b)** Evolution of the solute concentration. The solid markers represent the concentration estimate $\hat{c}$ and the solid lines represent the low-pass filtered concentration $\hat{c}_{\text{filt}}$ (see Appendix B.7). **(c)** Evolution of the supersaturation $\hat{S}$ calculated according to eq 3.16. **(d)** Evolution of the measured process temperature T.

93

boundary. The intermediate supersaturations lie within this cone-like area, which demonstrates the desired monotonic behavior of $\frac{\mathrm{d}\bar{L}_{1,\mathrm{v}}}{\mathrm{d}t}/\frac{\mathrm{d}\bar{L}_{2,\mathrm{v}}}{\mathrm{d}t}$ with respect to the supersaturation. The time-resolved evolution of concentration, supersaturation, and temperature is shown in Figure 3.9b-d. The concentration and the process temperature do not change significantly over the course of the experiments. From this observation, and as also discussed in Appendix B.7, one can conclude that a constant temperature would suffice to maintain an approximately constant supersaturation. It is also worth noting that the batch times are considerably different for the different experiments. Finally, the chosen lower bound on the supersaturation $S_{\min}$ can be justified by observing the evolution of the average dimensions in experiment θ, where, over a 40 h period, the average length and width increased only by approximately 19 µm and 3 µm, respectively. It would have been difficult to guarantee any observable growth in the population if a value lower than 1.10 had been allowed for $S_{\min}$. As a general comment, it can be said that the attainable region is narrow. This fact can be attributed to how BLGA crystals grow in water within the ranges of operating conditions explored within this experimental campaign.

3.7.2   Path Following Control

The attainable region obtained from the experiments discussed in Section 3.7.1 enabled an experimental campaign aimed at growing the BLGA seed population to reach different target dimensions within its attainable region. To this aim, two different target average dimensions were chosen in the crystal size and shape space spanned by the volume-weighted average length and width of the populations. One of these experiments was repeated to assess if the control scheme was robust enough to guide the seed population towards the desired target dimensions repeatedly. Additionally, experiments with three different integrator time constants τ_{I} (aimed at the same target dimensions) were performed to get a qualitative insight into the effect of the PI tuning parameters on the performance of the controller. Note that a detailed parametric study of the PI parameters is however beyond the scope of this section. For all these PFC experiments, the reference paths were chosen to be the straight lines connecting the initial measurement $[\hat{\bar{L}}_{1,0}\ \hat{\bar{L}}_{2,0}]^{\mathrm{T}}$ obtained from the

μ-DISCO and the assigned target $[\bar{L}_{1,\text{target}} \ \bar{L}_{2,\text{target}}]^{\text{T}}$.

A total of five closed-loop experiments using the PFC are presented here. The experiments with the two different targets $[\bar{L}_{1,\text{target}} \ \bar{L}_{2,\text{target}}]^{\text{T}} = [240\ 52]^{\text{T}}$ μm and $[\bar{L}_{1,\text{target}} \ \bar{L}_{2,\text{target}}]^{\text{T}} = [200\ 50]^{\text{T}}$ μm are henceforth distinguished by referring to them as γ and δ, respectively. The three experiments with target average dimensions corresponding to γ were performed by choosing three different integrator time constants τ_{I} while keeping the rest of the parameters listed in Table 3.3 constant. The values of τ_{I} were 5000 s, 10 000 s, and 50 000 s for $γ_1$, $γ_2$, and $γ_3$, respectively. The two experiments with target average dimensions corresponding to δ were performed with the same experimental and controller parameters as listed in Table 3.3. A constant feedforward temperature T_{ff} of 26.8 °C was set for both the targets, which corresponds to an initial supersaturation of 1.12.

The results obtained from the five experiments are illustrated in Figure 3.10. Out of the three γ experiments, the controller was successful in driving $γ_1$ to the target orthant, while this was not the case for $γ_2$ and $γ_3$. This can be attributed to two factors, namely, the different τ_{I} values and the maximum allowed batch times (duration of the main experimental phase, see Appendix B.6) for the three experiments. The batch time for $γ_1$ was about 30 h, hence it was decided to limit t_{max} to 30 h for $γ_2$ and $γ_3$. The evolution of the supersaturation and of the temperature for experiments $γ_1$ through $γ_3$ shown in Figure 3.10c,d is qualitatively similar, but shifted in time when compared among the experiments. These time shifts are a direct consequence of the different integrator time constants τ_{I}. For $γ_1$ ($\tau_{\text{I}} = 5000$ s), the integral part in eq 3.5 accumulated faster than for $γ_2$ ($\tau_{\text{I}} = 10\,000$ s), and that of the latter accumulated faster than that of $γ_3$ ($\tau_{\text{I}} = 50\,000$ s). In the extreme case of a very high value of τ_{I}, i.e., when the contribution from the integral part is negligible as in the case of $γ_3$, the feedback controller acts less aggressively, which can impact the path following performance and thus also the batch time. The outcome of experiments $γ_1$ through $γ_3$ indicates that the combination of the values $k_{\text{p}} = -0.5\,°\text{C}\,\mu\text{m}^{-1}$ and $\tau_{\text{I}} = 5000$ s is a reasonable choice for achieving a satisfactory closed-loop performance in the studied system.

As can be seen in Figure 3.10b-e, the batch time of experiment $δ_1$ was twice that of experiment $δ_2$. Experiment $δ_1$ was operated at a supersaturation level close to S_{max} for a significant portion of the batch duration,
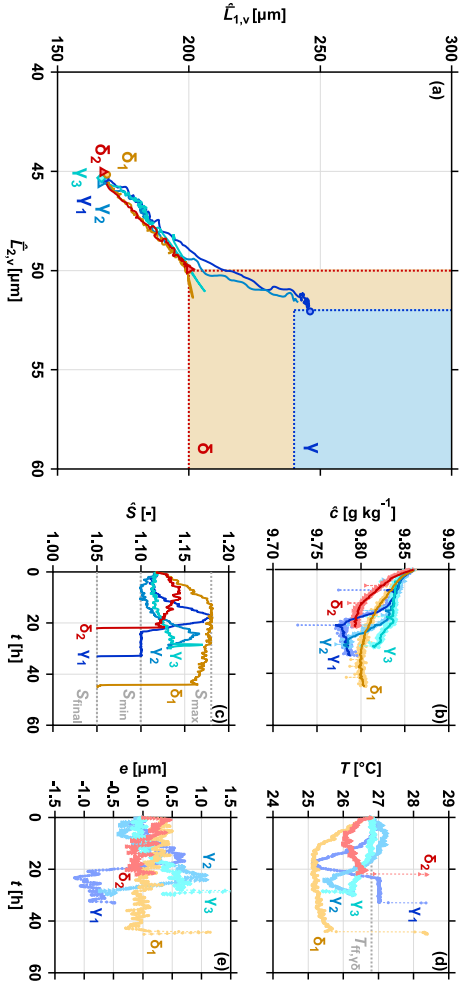
Figure 3.10: Results of the PFC experiments. **(a)** Evolution of the low-pass filtered volume-weighted average dimensions in the crystal size and shape space for two different target dimensions $[\bar{L}_{1,\text{target}} \quad \bar{L}_{2,\text{target}}]^{\text{T}}$, namely, $[240 \quad 52]^{\text{T}}$ μm (γ) and $[200 \quad 50]^{\text{T}}$ μm (δ). The subscripts denote the repetition of the PFC experiment performed for each target. **(b)** Evolution of the solute concentration. The solid markers represent the concentration estimate $\hat{c}$ and the solid lines represent the low-pass filtered concentration $\bar{c}_{\text{filt}}$ (see Appendix B.7). **(c)** Evolution of the supersaturation $\hat{S}$ calculated according to eq 3.16. **(d)** Evolution of the measured process temperature T. **(e)** Evolution of the control error e.

while the maximum supersaturation attained by δ_2 was about 1.15. The differences observed between the two repetitions may have different root causes. The presence of impurities in the suspension or surface defects in the seed crystals can alter the growth rates considerably. Moreover, the presence of a different fraction of fines or of a different number of large particles in the seed samples taken for the two experiments can also impact the evolution of the controlled average quantity of the population (i.e., the average dimensions). Nevertheless, it is crucial to notice that the controller was able to guide the population towards the target for both the repetitions, despite their obviously different behavior.

The initial (seeds) and final (products) PSSDs for experiments γ_1, γ_2, δ_1, and δ_2 are shown in Figure 3.11a-d, from which two important observations follow. First, both the seed and the final PSSDs of the two repetitions for each target are very similar. Second, as expected due to the different target average dimensions, the final PSSDs shown in Figure 3.11a,b have covered a larger distance in the crystal size and shape space than those shown in Figure 3.11c,d. A further interesting observation is the presence of fines in the products of the γ experiments in the form of peaks in the bottom left corner of Figure 3.11a,b. These peaks might seem minor, but it must be kept in mind that the volume-weighted representation of the PSSD attenuates the contribution of small particles. The presence of these fines in the products can be attributed to two main factors. First, small seed particles can be below the detection threshold of the μ-DISCO initially, but they cross such threshold at some point when growing at high supersaturations for extended periods. Second, secondary nucleation or breakage can never be ruled out completely. However, to the best of the author's knowledge, BLGA in water does not exhibit the latter two phenomena under the operating conditions explored in this experimental section. Notice that the product PSSDs for the δ experiments do not exhibit the presence of fines, even though δ_1 was operated at high supersaturations for a long duration. This observation can be explained with the specific behavior of this particular experiment, which has already been discussed above.
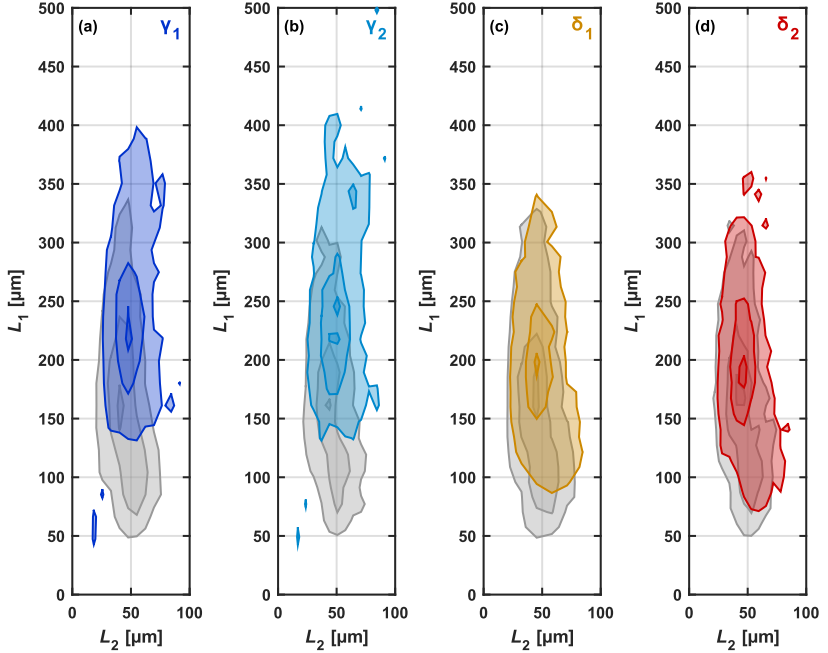
Figure 3.11: Volume-weighted PSSDs $\hat{f}_{\mathrm{v}}$ (see Appendix B.3) normalized by the maximum of each PSSD of the seeds (gray) and products (colored) at the end of the main experimental phase of the PFC experiments **(a)** γ_1, **(b)** γ_2, **(c)** δ_1, and **(d)** δ_2. The contour line values correspond to 0.1, 0.5, and 0.9 of each normalized PSSD. Along the L_1 direction, a regular grid with a spacing of $19\,\mu\mathrm{m}$, $14\,\mu\mathrm{m}$, $13\,\mu\mathrm{m}$, and $13\,\mu\mathrm{m}$ for both seeds and products was used for experiment γ_1, γ_2, δ_1, and δ_2, respectively. Along the L_2 direction, the corresponding grid spacing was $7\,\mu\mathrm{m}$, $7\,\mu\mathrm{m}$, $13\,\mu\mathrm{m}$, and $6\,\mu\mathrm{m}$.

3.8 Conclusions

In this chapter, two different feedback control strategies for the evolution of the two average particle dimensions of populations of needle-like crystals in growth-dominated batch cooling crystallization processes are proposed. The first strategy is a PFC approach that can be operated without kinetic models for crystal growth. The second approach is a considerably more complex NMPC that relies on multidimensional crystal growth rate models.

Being aware of the general lack of actuation in the considered process, and of the limited controllability thereof, it has been demonstrated in simulation studies how to automatically identify the boundaries of the attainable region for the average crystal dimensions of a given seed population (which is in fact defined independently of any control law) using either feedback control strategy. It has also been shown that the controllers are able to reach an arbitrary target average size and shape within the interior of this region. On a more general level, the incorporated feedback of crystal size and shape information provides robustness with respect to achieving process goals related to these quantities.

In the case of the considered growth-dominated batch process, the simulation studies have not revealed performance benefits for NMPC with respect to the model-free PFC, which is due to the unavoidable presence of model/plant mismatch. Considering also the major effort required to obtain multidimensional crystal growth rate models,[46,53–55] it is concluded that the NMPC approach is too complex for this type of application.

An experimental campaign confirmed that the model-free PFC, when combined with suitable online monitoring tools to characterize the evolution of the PSSD such as the μ-DISCO (see Section 1.2),[32] is able to guide the average dimensions of a population of needle-like BLGA seed crystals towards a sensible target region in the crystal size and shape space. Despite the likely presence of differences in the properties of the seed particles and in their growth rates, the controller ensured repeatability of the performed experiments in terms of reaching the assigned target. This fact clearly demonstrates that the controller introduces a considerable level of robustness with respect to unexpected disturbances, which makes the outcome of consecutive batches much more predictable.

For the system BLGA in water, the experiments showed that the attainable region is narrow. Hence, achieving a significant change in the shape of these crystals does not seem possible when only considering a growth process. However, it is to be noted that the operation of the model-free PFC strategy is not restricted to the system BLGA in water. Thus, for a different compound with a broader attainable region, applying this control law might already be sufficient to achieve a significant shape change. In any other case, there is a need to integrate the growth step with more complex processes exhibiting increased actuation with respect to the crystal size and shape, such as milling,[63] temperature cycling,[21,52,55,62,71] combined cooling and antisolvent crystallization,[43,111,125] cooling crystallization under the influence of additives,[5] or a combination thereof. One of way of operating such a process is proposed in Chapter 6. Despite the limitations in terms of shape change observed in the experiments, the work presented in this chapter provides a basis to develop and to robustly control such integrated crystallization processes in a model-free fashion.

Nomenclature

Acronyms

ATR-FTIR	attenuated total reflectance Fourier transform infrared
BLGA	β L-glutamic acid
CSC	constant supersaturation control/controller
DAE	differential algebraic equation
DISCO	dual imaging system for crystallization observation
KDP	potassium dihydrogen phosphate
(M)PBM	(morphological) population balance model
NLP	nonlinear program
(N)MPC	(nonlinear) model predictive control/controller
PFC	path following control/controller
PI	proportional-integral (controller)
PS(S)D	particle size (and shape) distribution
rpm	revolutions per minute
VTB	virtual test bench

Roman symbols

$a_{\hat{c}}$	multiplicative factor for mean of a Gaussian [–]
$b_{\hat{c}}$	standard deviation of a Gaussian [$\mathrm{g\,kg^{-1}}$]
c	solute concentration (per mass of solvent basis) [$\mathrm{g\,kg^{-1}}$]
c^*	solubility (per mass of solvent basis) [$\mathrm{g\,kg^{-1}}$]
e	PFC control error [µm]
f	number density function (PSSD) [$\mathrm{µm^{-2}\,kg^{-1}}$] (simulations) or [$\mathrm{µm^{-2}}$] (experiments)
f_{v}	volume-weighted PSSD [$\mathrm{µm^{-2}}$] (experiments only)
G_i	growth rate along ith particle dimension [$\mathrm{µm\,s^{-1}}$]
K	# intervals for piecewise linear discretization [–]
$k_{\mathrm{g},i,j}$	jth parameter of the growth rate $\tilde{G}_i$, unit varies
k_{p}	proportional gain of PI controller [$\mathrm{°C\,µm^{-1}}$]
k_{v}	volume shape factor [–]
L_i	ith particle dimension [µm]
$\bar{L}_{i,\mathrm{n}}$	number-weighted average of ith particle dimension [µm]
$\bar{L}_{i,\mathrm{v}}$	volume-weighted average of ith particle dimension [µm]
$\bar{L}_i$	placeholder for either $\bar{L}_{i,\mathrm{n}}$ or $\bar{L}_{i,\mathrm{v}}$ [µm]

$\bar{L}_{i,\text{target}}$	target average of ith particle dimension [µm]
m_{seed}	seed mass [g]
m_{solvent}	solvent mass [kg]
M	# implicit Euler steps [–]
N_{p}	# sampled particles placed in virtual flow cell [–]
N_{s}	# sampled particles (particle count) [–]
n_{grid}	# of grid points for binning (experiments only) [–]
R_i and R_i'	ith dimension of points on the reference path [µm]
S	relative supersaturation, c/c^* [–]
S_{final}	final supersaturation to end batch [–]
t	time, unit varies
t_0	seed addition time, unit varies
t_{f}	batch time in an optimization problem [s]
t_k	sampling instant (optimization and simulations) [s]
T	process temperature [°C] (unless specified otherwise)
T^*	saturation temperature [°C]
$\dot{T}$	rate of temperature change (NMPC) [°C s^{-1}]
$q_{\bar{L}_i}$	weighting factor for NMPC objective [µm^{-2}]
V	total visual hull volume [µm^3]
V_{c}	single crystal volume [µm^3]
V_{seed}	volume of seeds per mass of solvent [µm^3 kg^{-1}]

Greek symbols

α, β, γ, δ	labels for PFC or NMPC simulations or experiments
ε, ζ, η, θ	labels for CSC experiments
Γ	damping ratio [–]
μ_{ij}	ij-cross moment of PSSD [µm^{i+j} kg^{-1}] (simulations) or [µm^{i+j}] (experiments)
ρ_{c}	crystal density [g µm^{-3}]
τ_{I}	integrator time constant of PI controller [s]
ϕ_{n}	scaling factor for particle count [–]
ϕ_{v}	scaling factor for particle volume [kg^{-1}]
ω_0	natural frequency [s^{-1}]

Superscripts and subscripts

0	initial value or initial guess
–	average of the quantity
~	polyhedral particle model (for MPBM)
ˆ	measurement or estimate
fb	feedback
ff	feedforward
filt	low-pass filtered
final	final phase of experiment
initial	initial phase of experiment
max	upper limit
min	lower limit
opt	optimized
samp	sampling (interval)
set	set point

Chapter 4

Feedback Control for Wet Milling Processes

4.1 Introduction

Milling is a widely applied unit operation during the production of solid pharmaceuticals and fine chemicals. It has the potential to strongly modify the particle size and shape, either during or after a crystallization step, which can increase the efficiency of various downstream unit operations and improve important quality attributes of the final product. For instance, milling can enhance bioavailability, tablet content uniformity, and powder compactability. [126,127] Wet milling is often employed to produce narrow crystal size distributions without altering the crystallinity of the solids. Dry milling techniques can have several disadvantages, such as higher cost, generation of lattice defects, and amorphization, to name a few. [128–130]

Because of the importance of wet milling in the pharmaceutical industry, significant efforts have been directed toward studying and modeling the breakage processes of suspended crystals, using both *in situ* and

---

The work presented in this chapter has been adapted from ref 67 (Rajagopalan, A. K.; Bötschi, S.; Morari, M.; Mazzotti, M. Feedback Control for the Size and Shape Evolution of Needle-like Crystals in Suspension. III. Wet Milling. *Cryst. Growth Des.* **2019**, *19*, 2845–2861. DOI: 10.1021/acs.cgd.9b00080). A complete presentation of the material reported in ref 67 appears in Ashwin Kumar Rajagopalan's dissertation. [33]

ex situ wet mills.[64,127,129–138] These studies successfully demonstrate a number of benefits from integrating wet milling with crystallization processes. However, in all these studies, the mills were operated at predefined rotor speeds, thereby missing the opportunity to exploit the potential of applying feedback control to dynamically alter the rotor speed. Furthermore, most of the employed models were one-dimensional and the quantitative monitoring tools utilized in the experimental studies provided a one-dimensional particle size distribution (PSD). Thus, the evolution of the particle shape was neglected.

In recent years, thanks to increased efforts to develop solid phase characterization tools to monitor the evolution of both particle size and shape, breakage processes have been characterized with increased accuracy with respect to particle shape.[137,139] These and similar efforts facilitate the development of complex processes involving growth, milling, and dissolution stages that produce more equant particles starting from needle-like seeds.[64,136] The design of such processes should be followed by feedback control efforts to increase process robustness.

The purpose of this chapter is to develop and to validate model-free feedback control strategies to manipulate the size and the shape of needle-like crystals using a wet mill as the physical actuator. The goal of these controllers is to steer batches of needle-like seed particles to different target average lengths in the crystal size and shape space. The control laws were applied experimentally to the two needle-like compounds β L-glutamic acid (BLGA) and γ D-mannitol (GDM). During these studies, the stereoscopic imaging device μ-DISCO (see also Section 1.2)[32] was employed to obtain the required feedback of the particle size and shape evolution.

This chapter is structured as follows. First, a brief overview of the wet milling process is given in Section 4.2. Second, the control strategies are presented in Section 4.3. The results obtained from experiments using these control laws are discussed in Section 4.4. For the sake of brevity, the materials and methods employed in the corresponding experimental campaign are provided in Appendix C. More specifically, the materials are listed in Appendix C.1, the experimental setup is described in Appendix C.2, and the applied solid phase characterization technique is explained in Appendix C.3. The seed preparation protocol is given in Appendix C.4, the chosen limits for the operating conditions are listed

in Appendix C.5, and the experimental protocol is explained in Appendix C.6, the latter including a tabular listing of the employed experimental and controller parameters.

4.2 Overview of Wet Milling

Wet or slurry milling involves pumping a suspension of crystals from a well-mixed stirred tank through a mill to reduce the size of the crystals. Two different configurations have been discussed in the literature, namely, the *Two Crystallizer* (or single pass) configuration and the *Recirculation* configuration.[126,127] These configurations are illustrated in Figure 4.1. A brief summary of the advantages and the drawbacks of these two configurations is presented in the following sections. Note that in this work, only wet milling applied in the context of a batch crystallization process is considered.

4.2.1 Two Crystallizer Configuration

The *Two Crystallizer* configuration is shown in Figure 4.1a. In this configuration, the entire suspension is pumped from the primary crystallizer through an active wet mill to the secondary crystallizer. Then, the suspension is pumped back to the primary crystallizer through an inactive wet mill. The major advantage of this configuration is that all the particles in the suspension pass the mill. However, the setup is complex since it requires two temperature controlled stirred tank crystallizers. Because of this inherent complexity, the *Two Crystallizer* configuration is scarcely applied on an industrial scale.[127] In this chapter, this configuration will not be explored any further. The mathematical modeling of this configuration and a model-based operating policy are presented in refs 137 and 67. In the latter reference, the two configurations shown in Figure 4.1a are studied in detail and compared.

4.2.2 Recirculation Configuration

In the *Recirculation* configuration shown in Figure 4.1b, the suspension is continuously mixed in the crystallizer and circulated through the mill. The major advantage of this configuration is the fact that it does not require an additional temperature controlled stirred tank crystallizer. Therefore, the *Recirculation* configuration is often applied on an industrial scale.[126,127] In this chapter, this configuration is explored experi-
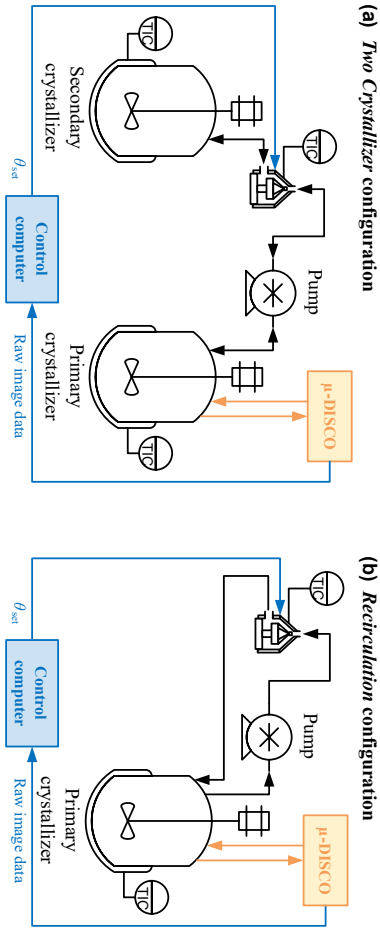
Figure 4.1: Schematic of the experimental setup for two different milling configurations. **(a)** *Two Crystallizer* configuration and **(b)** *Recirculation* configuration. In the *Two Crystallizer* configuration, the whole suspension is transferred from the primary crystallizer through an active mill into the secondary crystallizer. In the *Recirculation* configuration, the suspension is circulated through the active mill while being continuously mixed in the primary crystallizer. In both the configurations, the seed particles are suspended in the primary crystallizer. The solid phase is characterized online using the μ-DISCO (sampling loop shown using orange lines, see Appendices C.2 and C.3). The control computer is used to process the image data from the μ-DISCO and to command a rotor speed set point θ_{set} to the mill.

mentally using a lab-scale setup. In this context, a quantity of interest is the residence time of the suspension in the crystallizer τ_C, where this residence time is defined as the ratio of the volume of the suspension in the crystallizer V_C to the flow rate of the suspension F through the mill.

4.3 Control of Wet Milling Stages

4.3.1 Average Characteristics of a Population

In this chapter, the volume-weighted average dimensions ($\bar{L}_{i,v}$, $i = 1, 2$) of the population in the crystallizer, obtained from the cross-moments of the particle size and shape distribution (PSSD), are considered to be the quantities of interest for control. They are defined as

$$\bar{L}_{1,v}(t) = \frac{\mu_{22}(t)}{\mu_{12}(t)}$$

$$\bar{L}_{2,v}(t) = \frac{\mu_{13}(t)}{\mu_{12}(t)} \tag{4.1}$$

where

$$\mu_{ij}(t) = \int\limits_{0}^{\infty} \int\limits_{0}^{\infty} L_1^i L_2^j f(t, L_1, L_2) \, \mathrm{d}L_1 \, \mathrm{d}L_2 \tag{4.2}$$

is the ij-cross moment of the number density function $f(t, L_1, L_2)$ (i.e., the PSSD) at time t.

In the following sections, PSSDs obtained experimentally will be highlighted by the hat symbol, i.e., $\hat{f}$. Equations 4.1 and 4.2 can also be applied to $\hat{f}$, thus yielding the quantities $\hat{\bar{L}}_{i,v}$ ($i = 1, 2$). Please refer to Appendix C.4 for further useful PSSD characteristics.

4.3.2 Attainable Region for Particle Size and Shape

It was shown that there exists an attainable region in the crystal size and space, spanned by the average length and width of a crystal population characterized by two dimensions, for a seeded, growth-dominated batch cooling crystallization process by solely manipulating the process temperature.[21,62,65,66] This region provides an indication as to whether a target size and shape is accessible to the seed population under the given operating constraints. The concept of the attainable region can also be applied to breakage processes.

For the wet milling process considered in this chapter, it was demonstrated previously that the influence of the residence time of the suspension inside the wet mill τ_{WM} (and thus of the flow rate F) on the final average particle dimensions is negligible as long as this residence time is above a value of $5\,\mathrm{s}$.[137] Note that lower values of τ_{WM} usually pose too high requirements on the employed pump that provides the flow rate F. Thus, the rotor speed θ remains as the single control actuator and it becomes clear that only one of the two quantities $\bar{L}_{1,\mathrm{v}}$ and $\bar{L}_{2,\mathrm{v}}$ can be controlled independently. It is also well-known that needle-like crystals undergoing milling preferentially break along the length direction and exhibit a small change along the width direction even at high rotor speeds. On the basis of these considerations, it was decided to design feedback controllers and to subsequently perform experiments with the aim of manipulating the average length of the crystal population rather than its average width. In more detail, the goal of the developed control laws is to mill the particle populations in such a way that after completion of the milling operation, the volume-weighted average length $\bar{L}_{1,\mathrm{v}}$ is as close as possible to a given target value $\bar{L}_{1,\mathrm{target}}$. In this way, the volume-weighted average aspect ratio can be controlled.

4.3.3 Model-based Versus Model-free Control

Controlling the average length of a population of needle-like particles undergoing wet milling is challenging for two main reasons. First, overshooting the target is irreversible. Second, the milling process proceeds quickly when compared with the sampling period of a quantitative size and shape monitoring device such as the µ-DISCO.[32] Thus, the milling stages and the PSSD measurements have to be performed consecutively,

which makes it a discrete-time control problem.

If a quantitative model for a population of needle-like crystals undergoing breakage is available, the rotor speed θ of the mill that leads to a reduction of the initial measured volume-weighted average length $\hat{\bar{L}}_{1,\mathrm{v}}(t_0)$ to a given target length $\bar{L}_{1,\mathrm{target}}$ can be calculated and applied in an open-loop fashion. Unfortunately, multidimensional breakage models, such as the one for BLGA presented earlier, [137] are hardly ever available. Even if they were, they could never be fully predictive because of disturbances and modeling errors for some of the relevant phenomena. Feedback control is able to compensate for these undesirable effects. Also in the absence of any process model, model-free feedback controllers can be applied to operate processes automatically—most likely not optimally, but probably satisfactorily and robustly. In the following sections, a benchmark strategy is introduced and two different model-free feedback policies are proposed. The PSSD undergoes consecutive cycles of PSSD characterizations and milling stages, where the PSSD measurement in each cycle takes place either immediately before (Sections 4.3.4 and 4.3.5) or after (Section 4.3.6) the milling stage. The performance of these control laws has to be assessed with respect to their ability to reach a given target average length $\bar{L}_{1,\mathrm{target}}$ and with respect to the number of milling stages required to do so. Below, the index $k = 0, 1, 2, \ldots$ refers to the kth cycle and $\theta(k)$ denotes the rotor speed applied in the kth milling stage as calculated by the employed operating policy. Rotor speed bounds $\theta_{\min} \leq \theta \leq \theta_{\max}$ are enforced afterward. As soon as $\hat{\bar{L}}_{1,\mathrm{v}}(k)$ reaches the target, no further milling stages are run. Note that a target is considered to be reached if $\hat{\bar{L}}_{1,\mathrm{v}}$ lies within 3% of $\bar{L}_{1,\mathrm{target}}$ or below it.

4.3.4 Benchmark Strategy

The benchmark strategy (abbreviated with the letter C) consists of applying the same constant rotor speed θ_0 for each milling stage until the target $\bar{L}_{1,\mathrm{target}}$ is reached. The applied rotor speed is thus

$$\theta(k) = \theta_0 \qquad \forall k \geq 0 \tag{4.3}$$

where θ_0 is the only tuning parameter. This benchmark strategy is the simplest operating policy possible and it is useful for assessing the performance of the feedback controllers introduced below.

4.3.5 R Controller

The first feedback control law (abbreviated with the letter R, because it was developed for the *Recirculation* configuration) is motivated by the observation that the decrease in $\hat{\bar{L}}_{1,\mathrm{v}}$ becomes smaller and smaller with each milling stage when the same rotor speed is applied (see Section 4.4.1). The goal of the control law proposed in this section is thus to adjust the rotor speed to counteract this decrease in the change of the average length across the milling stages. To this end, a control error $e(k)$ can be defined as

$$e(k) = \frac{\Delta \hat{\bar{L}}_{1,\mathrm{v}}(1)}{\Delta \hat{\bar{L}}_{1,\mathrm{v}}(k)} - 1 \qquad \forall k > 0 \tag{4.4}$$

where the negative quantity $\Delta \hat{\bar{L}}_{1,\mathrm{v}}(k) = \hat{\bar{L}}_{1,\mathrm{v}}(k) - \hat{\bar{L}}_{1,\mathrm{v}}(k-1)$ is the decrease in the measured average length across the previous milling stage. This quantity is only defined for $k > 0$ and it holds $e(1) = 0$. By formulating the control law as

$$\theta(k) = \begin{cases} \theta_0 & \text{if } k = 0 \\ \theta_0\big(1 + \kappa e(k)\big) & \text{if } k > 0 \end{cases} \tag{4.5}$$

where θ_0 and κ are tuning parameters, it becomes clear that for $k > 1$, the feedback part $\kappa\theta_0 e(k)$ increases the rotor speed as a function of the decrease of $\hat{\bar{L}}_{1,\mathrm{v}}$ over the preceding milling stages.

4.3.6 Adaptive Controller

Besides either applying a model-based operating policy relying on a full population balance model or employing completely model-free operating

policies, there is the option to learn a simple process model online from past data in the spirit of adaptive control. As can be seen in Section 4.4.1, the evolution of $\hat{\bar{L}}_{1,\mathrm{v}}$ shows similarities to an exponential decay when the rotor speed is kept constant across the milling stages. This observation motivates a discrete-time model of the form

$$
\begin{aligned}
&\Delta \bar{L}_{1,\mathrm{v}}(0) = 0 \\
&\Delta \bar{L}_{1,\mathrm{v}}(k) = \alpha \Delta \bar{L}_{1,\mathrm{v}}(k-1) + \beta \theta(k) \qquad k \geq 1, \ 0 < \alpha < 1
\end{aligned}
\tag{4.6}
$$

where the negative quantity $\Delta \bar{L}_{1,\mathrm{v}}(k) = \bar{L}_{1,\mathrm{v}}(k) - \bar{L}_{1,\mathrm{v}}(0)$ $(k \geq 1)$ is the difference between the current and the initial volume-weighted average length. Notice that this definition of $\Delta \bar{L}_{1,\mathrm{v}}(k)$ is different than that of $\Delta \hat{\bar{L}}_{1,\mathrm{v}}(k)$ used in Section 4.3.5 and that $\bar{L}_{1,\mathrm{v}}(k)$ is obtained *after* milling at $\theta(k)$. The simple model given in eq 4.6 exhibits the following favorable features:

- The model is dynamic, i.e., it takes into account the past evolution of $\bar{L}_{1,\mathrm{v}}$ and also the effect of the rotor speed.

- The model has only two parameters (α and β) and they can be determined online automatically (see below).

- For $0 < \alpha < 1$ and $\theta(k) = $ const. $\forall k$, the model response is an exponential decay in discrete-time, where the parameter α determines the rate of decay.

- The second parameter β determines (together with α) the limit value of $\Delta \bar{L}_{1,\mathrm{v}}(k)$ as $k \to \infty$ for $\theta(k) = $ const. $\forall k$.

The adaptive control law (abbreviated with the letter A) based on the process model given in eq 4.6 works as follows:

- The rotor speed is kept constant at θ_0 for the first two milling stages because two measurements of $\Delta \bar{L}_{1,\mathrm{v}}$ are required to determine the two model parameters α and β, hence $\theta(k) = \theta_0$ for $k = 1, 2$.

- For $k \geq 3$, first, one estimates α and β using all past measurements, i.e., $\Delta \hat{\bar{L}}_{1,\mathrm{v}}(k-1), \Delta \hat{\bar{L}}_{1,\mathrm{v}}(k-2), \ldots$; then, one carries out a one-step

extrapolation of the fitted model to calculate the rotor speed $\theta(k)$ that yields the desired target average length after the kth milling stage, thus obtaining

$$\theta(k) = \frac{\bar{L}_{1,\text{target}} - \hat{\bar{L}}_{1,\text{v}}(0) - \alpha\Delta\hat{\bar{L}}_{1,\text{v}}(k-1)}{\beta} \qquad (4.7)$$

It is worth noting that the fitting of the two model parameters α and β can be formulated as a linear least-squares problem. However, to enforce the constraint $0 < \alpha < 1$, the sum of the squared deviations between $\Delta\hat{\bar{L}}_{1,\text{v}}(k)$ and the corresponding model predictions obtained from eq 4.6 was minimized with respect to α and β using MATLAB's `fmincon`.[140]

4.4 Results and Discussion

4.4.1 Comparison of the Benchmark and the Feedback Control Strategies

The two different feedback control strategies and the benchmark policy introduced in Sections 4.3.4 to 4.3.6 were tested experimentally using the *Recirculation* configuration according to the protocol detailed in Appendix C.6. Two performance criteria have to be assessed for all the policies: first, their ability to reach a given target average length $\bar{L}_{1,\text{target}}$; then, the required number of full suspension passes n_{WM} to do so, where one full suspension pass corresponds to pumping the suspension through the mill for a duration of one crystallizer residence time τ_{C}. To this aim, three experiments were performed, one each using the benchmark strategy, the R, and the A controller, all of them with Seeds ζ (see Appendix C.4) and an assigned target length $\bar{L}_{1,\text{target}}$ of 150 μm. All of these experiments were performed with a fixed set of controller tuning parameters listed in Table C.2 in Appendix C.6. The resulting evolution of the volume-weighted average length $\hat{\bar{L}}_{1,\text{v}}$ and of the rotor speed θ is shown in Figure 4.2 as a function of the number of full suspension passes. As expected, the different operating policies exhibit different behavior: the R and the A controller managed to reach the target, while the bench-

mark strategy (C) failed to do so even after 11 passes at a rotor speed θ of 7500 rpm. This failure can be attributed to the fact that there exists a grinding limit for any milling process with a fixed rotor speed, i.e., a minimum achievable average length. Since this grinding limit appears to be a function of the rotor speed under the conditions explored in this work and it is a priori unknown, selection of a reasonable constant rotor speed θ_0 is difficult and feedback action on the rotor speed is required.

Even though both feedback controllers (R and A) managed to reach the target, the corresponding closed-loop experiments differ in terms of the applied rotor speed and in terms of the number of passes required, as illustrated in Figure 4.2. The rotor speed is constant ($\theta_0 = 7500$ rpm) for the first two milling stages when using both controllers, which is a consequence of the definition of the control laws in Sections 4.3.5 and 4.3.6. For the third and the following passes, the A controller calculated set points that would enable reaching the target in a single pass according to the simple adaptive model (see eq 4.7). However, since these set points exceeded the upper bound of the rotor speed $\theta_{\max}$, the set point was constrained to this upper limit. In contrast to the A controller, the R controller selected significantly lower rotor speeds for the third and the following passes, which leads to a larger number of milling stages required to reach the target. On the one hand, this behavior can be attributed to the inherent differences in the control laws, and on the other hand, to the specific choice of tuning parameters of the R controller, which might be modified if necessary. In any case, both feedback controllers successfully increased the rotor speed in order to overcome the issue of the grinding limit observed when using the benchmark strategy.

The number of tuning parameters required by a given control law is also a factor to consider. The benchmark strategy and the two feedback controllers studied here have one tuning parameter in common, namely, the initial rotor speed θ_0. Contrary to the A controller, the R controller has an additional tuning parameter κ.

On the basis of the above discussion, it was decided to use the A controller to perform further closed-loop control experiments. This controller clearly has the ability to reach reasonable target average lengths and it makes use of the knowledge gained from prior milling stages regarding the evolution of the average length.
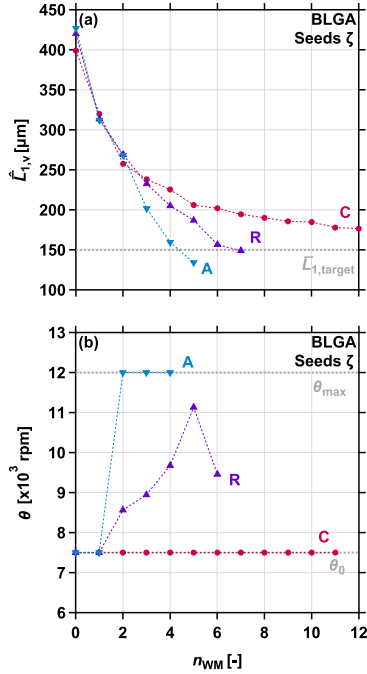
Figure 4.2: Evolution of **(a)** the measured volume-weighted average length $\hat{\bar{L}}_{1,v}$ and of **(b)** the rotor speed θ as a function of the number of full suspension passes n_{WM} for experiments using the benchmark strategy (red circles), the R controller (violet upward-pointing triangles), and the A controller (blue downward-pointing triangles) with BLGA Seeds ζ and a target average length $\bar{L}_{1,target} = 150\,\mu m$. Along the L_1 direction, a regular grid with 120 bins was used to reconstruct the PSSDs and to compute the average dimensions, with a grid spacing of $17\,\mu m$, $17\,\mu m$, and $16\,\mu m$ for the experiments using the benchmark strategy, the R controller, and the A controller, respectively. Along the L_2 direction, the corresponding grid spacing was $6\,\mu m$, $7\,\mu m$, and $9\,\mu m$ using 40 bins.

4.4.2 Adaptive Controller

The A controller was employed to perform a series of closed-loop control experiments using the recirculation configuration and the compound BLGA. A total of six experiments, three each for Seeds ε and Seeds ζ, was performed using the protocol described in Appendix C.6. The goal of these experiments was to reach three different targets for each batch of seeds. The experiments are distinguished by labeling them $\varepsilon_{1,A}$ through $\varepsilon_{3,A}$ for Seeds ε (targets 210 μm, 180 μm, and 150 μm) and $\zeta_{1,A}$ through $\zeta_{3,A}$ for Seeds ζ (targets 300 μm, 225 μm, and 150 μm).

The resulting evolution of the volume-weighted average length and width and the rotor speed θ for each full suspension pass are shown in Figure 4.3a-c and Figure 4.3d-f for Seeds ε and Seeds ζ, respectively. Two main observations can be made in these plots. First, it is clear that the controller managed to drive the population to the target average length $\bar{L}_{1,\text{target}}$ in all the cases except $\zeta_{1,A}$, where the target was overshot. The reason for the outcome of this experiment is that the A controller has to apply a constant rotor speed of 7500 rpm during the first two full suspension passes, where the outcome of these two passes is subsequently used to fit the adaptive model. Thus, to reach targets close to the average length of the seed population, such as in the case of $\zeta_{1,A}$, the design of the controller would require lowering the initial rotor speed θ_0. A second observation is that the different experiments showed a different evolution of the rotor speeds through the milling stages and a different number of full suspension passes required to reach the respective target. Experiments $\varepsilon_{1,A}$ and $\zeta_{1,A}$ required only two full suspension passes through the mill to terminate the controller action, while experiments $\varepsilon_{3,A}$ and $\zeta_{3,A}$ required five full suspension passes due to the lower target average length. Experiment $\varepsilon_{3,A}$ exhibits an interesting evolution of the rotor speed. After the first two full suspension passes, the controller applied a rotor speed of 11 651 rpm. The target was not yet reached using this rotor speed, but the average length ended up close to it. Being aware of the proximity to the target and having adapted the exponential discrete-time model, the controller applied a relatively low rotor speed of 6381 rpm, which was again not sufficient to reach the target. After adapting the model once more, the controller decided to use an intermediate rotor speed of 8163 rpm, which allowed reaching the target average length. The other
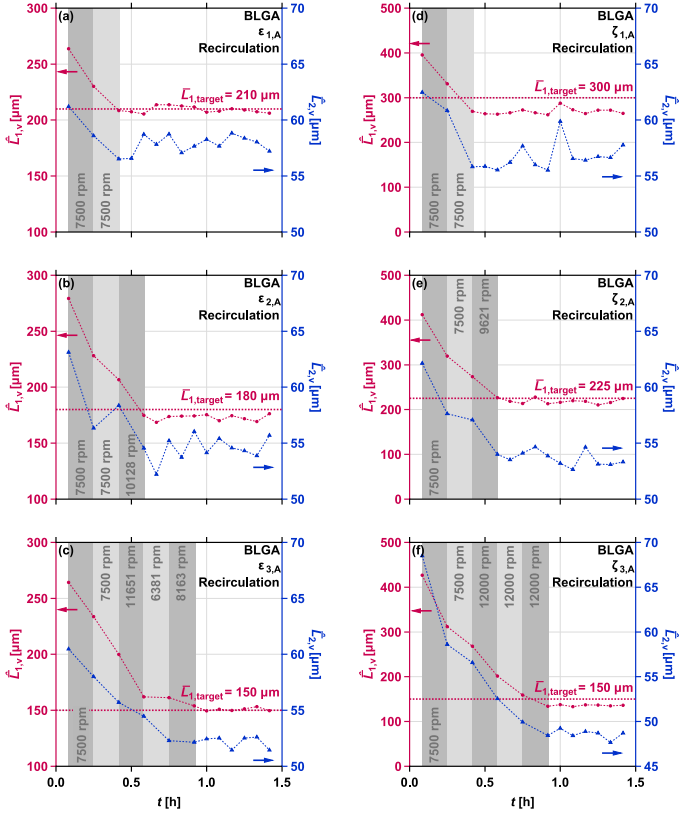
Figure 4.3: Time-resolved evolution of the measured volume-weighted average length $\hat{\bar{L}}_{1,\mathrm{v}}$ and width $\hat{\bar{L}}_{2,\mathrm{v}}$ for BLGA Seeds ε with target average lengths $\bar{L}_{1,\mathrm{target}}$ **(a)** 210 µm $(\varepsilon_{1,\mathrm{A}})$, **(b)** 180 µm $(\varepsilon_{2,\mathrm{A}})$, and **(c)** 150 µm $(\varepsilon_{3,\mathrm{A}})$ and for BLGA Seeds ς with target average lengths $\bar{L}_{1,\mathrm{target}}$ **(d)** 300 µm $(\varsigma_{1,\mathrm{A}})$, **(e)** 225 µm $(\varsigma_{2,\mathrm{A}})$, and **(f)** 150 µm $(\varsigma_{3,\mathrm{A}})$ using the A controller. Along the L_1 direction, a regular grid with 120 bins was used to reconstruct the PSSDs and to compute the average dimensions with a grid spacing of 11 µm, 13 µm, 14 µm, 21 µm, 16 µm, and 16 µm for the experiments in panels a through f, respectively. Along the L_2 direction, the corresponding grid spacing was 7 µm, 7 µm, 8 µm, 7 µm, 6 µm, and 9 µm using 40 bins. The shaded gray region indicates the milling stage, and the corresponding rotor speed θ is reported alongside.

extreme case is experiment $\zeta_{3,A}$, which was already explained in detail in Section 4.4.1 (see Figure 4.2).

In order to apply feedback control (for instance in the form proposed in Section 4.3.6), the availability of an online size and shape monitoring tool or method is a necessity. In the absence of such a tool or method, the simplified model given by eq 4.6 can still be useful. Its parameters can be estimated offline once for a given batch of seeds by conducting two or more milling operations with different rotor speeds and by performing intermediate measurements of the average crystal dimensions using any available offline characterization technique. This procedure is far less costly than developing a multidimensional population balance model and the obtained ad-hoc process model is certainly better than not having any model at all.

4.4.3 Generality of the Adaptive Controller

It is essential that the control strategies proposed in this chapter can be applied to any compound that exhibits a needle-like morphology. The breakage of crystals is a mechanical operation and the impact of the milling stage on the reduction of the average dimensions of the seed population depends on the physical properties of the crystals such as their brittleness. Still, the proposed A controller (and also the R controller) should be able to drive the average length of a seed population toward a target length independently of the compound. To check if this is indeed the case, closed-loop control experiments with GDM, also exhibiting needle-like morphology, were performed using the A controller.

Seeds $\mathfrak{n}$ (see Appendix C.4) were milled by employing the protocol described in Appendix C.6 with the aim of reaching the three different target average lengths of 225 µm ($\mathfrak{n}_{1,A}$), 200 µm ($\mathfrak{n}_{2,A}$), and 175 µm ($\mathfrak{n}_{3,A}$). On the basis of the observed evolution of the average length visualized in Figure 4.4, it is apparent that the controller was successful in achieving its goal. Similar to the observations made in Section 4.4.2, reaching the three targets requires different rotor speeds and a different number of full suspension passes n_{WM}. These experiments and the closed-loop control experiments discussed in Section 4.4.2 indicate that an initial rotor speed θ_0 of 7500 rpm is a reasonable choice for an acceptable closed-loop performance in many cases.
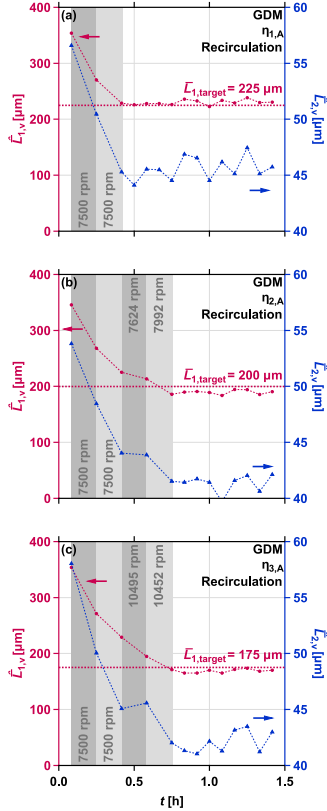
Figure 4.4: Time-resolved evolution of the measured volume-weighted average length $\hat{\bar{L}}_{1,v}$ and width $\hat{\bar{L}}_{2,v}$ for GDM Seeds n with target average lengths $\bar{L}_{1,target}$ **(a)** 225 µm ($n_{1,A}$), **(b)** 200 µm ($n_{2,A}$), and **(c)** 175 µm ($n_{3,A}$) using the A controller. Along the L_1 direction, a regular grid with 120 bins was used to reconstruct the PSSDs and to compute the average dimensions, with a grid spacing of 13 µm, 12 µm, and 13 µm for the experiments in panels a through c, respectively. Along the L_2 direction, the corresponding grid spacing was 7 µm, 6 µm, and 6 µm using 40 bins. The shaded gray region indicates the milling stage, and the corresponding rotor speed θ is reported alongside.

4.5 Conclusions

Model-free control laws have been presented with the aim to systematically manipulate the size and the shape of needle-like crystals using a rotor-stator wet mill. The proposed strategies have been tested in an experimental campaign to assess their performance, exploiting the online monitoring capabilities of the μ-DISCO (see also Section 1.2).[32] Specifically, the so-called adaptive (A) controller successfully managed to steer three different seed populations of two different needle-like compounds to desired target average lengths.

The control of wet milling operations represents a further step toward integrating different unit operations to robustly and effectively manipulate the size and the shape of needle-like crystals. Within such an integrated framework, controlled milling stages ensure a reduction in the aspect ratio of the crystals without the loss of any yield. This shape change comes at the cost of producing a lot of fine particles. Thus, a dissolution stage, which might further aid in the reduction of the particle aspect ratio, or a fines separator should be employed afterward to remove them. One way of performing such a dissolution stage is presented in Chapter 5.

Nomenclature

Acronyms

A	adaptive (controller)
BLGA	β L-glutamic acid
C	benchmark operating strategy
DISCO	dual imaging system for crystallization observation
GDM	γ D-mannitol
PS(S)D	particle size (and shape) distribution
R	variant of model-free feedback controller

Roman symbols

c	solute concentration (per mass of solvent basis) $[\mathrm{g\,kg^{-1}}]$
c^*	solubility (per mass of solvent basis) $[\mathrm{g\,kg^{-1}}]$
e	control error $[-]$
f	number density function (PSSD) $[\mathrm{\mu m^{-2}}]$
f_{v}	volume-weighted PSSD $[\mathrm{\mu m^{-2}}]$
F	volumetric flow rate $[\mathrm{L\,s^{-1}}]$
k	cycle index (for feedback controllers) $[-]$
L_i	ith particle dimension ($i = 1, 2$) $[\mathrm{\mu m}]$
$\bar{L}_{i,\mathrm{v}}$	volume-weighted average of ith particle dimension $[\mathrm{\mu m}]$
$\bar{L}_{1,\mathrm{target}}$	target average length $[\mathrm{\mu m}]$
m_{seed}	seed mass $[\mathrm{g}]$
m_{solvent}	solvent mass $[\mathrm{kg}]$
n_{grid}	number of grid points for the PSSD binning protocol $[-]$
n_{WM}	number of full suspension passes (wet mill) $[-]$
S	relative supersaturation, c/c^* $[-]$
t	time, unit varies
T	temperature $[\mathrm{°C}]$
T^*	saturation temperature $[\mathrm{°C}]$
V	volume $[\mathrm{L}]$

Greek symbols

α	model parameter (A controller) $[-]$

β	model parameter (A controller) [µm min]
ε, ζ, $\mathfrak{n}$	labels for seed populations
θ	rotor speed [rpm]
κ	tuning parameter (R controller) [–]
μ_{ij}	ij-cross moment of PSSD [μm^{i+j}]
ρ_{c}	crystal density [$\text{g}\,\mu\text{m}^{-3}$]
$\sigma_{ii,\text{v}}$	volume-weighted broadness of the PSSD along the ith dimension [µm]
τ	residence time [s]

Subscripts and superscripts

^	measurement or estimate
0	initial value
A	adaptive controller
C	crystallizer
exp	experimental
max	upper limit
min	lower limit
samp	sampling
set	set point
WM	wet mill

Chapter 5

Modeling and Control of Dissolution

5.1 Introduction

In the context of industrial crystallization from solution, dissolution processes are of interest for a number of reasons. For instance, dissolution plays an important role in solvent-mediated polymorphic transformations.[3,141] As to pharmaceuticals, the dissolution rate of drugs in the human body influences their bioavailability.[9,13] Dissolution processes can also be used to alter the relative area of crystal facets,[84] which could, for instance, be useful to increase the catalytic activity of solids.[17] Some of the aforementioned characteristics of the particles, and also others such as downstream processability, depend in fact on the particle size and shape distribution (PSSD). Cyclic processes involving dissolution stages have been proposed to modify the PSSD in a systematic way, since these stages add a degree of freedom for size and shape manipulation,[21,62,70,71,142,143] and because they can additionally be applied for the purpose of fines removal[63,64,78] or for the control of polymorphic

purity. [144,145]

Kinetic models of the dissolution process are valuable tools, be it for process design and optimization or for the development and the initial testing of feedback control strategies. Early investigations on dissolution rate modeling proposed that the mass depletion rate during the dissolution of crystalline solids in solution is controlled by diffusion. [146] In the case of spherical particles, Sherwood correlations are available for the corresponding mass transfer rates under various convection regimes. [18] However, dissolution mechanisms can vary as a function of the undersaturation, [83] and dissolution processes where the surface disintegration is the rate limiting mechanism were observed and modeled as well. [141,147–149] In any case, the dissolution rate is expected to be a function of many factors such as the undersaturation, the particle size and shape, the temperature, and the agitation of the suspension, but also of the solvent, of additives, and of the pH. Several studies in the literature present and apply dissolution rate models featuring a subset of these effects. Some of them model the dissolution rate based on mass or concentration. [141,149,150] If the evolution of the solid population is to be described as well, the population balance equation (PBE) framework is often applied, mostly using a single characteristic particle dimension. [76,142,151] In this framework, which is adopted in this chapter, the dissolution rate is defined as the rate of change of a characteristic particle dimension. By considering multiple characteristic particle dimensions, also the shape evolution of the solids in the population during dissolution can be modeled. [148] Only a very small number of experimental studies report multidimensional dissolution rate models for populations of particles, where their nature is empirical. [46,55]

The purpose of this chapter is to address two objectives concerning modeling and control of dissolution processes of needle-like crystals. First, empirical two-dimensional kinetic models of the dissolution of the needle-like compound β L-glutamic acid (BLGA) in water are identified from experimental data using a well-established parameter estimation technique. One of these models is discussed in the context of cyclic shape modification processes similar to that proposed in ref 63. Second, a model-free feedback control strategy with the goal to dissolve a given fraction of the initial particle volume, which is representative of the initial solid mass in a batch process, is presented. The idea behind this

control law is to operate dissolution stages robustly and reliably, where these stages can have various purposes on the process scale such as the removal of fines. The controller is tested in a simulation framework using the identified BLGA dissolution kinetics. Also, its performance and generality are validated in experiments using BLGA and a different compound also forming needle-like crystals, vanillin. Note that controlled dissolution has been addressed previously in the literature (see, e.g., refs 78 and 112). The novelty of the concept proposed in this chapter lies mainly in the fact that the particle volume is observed directly and that the controller works for very dilute suspensions, as demonstrated in Section 5.5. Furthermore, some implementation details are given that may reduce the required dissolution time without causing significant overshoot of the target. Note that working with dilute suspensions may prove useful during the development phase of a process when only small amounts of the compound of interest may be available.

This chapter is organized as follows. First, the experimental protocols are explained in Section 5.2. Second, the methods for the dissolution rate modeling and the parameter estimation are given in Section 5.3. Third, in Section 5.4, an important discussion of the issues that arise when graphically representing PSSDs is presented, followed by the modeling results and their discussion. Finally, the feedback control strategy is introduced, implemented, and assessed in Section 5.5.

5.2 Experimental Protocols

For the sake of brevity, the details of the used materials (BLGA and vanillin) and the employed seed preparation protocols are given in Appendix D.1 and Appendix D.2, respectively. In the following two subsections, the experiments used for the modeling study and those used to test the feedback controller are described.

5.2.1 Experiments for Dissolution Rate Estimation

For estimating the two-dimensional dissolution rate of BLGA in water, the data collected from 13 experiments (experiments E1 to E13) were used (see their main characteristics in Table 5.1). All these experiments were operated at low undersaturations, since higher driving forces would lead to rapid dissolution of the seed crystals, which in turn would make

it very challenging to monitor the particle size and shape evolution with an adequate time resolution. The temperature range covered by these experiments was chosen to be at or above room temperature since the employed monitoring device (i.e., the μ-DISCO[32]) features a sampling loop. The experiments were performed using either crash heating steps or temperature ramps with different heating rates and intermediate plateaus to widen the range of the explored operating conditions.

Experiments E1 to E6 correspond to experiments α to ζ in a previous work.[40] The detailed experimental protocol, as well as an explanation of the experimental setup and the device employed for characterizing both the solid and the liquid phase, is given in this reference. For the sake of completeness, a description of the setup is also provided in Appendix D.3.

The same experimental setup was applied for conducting experiments E7 to E13. For these experiments, saturated solutions of BLGA in water were prepared by adding excess BLGA, letting the solutions equilibrate for at least 6 h, and then filtering them off. Afterward, for each experiment, 2000.0 g of saturated solution were loaded into the reactor. The saturation temperature was either 29.9 °C (E7 to E11) or 25.9 °C (E12 and E13). For experiments E7 to E11, the clear solutions were cooled to 29.1 °C and 1.0 g of BLGA seeds (prepared as described in Appendix D.2) were suspended. These suspensions were kept at the initial temperature of 29.1 °C, which corresponds to a slightly supersaturated state ($S = 1.03$) with negligible growth, for 2 h in order to properly characterize the seed population. Afterward, for experiments E7 to E9, the suspensions were heated consecutively and linearly to the four different temperature plateaus 29.6 °C, 30.1 °C, 30.6 °C, and 31.1 °C, where the temperature at each plateau was kept constant for 1 h before heating to the next plateau. The heating rates in between these plateaus were $0.10\,°\mathrm{C\,h^{-1}}$, $0.25\,°\mathrm{C\,h^{-1}}$, and $0.50\,°\mathrm{C\,h^{-1}}$ for E7, E8, and E9, respectively. Experiments E10 to E13 were crash heating experiments. After the initial phase of 2 h at 29.1 °C, the suspensions in E10 and E11 were crash heated to 30.6 °C and 30.3 °C, respectively, and subsequently kept at these temperatures to let the suspensions equilibrate. Essentially the same protocol was followed for E12 and E13, but at different temperatures: the clear solutions were cooled to 25.1 °C before adding 1.0 g of BLGA seeds, characterizing the seed population at this temperature over 2 h, and then crash heating to 26.3 °C and 26.6 °C, respectively.

Table 5.1: List of experiments used to estimate the dissolution kinetics of BLGA in water.[a]

Exp.	Label in ref 40	T_0 [°C]	T_{sat} [°C]	T_{final} [°C]	Profile	Fit/Val.
E1	α	24.7	25.0	26.2	ramp	fit.
E2	β	25.5	25.8	27.0	ramp	fit.
E3	γ	26.7	27.0	28.2	ramp	fit.
E4	δ	27.9	28.2	29.4	ramp	fit.
E5	ϵ	29.1	29.4	30.6	ramp	val.
E6	ζ	25.9	26.2	27.4	ramp	val.
E7	–	29.1	29.9	31.1	ramp	val.
E8	–	29.1	29.9	31.1	ramp	val.
E9	–	29.1	29.9	31.1	ramp	fit.
E10	–	29.1	29.9	30.6	step	fit.
E11	–	29.1	29.9	30.3	step	fit.
E12	–	25.1	25.9	26.3	step	val.
E13	–	25.1	25.9	26.6	step	val.

[a] T_0 is the initial temperature (at seed addition), T_{sat} is the saturation temperature of the clear solution before seeding, and T_{final} is the final temperature of the experiment. The column Profile highlights whether the basic type of temperature profile applied during an experiment was a heating ramp or a heating step. In the column Fit./Val., fit. indicates that an experiment was used for fitting the parameters of the dissolution kinetics and val. indicates that it was only used for model validation.

5.2.2 Feedback Control Experiments

All the experiments performed using the feedback controller discussed in Section 5.5 consisted of two distinct experimental phases, namely, of an initial idle phase and of a main experimental phase. The protocols for these two phases slightly differed for the two model compounds and they are discussed below.

For each experiment performed with BLGA, a saturated solution at 29.9 °C was prepared by adding an excess amount of BLGA to water. The suspension was equilibrated at the desired temperature at a stirring rate of 400 rpm. The suspension was subsequently filtered off and 2000.0 g of the clear solution were loaded into the reactor and cooled down to an initial temperature of 29.1 °C corresponding to a supersaturation of $S_0 = 1.03$. For the experiments with the unmilled population discussed in Section 5.5.2, 0.8 g of seeds was added once the initial temperature was reached. For the experiments with the milled population discussed in Section 5.5.3, 0.5 g of Seeds ε of ref 67 was added once the initial temperature was reached. The population was then subjected to wet milling at a constant rotor speed of 7500 rpm for a duration of 102 s using the equipment and the recirculation configuration explained in detail elsewhere [67] (see Appendix D.3 for a summary; see also Chapter 4).

For each experiment performed with vanillin, a saturated solution at 25 °C was prepared by adding an excess amount of vanillin to water and stirring at 400 rpm. The suspension was equilibrated and filtered off, and 2000.0 g of saturated solution was loaded into the reactor. The clear solution was then cooled down to an initial temperature of 24.6 °C, corresponding to a supersaturation of $S_0 = 1.02$. Upon reaching this temperature, 1.0 g of vanillin seeds was added. Note that for both compounds, the chosen S_0 ensured that neither dissolution nor detectable growth took place before activating the feedback controller.

The initial phase started immediately after seed addition or wet milling. During this phase, the suspension was monitored and characterized for a duration of 2 h and 3.5 h for BLGA and vanillin, respectively. The same experimental setup and the same monitoring tool as referred to in Section 5.2.1 were used. The measurements obtained during the initial phase were not used for control purposes. For vanillin, a longer duration of the initial idle phase was necessary as the aggregated vanillin

seed crystals require about $1.5\,h$ of deaggregation time in the suspension to obtain a stable sampled particle count and a stable total visual hull volume.[40]

For both the compounds, the duration of the main experimental phase was set to $7\,h$. During this phase, the suspension was monitored and characterized and the particle volume controller (see Section 5.5) was operated with a sampling interval t_{samp} of $5\,min$. The total visual hull volume (see ref 40 or Appendix D.3) obtained from each measurement was fed back to the controller; below, this quantity will be referred to as the sampled or observed particle volume. The total particle count, comprising the particles of all the five shape classes identified and measured by the µ-DISCO (see also Section 1.2),[32] was logged as well and will be referred to as the particle count in Section 5.5.

5.3 Dissolution Rate Modeling and Parameter Estimation

Several candidate models for multidimensional dissolution kinetics were defined and their parameters were estimated by fitting the models to the available experimental observations. Afterward, in Section 5.4, one of the fitted models is selected and analyzed in detail.

5.3.1 Population Balance Model

The dissolution of an ensemble of needle-like particles in suspension can be modeled using a morphological population balance equation based on a generic particle shape model such as that of a cylinder with length L_1 and width L_2, coupled with a material balance. The PBE can be written as

$$\frac{\partial f}{\partial t} + \frac{\partial (D_1 f)}{\partial L_1} + \frac{\partial (D_2 f)}{\partial L_2} = 0 \tag{5.1}$$

where $f(t, L_1, L_2)$ is the number density function (called PSSD for brevity), which is defined on a per mass of solvent basis, and D_i is the dissolution rate of the ith characteristic particle dimension ($i = 1, 2$). In this chapter, D_i can be a function of L_i, of the temperature T, and of the relative

undersaturation $S = c/c^*(T)$, where c is the solute concentration defined on a per mass of solvent basis, and $c^*(T)$ is the corresponding solubility as a function of temperature. The effect of the agitation of the suspension is not considered here since all the experiments (see Section 5.2.1) were performed at the same stirring rate to keep the solids well suspended. Whenever the solution is undersaturated ($S < 1$), D_i is defined to be negative, and $D_i = 0$ otherwise. The initial and boundary conditions for eq 5.1 are

$$
\begin{aligned}
f(0, L_1, L_2) &= f_0(L_1, L_2) \\
f(t, \infty, L_2) &= 0 \\
f(t, L_1, \infty) &= 0
\end{aligned}
\tag{5.2}
$$

where $f_0(L_1, L_2)$ is the PSSD of the seed population. The PBE is coupled with the material balance

$$
\frac{\mathrm{d}c}{\mathrm{d}t} = -\rho_c k_v \frac{\mathrm{d}}{\mathrm{d}t} \int_0^\infty \int_0^\infty L_1 L_2^2 f(t, L_1, L_2) \, \mathrm{d}L_1 \, \mathrm{d}L_2
\tag{5.3}
$$

where ρ_c is the crystal density and k_v is the volume shape factor. The initial condition for eq 5.3 is $c(0) = c_0$, where c_0 is the initial solute concentration. The PBE model given by eqs 5.1 to 5.3 was solved numerically as explained in Appendix D.6.

The volume-weighted average particle length and width are quantities of interest in this chapter. They are defined as

$$
\begin{aligned}
\bar{L}_{1,v}(t) &= \frac{\mu_{22}(t)}{\mu_{12}(t)} \\
\bar{L}_{2,v}(t) &= \frac{\mu_{13}(t)}{\mu_{12}(t)}
\end{aligned}
\tag{5.4}
$$

where

$$\mu_{ij}(t) = \int\limits_{L_{2,\min}}^{\infty} \int\limits_{L_{1,\min}}^{\infty} L_1^i L_2^j f(t, L_1, L_2) \, \mathrm{d}L_1 \, \mathrm{d}L_2 \tag{5.5}$$

with $L_{i,\min} = 0$ $(i = 1, 2)$ is the ij-cross moment of the PSSD f.

An alternative would be to use number-based average particle dimensions, which are defined as

$$\bar{L}_{1,\mathrm{n}}(t) = \frac{\mu_{10}(t)}{\mu_{00}(t)}$$
$$\bar{L}_{2,\mathrm{n}}(t) = \frac{\mu_{01}(t)}{\mu_{00}(t)} \tag{5.6}$$

and which are barely used in this chapter for reasons that are explained in Section 5.4.1. A further quantity of interest is the volume-weighted PSSD

$$f_{\mathrm{v}}(t, L_1, L_2) = \frac{L_1 L_2^2 f(t, L_1, L_2)}{\mu_{12}(t)} \tag{5.7}$$

which indicates the mass distribution of the population.

5.3.2 Candidate Dissolution Rate Models

The four models considered in this chapter are based on the following empirical expressions for the dissolution rate:

$$\text{M1:} \qquad D_i = -k_{\mathrm{d},i}(1 - S) \qquad\qquad\qquad (5.8)$$

$$\text{M2:} \qquad D_i = -k_{\mathrm{d},i}(1 - S)^{k_{\mathrm{s},i}} \qquad\qquad\qquad (5.9)$$

$$\text{M3:} \qquad D_i = -k_{\mathrm{d},i}\exp\left(-\frac{k_{\mathrm{s},i}}{T}\right)(1 - S) \qquad\qquad (5.10)$$

$$\text{M4:} \qquad D_i = -k_{\mathrm{d},i}(1 - S)\left(1 + \frac{L_i}{L_{\mathrm{ref}}}\right)^{-k_{\mathrm{s},i}} \qquad (5.11)$$

where $i = 1, 2$ indicates the particle dimension, $k_{\mathrm{d},i}$ and $k_{\mathrm{s},i}$ are the parameters to be estimated, and L_{ref} is a unit reference length. Model M1 depends on two unknown parameters, namely, $k_{\mathrm{d},1}$ and $k_{\mathrm{d},2}$, it is linear in the undersaturation, and it depends neither explicitly on the temperature nor on the particle size. Model M2 is a four-parameter model that allows the dissolution rates to be nonlinear functions of the undersaturation. It is clear that M1 is a special case of M2, but with fewer degrees of freedom to prevent a potential overfit. Model M3 is also a four-parameter model, but it is linear in the undersaturation and includes an explicit temperature dependence (here, T is the process temperature in Kelvin). Finally, model M4, which depends on four parameters as well, is linear in the undersaturation and features a dissolution rate in the ith direction that depends on L_i.

Clearly, models M1 to M4 cover only a subset of the possible physical dependencies of the dissolution rates (and combinations thereof) and they were selected after prior testing to strike a balance between the experimental data available and the model complexity. Covering more dependencies is often not useful because such complicated models are heavily overparametrized in the sense that they cannot be explained by the data collected in a reasonable experimental campaign.

5.3.3 Fitting Procedure

The parameters in the models M1 to M4 were determined by the maximum likelihood estimation (MLE) method. A summary of this method, including the methodology to quantify the parameter uncertainty, is given in Appendix D.4.

Three measured quantities were chosen for fitting, namely, the volume-weighted average particle length $\bar{L}_{1,v}$, the volume-weighted average particle width $\bar{L}_{2,v}$, and the solute concentration c. As explained in Appendix D.5, not all the collected experimental data was used for fitting, but only a subset (that covers the whole temperature range), which enabled independent model validation. Prior to fitting, the experimental data set was preprocessed as detailed in Appendix D.5, mainly to obtain seed populations for the PBE model and to ensure equal weight of the experiments and the measured quantities in the fitting procedure.

5.4 Modeling Results and Discussion

5.4.1 Graphical Representation of PSSDs

Graphical representations of two-dimensional PSSDs have been presented in previous publications,[23,32,39,54,63,64,66,67,137] usually using the volume-weighted PSSD f_v defined in eq 5.7. The reason for not showing the PSSD f itself is that its graphical representation is generally dominated by fines. For each point in time, both f and f_v can be visualized, for instance, as two-dimensional contour plots.

Before being able to visualize the PSSD of a set of particles observed and characterized during an experiment, the PSSD itself needs to be obtained by binning the characteristic dimensions of the particles into a predefined size grid.[23] Thus, the quality of such a PSSD is inherently a function of the number of sampled particles and of the chosen grid resolution. If the number of particles sampled from a given PSSD becomes smaller and smaller for a fixed grid, both the graphical representation of the PSSD and the accuracy of its average particle dimensions are affected.

To illustrate the issue with the graphical representation of the PSSD analyzed here, the PSSD of the initial steady state phase of experiment E5 has been obtained using three different numbers of particles. The

Table 5.2: Properties of the PSSDs visualized in Figure 5.1 (seeds of experiment E5).

Quantity	Unit	Values		
N_t	–	10	30	60
N_s	–	80\,202	240\,458	475\,764
$\bar{L}_{1,\mathrm{v}}$	µm	376.2	375.7	374.8
$\bar{L}_{2,\mathrm{v}}$	µm	57.5	57.8	57.7

number of particles sampled to obtain these PSSDs, N_s, as well as their volume-weighted average particle dimensions are listed in Table 5.2. For instance, the first PSSD was obtained by binning $N_\mathrm{s} = 80\,202$ particles that were observed during the first $N_\mathrm{t} = 10$ sampling instants (corresponding to the first 20 min) of experiment E5. The details on the employed grid and the binning protocol can be found in Appendix D.6. A contour plot obtained by rescaling the corresponding f_v using its maximum is shown in Figure 5.1a. It is clear from Figure 5.1b,c that the graphical representation can be improved by increasing the number of data points N_t, which corresponds to sampling more particles. According to Table 5.2, a sixfold increase in the number of sampling instants and sampled particles (i.e., $N_\mathrm{t} = 60$ data points, corresponding to almost 500\,000 particles) is sufficient to obtain a rather smooth contour plot for this specific population without affecting the average dimensions. Thus, there is an important observation here. There appear to be two different accuracy thresholds in terms of required number of particles; one for obtaining a smooth graphical representation of f_v and one for obtaining converged values for the average dimensions. These thresholds are a function of the PSSD itself, of the grid resolution, and additionally, in the case of the graphical representation, also of the chosen contour levels. In any case, the threshold for a smooth graphical representation is at a much higher level than that for accurate average dimensions.

After the loss of many particles during dissolution, the number of sampling instants required to reach the threshold for the graphical representation is generally higher than before. To illustrate this issue, the
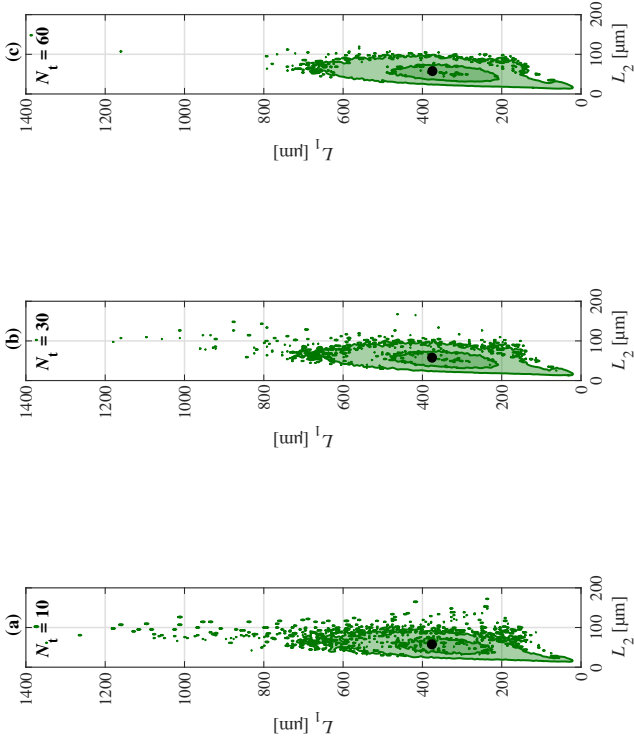
Figure 5.1: Volume-weighted PSSDs f_v (according to eq 5.7 and additionally normalized by the maximum of each PSSD) of the seed population of E5 obtained from all the particles observed during the first **(a)** $N_t = 10$, **(b)** $N_t = 30$, and **(c)** $N_t = 60$ sampling instants of the experiment. The contour line values correspond to 0.1, 0.5, and 0.9 of each normalized PSSD. The black markers indicate the volume-weighted average dimensions of each PSSD, which are also given in Table 5.2.

Table 5.3: Properties of the PSSDs visualized in Figure 5.2 (seeds and products of experiment E11).

Quantity	Unit	Values				
		Seeds	Products			
N_t	–	60	10	30	60	90
N_s	–	308 486	24 876	74 421	150 262	226 975
$\bar{L}_{1,\mathrm{n}}$	μm	199.5	216.0	216.7	216.5	216.3
$\bar{L}_{2,\mathrm{n}}$	μm	35.1	38.6	38.5	38.4	38.3
$\bar{L}_{1,\mathrm{v}}$	μm	489.0	454.4	453.5	453.3	454.4
$\bar{L}_{2,\mathrm{v}}$	μm	75.9	73.2	72.9	72.5	72.7

volume-weighted seed PSSD of experiment E11 and four of its volume-weighted product PSSDs (obtained by combining particles observed during different numbers of sampling instants) are shown in Figure 5.2 and their properties are listed in Table 5.3. The product PSSD in Figure 5.2b was obtained from only about $N_\mathrm{s} = 25\,000$ particles. When increasing N_s, the body of the PSSD becomes more pronounced and the PSSD appears less fragmented, as shown in Figure 5.2c-e. To obtain the relatively smooth contour plot shown in Figure 5.2e, about $N_\mathrm{s} = 225\,000$ particles were required by combining $N_\mathrm{t} = 90$ sampling instants corresponding to 180 min of experimental time. Thus, collecting enough data points at the end of a dissolution experiment to obtain a sufficiently smooth graphical representation of the volume-weighted product PSSD is often impractical. Nevertheless, it should be kept in mind that only the graphical representation is affected by this limitation but not the average dimensions, which is confirmed by the data reported in Table 5.3. It is also worth noting in Table 5.3 that both $\bar{L}_{i,\mathrm{n}}$ $(i = 1, 2)$ increased from the seed to the product PSSDs, whereas the $\bar{L}_{i,\mathrm{v}}$ $(i = 1, 2)$ decreased. The increase of $\bar{L}_{i,\mathrm{n}}$ $(i = 1, 2)$ might seem counterintuitive at first, but since these are unweighted average quantities, they are heavily affected by the disappearance of a large number of small particles. $\bar{L}_{i,\mathrm{v}}$ $(i = 1, 2)$, on the contrary, are hardly affected by small particles.

Figure 5.2: Volume-weighted PSSDs f_v (according to eq 5.7 and additionally normalized by the maximum of each PSSD) of **(a)** the seed population of E11 obtained from all the particles observed during the first $N_t = 60$ sampling instants of the experiment and of the product population of experiment E11 obtained from all the particles observed during the last **(b)** $N_t = 10$, **(c)** $N_t = 30$, **(d)** $N_t = 60$, and **(e)** $N_t = 90$ sampling instants of the experiment. The contour line values correspond to 0.1, 0.5, and 0.9 of each normalized PSSD. The black markers indicate the volume-weighted average dimensions of each PSSD, which are also given in Table 5.3.

5.4.2 Model Fit and Validation

The estimated parameter values are listed in Table D.1 in Appendix D.7. In the case of model M1, the result was $k_{d,1}^* = 2.32 \pm 0.14\,\mu\mathrm{m\,s}^{-1}$ and $k_{d,2}^* = 0.19 \pm 0.01\,\mu\mathrm{m\,s}^{-1}$. The confidence intervals for these two parameters are narrow, indicating that they are well determined. For the remaining models (M2 to M4), the optimized value of the objective function (see eq D.1 in Appendix D.4) is a bit lower (see Table D.1 in Appendix D.7), but at least some of the parameters, if not all, are badly determined in the sense that the confidence intervals are relatively large. On the basis of these considerations, and also for reasons of simplicity, only model M1 will be analyzed in detail and used in the work that follows below.

In Figure 5.3, the concatenated time series of the experimental data and of the corresponding model predictions using the fitted model M1 are plotted. Recall from Section 5.3.3 that the fitted outputs were $\bar{L}_{1,\mathrm{v}}$, $\bar{L}_{2,\mathrm{v}}$, and c. The relative supersaturation and undersaturation profiles were calculated using the concentration and the temperature profiles and the known solubility of BLGA in water. It can be seen in Figure 5.3 that the model tends to slightly underpredict the drop in $\bar{L}_{1,\mathrm{v}}$ and $\bar{L}_{2,\mathrm{v}}$, while the increase in c is slightly overpredicted in most cases. All considered, there is a reasonably good agreement between the experimental data and the model predictions for all the three fitted quantities. Note that it is not possible to perfectly fit all the three measured quantities at the same time, because the generic cylindrical particle model utilized is only an approximation of the true particle shape.[54] In Figure 5.3, the relative deviation of the predicted undersaturation profiles from the experimental ones is of about $0.5\,\%$ to $1.0\,\%$. The magnitude of this deviation is consistent with the estimated error of the employed concentration measurement technique.[40]

The predictive capabilities of the model M1 were tested by using the validation experiments listed in Table 5.1. The concatenated time series of these experiments and the corresponding model predictions are shown in Figure 5.4. It can be concluded that the model M1 can predict the validation experiments with a similar quality as that of the fitted ones.

The model fit with respect to the evolution of the PSSD is of interest as well. In Figure 5.5, the initial and the final volume-weighted PSSDs of
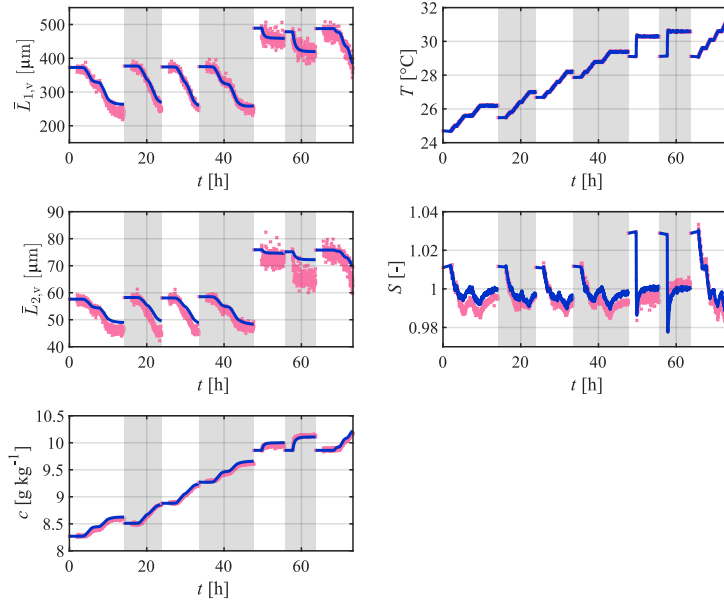
Figure 5.3: Concatenated time series of the experimental data used for fitting (pink markers) and the resulting model predictions (blue lines) using the fit of model M1. The sequence of the fitted experiments is E1, E2, E3, E4, E11, E10, and E9 (see Table 5.1) from left to right and the alternating shaded background indicates the different experiments.
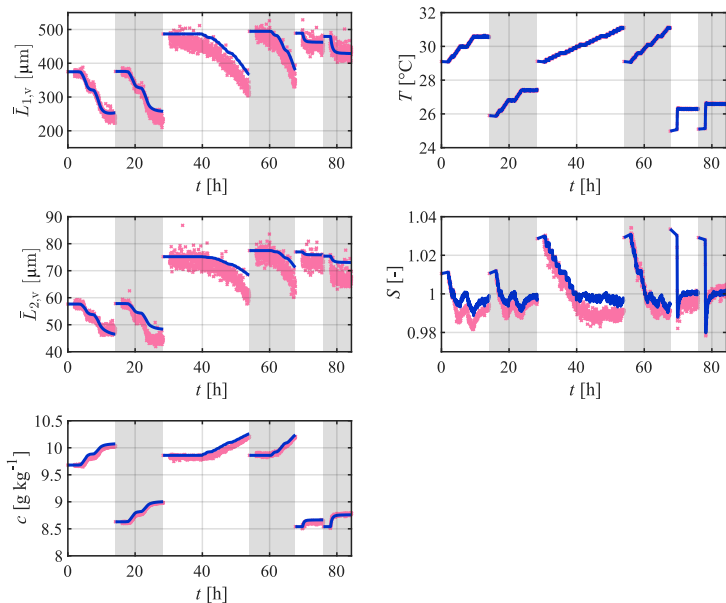
Figure 5.4: Concatenated time series of the experimental data used for validation (pink markers) and the corresponding predictions obtained from model M1 (blue lines). The sequence of the validation experiments is E5, E6, E7, E8, E12, and E13 (see Table 5.1) from left to right and the alternating shaded background indicates the different experiments.

the fitted experiments E1 and E11, respectively, are shown. By definition, the seed populations in the experiments and in the corresponding model simulations are identical. As shown in Figure 5.5b,c,e,f, the experimental and the modeled final PSSDs agree well qualitatively, even though the PSSDs themselves were not fitted. Compared with the simulated PSSDs, the experimental ones are based on a smaller number of particles, which causes their graphical representation to be considerably less smooth.

The PSSDs of the two validation experiments E6 and E13, which are shown in Figure 5.6, also exhibit good qualitative agreement between experiments and model predictions. It is worth noting that the experimental final population of experiment E13 (see Figure 5.6f) exhibits a better agreement with the corresponding simulation (see Figure 5.6e) than that of E11 (see Figure 5.5e,f). This observation is consistent with the data preprocessing steps described in Appendix D.5; i.e., the experimental final population of E13 consists of a larger number of particles than that of E11 and than those of most of the other experiments.

5.4.3 Considerations Concerning Processes for Crystal Shape Modification

Using the two-dimensional dissolution rate model M1 for BLGA in water, an assessment of the potential for crystal shape modification using temperature cycles (see, e.g., refs 62 and 21) or cycles of growth, milling, and dissolution (see, e.g., refs 63 and 64) can be conducted.

The modeled ratio D_1/D_2 is neither a function of undersaturation nor of temperature. Thus, in this case, it is not possible to control the particle shape evolution with a strategy such as the path following controller proposed previously.[65] This is a compound-specific feature and it might be different when applying a larger driving force. Still, it has to be kept in mind that quantitative online monitoring (and thus control) of particle size and shape at high dissolution rates is very challenging. This is not just due to the current limitations of available shape monitoring devices in terms of their sampling rate, but also because the more particles dissolve, the less accurate and the more noisy the measurement of the population becomes.

The model M1 predicts a ratio of D_1/D_2 of about 12, i.e., dissolution along L_1 is much faster than along L_2, thus yielding a reduction in aspect ratio. However, dissolution stages with the aim of shape mod-
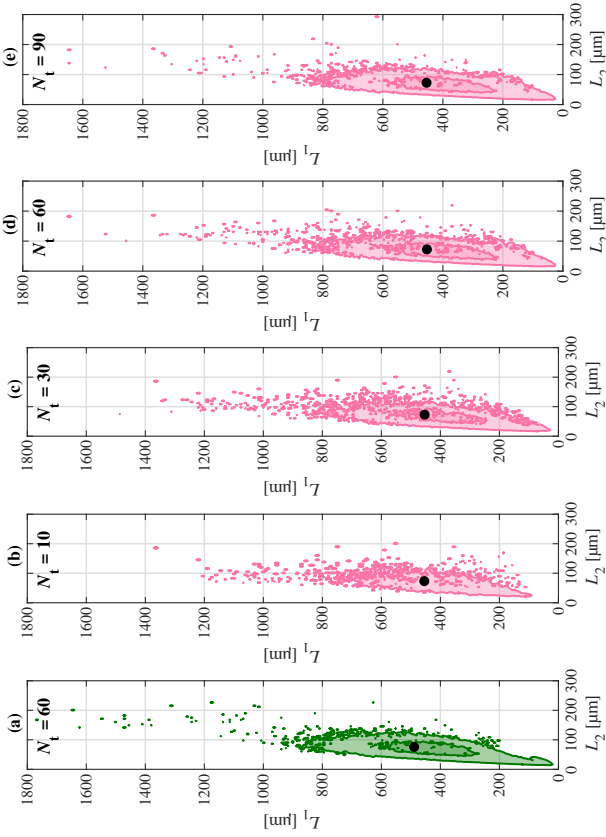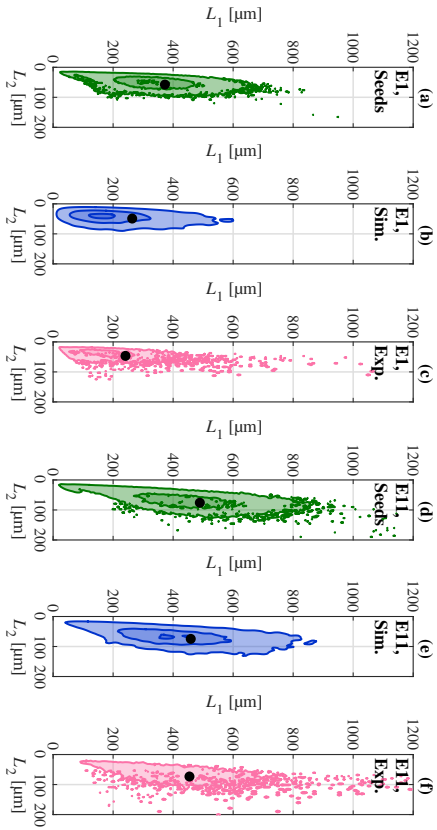
Figure 5.5: Volume-weighted PSSDs f_v (according to eq 5.7 and additionally normalized by the maximum of each PSSD) of **(a)** the seed population of E1, **(b)** the model prediction (M1) of the final population of E1, **(c)** the experimental final population of E1, **(d)** the seed population of E11, **(e)** the model prediction (M1) of the final population of E11, and **(f)** the experimental final population of E11. The contour line values correspond to 0.1, 0.5, and 0.9 of each normalized PSSD. The black markers indicate the volume-weighted average dimensions of each PSSD.
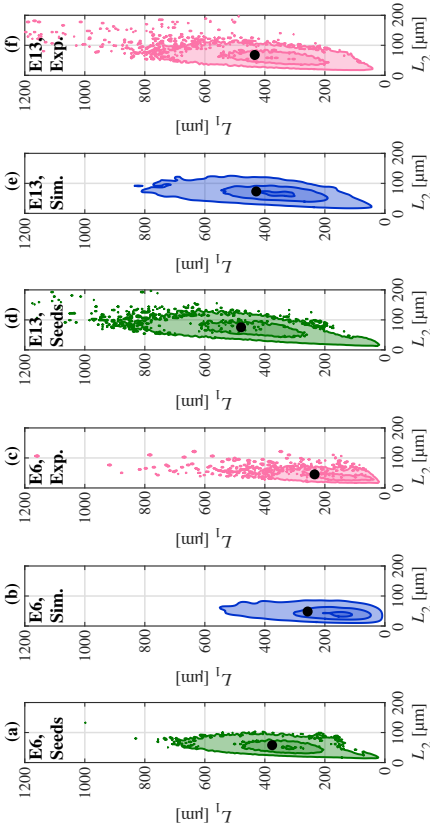
Figure 5.6: Volume-weighted PSSDs f_v (according to eq 5.7 and additionally normalized by the maximum of each PSSD) of **(a)** the seed population of E6, **(b)** the model prediction (M1) of the final population of E6, **(c)** the experimental final population of E6, **(d)** the seed population of E13, **(e)** the model prediction (M1) of the final population of E13, and **(f)** the experimental final population of E13. The contour line values correspond to 0.1, 0.5, and 0.9 of each normalized PSSD. The black markers indicate the volume–weighted average dimensions of each PSSD.

ification should be combined with time-consuming growth stages to recover the lost yield, and it was shown elsewhere that growth also evolves primarily along the length direction of the BLGA needles.[54] Thus, for BLGA, it can now be concluded that consecutive cycles of growth and dissolution would either have little impact on particle shape or require a large number of cycles to achieve such impact.

It was shown previously that wet milling also reduces the length of the needle-like BLGA particles while having little impact on their width.[67,137] Thus, wet milling can drastically reduce the particle aspect ratio in a short period of time without affecting the yield of the process, contrary to dissolution. Therefore, the relative productivity of the cyclic shape modification process can be increased by adding wet milling stages, while dissolution remains valuable as an intermediate fines removal step.

5.5 Particle Volume Control

5.5.1 Control Concept

Irrespective of the nature of the cyclic shape modification process considered and of the characteristics of a specific compound, operating dissolution stages in a controlled and reproducible way is a requirement for them to be effective. Since a high yield is generally required, it is important that a sufficient fraction of the solids survives the dissolution stage. Therefore, it suggests itself to measure and control online the volume of the solids during dissolution. The goal is to dissolve a given fraction of the initial particle volume—and not more—by manipulating the process temperature. An alternative would be to select a final temperature for the dissolution stage purely based on solubility data.[63] However, since reaching solid-liquid equilibrium can require a long time, the proposed controlled approach can be more time efficient. It is also more robust, since solubility curves can be uncertain in practice.[40]

A particle volume control strategy was developed and tested in a PBE simulation framework using the dissolution rate model M1 presented in Section 5.4.2. A dissolution stage operated by the resulting control scheme consists of three phases (all within the main experimental phase introduced in Section 5.2.2). In a first phase, if the system is supersaturated initially, crash heating to a temperature that corresponds to saturation or that lies close to saturation ($S_{\text{init}} \geq 1$) is performed. The

duration of this first phase is referred to as t_{init} and can be zero as it is optional ($t_{\text{init}} \geq 0\,\text{s}$).

In a second phase, a constant heating rate $\dot{T}_{\text{HR}}$ is applied to initiate dissolution. The open-loop set point for the process temperature is then

$$T_{\text{ol}}(t) = T(t_{\text{init}}) + \int_{t_{\text{init}}}^{t} \dot{T}_{\text{HR}}\,\mathrm{d}t' = T(t_{\text{init}}) + \dot{T}_{\text{HR}}(t - t_{\text{init}}) \qquad t \geq t_{\text{init}}$$

(5.12)

During the heating ramp, the evolution of the particle volume in the population, $V(t)$, is observed and the third phase is initiated as soon as $V_{\text{filt}}(t) \leq V_{\text{target}}$, where $V_{\text{filt}}(t)$ is the median filtered $V(t)$ (to attenuate rare measurement outliers) and V_{target} is the predefined final particle volume, i.e., the volume of crystals that survives dissolution. To reduce the time required for the second phase, a closed-loop contribution can be added to the process temperature set point. Its purpose is to increase the heating rate as long as the measured particle volume is still far away from the specified target. To this end, a control error e can be defined as

$$e(t) = \begin{cases} V_{\text{filt}}(t) - V_{\text{target}} & \text{if } V_{\text{filt}}(t) \geq V_{\text{target}} \\ 0 & \text{otherwise} \end{cases}$$

(5.13)

and proportional control can be applied to create a closed-loop contribution to the heating rate according to

$$\frac{\mathrm{d}}{\mathrm{d}t} T_{\text{cl}}(t) = \frac{\dot{T}_{\text{HR}}}{e(t_{\text{init}})} e(t) \qquad t \geq t_{\text{init}}$$

(5.14)

The choice of the proportional gain in eq 5.14 ensures both $\frac{\mathrm{d}}{\mathrm{d}t} T_{\text{cl}}(t_{\text{init}}) =$

$\dot{T}_{HR}$ and a gradual decrease of the closed-loop contribution to the heating rate toward zero as the observed particle volume approaches its target value from above. In terms of the temperature set point, the proportional control law given in eq 5.14 translates into an integral one, that is

$$T_{cl}(t) = \frac{\dot{T}_{HR}}{e(t_{init})} \int_{t_{init}}^{t} e(t') \, dt' \qquad t \geq t_{init} \tag{5.15}$$

The process temperature set point is thus $T_{set}(t) = T_{ol}(t)$ if the particle volume controller is operated in the open-loop mode and $T_{set}(t) = T_{ol}(t) + T_{cl}(t)$ if the closed-loop contribution is active as well. Note that despite the terminology used here, the open-loop mode of the controller also employs feedback of the quantity of interest (i.e., of the particle volume), but only to decide when the heating phase should be terminated.

During the third phase, i.e., after the target particle volume was reached for the first time ($V_{filt}(t) \leq V_{target}$ for some t), crash cooling to a temperature that corresponds to a saturated or to a slightly supersaturated state $S_{final} \geq 1$ is applied.

During the first and the last phase, a constant supersaturation controller (see, e.g., refs 123 and 124) is effectively active, so feedback of the solute concentration is applied as well. This is however not a requirement to operate the proposed controller. In fact, if the solubility curve is unknown for a given compound, but if the system starts from equilibrium, the first phase can be omitted and the last phase can alternatively be operated at constant temperature. Also note that instead of directly measuring the particle volume during the second phase, an accurate measurement of the solute concentration can be used: if the initial particle mass (and thus the volume) is known, the reduction in the particle volume can be inferred from the evolution of the solute concentration due to the mass conservation constraint.

5.5.2 Particle Volume Control Applied to an Unmilled BLGA Population

The performance of the particle volume controller was verified experimentally using unmilled BLGA seed particles. Two experiments were

conducted according to the protocol given in Section 5.2.2. Simulations of these two experiments were performed and their outcome was compared to that of the experiments. The experiments were seeded with one of the two batches of BLGA seeds that was also used for the dissolution rate modeling. This approach should correspond to the best case scenario in terms of further exploring the predictive capabilities of the model. The simulations were performed as follows:

- The PBE framework described in Section 5.3.1 was employed while using the fitted dissolution rate model M1 with the parameters $k_{d,1}$ and $k_{d,2}$ fixed at $2.30\,\mu\mathrm{m\,s^{-1}}$ and $0.19\,\mu\mathrm{m\,s^{-1}}$, respectively.

- The initial PSSD for each simulation was obtained in the same way as described in Appendices D.5 and D.6.

- At every sampling instant, a simulated concentration measurement was obtained by adding noise sampled from a Gaussian distribution with zero mean and a standard deviation of $0.01\,\mathrm{g\,kg^{-1}}$ to the simulated concentration $c(t)$. This noisy measurement was subsequently low-pass filtered in the same way as in the experiments (the details of the filtering are described elsewhere,[65] see Section 3.5.5). For the particle volume measurement, $N_s(t) = \lfloor N_{s,0}\mu_{00}(t)/\mu_{00}(0)\rceil$ particles were sampled from the simulated PSSD $f(t)$; sampled particles with $L_2 > L_1$ were discarded and the remaining particles were binned into a PSSD. Then, the volume of all the sampled particles $V(t)$ was computed from this binned PSSD and the same median filter as in the experiments was applied to obtain $V_{\mathrm{filt}}(t)$. The constant $N_{s,0}$ was chosen for each simulation so as the initial sampled particle volume $V(0)$ was the same as that in the corresponding experiment.

- The temperature set point $T_{\mathrm{set}}(t)$ was calculated according to the control laws introduced in Section 5.5.1 and filtered through a model of the thermal dynamics of the batch crystallizer employed to obtain the simulated process temperature (this thermal model was described previously,[65] see Section 3.5.3). The simulated measurement of this temperature was assumed to be exact.

For the experiments and the simulations, the parameters listed in

Table 5.4: Particle volume controller parameters used for the studies presented in Sections 5.5.2 to 5.5.4.

Parameter	Unit	Unmilled BLGA	Milled BLGA	Vanillin
$V_{\text{target}}/V(0)$	–	0.70	0.80 or 0.60	0.70 or 0.50
t_{samp}	min	5.00	5.00	5.00
t_{init}	min	20.00	20.00	20.00
S_{init}	–	1.01	1.01	1.01
S_{final}	–	1.03	1.03	1.02
$\dot{T}_{\text{HR}}$	$°C\,h^{-1}$	0.20	0.15	0.15

Table 5.4 were used. The results of the first experiment and of the corresponding simulation, where the open-loop mode of the controller was employed, are shown in Figure 5.7a,b. In the second experiment and in the corresponding simulation, the closed-loop mode was used instead. These results are plotted in Figure 5.7c,d. Note that all the time series shown in Figure 5.7 (and also those presented in Sections 5.5.3 and 5.5.4) start at the beginning of the main experimental phase, which corresponds to the starting point of the particle volume controller. It can be seen in Figure 5.7a that the evolution of the set point temperature and of the process temperature was virtually identical for the experiment and the simulation during the first 4 h. In both cases, the system state fell below the solubility curve after about 2 h (at 29.9 °C). At this point, the concentration in the simulation started to increase almost immediately, whereas the experimental concentration showed a somewhat delayed response. The same behavior can be seen for the evolution of the sampled particle volumes in Figure 5.7b. Because of this delay, the dissolution stage of the experiment (i.e., the second phase of the particle volume controller) took about 1 h longer than that of the simulation. Since the cylindrical particle model employed in the simulation only approximates the geometry of the real crystals, it is not possible to match both the initial sampled particle volume and the sampled particle count of the simulation and the experiment, as can be seen in Figure 5.7b. As already explained above, $N_{\text{s,0}}$ in the simulation was chosen such that the initial sampled particle volume matched with the experiment. In the
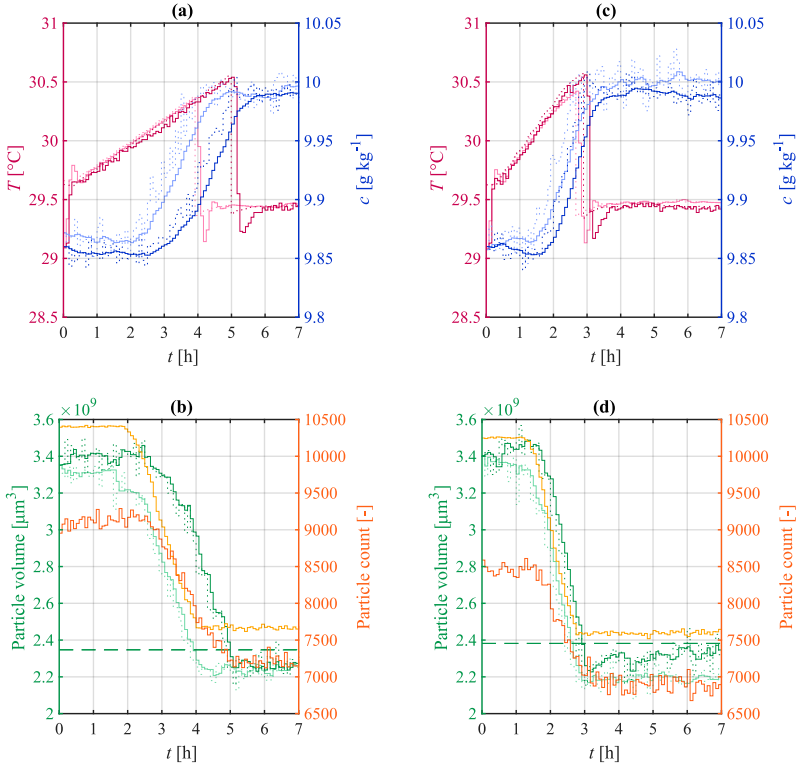
Figure 5.7: Comparison between two experimental runs of the particle volume controller using unmilled BLGA seed crystals and the corresponding simulations. Evolution of the process temperature set point (simulation: dotted light red, experimental: dotted dark red), of the process temperature (simulation: solid light red, experimental: solid dark red), and of the concentration measurement (raw simulation: dotted light blue, low-pass filtered simulation: solid light blue, raw experimental: dotted dark blue, low-pass filtered experimental: solid dark blue) for **(a)** the open-loop and **(c)** the closed-loop mode. Furthermore, evolution of the observed particle volume (raw simulation: dotted light green, median filtered simulation: solid light green, raw experimental: dotted dark green, median filtered experimental: solid dark green), evolution of the particle count (raw simulation: light orange, raw experimental: dark orange), and the target volume V_{target} (dashed green) for **(b)** the open-loop and **(d)** the closed-loop mode.

parts of the two experiments and the two simulations where the systems were slightly supersaturated, the observed particle count and particle volume are constant, as expected. In the transient parts, the slopes of the simulated and of the experimental concentration profile, as well as those of the sampled particle volume, were essentially the same, as shown in Figure 5.7a,b. The same observation can be made in Figure 5.7c,d for the second experiment. As expected, when activating the closed-loop contribution, it can be seen in Figure 5.7c that the heating rate applied by the controller initially doubled and then gradually decreased toward the end of the heating phase. In this way, the delay in the response of the experiment was reduced. This reduction enabled the evolution of the temperature, of the concentration, and of the sampled particle volume to be almost the same for the experiment and the simulation, as shown in Figure 5.7c,d.

The comparison between the experiments and the simulations presented in this section indicates that the developed PBE model is able to predict the evolution of the considered quantities rather well, but also that it is not fully predictive in any situation. Therefore, and since disturbances can additionally play a role, the application of feedback control will always be beneficial. In fact, Figure 5.7b,d shows that the controller was able to drive the observed particle volume to the target value with only a small overshoot in all the four cases, i.e., both in the two simulations and in the two experiments. Due to the slower heating rate, the open-loop mode of the controller required about 5 h to do so in the experiment, whereas the closed-loop mode needed only 3 h.

5.5.3 Particle Volume Control Applied to a Milled BLGA Population

The particle volume controller with the closed-loop action was also applied to a different BLGA seed population that underwent a wet milling step prior to dissolution. The purpose of this investigation was to verify that the control strategy can be applied independently from the characteristics of the seed particles. To this end, two experiments operated using the particle volume controller were performed according to the protocol described in Section 5.2.2, where the parameters listed in the corresponding column of Table 5.4 were used. Note that the heating rate parameter $\dot{T}_{\mathrm{HR}}$ was slightly decreased to $0.15\,^{\circ}\mathrm{C}\,\mathrm{h}^{-1}$ to reduce the risk

of overshooting the target volume.

The results of these two experiments are illustrated in Figure 5.8. The goal of the first experiment was to retain 80 % of the initial particle volume after the dissolution stage. The controller was able to achieve this goal, as shown in Figure 5.8b. According to the applied heating ramp in Figure 5.8a, the system state fell below the solubility curve (at 29.9 °C) after about 1.5 h. The response in the observed particle volume (see Figure 5.8b) and the concentration estimate derived from it (see Figure 5.8a) became apparent with a delay of about 1 h. Then, within another hour, the target volume was reached and the controller ended the dissolution stage by crash cooling to the final supersaturation ($S_{\mathrm{final}} = 1.03$). During the course of this experiment, the sampled particle count dropped from about 7500 to 5500. The second experiment, where the goal was to retain only 60 % of the initial particle volume after the dissolution stage, shows qualitatively the same behavior as the first one, as shown in Figure 5.8c,d. Again, the controller succeeded in stopping the dissolution process close to the target volume. The sampled particle count in the second experiment started from about the same value as in the first experiment, i.e., from around 7500, whereas a more pronounced drop to about 4500 was observed subsequently.

5.5.4 Particle Volume Control Applied to a Vanillin Population

To further examine its general applicability, the proposed controller was applied to a different system, namely, vanillin in water. Two experiments were performed according to the protocol described in Section 5.2.2. The controller was operated in the closed-loop mode using the parameters listed in the corresponding column of Table 5.4. The goal of the first experiment was to dissolve 30 % of the initially observed particle volume. The time series of this experiment are plotted in Figure 5.9a,b. The solubility curve was crossed after 1 h (at 25 °C). Then, as shown in Figure 5.9a,b, the onset of the dissolution was captured almost immediately in terms of a decrease in the sampled particle volume and a corresponding increase in the solute concentration. The target volume was reached after 2.5 h and the controller successfully terminated the dissolution stage by crash cooling. In Figure 5.9b, it can be seen that the particle count dropped from about 8500 to 3500 during this experiment.
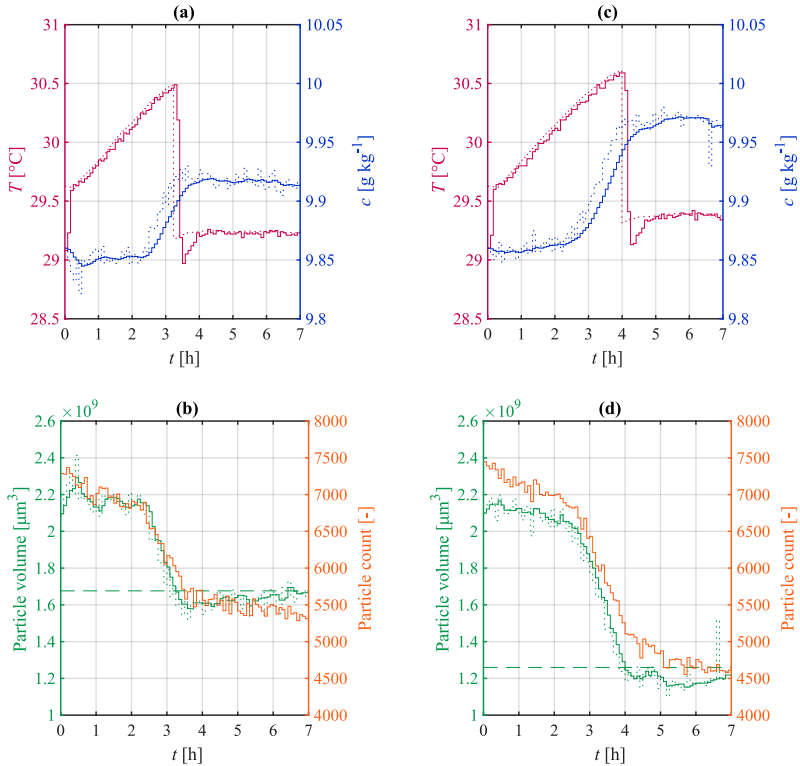
Figure 5.8: Two experimental runs of the closed-loop mode of the particle volume controller using milled BLGA seed crystals. Evolution of the process temperature set point (dotted red), of the process temperature (solid red), of the concentration measurement (raw: dotted blue, low-pass filtered: solid blue) for **(a)** $V_{target} = 0.8V(0)$ and **(c)** $V_{target} = 0.6V(0)$. Furthermore, evolution of the observed particle volume (raw: dotted green, median filtered: solid green), evolution of the particle count (raw: orange), and the target volume V_{target} (dashed green) for **(b)** $V_{target} = 0.8V(0)$ and **(d)** $V_{target} = 0.6V(0)$.
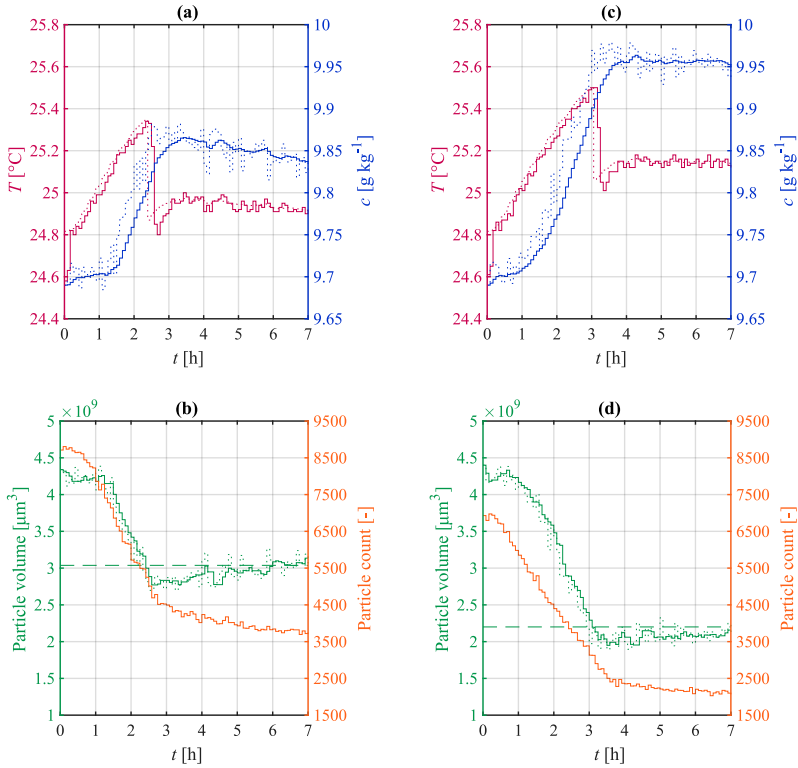
Figure 5.9: Two experimental runs of the closed-loop mode of the particle volume controller using vanillin seed crystals. Evolution of the process temperature set point (dotted red), of the process temperature (solid red), and of the concentration measurement (raw: dotted blue, low-pass filtered: solid blue) for **(a)** $V_{\text{target}} = 0.7V(0)$ and **(c)** $V_{\text{target}} = 0.5V(0)$. Furthermore, evolution of the observed particle volume (raw: dotted green, median filtered: solid green), evolution of the particle count (raw: orange), and the target volume V_{target} (dashed green) for **(b)** $V_{\text{target}} = 0.7V(0)$ and **(d)** $V_{\text{target}} = 0.5V(0)$.

The time series of the second experiment, where the goal was to dissolve 50 % of the initial particle volume, are plotted in Figure 5.9c,d. The outcome of this experiment is qualitatively similar to that of the first experiment. It can be seen in Figure 5.9d that the sampled particle count in this experiment started from about 6500, which is lower than in the first experiment (see Figure 5.9b). This difference can be explained by the fact that the vanillin seed particles show a significant degree of aggregation at the point of seeding, which slowly decreases over time and more quickly at undersaturated conditions. The initial degree of aggregation is difficult to reproduce from one experiment to the other. Still, both experiments show a very similar observed particle volume initially, which is consistent with using the same seed mass.

5.6   Conclusions

Two-dimensional population balance models for the dissolution of the needle-like compound BLGA in water have been obtained from experimental data. Within the considered range of temperatures (25.0 °C to 31.1 °C) and relative undersaturations (0.98 to 1.00), a simple expression for both dissolution rates was able to fit the data well, where this expression is linear in the driving force and independent explicitly of temperature with a resulting constant ratio D_1/D_2 of 12. The range of experimental operating conditions explored to obtain this model is admittedly narrow. Still, the presented model is, to the best of the author's knowledge, the first of this kind for the compound BLGA. For instance, it is useful for the presented discussion of the potential of cyclic size and shape modification processes.

The obtained dissolution kinetics were embedded in a simulation framework to test a model-free feedback control strategy that targets the dissolution of a given fraction of the initially observed particle volume. This particle volume controller can, for instance, be applied for controlled fines removal after wet milling stages or during temperature cycling processes. The controller has been tested further in a thorough experimental campaign involving seed populations of the two compounds BLGA and vanillin. It was able to operate the dissolution stages in all these experiments in a reliable and robust manner. Thus, a controlled method of operating dissolution stages is now available and ready to be

combined with feedback control strategies for growth [65,66] and milling [67] to realize a cyclic shape modification process for needle-like particles, where this process can be operated without the need of kinetic models describing the individual stages and the whole cycle. In Chapter 6, an approach to operating such a process is proposed.

Nomenclature

Acronyms

BLGA	β L-glutamic acid
DISCO	dual imaging system for crystallization observation
E	experiment
M	(candidate) model
MLE	maximum likelihood estimation/estimate
PBE	population balance equation
PSSD	particle size and shape distribution

Roman symbols

c	solute concentration (per mass of solvent basis) [g kg^{-1}]
c^*	solubility (per mass of solvent basis) [g kg^{-1}]
D_i	dissolution rate along ith particle dimension ($i = 1, 2$) [µm s^{-1}]
e	control error [µm^3]
$F_{\chi^2}^{-1}$	inverse of the chi-square cumulative distribution function [–]
f	number density function (PSSD) [µm^{-2} kg^{-1}]
f_v	volume-weighted PSSD [µm^{-2}]
J	MLE objective function [–]
$k_{\mathrm{d},i}$	parameter of a dissolution rate model [µm s^{-1}]
$k_{\mathrm{s},i}$	parameter of a dissolution rate model, unit varies
k_v	volume shape factor [–]
L_i	ith particle dimension ($i = 1, 2$) [µm]
L_ref	unit reference length [µm]
$\bar{L}_{i,\mathrm{n}}$	number-weighted average of ith particle dimension ($i = 1, 2$) [µm]
$\bar{L}_{i,\mathrm{v}}$	volume-weighted average of ith particle dimension ($i = 1, 2$) [µm]
N_p	number of parameters [–]
N_s	number of sampled particles [–]
N_t	number of data points [–]
N_v	number of measured quantities for fitting [–]
S	relative supersaturation or undersaturation, c/c^* [–]
T	temperature, unit varies
$\dot{T}_\mathrm{HR}$	heating rate [°C h^{-1}]
t	time, unit varies

V	(sampled) particle volume [µm³]
$\boldsymbol{V_\theta}$	parameter covariance matrix, units of the entries vary
y_{mk}	kth data point of the mth measured quantity, unit varies

Greek symbols

$\alpha, \ldots, \zeta$	experiment labels used in ref 40
η	confidence level (probability) [–]
$\boldsymbol{\theta}$	model parameter vector, units of the entries vary
μ_{ij}	ij-cross moment of a PSSD [µm^{i+j} kg^{-1}]
ρ_{c}	crystal density [g µm^{-3}]

Superscripts and subscripts

0	initial value
′	integration variable
ˆ	measurement
*	minimizer
cl	closed-loop
filt	low-pass or median filtered
final	final value
init	initial (first) phase of the particle volume controller
min	lower limit
ol	open-loop
samp	sampling
sat	saturation
set	set point
target	target value for controller

Mathematical operators

$\lfloor \cdot \rceil$	round to nearest integer

Chapter 6

A Controlled Multistage Process

6.1 Introduction

Imaging techniques to monitor the shape evolution of crystals in solution and populations thereof are becoming increasingly popular.[32,53,81,106] If the employed imaging devices feature online monitoring capabilities, many possibilities in terms of feedback control of crystal shape are opened up. So far, experimental studies of this type have appeared scarcely in the literature (see also Chapters 3 and 4),[20,21,66,67] while other contributions applied and exploited the feedback of crystal size, but not of shape.[61,109–111,125,152]

The purpose of this chapter is to present and validate experimentally a controlled and reproducible batch process that transforms needle-like seed crystals into more equant particles, including its experimental validation. As described elsewhere,[63,64,153] the process itself has been developed and applied previously in an uncontrolled fashion, mainly using a

model-based approach to select and to thus predefine suitable operating conditions, while considering the achievable size and shape change of the particles as well as the yield and the productivity of the process. It is evident that these are important process goals. However, there are additional and equally relevant aspects of the process that have not been considered so far, namely its automation, its operation without the need of kinetic process models, its robustness with respect to disturbances, and the repeatability of its outcome (i.e., the mitigation of batch-to-batch variations). Therefore, this chapter addresses the latter aspects, and its focus lies on establishing two important novelties: first, the fully automated and controlled process operation in the absence of kinetic process models, and second, the robustness of the process control scheme with respect to achieving product particle size and shape distributions (PSSDs) with consistent average characteristics over consecutive batches. Since achieving a significant size and shape change of the particles under these new prerequisites is already challenging, the yield and the productivity of the process are not considered here, leaving the treatment and the integration of these aspects for a potential future work. To achieve the two goals introduced above, the feedback controllers developed for wet milling (see Chapter 4) and dissolution (see Chapter 5) have been integrated and combined with a simple controlled growth stage (operated by a variant of the constant supersaturation controller, CSC, already used in Chapter 3) to form a controlled multistage process.

This chapter is organized as follows. First, an overview of the controlled multistage process is given in Section 6.2, including a summary of the individual stage controllers. Second, a cycle logic to plan the operation of the entire process is described in Section 6.3. Finally, the experimental validation of the proposed process control approach using two different needle-like compounds, namely, β L-glutamic acid (BLGA, an amino acid) and γ D-mannitol (GDM, a sugar alcohol), is discussed in Section 6.4.

6.2 Process Overview

A batch process, in this chapter referred to as the multistage process, to transform needle-like seed particles into more equant particles was previously modeled and tested experimentally.[63,64,153] To facilitate the

transition to nicely shaped, well-developed crystals, this process is operated in a cyclic fashion, where one cycle consists of three stages, namely, of a growth, a breakage, and a dissolution stage. These three stages serve different purposes: the growth stage is a cooling crystallization step that generates yield and increases the size of the particles by crystallizing the solute from the liquid phase, while avoiding observable nucleation; the breakage stage is a wet milling step that reduces the particle aspect ratio (defined as the ratio of the particle length to the particle width) by mechanical action, while leaving the yield unaffected; finally, the dissolution stage is a heating step, during which many of the fines generated in the breakage stage are dissolved and the particle size and thus the aspect ratio can be reduced further depending on the operating conditions. The PSSD can be modified by altering the operating conditions of the individual stages, by varying the number of cycles, or by a combination thereof. In principle, these operating conditions (here, the temperatures during the growth and the dissolution stages and the rotor speed of the wet mill in the breakage stage, as well as the duration of these stages) can be chosen using two different approaches: either by predefining them on the basis of available process models or prior experimental insight, as done previously,[64,153] or by employing feedback controllers that select the operating conditions automatically and dynamically, either in the presence (model-based) or in the absence (model-free) of process models. Often, the presence of process disturbances and unmodeled phenomena (in the case of model-based operating strategies) is a strong advocate to apply feedback control. Following this credo, feedback controllers already discussed above can be applied for each of the three stages (see Chapters 3, 4, and 5)[65–68] to form a controlled multistage process. In the context of these control laws, the needle-like particles are approximated as cylinders with length L_1 and width L_2, and the resulting particle size and shape distributions are reduced to corresponding average quantities, $\bar{L}_1$ and $\bar{L}_2$, to address the issue of polydispersity. On the basis of this simplification, the main goal of the controlled multistage process is a targeted reduction of the average particle aspect ratio $\bar{L}_1/\bar{L}_2$ by manipulating the size and shape evolution of the crystals. For the sake of independence of this chapter, the ideas behind the single control laws operating the individual stages are summarized below.

Within the scope of this thesis, two options to control the cooling

step (i.e., the growth stage) seem to be suitable. The first one is a model-free path following controller that manipulates the process temperature to drive the average particle dimensions of the seed population into a target orthant in the plane spanned by the average crystal length and width (see Section 3.3).[65,66] If the effect of the process temperature on the evolution of the average particle aspect ratio is small or if no prior knowledge is available to select reasonable target orthants, an alternative is to simply apply constant supersaturation control to run the cooling stage at a constant supersaturation level (CSC, see Section 3.7.1) and to terminate it when a given target average crystal length has been reached. In this chapter, this latter, simpler approach is applied. Even though the corresponding control law itself is not complicated, note that it still needs feedback of both the solute concentration and the average particle length.

During the breakage stage, the suspension in the batch crystallizer is initially circulated through a wet mill operated at a fixed rotor speed for a predefined amount of time. From the resulting change of the average particle length, a simple dynamic model can be identified and subsequently extrapolated to calculate a wet mill rotor speed that drives the average crystal length to a target value, thereby considerably reducing the aspect ratio of the majority of the particles in the ensemble (see also Section 4.3.6).[67]

The dissolution stage could in theory be operated using the same methods proposed for the growth stage, i.e., by driving the seed population into a target orthant by manipulating the temperature, or alternatively by operating the dissolution stage at a constant undersaturation and aborting the process when a given target average crystal length has been reached. A considerably simpler alternative is to dissolve a given fraction of the initially suspended particle volume (being proportional to the particle mass). To this end, the process temperature is increased slowly and the reduction of the particle volume is observed so as to terminate the heating stage as soon as enough dissolution has taken place. In this way, fine particles are dissolved automatically and the loss of yield remains contained, but control over the size and shape evolution is given up in this stage (see also Section 5.5.1).[68] In this chapter, this alternative is applied.

An important feature of the controllers for these individual stages is

that they require only thermodynamic knowledge (i.e., solubility data) to operate the process, but no kinetic models. It was shown that the individual controllers perform well under a variety of conditions (see Chapters 3, 4, and 5).[66–68] Therefore, a natural evolution of the preceding efforts is to integrate these individual controllers and to operate the multistage process in a fully controlled fashion, as opposed to how it was operated previously.[64,153]

6.3 The Cycle Logic

Since the stage control laws operate the individual stages and not the whole cycle, a cycle logic is required additionally that provides targets for the individual stage controllers on the basis of the overall process goals. Kinetic process models for the crystal shape evolution would obviously be useful to devise such logic, but they are hardly ever available. Even if such models were available, their predictive capabilities would be limited. Therefore, a simpler approach has been followed, the concept of which is best explained in the plane spanned by the two average particle dimensions $\bar{L}_1$ and $\bar{L}_2$. Below, these quantities are equivalent to the volume-weighted average particle dimensions defined as

$$
\bar{L}_{1,\mathrm{v}}(t) = \frac{\mu_{22}(t)}{\mu_{12}(t)}
$$
$$
\bar{L}_{2,\mathrm{v}}(t) = \frac{\mu_{13}(t)}{\mu_{12}(t)} \tag{6.1}
$$

where

$$
\mu_{ij}(t) = \int_0^\infty \int_0^\infty L_1^i L_2^j f(t, L_1, L_2) \, \mathrm{d}L_1 \, \mathrm{d}L_2 \tag{6.2}
$$

is the ij-cross moment of the measured number density function (i.e., the PSSD) $f(t, L_1, L_2)$ at time t. A schematic of the cycle logic is shown in
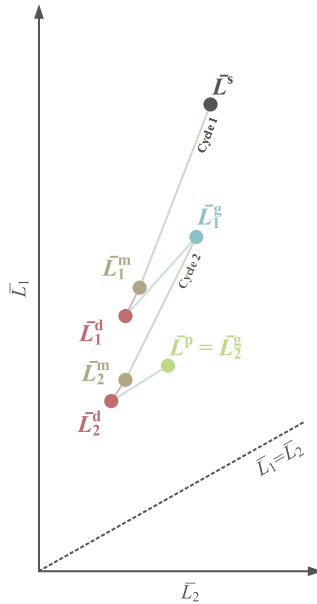
Figure 6.1: Schematic of the cycle logic of the controlled multistage process, including the evolution of the average particle dimensions over the individual stages. Note that this figure merely provides an illustration of the end points for each stage. It does not quantitatively represent the path undertaken by the average dimensions for each stage.

Figure 6.1. The average dimensions of the seed population are denoted by the point $\bar{\boldsymbol{L}}^{\mathrm{s}}$. The evolution of these average dimensions is shown qualitatively for the special case of two cycles. In the general case, the cycles transform the seed population into the product population with average dimensions denoted by the point $\bar{\boldsymbol{L}}^{\mathrm{p}}$, which corresponds to a significant reduction of the average particle aspect ratio. In more detail, the nth cycle transforms the average dimensions of the population from $\bar{\boldsymbol{L}}^{\mathrm{g}}_{n-1}$, the end point of the previous cycle (or, for $n = 1$, from the seed population $\bar{\boldsymbol{L}}^{\mathrm{s}}$), to $\bar{\boldsymbol{L}}^{\mathrm{g}}_{n}$, with intermediate points $\bar{\boldsymbol{L}}^{\mathrm{m}}_{n}$ and $\bar{\boldsymbol{L}}^{\mathrm{d}}_{n}$. The

transition from $\bar{\boldsymbol{L}}_{n-1}^{\mathrm{g}}$ to $\bar{\boldsymbol{L}}_n^{\mathrm{m}}$ is a wet milling stage, that from $\bar{\boldsymbol{L}}_n^{\mathrm{m}}$ to $\bar{\boldsymbol{L}}_n^{\mathrm{d}}$ is a dissolution stage, and that from $\bar{\boldsymbol{L}}_n^{\mathrm{d}}$ to $\bar{\boldsymbol{L}}_n^{\mathrm{g}}$ is a growth stage. For many compounds exhibiting a needle-like morphology, often not much can be done to control the average particle width $\bar{L}_2$ during the single stages (see Chapters 3, 4, and 5).[66–68] Therefore, it is suggested here to specify only the intermediate and the final average lengths of the needle-like particles. These average lengths can be considered as waypoints for the entire cyclic process. Note that in the context of this chapter, the exact values of these waypoints are not important, but defining them in some way is a prerequisite for the entire process to function. In their absence, or when a stage controller fails to reach its stage target, the target average length for the product population will be missed.

A suitable cycle logic can be defined using four parameters: ℓ^{ref}, ℓ_1^{m}, ω, and ξ. ℓ^{ref} should be set to a value that is in the order of the average particle length in the seed population. If the multistage process is run for several batches in a row using the same or a similar seed population, ℓ^{ref} should be kept constant over the batch runs to have the same stage targets. In the first cycle ($n = 1$), the target for the milling stage is defined by the parameter ℓ_1^{m}. In general terms, the milling target is $\ell_n^{\mathrm{m}} = \omega^{n-1}\ell_1^{\mathrm{m}}$ with $0 < \omega < 1$. The target for the dissolution stage is not fixed in the plane of the average dimensions, but simply specified as a fraction ξ of the total solid volume that should survive the dissolution stage. $\bar{\boldsymbol{L}}_n^{\mathrm{d}}$ is then an unknown function of $\bar{\boldsymbol{L}}_n^{\mathrm{m}}$ and ξ. To be more specific, the average dimensions and therefore the average particle aspect ratio are affected by the dissolution of the crystals, even if these quantities are not directly controlled. The target for the growth stage that terminates each cycle is given by $\ell_n^{\mathrm{g}} = \omega^n\ell^{\mathrm{ref}}$. Since $0 < \omega < 1$ and since $\bar{L}_2$ does not change much, this expression ensures a reduction of the average particle aspect ratio over each cycle. Note that the parameters ω and ξ need not take the same values for all the cycles. However, in this chapter, this is the case for reasons of simplicity. After selecting reasonable values for the above mentioned four constants that reflect the desired reduction of the average particle aspect ratio, the job of reaching the intermediate targets can conveniently be delegated to the feedback controllers for the single stages.

6.4 Experimental Validation

The main task of the process control scheme described above is to reach the target average particle length of the last cycle repeatedly over consecutive batches, even in the presence of disturbances or slight deviations in the initial conditions, e.g., in case of differences in the seed populations or in the initial solute concentration. Also, it needs to be proven that the process indeed provides the desired reduction of the particle aspect ratio and that it produces nice crystals. Its general applicability to a number of compounds is crucial as well, as it guarantees that the process is not tailor-made for a specific compound. To validate all these requirements, an experimental campaign has been conducted. Two different systems, namely, BLGA in water and GDM in a mixture of water and propan-2-ol have been considered. Apart from the fact that both BLGA and GDM crystals exhibit a needle-like morphology under the conditions explored in this chapter, other properties such as their thermodynamic (solubility) and kinetic (growth and dissolution rates) behavior are significantly different,[153] making them two suitable systems to test the effectiveness and the general applicability of the proposed controlled process. As already explained in Section 6.1, the yield and the productivity are not explicitly taken into account here. Nevertheless, note that an overall positive yield can always be achieved by arbitrarily growing the seed crystals *prior* to running the controlled multistage process.

The required feedback signals for the individual controllers (see Section 6.2) such as the average particle dimensions, the particle volume, or the solute concentration can be provided by the µ-DISCO, an ex situ stereoscopic imaging device (see Sections 1.2 and 1.3).[32,40] For the sake of brevity, the explanation of the employed materials and the experimental setup, including the µ-DISCO and the rotor-stator wet mill used for wet milling, is provided in Appendices E.1 to E.3. Note that any other solid phase characterization device that is able to provide a PSSD and any other liquid phase characterization device that is able to measure the solute concentration could be employed as well, as long as these devices provide measurements on a time scale significantly shorter than that of the process dynamics.

6.4.1 Multistage Process Experiments with BLGA Using One or Two Cycles

It was shown previously that the number of cycles used for the multi-stage process can significantly alter the characteristics of the product population.[64] It was thus decided to perform repeated controlled multi-stage experiments, starting from the same initial conditions and with the same cycle logic parameters, but with a different number of cycles. To this aim, a single cycle experiment, referred to as κ_1, and a two cycle experiment, referred to as κ_2, for the compound BLGA using Seeds κ (see Appendix E.4) were conducted. In both experiments, the aspect ratio reduction was achieved by setting the parameters of the cycle logic ℓ_1^{m} and ω to the values 200 µm and 0.7, respectively. Note that the latter choice corresponds to reducing the average crystal length by a factor of $\omega = 0.7$ per cycle. ℓ^{ref} was set to 360 µm, because this value is relatively close to the initial average particle lengths. The value of $\xi = 0.8$ was selected to strike a balance between removing fines and not losing too much solid mass during the dissolution stages. The detailed experimental protocol applied for these two experiments and the most important parameters of the individual stage controllers are explained in Appendix E.5. Note that all the four parameters of the cycle logic were identical for both experiments.

The initial and the final PSSDs of experiments κ_1 and κ_2 are shown in Figure 6.2. In this and in subsequent figures, the PSSDs are visualized as volume-weighted distributions defined as

$$f_{\mathrm{v}}(t, L_1, L_2) = \frac{L_1 L_2^2 f(t, L_1, L_2)}{\mu_{12}(t)} \tag{6.3}$$

All the particles characterized during the first six and the last six sampling instants of the experimental time series were combined to obtain the PSSDs before and after the experiments, respectively. As expected, it can be seen in Figure 6.2a,c that the PSSDs before initiating the controlled multistage process are indeed very similar. As experiment κ_1 was subjected to one cycle and experiment κ_2 was subjected to two cycles, the final PSSDs illustrated in Figure 6.2b,d are very different. Two observa-
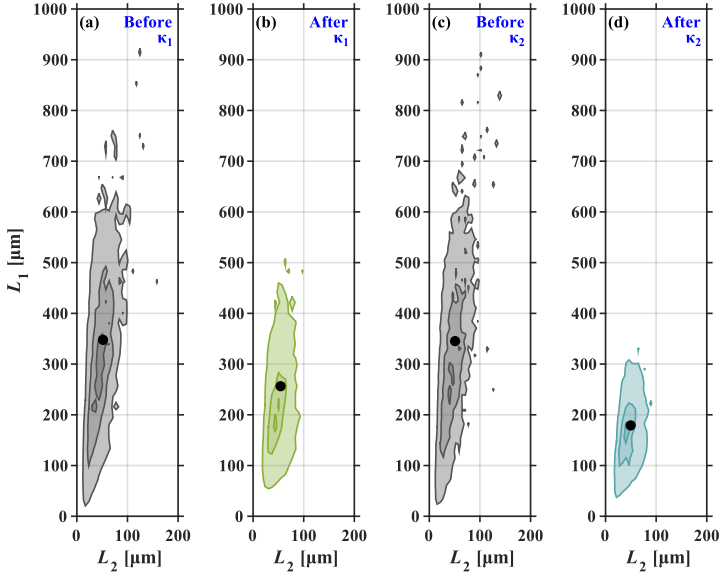
Figure 6.2: PSSDs f_v (obtained using eq 6.3 and normalized by the maximum of each PSSD) before experiment **(a)** κ_1 and **(c)** κ_2 and after experiment **(b)** κ_1 and **(d)** κ_2 for the controlled multistage process experiments using Seeds κ of BLGA crystals. Experiments κ_1 and κ_2 consisted of one and two cycles of the controlled multistage process, respectively. The contour levels correspond to 0.1, 0.5, and 0.9 of each normalized PSSD. Along the L_1 direction, a regular grid with 120 bins and a spacing of 21 μm and 13 μm was used for experiment κ_1 and κ_2, respectively. Along the L_2 direction, the corresponding grid spacing was 7 μm and 6 μm using 40 bins. The solid circular markers indicate the average dimensions of the populations.

tions can be made from these final PSSDs. First, the average dimensions of the population after κ_1 are larger than those of that after κ_2, which is a consequence of the lower target average lengths used in the stages of the second cycle. Second, due to the presence of a second milling stage, the broadness of the final PSSD of experiment κ_2 is smaller than that of experiment κ_1.

A detailed visualization of the results of experiments κ_1 and κ_2 is provided in Figure 6.3. In this figure, further quantities of interest are introduced, namely, the volume-weighted average particle aspect ratio, ϕ at time t, given by

$$\phi(t) = \frac{\bar{L}_{1,\mathrm{v}}(t)}{\bar{L}_{2,\mathrm{v}}(t)} \tag{6.4}$$

the volume-weighted broadness of the measured PSSD along each of the two dimensions at time t, which is defined as

$$\sigma_{11,\mathrm{v}}(t) = \sqrt{\mu_{32}(t)/\mu_{12}(t) - \big(\mu_{22}(t)/\mu_{12}(t)\big)^2}$$
$$\sigma_{22,\mathrm{v}}(t) = \sqrt{\mu_{14}(t)/\mu_{12}(t) - \big(\mu_{13}(t)/\mu_{12}(t)\big)^2} \tag{6.5}$$

and the volume-weighted ratio of the broadness along the two dimensions, ψ at time t, defined as

$$\psi(t) = \frac{\sigma_{11,\mathrm{v}}(t)}{\sigma_{22,\mathrm{v}}(t)} \tag{6.6}$$

Note that all the quantities defined in eqs 6.4 to 6.6 are volume-weighted. Below, for the sake of brevity, this feature of these quantities will no longer be called out in the text. Also note that all the quantities in Figure 6.3a-e are based on the low-pass filtered evolution of $\bar{L}_{i,\mathrm{v}}$ and $\sigma_{ii,\mathrm{v}}$ ($i = 1, 2$) to attenuate measurement noise. The low-pass filtered
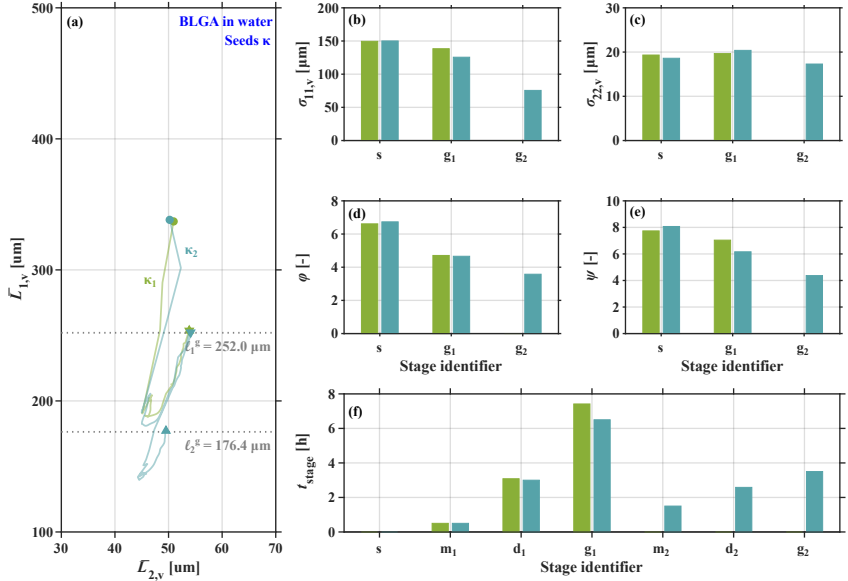
Figure 6.3: **(a)** Low-pass filtered evolution of the average length $\bar{L}_{1,v}$ and width $\bar{L}_{2,v}$ for BLGA experiment κ_1 (solid green line) and κ_2 (solid blue line). The circular markers, downward pointing triangular markers, and upward pointing triangular markers indicate the average dimensions before the experiment, at the end of the first cycle (both κ_1 and κ_2), and at the end of the second cycle (κ_2 only), respectively. The horizontal dashed lines indicate the target average length at the end of the first cycle (ℓ_1^g) and that at the end of the second cycle (ℓ_2^g). The broadness of the measured PSSD (obtained using eq 6.5 and low-pass filtered subsequently) along **(b)** the length and **(c)** the width direction, **(d)** the average particle aspect ratio (obtained using eq 6.4 with low-pass filtered arguments), and **(e)** the ratio of the broadness along the two dimensions (obtained using eq 6.6 with low-pass filtered arguments) before the experiment (s), at the end of the first cycle (g_1), and at the end of the second cycle (g_2). **(f)** Time t_{stage} required for the individual stages to reach their respective targets. κ_1 and κ_2 consisted of one and two cycles of the controlled multistage process, respectively. The bars in panels b through f share the color code for the two experiments with panel a.

evolution of $\bar{L}_{1,v}$ and $\bar{L}_{2,v}$ plotted in Figure 6.3a is similar until the end of the first cycle for both the experiments. The second cycle for experiment κ_2 leads to an additional considerable reduction of the average length $\bar{L}_{1,v}$. It is interesting to note that the average width $\bar{L}_{2,v}$ increased slightly over the course of the first cycle for both the experiments, while for experiment κ_2, this gain in the average width $\bar{L}_{2,v}$ was lost over the course of the second cycle. This can be attributed to two factors. The first factor is the reduction of the average width $\bar{L}_{2,v}$ during the second milling stage. The second factor is the effect of the relatively high supersaturation employed during the growth stages. In more detail, for the system BLGA in water, the ratio of the growth rates along the length direction of the particles to that along their width direction increases with supersaturation.[54,66] Since both the experiments had the same initial conditions and the same targets for the individual stages, the evolution of the two broadness measures, that of the average particle aspect ratio, and that of the ratio of the broadness along the two dimensions shown in Figure 6.3b-e is very similar until the end of the first cycle. Apart from the broadness measure along the width direction illustrated in Figure 6.3c, the second cycle of κ_2 yields a further significant decrease of these quantities, which is beneficial in terms of obtaining a more compact distribution consisting of more equant particles. From Figure 6.3f, it is clear that for the system BLGA in water, the growth stages are responsible for the largest part of the required process time. Still, the time required by the wet milling and the dissolution stages is significant as well. It can also be seen in Figure 6.3f that the times required for the milling and the dissolution stages are almost identical for the first cycle of both the experiments. However, the growth stage in experiment κ_1 took slightly longer than that in experiment κ_2 to reach the desired target. Based on the operating conditions of the milling and the dissolution stages (not shown here for the sake of brevity), it appears that this difference in the growth times is not due to any differences in the operating conditions of the preceding stages, but due to the batch-to-batch variations in the growth rates that can always occur.

The micrographs of Seeds κ and those of the crystals obtained after experiments κ_1 and κ_2 are presented in Figure 6.4. These micrographs, as expected, confirm the considerable reduction in the average length of the crystals, and thereby of the average particle aspect ratio, for each
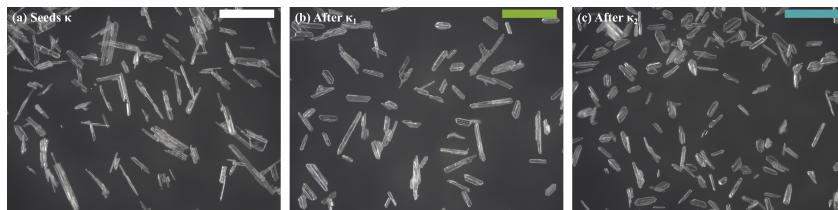
Figure 6.4: Darkfield micrographs of **(a)** Seeds κ, and of the crystals obtained **(b)** after experiment κ₁ and **(c)** after experiment κ₂. The scale bars in the micrographs correspond to 500 µm.

cycle of the controlled multistage process. It is interesting to note that upon undergoing the cyclic process, the surface of the crystals appears to be healed when compared with the seed particles. In more detail, the crystals obtained after the experiments have a smoother and a more regular surface, along with well developed facets that are characteristic of the compound BLGA.

Finally, it is concluded from the results presented in this section that performing two cycles instead of just one is preferable. The second cycle clearly helps to achieve a significant reduction of the average particle aspect ratio, which makes investing more process time acceptable. Therefore, the remaining experiments presented in this chapter were all performed using two cycles of the controlled multistage process.

6.4.2 Multistage Process Experiments with BLGA Using Two Cycles

In this section, three further experiments that were conducted with the system BLGA in water are presented. In a preliminary phase, a given batch of BLGA seed crystals, referred to as Seeds λ (see Appendix E.4), was grown to a given target average length by means of a growth stage at constant supersaturation. Subsequently, two cycles of the controlled multistage process were run to reduce the average particle aspect ratio of the particle populations obtained after this preliminary growth step. By varying the target average length of the preliminary growth step, the effect of differences in the initial conditions (seed population and initial

solute concentration) was investigated. Below, the main phases comprising the controlled multistage process will be referred to as experiments λ_1, λ_2, and λ_3. All the parameters of the cycle logic, especially also ℓ^{ref}, were kept constant to ensure that experiments λ_1 to λ_3 were run with the same targets. The detailed experimental protocol and the most important parameters of the individual stage controllers are explained in Appendix E.5.

The PSSDs before and after experiments λ_1 to λ_3, as well as micrographs of the corresponding final particle populations, are illustrated in Figure 6.5. In Figure 6.5a,c,e, it can be seen that the PSSDs obtained after the preliminary growth steps (i.e., before the experiments) are indeed different. Nevertheless, the final PSSDs visualized in Figure 6.5b,d,f are almost identical, as intended. The micrographs presented in Figure 6.5g-i confirm in a qualitative manner that the obtained crystal populations are indeed very similar, both in terms of the size and the shape of the particles.

More detailed results of experiments λ_1 to λ_3 are displayed in Figure 6.6. In Figure 6.6a, the low-pass filtered evolution of $\bar{L}_{1,\mathrm{v}}$ and $\bar{L}_{2,\mathrm{v}}$ shows that the controlled process operation enables the transformation of seed populations with different average dimensions (circular markers) into PSSDs with very similar average dimensions, either using one (downward pointing triangles) or two cycles (upward pointing triangles). Figure 6.6d illustrates that a reduction of the average particle aspect ratio over the two cycles was achieved, from an initial value of about 5 to 6 to a final value of about 3. Furthermore, Figure 6.6b,c indicates that also the broadness measure of the PSSDs along the L_1 direction decreased over the cycles, while that along the L_2 direction was barely affected. Clearly, this observation goes along with a reduction of the ratio of the broadness along the two dimensions ψ, as can be seen in Figure 6.6e.

The duration of each stage (three stages per cycle) is visualized in Figure 6.6f. As expected, the duration of the first milling stage (m_1) slightly increases with increasing initial average particle length of the three experiments. Since more milling has to be applied to the populations with a large initial average particle length, more particle surface area and rougher particle surfaces are created, thus increasing the growth rate and reducing the time required for the growth stage of the first cycle (g_1). Still, regardless of the initial condition, the growth stages make the
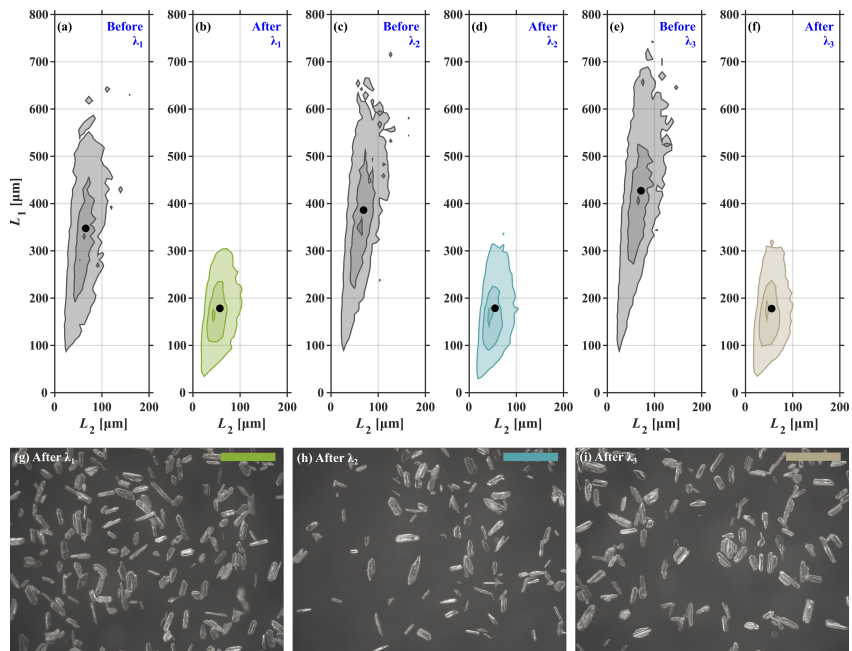
Figure 6.5: PSSDs f_v (obtained using eq 6.3 and normalized by the maximum of each PSSD) before experiment **(a)** λ_1, **(c)** λ_2, and **(e)** λ_3 and after experiment **(b)** λ_1, **(d)** λ_2, and **(f)** λ_3 for the controlled multistage process experiments using BLGA Seeds λ. The contour levels correspond to 0.1, 0.5, and 0.9 of each normalized PSSD. Along the L_1 direction, a regular grid with 120 bins and a spacing of 12 µm, 12 µm, and 12 µm was used for experiments λ_1 to λ_3, respectively. Along the L_2 direction, the corresponding grid spacing was 10 µm, 8 µm, and 10 µm using 40 bins. The solid circular markers indicate the average dimensions of the populations. Darkfield micrographs of the crystals obtained after experiment **(g)** λ_1, **(h)** λ_2, and **(i)** λ_3. The scale bars in the micrographs correspond to 500 µm.

Figure 6.6: **(a)** Low-pass filtered evolution of the average length $\bar{L}_{1,\mathrm{v}}$ and width $\bar{L}_{2,\mathrm{v}}$ for BLGA experiments λ_1 (solid green line), λ_2 (solid blue line), and λ_3 (solid brown line). The circular markers, downward pointing triangular markers, and upward pointing triangular markers indicate the average dimensions before the experiment, at the end of the first cycle, and at the end of the second cycle (after the experiment), respectively. The horizontal dashed lines indicate the target average length at the end of the first cycle (ℓ_1^{g}) and that at the end of the second cycle (ℓ_2^{g}). The broadness of the measured PSSD (obtained using eq 6.5 and low-pass filtered subsequently) along **(b)** the length and **(c)** the width direction, **(d)** the average particle aspect ratio (obtained using eq 6.4 with low-pass filtered arguments), and **(e)** the ratio of the broadness along the two dimensions (obtained using eq 6.6 with low-pass filtered arguments) before the experiment (s), at the end of the first cycle (g_1), and at the end of the second cycle (g_2, after the experiment). **(f)** Time t_{stage} required for the individual stages to reach their respective targets. The bars in panels b through f share the color code for the three experiments with panel a.

177

largest contribution to the overall process time.

6.4.3 Repeatability of Multistage Process Experiments with BLGA

Two further controlled multistage process experiments with the compound BLGA and an initial growth stage were performed. These experiments are referred to as experiments λ_4 and λ_5. Their purpose was to check the repeatability of the process outcome (i.e., the properties of the final PSSD) when using virtually identical initial conditions, identical cycle parameters, and the same number of cycles. The detailed experimental protocol applied for these two experiments is explained in Appendix E.5. Note that these experiments had a preliminary growth stage with a target average length of $360\,\mu m$.

The initial and the final PSSDs of experiments λ_4 and λ_5 are visualized in Figure 6.7. It can be seen in Figure 6.7a,c that the PSSDs obtained after the preliminary growth steps are very similar, which corresponds to nearly identical initial conditions for the subsequent controlled multistage process. The final PSSDs illustrated in Figure 6.7b,d are very similar as well, as expected when applying the controlled size and shape modification process.

More detailed results of experiments λ_4 and λ_5 are provided in Figure 6.8. In Figure 6.8a, it can be seen that the low-pass filtered evolution of $\bar{L}_{1,v}$ and $\bar{L}_{2,v}$ is similar, with a slight difference in $\bar{L}_{2,v}$. It can also be seen that experiment λ_4 failed to reach ℓ_2^g, the target average particle length of the second growth stage, by a few microns. The reason is that the control computer (see Appendix E.3) accidentally ran out of disk space shortly before the end of this experiment, preventing it from saving the data and terminating the controlled process properly. Figure 6.8b-e confirms that the evolution of the two broadness measures, that of the average particle aspect ratio, and that of the ratio of the broadness along the two dimensions (as defined in Section 6.4.1) is indeed very similar for the two experiments. As can be seen in Figure 6.8f, the times required for the constituent stages are similar as well, with the exception of that of the first growth stage (g_1), where experiment λ_4 took significantly longer. This difference will be explained at the end of this section.

In Figure 6.9a-e, the time series of the solute concentration, the temperature, the supersaturation, the average length, and the average width
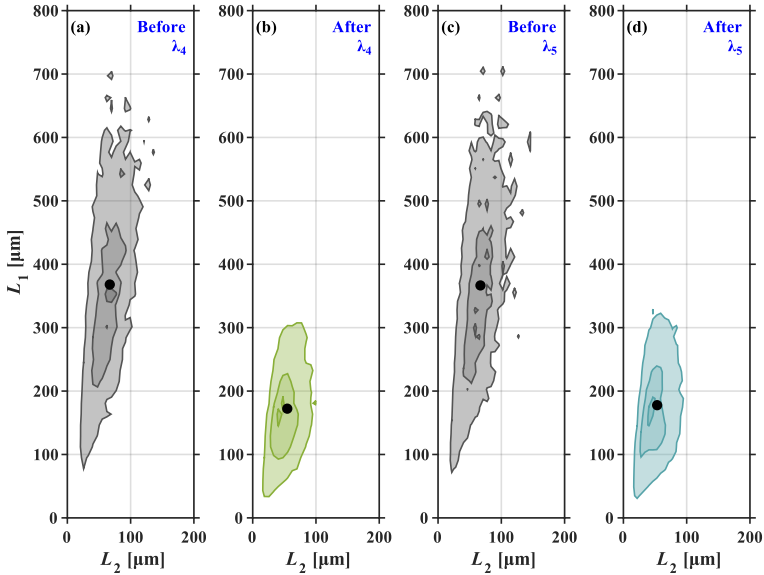
Figure 6.7: PSSDs f_v (obtained using eq 6.3 and normalized by the maximum of each PSSD) before experiment **(a)** λ_4 and **(c)** λ_5 and after experiment **(b)** λ_4 and **(d)** λ_5 for the controlled multistage process experiments using Seeds λ of BLGA crystals. The contour levels correspond to 0.1, 0.5, and 0.9 of each normalized PSSD. Along the L_1 direction, a regular grid with 120 bins and a spacing of 17 μm and 14 μm was used for experiment λ_4 and λ_5, respectively. Along the L_2 direction, the corresponding grid spacing was 7 μm and 6 μm using 40 bins. The solid circular markers indicate the average dimensions of the populations.
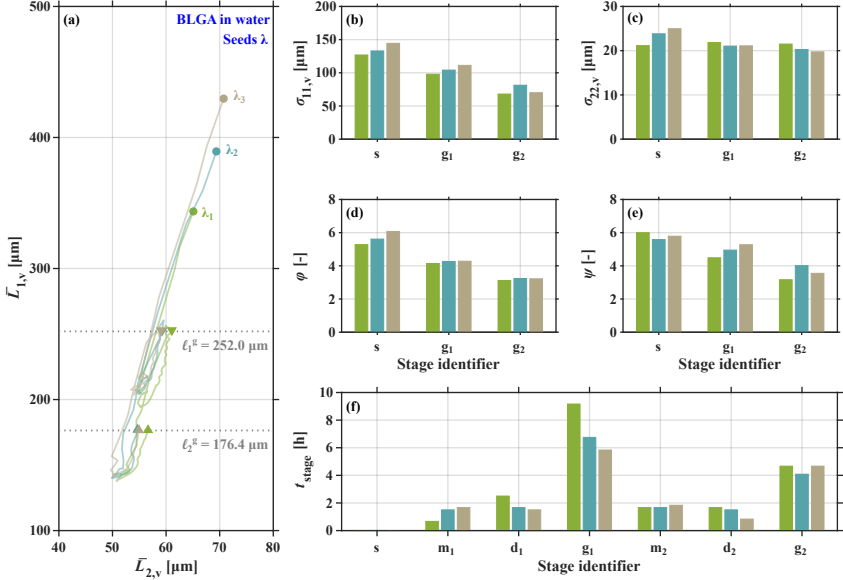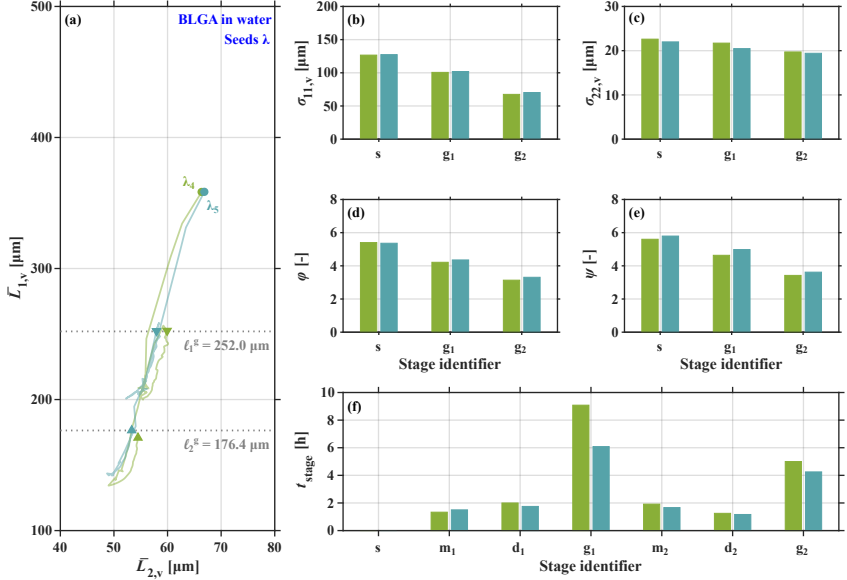
Figure 6.8: **(a)** Low-pass filtered evolution of the average length $\bar{L}_{1,\mathrm{v}}$ and width $\bar{L}_{2,\mathrm{v}}$ for BLGA experiment λ_4 (solid green line) and λ_5 (solid blue line). The circular markers, downward pointing triangular markers, and upward pointing triangular markers indicate the average dimensions before the experiment, at the end of the first cycle, and at the end of the second cycle (after the experiment), respectively. The horizontal dashed lines indicate the target average length at the end of the first cycle (ℓ_1^{g}) and that at the end of the second cycle (ℓ_2^{g}). The broadness of the measured PSSD (obtained using eq 6.5 and low-pass filtered subsequently) along **(b)** the length and **(c)** the width direction, **(d)** the average particle aspect ratio (obtained using eq 6.4 with low-pass filtered arguments), and **(e)** the ratio of the broadness along the two dimensions (obtained using eq 6.6 with low-pass filtered arguments) before the experiment (s), at the end of the first cycle (g_1), and at the end of the second cycle (g_2). **(f)** Time t_{stage} required for the individual stages to reach their respective targets. The bars in panels b through f share the color code for the different experiments with panel a.

are provided for experiments λ_4 and λ_5. Additionally, the evolution of the wet mill rotor speed during the two milling stages of these two experiments is visualized in Figure 6.9f. Note that the rotor speed evolution is not plotted against the process time, but against the number of wet milling steps n_{WM}. The solute concentration estimate was rather noisy during the milling stages, as can be seen in Figure 6.9a. As expected for the compound BLGA, a relatively quick increase was observed during the subsequent dissolution stages, whereas a slow decrease took place during the growth stages. Comparing the final with the initial concentration values, it can be said that a small positive yield resulted for both experiments. The temperature profiles visualized in Figure 6.9b show that the temperature was kept constant during the milling stages, that slow heating ramps were applied during the dissolution stages, and that, due to the low seed mass, little cooling was required to keep the supersaturation constant during the growth stages. The evolution of the estimated supersaturation profiles plotted in Figure 6.9c is sensible as well, with one exception: during the dissolution stages, it seems that the solution was slightly supersaturated instead of undersaturated. However, from the experimental observations it can be said that the particle volume was decreasing, i.e., the particles were dissolving. Therefore, the slight deviation from the expected undersaturation could be explained by a combination of the errors in the employed concentration estimation technique (which are in the order of 1 %, see ref 40) and uncertainties in the solubility curve (see eq E.1 in Appendix E.2) that have to be expected always. Since the dissolution stages were operated by a feedback controller that observes the particle volume directly and not the solute concentration estimate,[68] these deviations do not matter and the dissolution was performed successfully. The time series of the average particle dimensions are visualized in Figure 6.9d,e. During the first growth stage (i.e., between d_1 and g_1), the increase of the average length in λ_5 was quicker than that in λ_4. The higher growth rate during that stage is confirmed by the faster depletion of the concentration, as can be seen in Figure 6.9a. It is clear that batch-to-batch variations in the growth rates can always occur. Here, the reason for the observed difference in the growth rate may also be that one additional milling step and higher wet mill rotor speeds were applied by the milling controller towards the end of the first milling stage of λ_5, as illustrated in Figure 6.9f. As al-
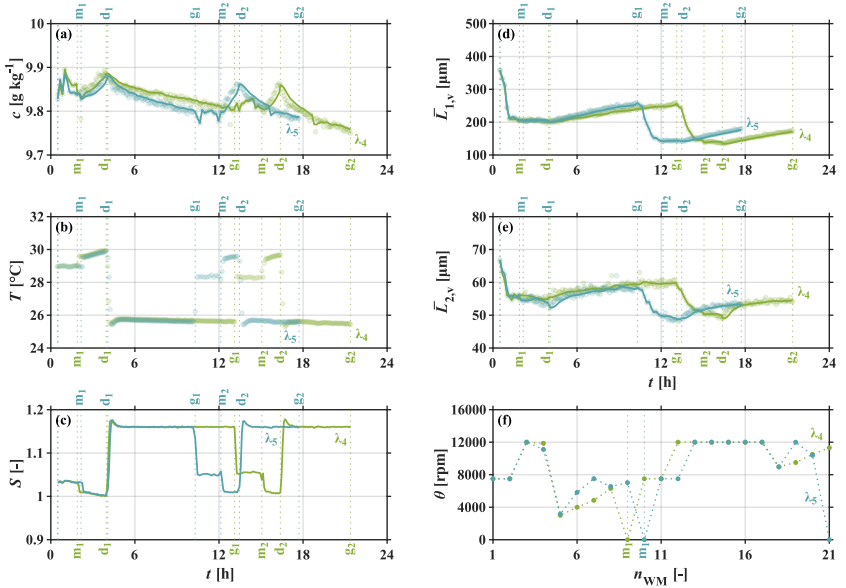
Figure 6.9: Time series of the controlled multistage process experiments λ_4 (green) and λ_5 (blue) using BLGA Seeds λ. **(a)** Evolution of the solute concentration. The solid markers represent the concentration estimate c and the solid lines represent the corresponding low-pass filtered signal c_{filt} (see Appendix E.2). **(b)** Evolution of the measured process temperature T. **(c)** Evolution of the supersaturation S (calculated according to eq E.3 given in Appendix E.2). Evolution of **(d)** the average length $\bar{L}_{1,\text{v}}$ and **(e)** the average width $\bar{L}_{2,\text{v}}$. The solid markers represent the experimentally obtained average dimensions and the solid lines are the corresponding low-pass filtered signals. **(f)** Evolution of the rotor speed θ in the wet mill as a function of the number of wet milling steps n_{WM}. The identifiers m_n, d_n, and g_n indicate the end of the milling, of the dissolution, and of the growth stage for the nth cycle, respectively.

ready explained in Section 6.4.2, more intense wet milling creates more particle surface area and also rougher crystal surfaces, thus leading to quicker growth in the next growth stage.

All considered, it can be said that the experiments presented in this section confirm that the proposed control approach manages to reach the desired target repeatedly.

6.4.4 Multistage Process Experiments with GDM

Before applying the controlled multistage process to a different compound (such as GDM in a 10/90 wt-% mixture of propan-2-ol and water), a few preliminary characterization steps need to be performed. First, the properties of the seed population need to be known and the parameters of the cycle logic should be adapted to these properties and to the desired shape change of the particles. In this work, however, this first step was not required, because these properties and goals were similar to those in the BLGA experiments. Therefore, the values for ℓ^{ref}, ℓ_1^{m}, ω, and ξ were left unchanged such that the individual stages had the same goals (or targets) as those of the experiments with BLGA presented in Sections 6.4.1 to 6.4.3. In a second step, a basic understanding of the kinetics of the compound should be acquired to be able to tune the individual stage controllers. To this end, a few preliminary seeded growth experiments were performed with GDM to identify a constant supersaturation level at which growth occurs at a reasonable rate, but no significant nucleation is observed. The outcome of these experiments is not shown here for the sake of brevity, but it became clear quickly that the growth rate was significantly higher than that of BLGA. Thus, the superaturation applied during the growth stages was lowered. In addition to these growth tests, heating ramps were applied to a batch of milled seeds starting from a slightly supersaturated state. GDM was observed to have a high dissolution rate, thereby leading to the loss of a large number of crystals within a short period of time (in the order of 15 min). Therefore, the heating rate applied in the dissolution controller (see Section 5.5.1 or ref 68) was halved. For the milling stages, no initial characterization steps were required, because the milling controller is adaptive and because it works well for the compound GDM,[67] as demonstrated in Section 4.4.3.

Two experiments were conducted with GDM in a 10/90 wt-% mixture of propan-2-ol and water. The first experiment was seeded with a

batch of GDM seed crystals, referred to as Seeds ν (see Appendix E.4), and the controlled multistage process was run right after seeding. In case of the second experiment, the seeds were grown to a given target average length by means of a preliminary growth step at constant supersaturation. Subsequently, the controlled multistage process was run. The main phases operated by the multistage process of these two experiments will be referred to as experiments ν_1 and ν_2, respectively. The detailed experimental protocol for the GDM experiments and the most important parameters of the individual stage controllers are explained in detail in Appendix E.6.

The PSSDs before and after experiments ν_1 and ν_2 are visualized in Figure 6.10. As expected, the initial PSSDs are different for the two experiments, as can be seen in Figure 6.10a,c, whereas the final PSSDs are very similar, as shown in Figure 6.10b,d. More detailed results of experiments ν_1 and ν_2 are visualized in Figure 6.11. Figure 6.11a confirms that the controlled multistage process can transform populations with different average particle dimensions to populations with very similar average dimensions also in the case of GDM. In Figure 6.11d, it can be seen that the average particle aspect ratio was reduced from about 6 to a value slightly below 4. The broadness measures depicted in Figure 6.11b,c decreased over each cycle for both the length and the width direction. Thus, the ratio of the broadness along the two dimensions shown in Figure 6.11e remained approximately the same over the two cycles. In Figure 6.11f, it can be seen that the growth stages for the two GDM experiments, contrary to those of the BLGA experiments, did not require more time than the milling and the dissolution stages. This can partially be attributed to the higher growth rate of GDM. The second reason for this observation can be traced back to the wet milling stages: it was observed that the GDM crystals are more brittle than those of BLGA, with a tendency to shatter into a large number of small fragments. In their entirety, these fragments contribute significantly to the overall solid volume, thus influencing even the average dimensions. During the dissolution stages, many of these fragments disappeared, which thereby increased the average dimensions. The increase in $\bar{L}_{1,\mathrm{v}}$ to be covered during the subsequent growth stage is thus smaller. Note that due to the high dissolution rate combined with the thermal inertia of the crystallizer and that of the thermostat, the particle volume
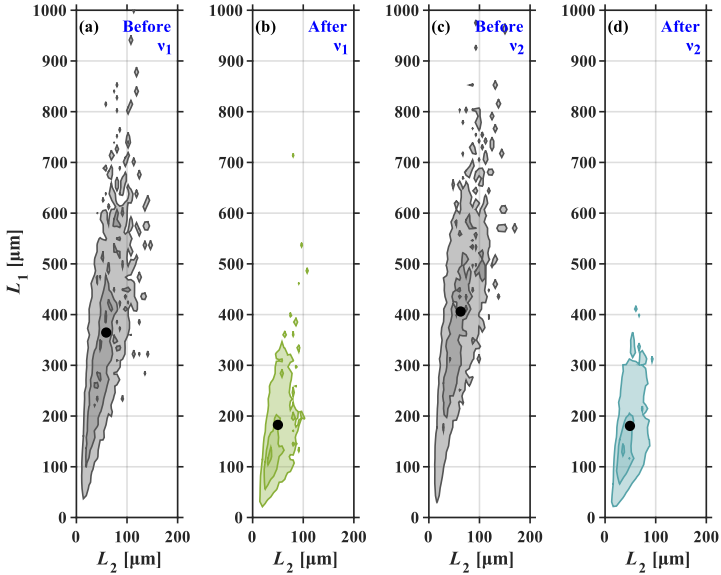
Figure 6.10: PSSDs f_v (obtained using eq 6.3 and normalized by the maximum of each PSSD) before experiment **(a)** v_1 and **(c)** v_2 and after experiment **(b)** v_1 and **(d)** v_2 for the controlled multistage process experiments using GDM Seeds v. The contour levels correspond to 0.1, 0.5, and 0.9 of each normalized PSSD. Along the L_1 direction, a regular grid with 120 bins and a spacing of 13 μm and 12 μm was used for experiment v_1 and v_2, respectively. Along the L_2 direction, the corresponding grid spacing was 6 μm and 6 μm using 40 bins. The solid circular markers indicate the average dimensions of the populations.
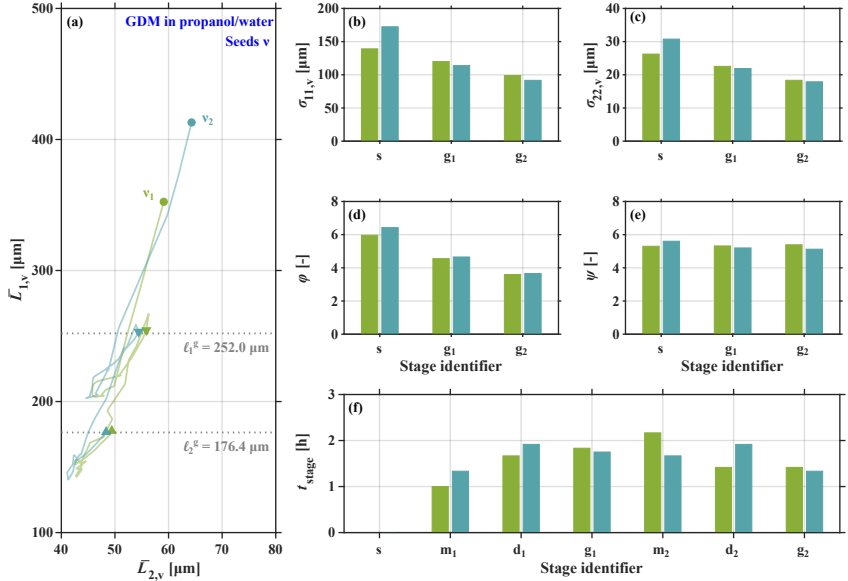
Figure 6.11: **(a)** Low-pass filtered evolution of the average length $\bar{L}_{1,\mathrm{v}}$ and width $\bar{L}_{2,\mathrm{v}}$ for GDM experiments ν_1 (solid green line) and ν_2 (solid blue line). The circular markers, downward pointing triangular markers, and upward pointing triangular markers indicate the average dimensions before the experiment, at the end of the first cycle, and at the end of the second cycle (after the experiment), respectively. The horizontal dashed lines indicate the target average length at the end of the first cycle (ℓ_1^{g}) and that at the end of the second cycle (ℓ_2^{g}). The broadness of the measured PSSD (obtained using eq 6.5 and low-pass filtered subsequently) along **(b)** the length and **(c)** the width direction, **(d)** the average particle aspect ratio (obtained using eq 6.4 with low-pass filtered arguments), and **(e)** the ratio of the broadness along the two dimensions (obtained using eq 6.6 with low-pass filtered arguments) before the experiment (s), at the end of the first cycle (g_1), and at the end of the second cycle (g_2, after the experiment). **(f)** Time t_{stage} required for the individual stages to reach their respective targets. The bars in panels b through f share the color code for the two experiments with panel a.

undershot its target during the dissolution stages (not shown here for the sake of brevity). In general, it can be said that running the controlled multistage process for GDM is more challenging, also because both its solubility and its growth and dissolution rates in the chosen solvent mixture are higher than those of BLGA in water. Still, it has been shown that the controlled multistage process is able to achieve the process goals and to yield a significant shape change to more equant particles also in this case.

6.5 Conclusions

An extension of a previously suggested multistage process [63,64] for the batch-wise transformation of needle-like seed crystals into more equant particles has been presented. The two previously unexplored and striking features of this extension are, first, that the process is operated in a fully automated and controlled manner without the need of kinetic process models, and second, that it provides robustness with respect to achieving PSSDs with desirable properties repeatedly over consecutive batches. Both of these developments have been enabled by a combination of online monitoring of the particle size and shape evolution with feedback control techniques.

The robustness of the proposed approach has been validated by means of an experimental campaign for the system BLGA in water, during which batch experiments with different initial conditions were successfully steered toward final PSSDs with nearly identical properties. This capability of the proposed process control scheme is very valuable in terms of mitigating undesirable batch-to-batch variations in the solid product. Further experiments using the same system were conducted to investigate the impact of the number of cycles on the products and to assess the repeatability of the process outcome. The general applicability of the approach has been demonstrated as well by successfully applying it to a different, more challenging system, namely, to GDM in a mixture of propan-2-ol and water. In all the experiments, a significant reduction of the average particle aspect ratio (from about 5 to 6 to about 3 for BLGA, and from about 6 to slightly below 4 for GDM) and of the broadness of the final PSSD was achieved. Such a shape transformation would be of interest, e.g., in the pharmaceutical industry for facilitating

downstream operations.

While the advantages of the controlled multistage process are clear, there is still room for improvement. For instance, the proposed cycle logic, including the chosen sequence of stages (milling followed by dissolution followed by growth), has not been optimized with respect to any performance criteria. Therefore, the stage targets were chosen more or less arbitrarily and the impact of these decisions on the batch time and the productivity is not taken into account. Obviously, some sort of process model would be helpful to design a better cycle logic, while feedback control would still be essential to counteract uncertainties and disturbances.

Nomenclature

Acronyms

BLGA	β L-glutamic acid
DISCO	dual imaging system for crystallization observation
GDM	γ D-mannitol
PSSD	particle size and shape distribution

Roman symbols

c	solute concentration (per mass of solvent basis) $[\mathrm{g\,kg^{-1}}]$
c^*	solubility (per mass of solvent basis) $[\mathrm{g\,kg^{-1}}]$
d	dissolution stage identifier
f	number density function (PSSD) $[\mu\mathrm{m}^{-2}]$
f_{v}	volume-weighted PSSD $[\mu\mathrm{m}^{-2}]$
g	growth stage identifier
k	placeholder for stage identifier, k = {d, g, m, p, s}
ℓ_n^{k}	target average length of stage k in the nth cycle
ℓ_1^{m}	parameter of the cycle logic $[\mu\mathrm{m}]$
ℓ^{ref}	parameter of the cycle logic $[\mu\mathrm{m}]$
L_i	ith particle dimension ($i = 1, 2$) $[\mu\mathrm{m}]$
$\bar{L}_i$	average of ith particle dimension ($i = 1, 2$) $[\mu\mathrm{m}]$
$\bar{\boldsymbol{L}}_n^{\mathrm{k}}$	vector of average particle dimensions $\bar{\boldsymbol{L}}_n^{\mathrm{k}} = [\bar{L}_1\ \bar{L}_2]^{\mathrm{T}}$ $[\mu\mathrm{m}]$, at the end of stage k of the nth cycle
$\bar{L}_{i,\mathrm{v}}$	volume-weighted average of ith dimension ($i = 1, 2$) $[\mu\mathrm{m}]$
m	milling stage identifier
n	cycle counter
n_{WM}	number of wet milling steps
p	product identifier
S	(relative) supersaturation, c/c^* $[-]$
s	seed identifier
T	temperature $[^\circ\mathrm{C}]$
t	time $[\mathrm{h}]$
t_{stage}	stage duration $[\mathrm{h}]$

Greek symbols

θ	rotor speed (of the wet mill) [rpm]
κ	BLGA seed population; experiment label
λ	BLGA seed population; experiment label
μ_{ij}	ij-cross moment of the PSSD [μm^{i+j}]
ν	GDM seed population; experiment label
ξ	parameter of the cycle logic [–]
$\sigma_{ii,\mathrm{v}}$	volume-weighted broadness of the PSSD along ith dimension ($i = 1, 2$) [µm]
ϕ	volume-weighted particle aspect ratio [–]
ψ	volume-weighted ratio of the broadness along the two dimensions [–]
ω	parameter of the cycle logic [–]

Subscripts and superscripts

filt	filtered (low-pass or median)

Chapter 7

Concluding Remarks and Outlook

The work collected in this thesis represents a step toward the robust operation of batch crystallization processes, where the term robust here refers to obtaining a product PSSD with desirable properties repeatedly in consecutive batches, despite the presence of unpredictable process disturbances. Achieving the presented results was enabled by a combination of advanced online monitoring and a number of feedback control laws, mostly without the need of kinetic process models. From a control systems engineering point of view, most of the applied techniques are rather basic and this thesis simply embodies another example of the potential of feedback control. However, from a crystallization perspective, the chosen approaches to achieving target crystal sizes and shapes are both novel and promising. As outlined in Chapter 1, producing tailored crystal sizes and shapes is highly desirable in many applications of crystalline solids. Even in cases when the engineering tools presented in this thesis are not sufficient to fully achieve this goal, their capability to operate the process automatically and to reduce batch-to-batch variations in terms of selected properties of the final PSSD are valuable.

In this chapter, a few general conclusions are drawn and some perspectives are given concerning the vital online monitoring aspect and concerning the modeling and control aspects of batch crystallization processes with particle size and shape objectives. Afterward, some reflections

on the specific approaches proposed in this thesis are provided.

7.1 Thoughts on Online Monitoring

The slowly increasing availability of quantitative online size and shape monitoring tools will pave the way for a larger number of studies on feedback control of crystal size and shape. From today's point of view, imaging is the only promising technique to tackle the online shape monitoring problem. In terms of employing either *ex situ* or *in situ* imaging devices, it is clear that the former offer distinct advantages when it comes to monitoring accuracy, whereas the latter do not suffer from the drawbacks of a sampling loop (invasive nature and potentially biased sampling). Regardless of the type of the imaging device, it is desirable from a control perspective to reduce the processing time of the images (the µ-DISCO currently requires in the order of 2 min per meassurement) by optimizing the image analysis software. The benefits would be that the online monitoring could be performed either with a shorter sampling time, which would enable observing processes on a faster time scale, or that more images could be acquired per time, which would provide more accurate PSSD data. In light of today's abundance of powerful computing hardware, this is simply a software engineering effort.

Coming back to *ex-situ* monitoring, devices designed for this task should be enhanced with dilution loops[23,33]—preferably fully automated ones—to make them applicable to suspension densities higher than those explored in this work. Given the high dilution ratios that would be required, it could be favorable to no longer continuously sample the suspension and pump it through the monitoring device, but to sample, dilute, and measure in a batch-wise manner. Clearly, the development of such a dilution loop would make the online monitoring and control approaches proposed in this thesis more appealing from an industrial point of view. On an industrial scale, sampling a bit of suspension from a large tank will hardly pose a problem in terms of the invasise nature of the measurement, but more likely in terms of obtaining a representative sample of the population inside the crystallizer. Also, note that diluting the observed suspension is an option that cannot be offered by *in situ* techniques.

7.2 Thoughts on Modeling and Control

In terms of the control aspect, this thesis spotlights the trade-off between the model-based and the model-free approach to systematic crystal size and shape modification. Modeling of the kinetics (e.g., crystal growth, dissolution, and breakage rates) clearly provides an increased understanding of the process itself. It also permits simulation studies for the purpose of process analysis, process optimization, or the development and the initial testing of suitable feedback control laws. Nevertheless, developing such models is difficult, time-consuming, very compound-specific, and the resulting models are still quantitatively uncertain. It has been shown in this thesis that online monitoring combined with model-free feedback control is a viable alternative to operating the process. This approach is especially useful when multiple compounds are to be considered and when the development time should remain relatively low.

From a control engineering point of view, there is no doubt that model-based control laws are generally more powerful than their model-free counterparts. The reason for the bias in this thesis toward model-free techniques is in fact not the unavailability of more sophisticated control algorithms, but the obvious lack of quantitatively predictive crystal size and shape evolution models. Model-based control algorithms to make use of a priori quantified model uncertainty have been proposed also for crystallization processes.[74,107] Thus, Bayesian estimation could be applied more frequently in modeling studies to better quantify parametric uncertainty (see, e.g., refs 154 and 155). However, it also needs to be said that these approaches do not help in keeping the complexity of the modeling and control tasks at bay; in fact, quite the contrary is the case. This issue has to be kept in mind, especially since taking into account also particle shape, and not only size, automatically increases the dimensionality of the problem.

A general credo in process modeling is that every model needs a purpose and that the chosen type of model needs to serve this purpose. While certainly being the means of choice when performing modeling to increase the understanding of the process, the widely applied population balance framework is not the most suitable tool for obtaining control-oriented models, mainly due to its comparatively high complexity and

associated computational costs. An alternative presents itself in the form of a combination of data-driven modeling with simpler model structures that can reliably capture the principal dynamics of the process. A few studies in the literature [109,152] and the adaptive controller for the wet milling process presented in Chapter 4 represent steps in that direction.

Two methods from control systems engineering that have not been explored in this work are iterative learning control (ILC) [156] and batch-to-batch techniques to adapt process models. There are a number of studies in the literature that apply these techniques also to batch crystallization, thereby exploiting the repetitive nature of batch processes (see, e.g., refs 157 and 158 and refs therein). It is clear that basic ILC and batch-to-batch model adaption techniques cannot anticipate and compensate for process disturbances that vary from batch to batch. Thus, and in terms of applying the benefits of ILC and similar concepts also to crystal shape control, these methods could be an excellent extension of some of the model-free feedback controllers proposed in this thesis. For instance, ILC could be applied to augment some of the presented feedback controllers with feedforward signals that are improved from batch to batch.

7.3   Some Reflections on More Specific Points

The single crystal temperature cycling approach proposed in Chapter 2 has not been implemented experimentally. The developed path planning algorithms could easily be used as a basis to develop a suitable feedback controller. Since single crystals are known to exhibit significant growth rate dispersion, [56] an experimental study on single crystal shape control might be useful in the sense of providing another example on how the introduction of feedback can mitigate model uncertainties.

The PFC strategy introduced in Chapter 3 has been proven to work well both in simulations and in experiments in the sense of yielding very similar product PSSDs for consecutive batches. In the case of seed populations with an unknown or with a very narrow attainable region, the process goals of the PFC might prove to be too stringent and could be relaxed straightforwardly. For instance, the target orthant of the PFC could be expanded to a target half-plane for the average particle length

in order to ensure termination of the growth process. If means of shape actuation other than a growth phase are available, it can prove useful to replace the PFC with an even simpler CSC approach that automatically ends the growth process as soon as a certain minimum crystal length (or process yield) is achieved, as demonstrated in Chapter 6. Applying the PFC to batch crystallizations operated with higher suspension densities is feasible provided that the online monitoring problem for this case is solved and as long as the process remains growth-dominated. If significant nucleation takes place, additional monitoring efforts have to be undertaken to distinguish the population of nucleated crystals from that of the seeds, while the PFC should only be applied to the seed population. Considerable agglomeration or breakage should be avoided since the PFC has not been designed to handle these phenomena.

The adaptive controller for the milling process introduced in Chapter 4 relies on a very simple model of the breakage process. The control strategy has been proven to perform well in experiments using different compounds in the sense of reaching different target average particle lengths as long as the allowed range of rotor speeds is not too wide. Still, widening this range would be useful for increased or more efficient shape actuation. The inherently nonlinear nature of the milling process might be captured in a better way by using a slightly more complex model in the adaptive controller, probably featuring an additional parameter to be estimated online. A potential shortcoming of the milling controller is that it estimates the parameters of its internal process model based on only a few, noisy measurements of the average particle dimensions. While this is unavoidable when milling a previously unknown particle population for the first time, the model could be estimated offline and its parameters could be adapted only moderately when milling the same population repeatedly in consecutive batches. As of the applicability of the proposed milling controller to higher suspension densities, this should be possible without modification of the control law, of course provided that the online monitoring works reliably.

Most likely due to its simplicity, the particle volume controller proposed in Chapter 5 has proven to perform very reliably on the lab-scale provided that the dissolution kinetics are not too fast compared with the sampling rate of the online monitoring tool and compared with the thermal dynamics of the crystallizer. The particle volume controller can

represent both a controlled fines removal strategy and a tool to indirectly reduce the aspect ratio of needle-like particles. For pure fines removal purposes, the heating of the entire slurry in a batch crystallizer can be inefficient both energetically and timewise. In such a context, a similar controller could also be used in combination with a dedicated, heated fines removal loop. Similar to the milling controller, it should be possible to apply the particle volume controller to high suspension densities, provided that reliable online monitoring of the evolution of the particle volume is feasible.

As of the cyclic size and shape modification process consisting of controlled growth, milling, and dissolution stages, it would be desirable to increase its productivity, where productivity is considered to be the ratio of yield and process time. Fines removal using a dedicated loop could already help to do so. Alternatively, to reduce the time required to perform temperature cycles, two stirred tanks or two separate temperature baths (thermostats) for the crystallizer jacket could be employed (see, e.g., ref 21). A natural way of introducing also control over the width of the needle-like particles would be to apply the PFC strategy in the growth stages instead of the more basic CSC. Of course, it would also be interesting to experimentally validate the controlled multistage process proposed in Chapter 6 at higher suspension densities. Concerning the process goals of any size and shape modification process, it is essential that more research efforts such as that presented in ref 159 investigate the quantitative relation between properties of the PSSD and downstream processing efficiency and product quality. Such efforts would enable a systematic selection of targets for the control algorithms, which in turn would lay the foundations for developing a less arbitrary and thus a more purposeful cycle logic than that presented in Chapter 6.

Finally, it is vital to keep in mind the underactuation problem in terms of the particle size and shape evolution mentioned in Chapter 1. Thus, continued efforts should be directed toward developing control laws for additional and potentially unconventional actuators or processes. For instance, the addition of anti-solvent or additives, sonication, or spherical agglomeration could be explored and robustified by introducing feedback control.

Bibliography

[1] Yu, W.; Liao, L.; Bharadwaj, R.; Hancock, B. C. What is the "typical" particle shape of active pharmaceutical ingredients? *Powder Technol.* **2017**, *313*, 1–8.

[2] Nichols, G.; Frampton, C. S. Physicochemical Characterization of the Orthorhombic Polymorph of Paracetamol Crystallized from Solution. *J. Pharm. Sci.* **1998**, *87*, 684–693.

[3] Schöll, J.; Bonalumi, D.; Vicum, L.; Mazzotti, M.; Müller, M. In Situ Monitoring and Modeling of the Solvent-Mediated Polymorphic Transformation of L-Glutamic Acid. *Cryst. Growth Des.* **2006**, *6*, 881–891.

[4] Davey, R. J.; Mullin, J. W.; Whiting, M. J. L. Habit modification of succinic acid crystals grown from different solvents. *J. Cryst. Growth* **1982**, *58*, 304–312.

[5] Salvalaglio, M.; Vetter, T.; Mazzotti, M.; Parrinello, M. Controlling and Predicting Crystal Shapes: The Case of Urea. *Angew. Chem., Int. Ed.* **2013**, *52*, 13369–13372.

[6] Davey, R. J.; Black, S. N.; Logan, D.; Maginn, S. J.; Fairbrother, J. E.; Grant, D. J. W. Structural and Kinetic Features of Crystal Growth Inhibition: Adipic Acid Growing in the Presence of *n*-Alkanoic Acids. *J. Chem. Soc., Faraday Trans.* **1992**, *88*, 3461–3466.

[7] Ristic, R. I.; Finnie, S.; Sheen, D. B.; Sherwood, J. N. Macro- and Micromorphology of Monoclinic Paracetamol Grown from Pure Aqueous Solution. *J. Phys. Chem. B* **2001**, *105*, 9057–9066.

[8] Yang, G.; Kubota, N.; Sha, Z.; Louhi-Kultanen, M.; Wang, J. Crystal Shape Control by Manipulating Supersaturation in Batch Cooling Crystallization. *Cryst. Growth Des.* **2006**, *6*, 2799–2803.

[9] Davey, R.; Garside, J. *From Molecules to Crystallizers: An Introduction to Crystallization*; Oxford University Press: New York, NY, 2000.

[10] Lovette, M. A.; Browning, A. R.; Griffin, D. W.; Sizemore, J. P.; Snyder, R. C.; Doherty, M. F. Crystal Shape Engineering. *Ind. Eng. Chem. Res.* **2008**, *47*, 9812–9833.

[11] Chow, K.; Tong, H. H. Y.; Lum, S.; Chow, A. H. L. Engineering of Pharmaceutical Materials: An Industrial Perspective. *J. Pharm. Sci.* **2008**, *97*, 2855–2877.

[12] Fee, J.; Collier, P.; Launchbury, A.; Clarke, R. The influence of particle size on the bioavailability of inhaled temazepam. *Br. J. Clin. Pharmacol.* **1992**, *33*, 641–644.

[13] Modi, S. R.; Dantuluri, A. K. R.; Puri, V.; Pawar, Y. B.; Nandekar, P.; Sangamwar, A. T.; Perumalla, S. R.; Sun, C. C.; Bansal, A. K. Impact of Crystal Habit on Biopharmaceutical Performance of Celecoxib. *Cryst. Growth Des.* **2013**, *13*, 2824–2832.

[14] Wibowo, C.; Chang, W.-C.; Ng, K. M. Design of Integrated Crystallization Systems. *AIChE J.* **2001**, *47*, 2474–2492.

[15] Beck, R.; Nysæter, T. O.; Enstad, G. G.; Malthe-Sørenssen, D.; Andreassen, J. P. Influence of Crystal Properties on Powder Flow Behavior of an Aromatic Amine and L-Glutamic Acid. *Part. Sci. Technol.* **2010**, *28*, 146–160.

[16] Pudasaini, N.; Upadhyay, P. P.; Parker, C. R.; Hagen, S. U.; Bond, A. D.; Rantanen, J. Downstream Processability of Crystal Habit-Modified Active Pharmaceutical Ingredient. *Org. Process Res. Dev.* **2017**, *21*, 571–577.

[17] Yang, H. G.; Sun, C. H.; Qiao, S. Z.; Zou, J.; Liu, G.; Smith, S. C.; Cheng, H. M.; Lu, G. Q. Anatase TiO2 single crystals with a large percentage of reactive facets. *Nature* **2008**, *453*, 638–641.

[18] Mullin, J. W. *Crystallization*, 4th ed.; Butterworth-Heinemann: Oxford, UK, 2001.

[19] Variankaval, N.; Cote, A. S.; Doherty, M. F. From Form to Function: Crystallization of Active Pharmaceutical Ingredients. *AIChE J.* **2008**, *54*, 1682–1688.

[20] Patience, D. B.; Rawlings, J. B. Particle-Shape Monitoring and Control in Crystallization Processes. *AIChE J.* **2001**, *47*, 2125–2130.

[21] Eisenschmidt, H.; Bajcinca, N.; Sundmacher, K. Optimal Control of Crystal Shapes in Batch Crystallization Experiments by Growth-Dissolution Cycles. *Cryst. Growth Des.* **2016**, *16*, 3297–3306.

[22] Borchert, C.; Sundmacher, K. Efficient formulation of crystal shape evolution equations. *Chem. Eng. Sci.* **2012**, *84*, 85–99.

[23] Schorsch, S.; Vetter, T.; Mazzotti, M. Measuring multidimensional particle size distributions during crystallization. *Chem. Eng. Sci.* **2012**, *77*, 130–142.

[24] Ramkrishna, D. *Population Balances: Theory and Applications to Particulate Systems in Engineering*; Academic Press: San Diego, CA, 2000.

[25] Hulburt, H. M.; Katz, S. Some problems in particle technology: A statistical mechanical formulation. *Chem. Eng. Sci.* **1964**, *19*, 555–574.

[26] Marchisio, D. L.; Pikturna, J. T.; Fox, R. O.; Vigil, R. D.; Barresi, A. A. Quadrature Method of Moments for Population-Balance Equations. *AIChE J.* **2003**, *49*, 1266–1276.

[27] Ma, D. L.; Tafti, D. K.; Braatz, R. D. High-Resolution Simulation of Multidimensional Crystal Growth. *Ind. Eng. Chem. Res.* **2002**, *41*, 6217–6223.

[28] Gunawan, R.; Fusman, I.; Braatz, R. D. High Resolution Algorithms for Multidimensional Population Balance Equations. *AIChE J.* **2004**, *50*, 2738–2749.

[29] Mesbah, A.; Kramer, H. J.; Huesman, A. E.; Van den Hof, P. M. A control oriented study on the numerical solution of the population balance equation for crystallization processes. *Chem. Eng. Sci.* **2009**, *64*, 4262–4277.

[30] Borchert, C. Topics in Crystal Shape Dynamics. Doctoral Thesis, Otto von Guericke University Magdeburg, Germany, 2012.

[31] Ochsenbein, D. R. Modeling and Characterizing Populations of Nonequant Particles in Crystallization Processes. Doctoral Thesis, ETH Zurich, Switzerland, 2015.

[32] Rajagopalan, A. K.; Schneeberger, J.; Salvatori, F.; Bötschi, S.; Ochsenbein, D. R.; Oswald, M. R.; Pollefeys, M.; Mazzotti, M. A comprehensive shape analysis pipeline for stereoscopic measurements of particulate populations in suspension. *Powder Technol.* **2017**, *321*, 479–493.

[33] Rajagopalan, A. K. A Dual Projection Imaging System to Characterize Crystallization Processes: Design and Applications. Doctoral Thesis, ETH Zurich, Switzerland, 2019.

[34] Singh, M. R.; Chakraborty, J.; Nere, N.; Tung, H.-H.; Bordawekar, S.; Ramkrishna, D. Image-Analysis-Based Method for 3D Crystal Morphology Measurement and Polymorph Identification Using Confocal Microscopy. *Cryst. Growth Des.* **2012**, *12*, 3735–3748.

[35] de Albuquerque, I.; Mazzotti, M.; Ochsenbein, D. R.; Morari, M. Effect of Needle-Like Crystal Shape on Measured Particle Size Distributions. *AIChE J.* **2016**, *62*, 2974–2985.

[36] Bujak, B.; Bottlinger, M. Three-Dimensional Measurement of Particle Shape. *Part. Part. Syst. Char.* **2008**, *25*, 293–297.

[37] Wang, X. Z.; Calderon De Anda, J.; Roberts, K. J. Real-Time Measurement of the Growth Rates of Individual Crystal Facets Using Imaging and Image Analysis: A Feasibility Study on Needle-shaped Crystals of L-Glutamic Acid. *Chem. Eng. Res. Des.* **2007**, *85*, 921–927.

[38] Kempkes, M.; Vetter, T.; Mazzotti, M. Measurement of 3D particle size distributions by stereoscopic imaging. *Chem. Eng. Sci.* **2010**, *65*, 1362–1373.

[39] Schorsch, S.; Ochsenbein, D. R.; Vetter, T.; Morari, M.; Mazzotti, M. High accuracy online measurement of multidimensional particle size distributions during crystallization. *Chem. Eng. Sci.* **2014**, *105*, 155–168.

[40] Bötschi, S.; Rajagopalan, A. K.; Morari, M.; Mazzotti, M. An Alternative Approach to Estimate Solute Concentration: Exploiting the Information Embedded in the Solid Phase. *J. Phys. Chem. Lett.* **2018**, *9*, 4210–4214.

[41] de Albuquerque, I.; Mazzotti, M. Crystallization Process Design Using Thermodynamics To Avoid Oiling Out in a Mixture of Vanillin and Water. *Cryst. Growth Des.* **2014**, *14*, 5617–5625.

[42] Togkalidou, T.; Tung, H.-H.; Sun, Y.; Andrews, A.; Braatz, R. D. Solution Concentration Prediction for Pharmaceutical Crystallization Processes Using Robust Chemometrics and ATR FTIR Spectroscopy. *Org. Process Res. Dev.* **2002**, *6*, 317–322.

[43] Lindenberg, C.; Krättli, M.; Cornel, J.; Mazzotti, M.; Brozio, J. Design and Optimization of a Combined Cooling/Antisolvent Crystallization Process. *Cryst. Growth Des.* **2009**, *9*, 1124–1136.

[44] Schöll, J.; Vicum, L.; Müller, M.; Mazzotti, M. Precipitation of L-Glutamic Acid: Determination of Nucleation Kinetics. *Chem. Eng. Technol.* **2006**, *29*, 257–264.

[45] Schöll, J.; Lindenberg, C.; Vicum, L.; Brozio, J.; Mazzotti, M. Precipitation of α L-glutamic acid: determination of growth kinetics. *Faraday Discuss.* **2007**, *136*, 247–264.

[46] Eisenschmidt, H.; Voigt, A.; Sundmacher, K. Face-Specific Growth and Dissolution Kinetics of Potassium Dihydrogen Phosphate Crystals from Batch Crystallization Experiments. *Cryst. Growth Des.* **2015**, *15*, 219–227.

[47] O'Sullivan, B.; Glennon, B. Application of in Situ FBRM and ATR-FTIR to the Monitoring of the Polymorphic Transformation of D-Mannitol. *Org. Process Res. Dev.* **2005**, *9*, 884–889.

[48] Nagy, Z. K.; Braatz, R. D. Advances and New Directions in Crystallization Control. *Annu. Rev. Chem. Biomol. Eng.* **2012**, *3*, 55–75.

[49] Cornel, J.; Lindenberg, C.; Mazzotti, M. Quantitative Application of in Situ ATR-FTIR and Raman Spectroscopy in Crystallization Processes. *Ind. Eng. Chem. Res.* **2008**, *47*, 4870–4882.

[50] Borissova, A.; Khan, S.; Mahmud, T.; Roberts, K. J.; Andrews, J.; Dallin, P.; Chen, Z.-P.; Morris, J. In Situ Measurement of Solution Concentration during the Batch Cooling Crystallization of L-Glutamic Acid using ATR-FTIR Spectroscopy Coupled with Chemometrics. *Cryst. Growth Des.* **2009**, *9*, 692–706.

[51] Laurentini, A. The Visual Hull Concept for Silhouette-Based Image Understanding. *IEEE Trans. Pattern Anal. Mach. Intell.* **1994**, *16*, 150–162.

[52] Bötschi, S.; Ochsenbein, D. R.; Morari, M.; Mazzotti, M. Multi-Objective Path Planning for Single Crystal Size and Shape Modification. *Cryst. Growth Des.* **2017**, *17*, 4873–4886.

[53] Borchert, C.; Temmel, E.; Eisenschmidt, H.; Lorenz, H.; Seidel-Morgenstern, A.; Sundmacher, K. Image-Based in Situ Identification of Face Specific Crystal Growth Rates from Crystal Populations. *Cryst. Growth Des.* **2014**, *14*, 952–971.

[54] Ochsenbein, D. R.; Schorsch, S.; Vetter, T.; Mazzotti, M.; Morari, M. Growth Rate Estimation of β L-Glutamic Acid from Online Measurements of Multidimensional Particle Size Distributions and Concentration. *Ind. Eng. Chem. Res.* **2014**, *53*, 9136–9148.

[55] Jiang, M.; Zhu, X.; Molaro, M. C.; Rasche, M. L.; Zhang, H.; Chadwick, K.; Raimondo, D. M.; Kim, K.-K. K.; Zhou, L.; Zhu, Z.; Wong, M. H.; O'Grady, D.; Hebrault, D.; Tedesco, J.; Braatz, R. D. Modification of Crystal Shape through Deep Temperature Cycling. *Ind. Eng. Chem. Res.* **2014**, *53*, 5325–5336.

[56] Ochsenbein, D. R.; Schorsch, S.; Salvatori, F.; Vetter, T.; Morari, M.; Mazzotti, M. Modeling the facet growth rate dispersion of β L-glutamic acid—Combining single crystal experiments with nD particle size distribution data. *Chem. Eng. Sci.* **2015**, *133*, 30–43.

[57] Rawlings, J. B.; Miller, S. M.; Witkowski, W. R. Model Identification and Control of Solution Crystallization Processes: A Review. *Ind. Eng. Chem. Res.* **1993**, *32*, 1275–1296.

[58] Braatz, R. D. Advanced control of crystallization processes. *Annu. Rev. Contr.* **2002**, *26*, 87–99.

[59] Nagy, Z. K.; Fevotte, G.; Kramer, H.; Simon, L. L. Recent advances in the monitoring, modelling and control of crystallization systems. *Chem. Eng. Res. Des.* **2013**, *91*, 1903–1922.

[60] Srinivasan, B.; Bonvin, D. Controllability and stability of repetitive batch processes. *J. Process Control* **2007**, *17*, 285–295.

[61] Mesbah, A.; Nagy, Z. K.; Huesman, A. E.; Kramer, H. J.; Van den Hof, P. M. Nonlinear Model-Based Control of a Semi-Industrial Batch Crystallizer Using a Population Balance Modeling Framework. *IEEE Trans. Control Syst. Technol.* **2012**, *20*, 1188–1201.

[62] Bajcinca, N. Time optimal cyclic crystallization. *Comput. Chem. Eng.* **2013**, *58*, 381–389.

[63] Salvatori, F.; Mazzotti, M. Manipulation of Particle Morphology by Crystallization, Milling, and Heating Cycles—A Mathematical Modeling Approach. *Ind. Eng. Chem. Res.* **2017**, *56*, 9188–9201.

[64] Salvatori, F.; Mazzotti, M. Manipulation of Particle Morphology by Crystallization, Milling, and Heating Cycles: Experimental Characterization. *Ind. Eng. Chem. Res.* **2018**, *57*, 15522–15533.

[65] Bötschi, S.; Rajagopalan, A. K.; Morari, M.; Mazzotti, M. Feedback Control for the Size and Shape Evolution of Needle-like Crystals in Suspension. I. Concepts and Simulation Studies. *Cryst. Growth Des.* **2018**, *18*, 4470–4483.

[66] Rajagopalan, A. K.; Bötschi, S.; Morari, M.; Mazzotti, M. Feedback Control for the Size and Shape Evolution of Needle-like Crystals in Suspension. II. Cooling Crystallization Experiments. *Cryst. Growth Des.* **2018**, *18*, 6185–6196.

[67] Rajagopalan, A. K.; Bötschi, S.; Morari, M.; Mazzotti, M. Feedback Control for the Size and Shape Evolution of Needle-like Crystals in Suspension. III. Wet Milling. *Cryst. Growth Des.* **2019**, *19*, 2845–2861.

[68] Bötschi, S.; Rajagopalan, A. K.; Morari, M.; Mazzotti, M. Feedback Control for the Size and Shape Evolution of Needle-like Crystals in Suspension. IV. Modeling and Control of Dissolution. *Cryst. Growth Des.* **2019**, *19*, 4029–4043.

[69] Bötschi, S.; Rajagopalan, A. K.; Rombaut, I.; Morari, M.; Mazzotti, M. From needle-like toward equant particles: A controlled crystal shape engineering pathway. *Comput. Chem. Eng.* **2019**, in press.

[70] Snyder, R. C.; Studener, S.; Doherty, M. F. Manipulation of Crystal Shape by Cycles of Growth and Dissolution. *AIChE J.* **2007**, *53*, 1510–1517.

[71] Lovette, M. A.; Muratore, M.; Doherty, M. F. Crystal Shape Modification Through Cycles of Dissolution and Growth: Attainable Regions and Experimental Validation. *AIChE J.* **2012**, *58*, 1465–1474.

[72] Bajcinca, N.; de Oliveira, V.; Borchert, C.; Raisch, J.; Sundmacher, K. Optimal control solutions for crystal shape manipulation. In *20th European Symposium on Computer Aided Process Engineering*; Pierucci, S., Ferraris, G. B., Eds.; Comput.-Aided Chem. Eng.; Elsevier: Amsterdam, Netherlands, 2010; Vol. 28; pp 751–756.

[73] Bajcinca, N.; Perl, R.; Sundmacher, K. Convex optimization for shape manipulation of multidimensional crystal particles. In *21st European Symposium on Computer Aided Process Engineering*; Pistikopoulos, E., Georgiadis, M., Kokossis, A., Eds.; Comput.-Aided Chem. Eng.; Elsevier: Amsterdam, Netherlands, 2011; Vol. 29; pp 855–859.

[74] Nagy, Z. K. Model based robust control approach for batch crystallization product design. *Comput. Chem. Eng.* **2009**, *33*, 1685–1691.

[75] Nagy, Z. K.; Aamir, E.; Rielly, C. D. Internal Fines Removal Using Population Balance Model Based Control of Crystal Size Distribution under Dissolution, Growth and Nucleation Mechanisms. *Cryst. Growth Des.* **2011**, *11*, 2205–2219.

[76] Seki, H.; Su, Y. Robust optimal temperature swing operations for size control of seeded batch cooling crystallization. *Chem. Eng. Sci.* **2015**, *133*, 16–23.

[77] Heffels, S.; De Jong, E.; Nienoord, M. Improved Operation and Control of Batch Crystallizers. *AIChE Symp. Ser.* **1991**, *87*, 170–181.

[78] Abu Bakar, M. R.; Nagy, Z. K.; Saleemi, A. N.; Rielly, C. D. The Impact of Direct Nucleation Control on Crystal Size Distribution in Pharmaceutical Crystallization Processes. *Cryst. Growth Des.* **2009**, *9*, 1378–1384.

[79] Saleemi, A. N.; Rielly, C. D.; Nagy, Z. K. Comparative Investigation of Supersaturation and Automated Direct Nucleation Control of Crystal Size Distributions using ATR-UV/vis Spectroscopy and FBRM. *Cryst. Growth Des.* **2012**, *12*, 1792–1807.

[80] Simone, E.; Zhang, W.; Nagy, Z. K. Application of Process Analytical Technology-Based Feedback Control Strategies To Improve Purity and Size Distribution in Biopharmaceutical Crystallization. *Cryst. Growth Des.* **2015**, *15*, 2908–2919.

[81] Zhang, R.; Ma, C. Y.; Liu, J. J.; Wang, X. Z. On-line measurement of the real size and shape of crystals in stirred tank crystalliser

using non-invasive stereo vision imaging. *Chem. Eng. Sci.* **2015**, *137*, 9–21.

[82] Zhang, Y.; Sizemore, J. P.; Doherty, M. F. Shape Evolution of 3-Dimensional Faceted Crystals. *AIChE J.* **2006**, *52*, 1906–1915.

[83] Snyder, R. C.; Doherty, M. F. Faceted Crystal Shape Evolution During Dissolution or Growth. *AIChE J.* **2007**, *53*, 1337–1348.

[84] Snyder, R. C.; Veesler, S.; Doherty, M. F. The Evolution of Crystal Shape During Dissolution: Predictions and Experiments. *Cryst. Growth Des.* **2008**, *8*, 1100–1101.

[85] Dijkstra, E. W. A Note on Two Problems in Connexion with Graphs. *Numer. Math.* **1959**, *1*, 269–271.

[86] Bertsekas, D. P. *Dynamic Programming and Optimal Control*, 3rd ed.; Athena Scientific: Belmont, MA, 2005; Vol. 1; pp 63–68.

[87] Elbert, P.; Ebbesen, S.; Guzzella, L. Implementation of Dynamic Programming for n-Dimensional Optimal Control Problems With Final State Constraints. *IEEE Trans. Control Syst. Technol.* **2013**, *21*, 924–931.

[88] Zenklusen, R. ETH Zurich, Zürich, Switzerland. Personal communication, 2015.

[89] Biegler, L. T. *Nonlinear Programming: Concepts, Algorithms, and Applications to Chemical Processes*; MOS-SIAM Series on Optimization; Society for Industrial and Applied Mathematics: Philadelphia, PA, 2010; Vol. 10.

[90] *MATLAB 8.6*; The MathWorks, Inc.: Natick, MA, 2015.

[91] Andersson, J. A General-Purpose Software Framework for Dynamic Optimization. Doctoral Thesis, Katholieke Universiteit Leuven, Belgium, 2013.

[92] Wächter, A.; Biegler, L. T. On the implementation of an interior-point filter line-search algorithm for large-scale nonlinear programming. *Math. Program.* **2006**, *106*, 25–57.

[93] Herceg, M.; Kvasnica, M.; Jones, C. N.; Morari, M. Multi-Parametric Toolbox 3.0. 2013 European Control Conference (ECC). Zurich, Switzerland, 2013; pp 502–510.

[94] Haynes, W. M., Ed. Physical Constants of Inorganic Compounds. In *CRC Handbook of Chemistry and Physics*, 97th ed.; CRC Press/Taylor & Francis: Boca Raton, FL, 2017.

[95] Kitamura, M.; Ishizu, T. Growth kinetics and morphological change of polymorphs of L-glutamic acid. *J. Cryst. Growth* **2000**, *209*, 138–145.

[96] Lehmann, M. S.; Koetzle, T. F.; Hamilton, W. C. Precision neutron diffraction structure determination of protein and nucleic acid components. VIII: the crystal and molecular structure of the β-form of the amino acid L-glutamic acid. *J. Cryst. Mol. Struct.* **1972**, *2*, 225–233.

[97] Morari, M. Some Comments on the Optimal Operation of Batch Crystallizers. *Chem. Eng. Commun.* **1980**, *4*, 167–171.

[98] Yang, Y.; Nagy, Z. K. Model-Based Systematic Design and Analysis Approach for Unseeded Combined Cooling and Antisolvent Crystallization (CCAC) Systems. *Cryst. Growth Des.* **2014**, *14*, 687–698.

[99] Wan, J.; Wang, X. Z.; Ma, C. Y. Particle Shape Manipulation and Optimization in Cooling Crystallization Involving Multiple Crystal Morphological Forms. *AIChE J.* **2009**, *55*, 2049–2061.

[100] Liu, J. J.; Hu, Y. D.; Wang, X. Z. Optimization and control of crystal shape and size in protein crystallization process. *Comput. Chem. Eng.* **2013**, *57*, 133–140.

[101] Bajcinca, N. Analytic solutions to optimal control problems in crystal growth processes. *J. Process Control* **2013**, *23*, 224–241.

[102] Acevedo, D.; Tandy, Y.; Nagy, Z. K. Multiobjective Optimization of an Unseeded Batch Cooling Crystallizer for Shape and Size Manipulation. *Ind. Eng. Chem. Res.* **2015**, *54*, 2156–2166.

[103] Hofmann, S.; Bajcinca, N.; Raisch, J.; Sundmacher, K. Optimal control of univariate and multivariate population balance systems involving external fines removal. *Chem. Eng. Sci.* **2017**, *168*, 101–123.

[104] Yu, Z. Q.; Chew, J. W.; Chow, P. S.; Tan, R. B. H. Recent Advances in Crystallization Control: An Industrial Perspective. *Chem. Eng. Res. Des.* **2007**, *85*, 893–905.

[105] Ma, C. Y.; Liu, J. J.; Wang, X. Z. Measurement, modelling, and closed-loop control of crystal shape distribution: Literature review and future perspectives. *Particuology* **2016**, *26*, 1–18.

[106] Cardona, J.; Ferreira, C.; McGinty, J.; Hamilton, A.; Agimelen, O. S.; Cleary, A.; Atkinson, R.; Michie, C.; Marshall, S.; Chen, Y.-C.; Sefcik, J.; Andonovic, I.; Tachtatzis, C. Image analysis framework with focus evaluation for in situ characterisation of particle size and shape attributes. *Chem. Eng. Sci.* **2018**, *191*, 208–231.

[107] Nagy, Z. K.; Braatz, R. D. Robust Nonlinear Model Predictive Control of Batch Processes. *AIChE J.* **2003**, *49*, 1776–1786.

[108] Shi, D.; El-Farra, N. H.; Li, M.; Mhaskar, P.; Christofides, P. D. Predictive control of particle size distribution in particulate processes. *Chem. Eng. Sci.* **2006**, *61*, 268–281.

[109] Griffin, D. J.; Grover, M. A.; Kawajiri, Y.; Rousseau, R. W. Data-Driven Modeling and Dynamic Programming Applied to Batch Cooling Crystallization. *Ind. Eng. Chem. Res.* **2016**, *55*, 1361–1372.

[110] Szilágyi, B.; Borsos, A.; Pal, K.; Nagy, Z. K. Experimental implementation of a Quality-by-Control (QbC) framework using a mechanistic PBM-based nonlinear model predictive control involving chord length distribution measurement for the batch cooling crystallization of L-ascorbic acid. *Chem. Eng. Sci.* **2019**, *195*, 335–346.

[111] Ghadipasha, N.; Romagnoli, J. A.; Tronci, S.; Baratti, R. On-Line Control of Crystal Properties in Nonisothermal Antisolvent Crystallization. *AIChE J.* **2015**, *61*, 2188–2201.

[112] Griffin, D. J.; Grover, M. A.; Kawajiri, Y.; Rousseau, R. W. Mass-count plots for crystal size control. *Chem. Eng. Sci.* **2015**, *137*, 338–351.

[113] Majumder, A.; Nagy, Z. K. Prediction and control of crystal shape distribution in the presence of crystal growth modifiers. *Chem. Eng. Sci.* **2013**, *101*, 593–602.

[114] Cao, Y.; Kang, J.; Nagy, Z. K.; Laird, C. D. Parallel Solution of Robust Nonlinear Model Predictive Control Problems in Batch Crystallization. *Processes* **2016**, *4*, 20.

[115] Cao, Y.; Acevedo, D.; Nagy, Z. K.; Laird, C. D. Real-time feasible multi-objective optimization based nonlinear model predictive control of particle size and shape in a batch crystallization process. *Control Eng. Pract.* **2017**, *69*, 1–8.

[116] Nayhouse, M.; Kwon, J. S.-I.; Christofides, P. D.; Orkoulas, G. Crystal shape modeling and control in protein crystal growth. *Chem. Eng. Sci.* **2013**, *87*, 216–223.

[117] Kwon, J. S.-I.; Nayhouse, M.; Christofides, P. D.; Orkoulas, G. Modeling and Control of Protein Crystal Shape and Size in Batch Crystallization. *AIChE J.* **2013**, *59*, 2317–2327.

[118] Kanayama, Y.; Nilipour, A.; Lelm, C. A. A locomotion control method for autonomous vehicles. Proceedings of the 1988 IEEE Int. Conf. Robot. Autom. 1988; pp 1315–1317.

[119] Soetanto, D.; Lapierre, L.; Pascoal, A. Adaptive, Non-Singular Path-Following Control of Dynamic Wheeled Robots. Proceedings of the 42nd IEEE Conf. Decision Control. 2003; pp 1765–1770.

[120] Mesbah, A.; Huesman, A. E. M.; Kramer, H. J. M.; Van den Hof, P. M. J. A comparison of nonlinear observers for output feedback model-based control of seeded batch crystallization processes. *J. Process Control* **2011**, *21*, 652–666.

[121] LeVeque, R. J. *Finite Volume Methods for Hyperbolic Problems*; Cambridge Texts in Applied Mathematics; Cambridge University Press: Cambridge, UK, 2002; Vol. 31.

[122] *MATLAB 9.2 and Signal Processing Toolbox 7.4*; The MathWorks, Inc.: Natick, MA, 2017.

[123] Gutwald, T.; Mersmann, A. Batch Cooling Crystallization at Constant Supersaturation: Technique and Experimental Results. *Chem. Eng. Technol.* **1990**, *13*, 229–237.

[124] Nagy, Z. K.; Chew, J. W.; Fujiwara, M.; Braatz, R. D. Comparative performance of concentration and temperature controlled batch crystallizations. *J. Process Control* **2008**, *18*, 399–407.

[125] Ghadipasha, N.; Romagnoli, J. A.; Tronci, S.; Baratti, R. A model-based approach for controlling particle size distribution in combined cooling-antisolvent crystallization processes. *Chem. Eng. Sci.* **2018**, *190*, 260–272.

[126] Seibert, K. D.; Collins, P. C.; Fisher, E. Milling Operations in the Pharmaceutical Industry. In *Chemical Engineering in the Pharmaceutical Industry: R&D to Manufacturing*; am Ende, D. J., Ed.; John Wiley & Sons, Inc.: Hoboken, NJ, 2010; pp 365–378.

[127] Luciani, C. V.; Conder, E. W.; Seibert, K. D. Modeling-Aided Scale-Up of High-Shear Rotor–Stator Wet Milling for Pharmaceutical Applications. *Org. Process Res. Dev.* **2015**, *19*, 582–589.

[128] Adi, H.; Larson, I.; Stewart, P. Use of milling and wet sieving to produce narrow particle size distributions of lactose monohydrate in the sub-sieve range. *Powder Technol.* **2007**, *179*, 95–99.

[129] Harter, A.; Schenck, L.; Lee, I.; Cote, A. High-Shear Rotor–Stator Wet Milling for Drug Substances: Expanding Capability with Improved Scalability. *Org. Process Res. Dev.* **2013**, *17*, 1335–1344.

[130] Engstrom, J.; Wang, C.; Lai, C.; Sweeney, J. Introduction of a new scaling approach for particle size reduction in toothed rotor-stator wet mills. *Int. J. Pharm.* **2013**, *456*, 261–268.

[131] Cote, A.; Sirota, E.; Moment, A. The Pursuit of a Robust Approach for Growing Crystals Directly to Target Size. *Am. Pharm. Rev.* **2010**, *13*, 46–51.

[132] Yang, Y.; Song, L.; Zhang, Y.; Nagy, Z. K. Application of Wet Milling-Based Automated Direct Nucleation Control in Continuous Cooling Crystallization Processes. *Ind. Eng. Chem. Res.* **2016**, *55*, 4987–4996.

[133] Acevedo, D.; Kamaraju, V. K.; Glennon, B.; Nagy, Z. K. Modeling and Characterization of an in Situ Wet Mill Operation. *Org. Process Res. Dev.* **2017**, *21*, 1069–1079.

[134] Yang, Y.; Pal, K.; Koswara, A.; Sun, Q.; Zhang, Y.; Quon, J.; McKeown, R.; Goss, C.; Nagy, Z. K. Application of feedback control and in situ milling to improve particle size and shape in the crystallization of a slow growing needle-like active pharmaceutical ingredient. *Int. J. Pharm.* **2017**, *533*, 49–61.

[135] Szilágyi, B.; Nagy, Z. K. Population Balance Modeling and Optimization of an Integrated Batch Crystallizer–Wet Mill System for Crystal Size Distribution Control. *Cryst. Growth Des.* **2018**, *18*, 1415–1424.

[136] Wilson, D.; Bunker, M.; Milne, D.; Jawor-Baczynska, A.; Powell, A.; Blyth, J.; Streather, D. Particle engineering of needle shaped crystals by wet milling and temperature cycling: Optimisation for roller compaction. *Powder Technol.* **2018**, *339*, 641–650.

[137] Salvatori, F.; Mazzotti, M. Experimental Characterization and Mathematical Modeling of Breakage of Needle-like Crystals in a Continuous Rotor-Stator Wet Mill. *Cryst. Growth Des.* **2018**, *18*, 5957–5972.

[138] Ahmed, B.; Brown, C. J.; McGlone, T.; Bowering, D. L.; Sefcik, J.; Florence, A. J. Engineering of acetaminophen particle attributes using a wet milling crystallisation platform. *Int. J. Pharm.* **2019**, *554*, 201–211.

[139] Agimelen, O. S.; Svoboda, V.; Ahmed, B.; Cardona, J.; Dziewierz, J.; Brown, C. J.; McGlone, T.; Cleary, A.; Tachtatzis, C.; Michie, C.; Florence, A. J.; Andonovic, I.; Mulholland, A. J.; Sefcik, J. Multi-sensor inline measurements of crystal size and shape distributions during high shear wet milling of crystal slurries. *Adv. Powder Technol.* **2018**, *29*, 2987–2995.

[140] *MATLAB 9.2 and Optimization Toolbox 7.6*; The MathWorks, Inc.: Natick, MA, 2017.

[141] Garcia, E.; Hoff, C.; Veesler, S. Dissolution and phase transition of pharmaceutical compounds. *J. Cryst. Growth* **2002**, *237-239, Part 3*, 2233–2239.

[142] Shoji, M.; Eto, T.; Takiyama, H. A Kinetic Study of the Influence of Modulated Undersaturation Operation on Crystal Size Distribution in Cooling-Type Batch Crystallization. *J. Chem. Eng. Jpn.* **2011**, *44*, 191–196.

[143] Simone, E.; Klapwijk, A. R.; Wilson, C. C.; Nagy, Z. K. Investigation of the Evolution of Crystal Size and Shape during Temperature Cycling and in the Presence of a Polymeric Additive Using Combined Process Analytical Technologies. *Cryst. Growth Des.* **2017**, *17*, 1695–1706.

[144] Simone, E.; Saleemi, A. N.; Tonnon, N.; Nagy, Z. K. Active Polymorphic Feedback Control of Crystallization Processes Using a Combined Raman and ATR-UV/Vis Spectroscopy Approach. *Cryst. Growth Des.* **2014**, *14*, 1839–1850.

[145] Simone, E.; Szilágyi, B.; Nagy, Z. K. Systematic model identification and optimization-based active polymorphic control of crystallization processes. *Chem. Eng. Sci.* **2017**, *174*, 374–386.

[146] Noyes, A. A.; Whitney, W. R. The Rate of Solution of Solid Substances in Their Own Solution. *J. Am. Chem. Soc.* **1897**, *19*, 930–934.

[147] Bovington, C. H.; Jones, A. L. Tracer Study of the Kinetics of Dissolution of Lead Sulphate. *Trans. Faraday Soc.* **1970**, *66*, 2088–2091.

[148] Singh, M. R.; Nere, N.; Tung, H.-H.; Mukherjee, S.; Bordawekar, S.; Ramkrishna, D. Measurement of Polar Plots of Crystal Dissolution Rates Using Hot-Stage Microscopy. Some Further Insights into Dissolution Morphologies. *Cryst. Growth Des.* **2014**, *14*, 5647–5661.

[149] Gao, Y.; Glennon, B.; Kamaraju, V. K.; Hou, G.; Donnellan, P. Dissolution Kinetics of a BCS Class II Active Pharmaceutical Ingredient. *Org. Process Res. Dev.* **2018**, *22*, 328–336.

[150] Lu, A. T. K.; Frisella, M. E.; Johnson, K. C. Dissolution Modeling: Factors Affecting the Dissolution Rates of Polydisperse Powders. *Pharm. Res.* **1993**, *10*, 1308–1314.

[151] Mangin, D.; Garcia, E.; Gerard, S.; Hoff, C.; Klein, J. P.; Veesler, S. Modeling of the dissolution of a pharmaceutical compound. *J. Cryst. Growth* **2006**, *286*, 121–125.

[152] Griffin, D. J.; Kawajiri, Y.; Rousseau, R. W.; Grover, M. A. Using MC plots for control of paracetamol crystallization. *Chem. Eng. Sci.* **2017**, *164*, 344–360.

[153] Salvatori, F.; Binel, P.; Mazzotti, M. Efficient assessment of combined crystallization, milling, and dissolution cycles for crystal size and shape manipulation. *Chem. Eng. Sci. X* **2019**, *1*, 100004.

[154] Hermanto, M. W.; Kee, N. C.; Tan, R. B. H. T.; Chiu, M.-S.; Braatz, R. D. Robust Bayesian Estimation of Kinetics for the Polymorphic Transformation of L-Glutamic Acid Crystals. *AIChE J.* **2008**, *54*, 3248–3259.

[155] Su, Q.-L.; Chiu, M.-S.; Braatz, R. D. Modeling and Bayesian Parameter Estimation for Semibatch pH-Shift Reactive Crystallization of L-Glutamic acid. *AIChE J.* **2014**, *60*, 2828–2838.

[156] Bristow, D. A.; Tharayil, M.; Alleyne, A. G. A Survey of Iterative Learning Control. *IEEE Control Syst. Mag.* **2006**, *26*, 96–114.

[157] Forgione, M.; Mesbah, A.; Bombois, X.; Van den Hof, P. M. J. Iterative Learning Control of Supersaturation in Batch Cooling

Crystallization. Proceedings of the 2012 Am. Control Conf. (ACC). 2012; pp 6455–6460.

[158] Su, Q.; Chiu, M.-S.; Braatz, R. D. Integrated B2B-NMPC Control Strategy for Batch/Semibatch Crystallization Processes. *AIChE J.* **2017**, *63*, 5007–5018.

[159] Perini, G.; Salvatori, F.; Ochsenbein, D. R.; Mazzotti, M.; Vetter, T. Filterability prediction of needle-like crystals based on particle size and shape distribution data. *Sep. Purif. Technol.* **2019**, *211*, 768–781.

[160] Cornel, J.; Lindenberg, C.; Mazzotti, M. Experimental Characterization and Population Balance Modeling of the Polymorph Transformation of L-Glutamic Acid. *Cryst. Growth Des.* **2009**, *9*, 243–252.

[161] Cornel, J.; Kidambi, P.; Mazzotti, M. Precipitation and Transformation of the Three Polymorphs of D-Mannitol. *Ind. Eng. Chem. Res.* **2010**, *49*, 5854–5862.

[162] *MATLAB 9.2*; The MathWorks, Inc.: Natick, MA, 2017.

[163] Bard, Y. *Nonlinear Parameter Estimation*; Academic Press: New York, NY, 1974.

[164] Miller, S. M.; Rawlings, J. B. Model Identification and Control Strategies for Batch Cooling Crystallizers. *AIChE J.* **1994**, *40*, 1312–1327.

[165] *MATLAB 9.4 and Optimization Toolbox 8.1*; The MathWorks, Inc.: Natick, MA, 2018.

[166] *MATLAB 9.4 and Global Optimization Toolbox 3.4.4*; The MathWorks, Inc.: Natick, MA, 2018.

Appendix A

Supplementary Material for Chapter 2

Table A.1: Algorithm to construct an extended directed graph $\mathcal{K}_G$, starting from a directed graph $\mathcal{H} = (\mathcal{V}, \mathcal{A})$ (see Section 2.3.3).

Step	Description
1.	Let $n_{\max} \in \{0, 1, 2, \ldots\}$ be the maximum number of switches between growth and dissolution that is allowed.
2.	Assign a unique label to each node $v \in \mathcal{V}$ of the directed graph $\mathcal{H} = (\mathcal{V}, \mathcal{A})$. In particular, let $I \in \mathcal{V}$ be the label of the node that corresponds to the grid point $\boldsymbol{L}_0$.
3.	Split the set of arcs $\mathcal{A}$ of the graph $\mathcal{H}$ into two disjoint sets $\mathcal{A}_G$ and $\mathcal{A}_D$, where $\mathcal{A}_G$ contains all the growth arcs, and $\mathcal{A}_D$ contains all the dissolution arcs. Additionally, let $\mathcal{A}_{G,I} \subset \mathcal{A}_G$ be the set of all growth arcs that have either end at the node I. Also, define $\mathcal{A}_{D,I} \subset \mathcal{A}_D$ to be the set of all dissolution arcs that have either end at the node I.
4.	Create a new directed graph $\mathcal{K}_G = (\mathcal{W}_G, \mathcal{B}_G)$ with initially empty sets of nodes and arcs $\mathcal{W}_G$ and $\mathcal{B}_G$, respectively. Initialize the counter variable $n = 0$.

5.   If $n = 0$, let $\mathcal{B}_n = \mathcal{A}_\mathrm{G}$; otherwise, let $\mathcal{B}_n = \mathcal{A}_\mathrm{G} \setminus \mathcal{A}_{\mathrm{G},I}$. Then, let $\mathcal{W}_n \subseteq \mathcal{V}$ be the set of nodes that are connected to at least one of the arcs in $\mathcal{B}_n$. If $n > 0$, assign a new, unique label to all the nodes in $\mathcal{W}_n$ and update also the labels of the arc heads and tails in $\mathcal{B}_n$. Finally, add $\mathcal{W}_n$ to $\mathcal{W}_\mathrm{G}$, i.e., $\mathcal{W}_\mathrm{G} \leftarrow \mathcal{W}_\mathrm{G} \cup \mathcal{W}_n$, and add $\mathcal{B}_n$ to $\mathcal{B}_\mathrm{G}$, i.e., $\mathcal{B}_\mathrm{G} \leftarrow \mathcal{B}_\mathrm{G} \cup \mathcal{B}_n$.

6.   If $n = 0$, skip this step. Otherwise, note that every node in the two sets $\mathcal{W}_{n-1}$ and $\mathcal{W}_n$ is a relabeled copy of a node in the set $\mathcal{V}$. For each node $v \in \mathcal{V} \setminus I$, check if copies of this node are present in both $\mathcal{W}_{n-1}$ and $\mathcal{W}_n$. If this is the case, add an arc with weight 0 to $\mathcal{B}_\mathrm{G}$ with its tail and head at the node copies in $\mathcal{W}_{n-1}$ and $\mathcal{W}_n$, respectively.

7.   Increment the counter, i.e., $n \leftarrow n+1$. Terminate if $n_\mathrm{max} = 0$

8.   Let $\mathcal{B}_n = \mathcal{A}_\mathrm{D} \setminus \mathcal{A}_{\mathrm{D},I}$. Also, let $\mathcal{W}_n \subseteq \mathcal{V}$ be the set of nodes that are connected to at least one of the arcs in $\mathcal{B}_n$. Assign a new, unique label to all the nodes in $\mathcal{W}_n$ and update also the labels of the arc heads and tails in $\mathcal{B}_n$. Then, add $\mathcal{W}_n$ to $\mathcal{W}_\mathrm{G}$, i.e., $\mathcal{W}_\mathrm{G} \leftarrow \mathcal{W}_\mathrm{G} \cup \mathcal{W}_n$, and add $\mathcal{B}_n$ to $\mathcal{B}_\mathrm{G}$, i.e., $\mathcal{B}_\mathrm{G} \leftarrow \mathcal{B}_\mathrm{G} \cup \mathcal{B}_n$.

9.   For each node $v \in \mathcal{V} \setminus I$, check if copies of this node are present in both $\mathcal{W}_{n-1}$ and $\mathcal{W}_n$. If this is the case, add an arc with weight 0 to $\mathcal{B}_\mathrm{G}$ with its tail and head at the node copies in $\mathcal{W}_{n-1}$ and $\mathcal{W}_n$, respectively.

10.   Increment the counter, i.e., $n \leftarrow n+1$.

11.   Repeat steps 5 through 10, and terminate as soon as $n = n_\mathrm{max} + 1$.

Appendix B

Supplementary Material for Chapter 3

B.1 Materials

Deionized and filtered (filter size of 0.22 µm) water obtained from a Milli-Q Advantage A10 system (Millipore, Zug, Switzerland) was used for all the experiments performed in the scope of Chapter 3. Monosodium L-glutamic acid monohydrate (NaGlu, Sigma-Aldrich, Buchs, Switzerland, purity $> 99\%$) and hydrochloric acid (HCl, Sigma-Aldrich, Buchs, Switzerland, 37-38 %) were used as delivered for the preparation of seed crystals. Two different polymorphs of L-glutamic acid exist, namely, the prismatic, metastable α polymorph and the needle-like, stable β polymorph.[49] β L-glutamic acid (Sigma-Aldrich, Buchs, Switzerland, purity $> 99\%$) was used to prepare saturated solutions. Since BLGA crystals obtained from the manufacturer were milled, they were not used as seeds for the experiments. Instead, the seed preparation protocol described in Appendix B.4 was employed.

B.2 Experimental Setup

All the experiments were performed in a 2 L glass jacketed stirred tank crystallizer (inner diameter = 15 cm) connected to a ministat 230-CC3 thermostat (Huber, Offenburg, Germany) with fixed internal controller parameters (P-cascade = 1000, I-cascade = 750, D-cascade = 0). The

suspension was stirred by a four-blade glass impeller with 45° inclined blades and a diameter of 60 mm (LaboTechSystems LTS AG, Reinach, Switzerland). A stirring rate of 400 rpm was used for all the experiments, except during seed preparation. To monitor and characterize the evolution of the process, the suspension from the crystallizer was pumped through an *ex situ* stereoscopic imaging device using a sampling loop (see Appendix B.3).

B.3 Characterization Technique

A stereoscopic imaging device, the µ-DISCO shown in Figure B.1, was used to measure the evolution of the PSSD.[32] The suspension sampled from the reactor was pumped through a square quartz channel embedded in a sampling loop at a flow rate of $400\,\mathrm{mL\,min^{-1}}$. It was observed that this flow rate was adequate to ensure minimum sedimentation of the particles along the sampling loop. Every 5 min, 800 images of the suspension were acquired using the burst mode at frame rates of up to 75 fps. Motion blur in such imaging systems can often be encountered when the suspension is pumped at a high flow rate and when the images are acquired with long exposure times. Eventually, motion blur can lead to an inaccurate characterization of the size and shape of the observed particles. Therefore, during the image acquisition phase, the flow rate of the suspension was reduced to $100\,\mathrm{mL\,min^{-1}}$ in order to eliminate motion blur. Upon the acquisition of the images, the original flow rate of $400\,\mathrm{mL\,min^{-1}}$ was resumed.

The images were processed online using an automated image analysis routine, which provided the size and shape of the imaged crystals. At each sampling instant, on an average, around 10 000 particles were characterized by the µ-DISCO. The elongated BLGA crystals were mostly classified as needles and quasi-equant particles using the classification algorithm described elsewhere.[32] Particles assigned to these two classes were assumed to be primary particles and, based on the generic particle shape models proposed previously, each primary particle was approximated by a cylinder with length L_1 and width L_2.[23] The PSSDs were reconstructed by applying a binning protocol using a regular grid along the length and width dimension over all the primary particles characterized by the µ-DISCO.[23] Upon the reconstruction of the PSSD for the pri-

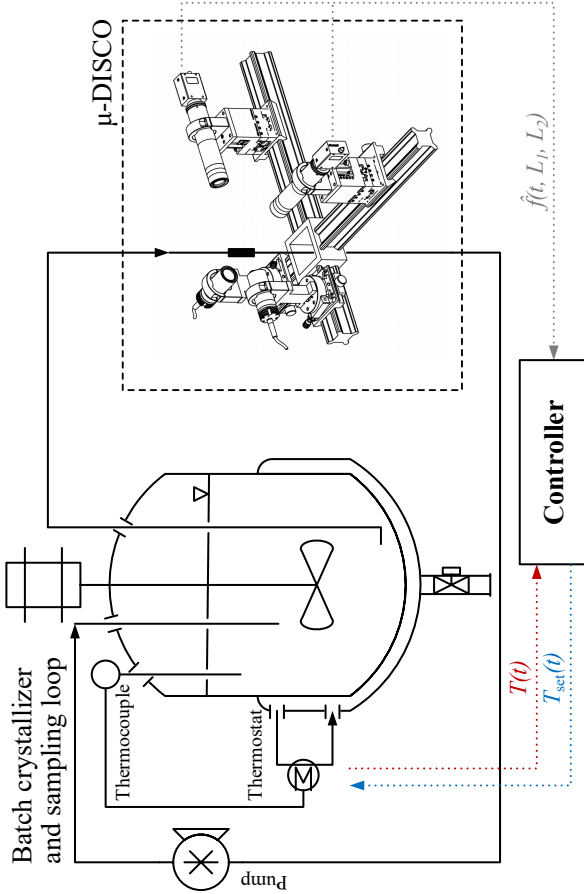Figure B.1: Schematic of the experimental setup coupled with the online characterization tool (μ-DISCO) and the feedback controller. The control algorithm is implemented in a personal computer running MATLAB with the measured process temperature T and the measured PSSD $\hat{f}(t, L_1, L_2)$ as inputs. The output from the controller is the set point temperature T_{set} for the process.

mary particles, the characteristics of the distribution such as the average particle length and width can be described using different combinations of cross moments of the PSSD. For instance, the average dimensions of the population can be defined on a number- or on a volume-weighted basis,[23,39] as already described in Section 3.2.

The measurement technique has a threshold on the smallest size of the particle that can be observed.[32] During a growth process, particles generated due to secondary nucleation, or fines present in the batch of seed crystals, if any, can lead to new particles being observed by the µ-DISCO once they reach the minimum detectable size. Eventually, this can have a significant impact on the number-weighted average dimensions. On the contrary, the volume-weighted average dimensions are usually only slightly affected, if at all. Hence, the volume-weighted average length and width of the measured PSSD were used, as defined in eq 3.2. Note that in the experimental part of Chapter 3 (i.e., in Section 3.7 and in this Appendix), the cross moments are obtained from the experimentally measured number density function $\hat{f}(t, L_1, L_2)$ that is not defined with respect to the solvent mass; i.e., $\hat{f}$ has units of μm^{-2}.

A regular grid with 500 bins along the L_1 direction and with 150 bins along the L_2 direction was used for the online reconstruction of the PSSDs and for the evaluation of the cross moments of the distribution for all the PFC experiments. The two quantities $\hat{\bar{L}}_{1,v}$ and $\hat{\bar{L}}_{2,v}$ were fed back to the PFC control algorithm to provide size and shape feedback. Prior to using them in the control algorithm described in Section 3.3, they were low-pass filtered as described in Section 3.5.5. After conducting the CSC experiments (see Section 3.7.1), the cutoff frequency of the low-pass filter was reduced to 1/20 of the sampling frequency to reduce the noise level even further during the PFC experiments.

The volume-weighted PSSD $\hat{f}_v$ visualized in Section 3.7.2 is defined as

$$\hat{f}_v(t, L_1, L_2) = \frac{L_1 L_2^2 \hat{f}(t, L_1, L_2)}{\hat{\mu}_{12}(t)} \tag{B.1}$$

B.4 Preparation of Seed Crystals

The seed crystals of BLGA were obtained via pH-shift precipitation followed by polymorphic transformation, i.e., involving two steps. In the first step, equimolar amounts of NaGlu and HCl were mixed in deionized and filtered water with continuous stirring at 300 rpm at 5.0 °C for 1 h to produce crystals of the α polymorph. The α crystals obtained were filtered and dried. Subsequently, a solution saturated with respect to α L-glutamic acid at 45 °C was created by mixing equimolar amounts of NaGlu and HCl. The α crystals obtained from the previous step were allowed to undergo a polymorphic transformation over 36 h to form the β polymorph. [160] The transformed crystals were subsequently filtered and dried.

One batch of seed crystals was used for the results presented in Sections 3.7.1 and 3.7.2. This batch was obtained by wet-milling at 10 000 rpm (IKA Magic Lab rotor-stator wet mill equipped with the MK/MKO 300 module) BLGA crystals obtained at the end of the precipitation process, followed by dry sieving (40-63 μm).

B.5 Limits on Operating Conditions

A lower and an upper limit both on the supersaturation and on the temperature were defined for the experiments to satisfy various operational constraints. The limits were chosen based on experimental experience with BLGA in water. The lower limit on the supersaturation $S_{\min}$ was set to 1.10 to ensure significant growth, whereas the upper limit $S_{\max}$ was set to 1.18 to prevent observable nucleation and agglomeration. The bounds on the operating limits of the temperature $T_{\min}$ and $T_{\max}$ were fixed at 20 °C and 41 °C, respectively. In the considered system BLGA in water, the temperature limits themselves are not critical. They were chosen so that the bounds on the supersaturation can be satisfied at any time by selecting an appropriate process temperature, and so that the upper boundary of the temperature range explored elsewhere [54] was not exceeded. A final supersaturation S_{final} of 1.05 was defined to end batches controlled by the PFC upon reaching the target orthant (see Figure 3.1). The value of S_{final} was chosen to ensure that no dissolution of the product crystals occurs, possibly due to the uncertainty in the solubility data. Crystal growth was not observed at $S = 1.05$.

B.6 Experimental Protocol

All the experiments presented in Sections 3.7.1 and 3.7.2 had three distinct phases, namely, an initial idle phase, a main experimental phase, and a final phase.

For all the experiments, a saturated solution of BLGA in water was prepared at 29.9 °C by adding excess BLGA crystals to the pure solvent. The reactor was kept at constant temperature and at the desired stirring rate to let the suspension equilibrate. The saturated solution was then filtered off and 2000.0 g were put back into the reactor. The temperature of the reactor was then reduced to the initial temperature $T(t_0)$ corresponding to the desired initial supersaturation $S(t_0)$ for a given experiment. When $T(t_0)$ was reached, 0.35 g of BLGA seeds prepared using the protocol described in Appendix B.4 were added and the experiments were subjected to the three distinct measurement phases explained below. Note that the low seed loading was chosen so that particles rarely overlapped in the images, thereby ensuring the accuracy of the characterization technique (see Appendix B.3). To operate with higher solid phase concentrations (amount of seed crystals suspended in the solution), a dilution loop would be required, as described previously.[23]

During the initial idle phase, the controller was inactive, i.e., the suspension was monitored and characterized, but the process temperature set point in the thermostat was not updated. The duration of the initial idle phase, t_{initial}, was 5 min and 30 min for CSC and PFC experiments, respectively.

During the main experimental phase, the controller was operated with a sampling time of 5 min, i.e., the suspension was monitored and characterized, and based on the desired controller action (CSC or PFC), an updated process temperature set point was assigned to the thermostat. The maximum allowed duration of the main experimental phase for a given experiment was t_{max} and the value assigned to this upper limit depended on the type of experiment being conducted. For the CSC experiments, t_{max} ranged from 14 h to 40 h, depending on the desired supersaturation at which the experiment was conducted, and the main experimental phase was always ended after t_{max}. For the PFC experiments, t_{max} was set to 50 h, unless explicitly stated otherwise in Section 3.7.2. If the PFC was able to drive the measured average dimensions

into the target orthant before t_{max}, the controller switched to a process temperature set point corresponding to a supersaturation of S_{final} to end the batch. The PFC did the same if the target orthant was not reached until the end of the main phase, i.e., at t_{max}.

During the final phase, the PFC was inactive. A constant supersaturation of S_{final} was maintained for 70 min (t_{final}) for all the CSC and PFC experiments.

B.7 Solute Concentration Estimation

To determine the correct temperature set point during a CSC experiment, or to keep the supersaturation of the liquid phase within the chosen supersaturation limits during a PFC experiment, a measurement of the current solute concentration is required. For the experiments presented in Section 3.7, the solute concentration estimation technique explained in Section 1.3 was slightly modified. In more detail, a second scaling factor ϕ_{n} was introduced in eq 1.2, yielding the concentration estimate

$$\hat{c}(t) = c_0 - \rho_{\text{c}}\big(\phi_{\text{v}}\phi_{\text{n}}\hat{V}(t) - V_{\text{seed}}\big) \tag{B.2}$$

where ϕ_{n} compensates for unwanted changes in the observed particle count over the course of a growth experiment. This scaling factor is defined as

$$\phi_{\text{n}} = \frac{\hat{N}_{s,0}}{\hat{N}_{\text{s}}(t)} \tag{B.3}$$

where $\hat{N}_{\text{s}}(t)$ is the particle count at time t and $\hat{N}_{s,0}$ is the initial particle count at seed addition. Prior to using $\hat{c}$ defined in eq B.2 in the controllers, it was low-pass filtered as described in Section 3.5.5, thus yielding $\hat{c}_{\text{filt}}(t)$. The supersaturation estimate $\hat{S}$ at time t was then obtained using eq 3.16.

For the experiments presented in Sections 3.7.1 and 3.7.2, a combination of the low seed loading and the slow growth of BLGA in water

resulted in a small change in the solute concentration over time. Thus, a viable alternative may be to approximate CSC experiments by simply operating at a constant temperature, where such temperature, given the initial solute concentration c_0, corresponds to the desired constant supersaturation. Similarly, for PFC experiments, instead of supersaturation limits, the temperatures corresponding to $S_{\min}$ and $S_{\max}$ at the known initial solute concentration c_0 could be used as limits for the temperature set point to ensure that there is considerable growth of the population without significant nucleation and agglomeration. This alternative would completely eliminate the need for online solute concentration measurements when performing batches controlled by both controllers. Nevertheless, to operate the controlled process in the most general way, concentration estimation (here, based on stereoscopic imaging using the μ-DISCO) was employed for both CSC and PFC experiments.

Appendix C

Supplementary Material for Chapter 4

C.1 Materials

For all the experiments performed in Chapter 4, deionized and filtered (filter size of 0.22 µm) water obtained from a Milli-Q Advantage A10 system (Millipore, Zug, Switzerland) was used. For the preparation of β L-glutamic acid (BLGA) seed crystals, monosodium L-glutamic acid monohydrate (Sigma-Aldrich, Buchs, Switzerland, purity > 99 %) and hydrochloric acid (Sigma-Aldrich, Buchs, Switzerland, 37-38 %) were used as delivered. BLGA obtained from the manufacturer (Sigma-Aldrich, Buchs, Switzerland, purity > 99 %) was used to prepare saturated solutions in water. D-mannitol (DM, Sigma-Aldrich, Buchs, Switzerland, purity > 98 %) obtained from the manufacturer was used to prepare saturated solutions in ethanol (Fisher Scientific, Reinach, Switzerland, analytical reagent grade). D-mannitol exhibits three different polymorphs. The γ polymorph (GDM), which is needle-like, is the thermodynamically stable form[161] and was used as seed crystals. The seed crystals of BLGA and GDM used were prepared using the protocols described in Appendix C.4. It is worth noting that BLGA is weakly soluble in water ($9.86\,\mathrm{g\,kg^{-1}}$ at $29.9\,°\mathrm{C}$), whereas GDM is almost insoluble in ethanol ($0.16\,\mathrm{g\,kg^{-1}}$ at $25.0\,°\mathrm{C}$).

C.2 Experimental Setup

The experimental setup consists of four main elements, namely, the crystallizer, the online solid phase characterization device µ-DISCO,[32] the rotor-stator wet mill, and the control computer, as shown in Figure 4.1 in Section 4.2.

All the experiments performed in the scope of Chapter 4 made use of a 2 L glass jacketed stirred tank crystallizer (inner diameter = 15 cm) connected to a ministat 230-CC3 thermostat (Huber, Offenburg, Germany). The suspension was sampled from this crystallizer to characterize the evolution of the solid phase using the µ-DISCO as described in Appendix C.3. The suspension was stirred at 400 rpm by a 4-blade glass impeller with 45° inclined blades and a diameter of 60 mm (LaboTech-Systems LTS AG, Reinach, Switzerland).

An IKA Magic Lab equipped with the MK/MKO module (IKA-Werke, Staufen im Breisgau, Germany) served as the rotor-stator wet mill in all the experiments. The suspension was pumped through the mill using a peristaltic pump (Ismatec, Wertheim, Germany) at a flow rate of $1.18 \, \mathrm{L \, min^{-1}}$. The wet mill was connected to a ministat 230-NR Pilot ONE thermostat (Huber, Offenburg, Germany) to regulate the temperature of the wet mill jacket.

The image analysis routines described elsewhere[32] and the wet mill operating and control algorithms discussed in Sections 4.3.3 to 4.3.6 were implemented in a personal computer (control computer, see Figure 4.1 in Section 4.2) running MATLAB.[140] The interface between the control computer and the rotor-stator wet mill, as well as that between the computer and the peristaltic pump of the wet mill, was realized using an ATmega32U4 microcontroller (Atmel Corporation, San Jose, USA) running a custom firmware (not shown in Figure 4.1). The output from the control computer running the wet mill operating and control algorithms is the rotor speed set point θ_{set} for the wet mill.

C.3 Characterization of the Solid Phase

The µ-DISCO,[32] an *ex situ* stereoscopic imaging device that monitors the evolution of the multidimensional PSSD, was used to characterize the crystals suspended in the crystallizer. In the case of the *Recirculation* configuration (see Section 4.2), the solid phase is characterized

by the μ-DISCO after one full suspension pass, where one full suspension pass corresponds to pumping the suspension through the mill for a duration of one crystallizer residence time τ_C. A total of 800 pairs of images were obtained at a frequency of up to 75 fps either every 5 min or every 10 min. The images thus obtained were processed online using automated image analysis routines; most of the detected particles were classified either as needle-like or as quasi-equant. The particles that fell under these two classes were assumed to be primary particles and each of them was approximated as a cylinder of length L_1 and width L_2 using the generic particle shape model proposed previously.[23] Afterward, a binning protocol was applied to the characterized particles to generate online a two-dimensional PSSD using a regular grid with 500 and 150 bins along the L_1 and the L_2 direction, respectively. This PSSD was used for control. For illustration purposes in Chapter 4, a regular grid with a different number of bins is used. The grid properties will be specified whenever the quantities of interests are shown. Note that all the number of bins along each dimension used in the scope of Chapter 4 guaranteed the convergence of the volume-weighted average dimensions of the distribution.

C.4   Preparation of Seed Crystals

The BLGA seed crystals were obtained using a two-step process, namely, pH-shift precipitation followed by a solvent-mediated polymorphic transformation of L-glutamic acid from the α form to the β form (see Appendix B.4). Two different batches of BLGA seeds, referred to as Seeds ε and Seeds ζ, were prepared.

Seeds ε were obtained by wet milling BLGA crystals obtained at the end of the two-step process described above at 7000 rpm. The milled crystals were subsequently suspended in a saturated solution at 30 °C and heated up to 32 °C to dissolve the fines produced during the milling step. After the solution was filtered off, the crystals were dry-sieved ($>$ 40 μm) and suspended in a saturated solution at 29.9 °C. This suspension was subsequently heated up to 33.5 °C to remove additional fines. After filtration and drying, Seeds ε were obtained.

Seeds ζ were obtained by suspending the BLGA crystals obtained at the end of the two-step process described above in a saturated solu-

tion at $29.9\,°\mathrm{C}$ and by heating this suspension to $32\,°\mathrm{C}$ at $0.4\,°\mathrm{C\,h^{-1}}$. Subsequently, the suspension was cooled down to $30\,°\mathrm{C}$ at $0.3\,°\mathrm{C\,h^{-1}}$. Upon reaching the final temperature, the suspension was filtered and the retained solids were dried.

GDM seeds were not prepared specifically for the experiments performed in the scope of Chapter 4. The seed crystals were the products obtained at the end of a process experiment (Experiment M3 in ref 153) involving consecutive cycles of crystallization, milling, and dissolution, as described elsewhere.[153] The GDM seed crystals are referred to as Seeds ɳ.

The average characteristics of the populations of Seeds ε, Seeds ζ, and Seeds ɳ are given in Table C.1 and the corresponding PSSDs are shown in Figure C.1. Recall that the volume-weighted average dimensions ($\bar{L}_{i,\mathrm{v}}$, $i = 1, 2$) are defined in eq 4.1. The volume-weighted broadnesses ($\sigma_{ii,\mathrm{v}}$, $i = 1, 2$) listed in Table C.1 are additional useful characteristics of a PSSD that can be seen as measures of the spread of the distribution along the characteristic particle dimensions. They are defined as

$$\sigma_{11,\mathrm{v}}(t) = \sqrt{\mu_{32}(t)/\mu_{12}(t) - \big(\mu_{22}(t)/\mu_{12}(t)\big)^2}$$
$$\sigma_{22,\mathrm{v}}(t) = \sqrt{\mu_{14}(t)/\mu_{12}(t) - \big(\mu_{13}(t)/\mu_{12}(t)\big)^2} \tag{C.1}$$

The volume-weighted PSSDs f_v illustrated in Figure C.1 are defined as

$$f_\mathrm{v}(t, L_1, L_2) = \frac{L_1 L_2^2 f(t, L_1, L_2)}{\mu_{12}(t)} \tag{C.2}$$

Equations C.1 and C.2 can also be applied to an experimentally measured PSSD $\hat{f}$, thus yielding the quantities $\hat{\sigma}_{ii,\mathrm{v}}$ ($i = 1, 2$) and $\hat{f}_\mathrm{v}$, respectively.
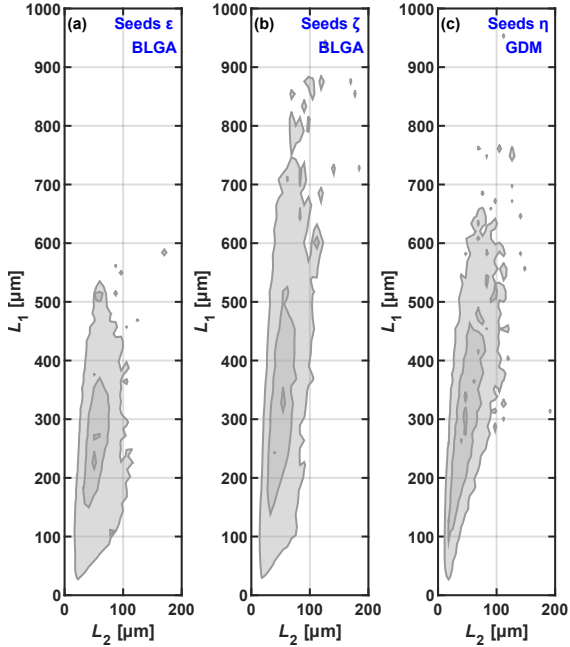
Figure C.1: Volume-weighted PSSDs $\hat{f}_v$ (obtained using eq C.2 and normalized by the maximum of each PSSD) of **(a)** Seeds ε and **(b)** Seeds ζ of BLGA crystals, and of **(c)** Seeds η of GDM crystals. The contour levels correspond to 0.1, 0.5, and 0.9 of each normalized PSSD. Along the L_1 direction, a regular grid with 120 bins and a spacing of 12 µm, 21 µm, and 13 µm was used for Seeds ε, Seeds ζ, and Seeds η, respectively. Along the L_2 direction, the corresponding grid spacing was 9 µm, 7 µm, and 7 µm using 40 bins.

Table C.1: Measured volume-weighted average length $\hat{\bar{L}}_{1,\text{v}}$, width $\hat{\bar{L}}_{2,\text{v}}$, and the measured volume-weighted broadness of the seed PSSD along the length direction $\hat{\sigma}_{11,\text{v}}$ and along the width direction $\hat{\sigma}_{22,\text{v}}$ for the BLGA and the GDM seeds.

Compound	Seeds	$\hat{\bar{L}}_{1,\text{v}}$ [µm]	$\hat{\bar{L}}_{2,\text{v}}$ [µm]	$\hat{\sigma}_{11,\text{v}}$ [µm]	$\hat{\sigma}_{22,\text{v}}$ [µm]
BLGA	ε	278	62	125	25
	ζ	418	63	229	27
GDM	η	356	57	149	25

C.5 Limits on Operating Conditions

Two different operating conditions were constrained for all the experiments, namely, the rotor speed θ of the wet mill and the duration of the main experimental phase t_{max} (see Appendix C.6). The rotor speed was limited to the interval from 3000 to 12 000 rpm. The upper limit was set to 12 000 rpm in order to prevent excessive breakage that would occur at higher rotor speeds and that could easily lead to irreversible overshooting of the target average length.

C.6 Experimental Protocol

The experiments performed in the scope of Chapter 4 consisted of three phases, namely, an initial idle phase, a main experimental phase, and a final phase. Since different control strategies and compounds were used in the experimental campaign, the protocols for the experiments differed slightly, as detailed below.

For all the experiments performed with BLGA, an excess amount of BLGA crystals was added to water at 29.9 °C to prepare a saturated solution. The suspension was equilibrated by keeping the crystallizer at the desired temperature and stirring rate. The suspension was then filtered off and 2000.0 g of clear solution was loaded into the crystallizer. The temperature of the crystallizer was then reduced to the experimental temperature T_{exp} of 29.1 °C corresponding to a supersaturation S_{exp} of 1.03. Upon reaching the desired temperature, 0.50 g of BLGA seeds

prepared as described in Appendix C.4 was added to the saturated solution. Note that the mild supersaturation level chosen ensured that neither dissolution nor detectable growth of the crystals occurred during the milling experiments.

For all the experiments performed with GDM, an excess amount of GDM crystals was added to ethanol at $25.0\,^\circ$C to prepare a saturated solution. The suspension was equilibrated by keeping the crystallizer at the desired temperature and stirring rate. The suspension was then filtered off and $1500.0\,$g of clear solution was put back into the crystallizer. Since GDM is practically insoluble in ethanol, the experiments were conducted at $25.0\,^\circ$C corresponding to a saturated solution ($S_{\mathrm{exp}} = 1.00$). Subsequently, $0.35\,$g of GDM seeds obtained using the protocol described in Appendix C.4 were added to the saturated solution.

It is acknowledged that the suspension density used in the experiments is quite low, but a dilution loop could potentially be employed to deal with higher suspension densities.[23]

During the initial idle phase, the suspension was monitored and characterized, but the measurements thus obtained were not used for control purposes. The duration of this phase was $t_{\mathrm{initial}} = 5\,$min. The measurements obtained during this phase are not shown in Section 4.4.

The duration of the main experimental phase was $t_{\mathrm{max}} = 75\,$min. During this phase, the control laws were active and the suspension was characterized every $t_{\mathrm{samp}} = 10\,$min. Except for the benchmark strategy, the volume-weighted average length of each PSSD measurement was fed to the employed control law to determine the rotor speed set point θ_{set}. Subsequently, the suspension was milled for a duration of τ_{C} using the *Recirculation* configuration (see Section 4.2.2), which corresponds to one full suspension pass. The sequence of PSSD characterization, control law execution, and milling was repeated every $10\,$min either until the target average length was reached or until the end of the main experimental phase.

During the final phase, the controllers were inactive and the suspension was characterized for a duration of $t_{\mathrm{final}} = 10\,$min.

Table C.2: Experimental and controller parameters used in Chapter 4.

Parameter	Unit	Value
BLGA experiments		
ρ_{c}	$\mathrm{g\,\mu m^{-3}}$	1.59×10^{-12}
$c^{*\,3,52}$	$\mathrm{g\,kg^{-1}}$	$3.37\,\mathrm{e}^{(3.59\,\times\,10^{-2}\,T)}$
c_0	$\mathrm{g\,kg^{-1}}$	9.86
m_{seed}	g	0.50
m_{solvent}	kg	1.98
T^*	°C	29.90
S_{exp}	–	1.03
GDM experiments		
c_0	$\mathrm{g\,kg^{-1}}$	0.16
m_{seed}	g	0.35
m_{solvent}	kg	1.50
T^*	°C	25.00
S_{exp}	–	1.00
Wet mill		
τ_{WM}	s	5.72
τ_{C}	s	102.00
Controllers		
n_{grid}	–	500 (L_1)
	–	150 (L_2)
t_{samp}	min	10
t_{initial}	min	5
t_{max}	min	75
t_{final}	min	10
θ_{min}	rpm	3000
θ_{max}	rpm	12000
θ_0	rpm	7500
κ	$\mathrm{\mu m^{-1}}$	0.1

Appendix D

Supplementary Material for Chapter 5

D.1 Materials

Deionized and filtered (filter size of 0.22 µm) water was obtained from a Milli-Q Advantage A10 system (Millipore, Zug, Switzerland, resistance 18.2 MΩ cm at 25 °C) and used as a solvent in all experiments.

For the experiments with the compound ʟ-glutamic acid, the needle-like, stable β polymorph was used to prepare saturated solutions (Sigma-Aldrich, Buchs, Switzerland, purity > 99 %). The stable form I of vanillin (Sigma-Aldrich, Buchs, Switzerland, tested according to Ph. Eur.) was purchased and used for the preparation of saturated solutions. The purchased BLGA and vanillin crystals were not used for seeding the experiments. Instead, a dedicated seed preparation protocol was applied, as described in Appendix D.2.

For determining relative supersaturation and undersaturation levels and the corresponding temperatures, the same solubility curves as in ref 40 were used for both BLGA and vanillin. These solubility curves are provided in Figure D.1.

D.2 Preparation of Seed Crystals

For BLGA, the seed crystals were initially obtained using a two-step pH-shift precipitation process. In the first step, equimolar quantities
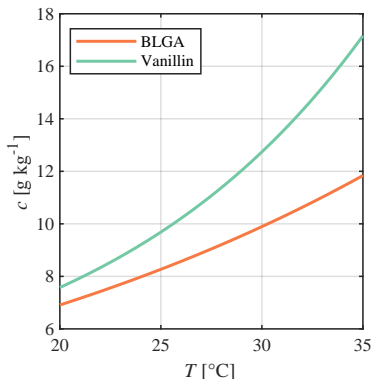
Figure D.1: Solubility curves (on a per mass of solvent basis) of BLGA [3,52] (orange solid line) and vanillin [41] (green solid line) in water.

of monosodium L-glutamic acid monohydrate (NaGlu, Sigma-Aldrich, Buchs, Switzerland, purity > 99 %) and hydrochloric acid (HCl, Sigma-Aldrich, Buchs, Switzerland, 37-38 %) in deionized and filtered water were mixed, while constantly stirring at 300 rpm at 5.0 °C for 1 h. This step produces crystals of the α polymorph of L-glutamic acid (ALGA). The suspension was subsequently filtered off and the ALGA crystals were dried. In the second step, the ALGA crystals obtained in the previous step were suspended in a saturated solution of ALGA in water at 45.0 °C (prepared by mixing equimolar quantities of NaGlu and HCl). The crystals of the α polymorph were then allowed to undergo a solvent-mediated polymorphic transformation to the β polymorph. This suspension was filtered off after 48 h and the BLGA crystals thus obtained were dried. [40]

The seeds for experiments E1 to E6 (see Section 5.2.1) and for the feedback control experiments discussed in Sections 5.2.2 and 5.5.2 were obtained by dry-sieving the crystals collected at the end of the afore-mentioned two-step process using the sieve fraction 90-180 µm. [40]

The seeds for experiments E7 to E13 (also see Section 5.2.1) were produced as follows: 2500.0 g of saturated solution of BLGA in water were prepared at 29.9 °C by adding excess amounts of commercial BLGA

and letting the suspension equilibrate for at least 6 h while stirring at 400 rpm before filtering off the solution. Then, 15 g of the BLGA crystals obtained from the pH-shift precipitation were suspended in this solution. Subsequently, the suspension was cooled to let the BLGA crystals grow, first with a linear temperature ramp to 25.0 °C over 2 h and then with another linear temperature ramp to 23.0 °C for a duration of 12 h. Then, the solution was filtered off and the retained BLGA crystals were dried. Finally, the particles were dry-sieved using the sieve fraction 90-355 µm.

The seeds for the feedback control experiments using milled seeds (see Section 5.5.3) correspond to Seeds ε of ref 67 (see also Appendix C.4). First, BLGA crystals obtained at the end of the two-step process described above were wet milled at 7000 rpm. The milled crystals were subsequently suspended in a saturated solution at 30 °C. This suspension was then heated up to 32 °C to dissolve the fines produced in the previous milling step. The crystals obtained after filtering the suspension were dry-sieved ($> 40 \, \mu m$). These crystals were then suspended in a saturated solution at 29.9 °C and heated up to 33.5 °C to remove additional fines. The suspension was filtered off and then dried to obtain the batch of Seeds ε.[67]

The vanillin seeds used for the feedback control experiments discussed in Sections 5.2.2 and 5.5.4 are the same as those reported elsewhere.[40] These seed crystals were obtained as follows: first, a saturated solution of vanillin in water was prepared at 40 °C, corresponding to a concentration of $23.49 \, \mathrm{g \, kg^{-1}}$ on a per mass of solvent basis; subsequently, the saturated solution was crash-cooled to 20 °C to nucleate and grow the vanillin crystals; and finally, once the temperature reached 20 °C, the suspension was filtered off and the retained solids were dried overnight.[40]

D.3   Experimental Setup

The experiments presented in this chapter were performed in a 2 L glass jacketed stirred crystallizer. A ministat 230-CC3 thermostat (Huber, Offenburg, Germany) was used to control its temperature. The suspensions were stirred at a constant rate of 400 rpm using a 4-blade glass impeller of 60 mm diameter at an inclination of 45° (LaboTechSystems LTS AG, Reinach, Switzerland).

The characterization of the solid phase was performed using an *ex situ*

stereoscopic imaging device, the μ-DISCO.[32] A total of 500 or 800 pairs of images were obtained at a frequency of up to 75 fps every 2 min or 5 min. The images thus obtained were processed using fully automated image analysis routines implemented in a control PC to generate a two-dimensional PSSD using a regular grid. These image analysis routines, apart from providing a PSSD, also provide an estimate of the visual hull[51] of a particle observed in the flow channel, which serves as an approximate, but direct observation of the volume of the corresponding particle. In the batch system employed here, the change in the solute concentration can thus be inferred from the observed change in the total visual hull volume (which is simply the sum of all the single particle visual hull volumes obtained from a sequence of images taken at a given time instant) by means of the mass conservation constraint. The interested reader can find a detailed explanation of this procedure in Section 1.3 or in ref 40. The total visual hull volume also served as the feedback signal for the control algorithm introduced in Section 5.5. A schematic of the experimental setup is shown in Figure D.2. The image analysis routines[32] and the control algorithms were implemented in a control PC running MATLAB.[162]

An IKA Magic Lab equipped with the MK/MKO module (IKA-Werke, Staufen im Breisgau, Germany) was additionally used as the rotor-stator wet mill in the feedback control experiments using the milled seeds (see Section 5.5.3). The suspension was pumped from the crystallizer through the mill using a peristaltic pump (Ismatec, Wertheim, Germany) at a flow rate of $0.9\,\mathrm{L\,min^{-1}}$ and immediately recirculated back into the crystallizer afterward. The jacket temperature of the wet mill was regulated using a ministat 230-NR Pilot ONE thermostat (Huber, Offenburg, Germany).

D.4   Maximum Likelihood Estimation

According to the procedure and the underlying assumptions described elsewhere in detail,[54,163,164] it can be shown that the MLE, i.e., the parameter vector $\boldsymbol{\theta}$ that maximizes the probability of observing the ex-
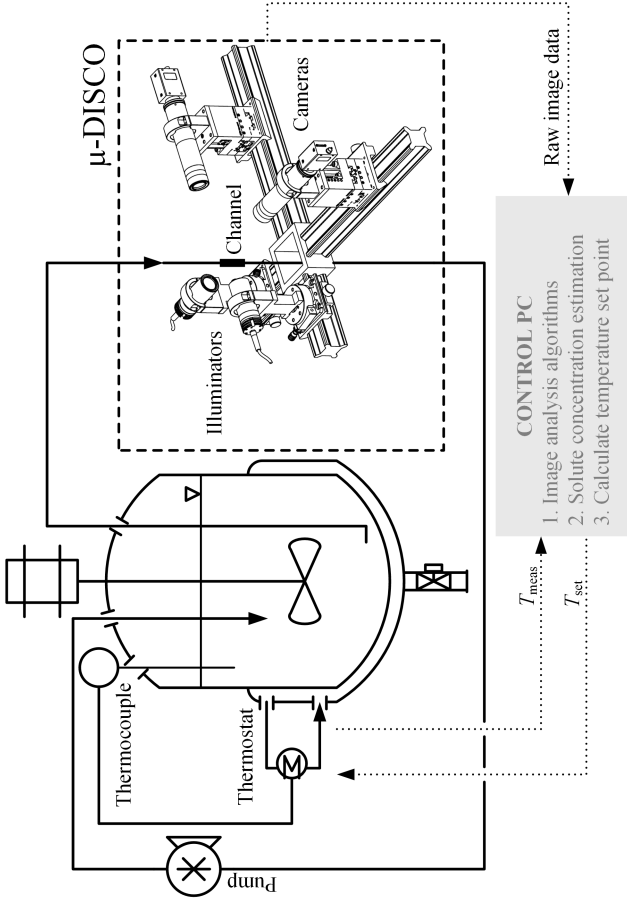
Figure D.2: Schematic of the experimental setup (excluding the wet mill) coupled with the online characterization tool (μ-DISCO) using a sampling loop. The raw images of the crystals are processed to provide the PSSD, the total visual hull volume, and the solute concentration estimate using image analysis algorithms implemented in the control PC. The current process temperature T_{meas} is recorded in the control PC. The thermostat set point temperature T_{set} for the process is also assigned by the control PC. In the case of the dissolution rate modeling experiments, a predefined temperature profile, and in the case of the feedback control experiments, a temperature set point obtained from the control law (see Section 5.5) was assigned.

perimental data set, is the minimizer of the function[163]

$$J(\boldsymbol{\theta}) = \frac{N_\mathrm{t}}{2} \sum_{m=1}^{N_\mathrm{v}} \ln\left(\sum_{k=1}^{N_\mathrm{t}} \left(\hat{y}_{mk} - y_{mk}(\boldsymbol{\theta}) \right)^2 \right) \tag{D.1}$$

where N_t is the total number of data points in the experimental time series, N_v is the number of measured quantities, $\hat{y}_{mk}$ is the kth data point of the mth measured quantity, and $y_{mk}(\boldsymbol{\theta})$ is the corresponding model prediction, which depends on the parameter vector $\boldsymbol{\theta}$.

This optimization problem is nonlinear and nonconvex in general, which means that finding a global minimizer cannot be guaranteed. To rate the quality of any local minimizer, a visual inspection of the fit between the experimentally measured quantities and the model predictions was performed. Furthermore, confidence regions were computed to assess how well a minimizer $\boldsymbol{\theta}^*$ was determined for each candidate model. As explained elsewhere,[54,163,164] after approximating the measurement error covariance matrix and computing the sensitivities of the model predictions with respect to the parameters, an estimate of the positive semidefinite parameter covariance matrix $\boldsymbol{V_\theta}$ can be obtained. The hyperellipsoidal confidence region in the N_p-dimensional parameter space is then given as

$$\{\boldsymbol{\theta} \in \mathbb{R}^{N_\mathrm{P}} \mid (\boldsymbol{\theta} - \boldsymbol{\theta}^*)^\mathrm{T} \boldsymbol{V_\theta}^{-1} (\boldsymbol{\theta} - \boldsymbol{\theta}^*) \leq F_{\chi^2}^{-1}(\eta, N_\mathrm{p})\} \tag{D.2}$$

where $F_{\chi^2}^{-1}(\eta, N_\mathrm{p})$ is the inverse of the chi-square cumulative distribution function with N_p degrees of freedom at the probability η. As a simplified representation of the multidimensional confidence region, the dimensions of its axis-aligned bounding box are taken as parameter confidence intervals (see Section 5.4.2 and Appendix D.7).

D.5 Data Preprocessing

As indicated in Table 5.1, the experiments were split into a subset of experiments used for fitting and a second subset used solely for vali-

dation. The experiments used for fitting were selected such that their subset spans the whole temperature range explored and contains data from both seed populations and from both temperature ramp and step profiles.

The first 2 h for each experiment were combined into a single data point to obtain the seed population. The same was done for the last 2 h (E12 and E13) or the last 20 min (remaining experiments) to obtain the product population. This was done to increase the number of particles constituting the seed and product PSSDs, which in turn improves the accuracy of the simulation and of the graphical representation of the PSSDs (see also Sections 5.4.1 and 5.4.2).

Prior to evaluating the objective function given in eq D.1, further preprocessing steps were applied to the experimental data as follows:

- All the experiments listed in Table 5.1 were started at slightly supersaturated conditions; these initial phases with $S > 1$ were removed from the data.

- The time series of experiments with a significantly longer duration than that of the shortest experiment were down-sampled to ensure that the objective function was not dominated by the longer experiments.

- After down-sampling, the time series of all the experiments considered for fitting were concatenated, thus resulting in a total number of N_t data points.

- The time series of the three measured quantities $\bar{L}_{1,\mathrm{v}}$, $\bar{L}_{2,\mathrm{v}}$, and c (i.e., $N_\mathrm{v} = 3$ in eq D.1) were scaled relative to each other such that they had comparable magnitudes (maximum measured concentration divided by the measured maximum of each of the three outputs). Note that the lower bounds of the integrals in eq 5.5, i.e., $L_{1,\mathrm{min}}$ and $L_{2,\mathrm{min}}$, were left at zero in the case of experimental data.

D.6 Solution of the Population Balance Equation

The PBE model given by eqs 5.1 to 5.3 was solved numerically using a fully discrete high resolution finite volume method with the van Leer flux limiter. At the lower boundary of the physical domain, which is given by $L_1 = 0$ or $L_2 = 0$, a numerical outflow boundary condition was applied.[121] As explained in Appendix D.5, the seed PSSDs f_0 consisted of the particles observed during the initial 2 h (steady state phase) for each experiment listed in Section 5.2.1. The applied binning protocol used a regular grid with a constant resolution of 360 (along L_1) by 120 (along L_2). The bin sizes along L_1 and L_2 ranged from 6.3 μm to 8.4 μm and from 2.4 μm to 4.1 μm, respectively. They were determined individually for each experiment based on the largest experimentally detected particle dimensions. Note that the grid resolution was ensured to be high enough by running test simulations and comparing the results obtained from the HFRVM with those from the standard method of moments. After binning, the seed PSSDs were rescaled to match the experimental seed mass. The constants ρ_c and k_v in eq 5.3 were set to 1.59×10^{-12} g μm^{-3} (the density of BLGA) and $\pi/4$ (for cylinders), respectively.

To simulate the volume-weighted average dimensions defined in eq 5.4 realistically, the lower detection limits $L_{1,\mathrm{min}}$ and $L_{2,\mathrm{min}}$ of the employed solid phase characterization device should be taken into account. These quantities were set to the smallest experimentally characterized particle length and width, which was about 10 μm and 3 μm, respectively. Additionally, before evaluating eq 5.5 in the simulations, f was set to zero for the regions where $L_2 > L_1$, because the employed solid phase monitoring device always assigns the larger measured dimension of a needle-like particle to the length L_1 and the smaller one to the width L_2. Finally, the same scaling factors as mentioned at the end of Appendix D.5 (last point) were applied to the model predictions prior to evaluating the objective function given in eq D.1.

D.7 Parameter Estimation Results

The results obtained by fitting the candidate models M1 to M4 to the preprocessed experimental data are reported in Table D.1. For each
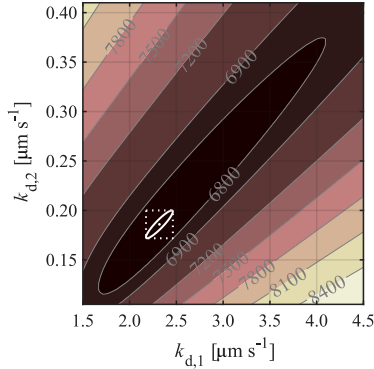
Figure D.3: Objective function value $J(\boldsymbol{\theta})$ (see eq D.1) and parameter confidence region for the fit of model M1. The objective function values are visualized by a selection of contour levels (colored areas and gray lines) and the numbers are reported alongside. The white ellipsoid represents the 95 % parameter confidence region (determined according to eq D.2). The white dotted rectangle highlights the axis-aligned bounding box of this confidence region. The white point in the center of the ellipsoid corresponds to the nominal values of $k_{\mathrm{d},1}^*$ and $k_{\mathrm{d},2}^*$ given in Table D.1.

model, the value $J(\boldsymbol{\theta}^*)$ of the objective function (see eq D.1) at the local minimizer $\boldsymbol{\theta}^*$, as well as the corresponding parameter values and their confidence intervals (confidence level $\eta = 95\,\%$), are given. All these values were computed separately using both a sequential quadratic programming routine (MATLAB's `fmincon`[165]) and a particle swarm algorithm (MATLAB's `particleswarm`[166]). Since the latter did not improve the fit and for the sake of brevity, its detailed results are not reported.

Since M1 defines a two-dimensional parameter space, the objective function $J(\boldsymbol{\theta})$ can be evaluated and visualized, as shown in Figure D.3. It can be readily seen that the objective function for model M1—given the available experimental data—is at least locally convex and exhibits a rather shallow minimum that extends along a constant ratio of the two parameters $k_{\mathrm{d},1}$ to $k_{\mathrm{d},2}$. Nevertheless, the minimizer can be found

reliably, as indicated by the small $95\,\%$ confidence region.

Table D.1: Parameter estimation results for all the candidate models.

Model	Quantity	Unit	fmincon [165]
M1	$J(\boldsymbol{\theta}^*)$	–	6745
	$k_{d,1}^*$	$\mu m\,s^{-1}$	$2.32 \ \pm \ 0.14$
	$k_{d,2}^*$	$\mu m\,s^{-1}$	$0.19 \ \pm \ 0.01$
M2	$J(\boldsymbol{\theta}^*)$	–	6600
	$k_{d,1}^*$	$\mu m\,s^{-1}$	$(6.66 \pm 8.43) \times 10^1$
	$k_{d,2}^*$	$\mu m\,s^{-1}$	$(1.09 \pm 1.60) \times 10^2$
	$k_{s,1}^*$	–	$1.73 \ \pm \ 0.26$
	$k_{s,2}^*$	–	$2.37 \ \pm \ 0.31$
M3	$J(\boldsymbol{\theta}^*)$	–	6713
	$k_{d,1}^*$	$\mu m\,s^{-1}$	$(0.23 \pm 3.01) \times 10^1$
	$k_{d,2}^*$	$\mu m\,s^{-1}$	$(0.10 \pm 1.61) \times 10^4$
	$k_{s,1}^*$	K	$(0.00 \pm 3.96) \times 10^3$
	$k_{s,2}^*$	K	$(2.59 \pm 4.86) \times 10^3$
M4	$J(\boldsymbol{\theta}^*)$	–	5670
	$k_{d,1}^*$	$\mu m\,s^{-1}$	$2.24 \ \pm \ 0.33$
	$k_{d,2}^*$	$\mu m\,s^{-1}$	$(6.43 \pm 3.47) \times 10^{-4}$
	$k_{s,1}^*$	–	$(5.05 \pm 1.89) \times 10^{-2}$
	$k_{s,2}^*$	–	$-1.29 \ \pm \ 0.12$

Appendix E

Supplementary Material for Chapter 6

E.1   Materials

Monosodium L-glutamic acid monohydrate (NaGlu, Sigma-Aldrich, Buchs, Switzerland, purity > 99 %) and hydrochloric acid (HCl, Sigma-Aldrich, Buchs, Switzerland, 37-38 %) were used as purchased to prepare seed crystals. Deionized and filtered (filter size of $0.22\,\mu m$) water taken from a Milli-Q Advantage A10 system (Millipore, Zug, Switzerland) was used as a solvent for all the experiments. The needle-like, stable β polymorph of L-glutamic acid was used for all the experiments with that compound. The saturated solutions were prepared using commercially purchased β L-glutamic acid (BLGA, Sigma-Aldrich, Buchs, Switzerland, purity > 99 %).

D-mannitol (DM, Sigma-Aldrich, Buchs, Switzerland, purity > 98 %) obtained from the manufacturer was used to prepare saturated solutions in a 10/90 wt-% mixture of propan-2-ol (VWR International S.A.S, Fontenay-sous-Bois, France, analytical reagent grade) and deionized and filtered water. The γ polymorph (GDM), which exhibits a needle-like morphology, is the thermodynamically stable form[161] and was used to seed the experiments with this compound.

Dedicated seed preparation protocols, which are described in Appendix E.4, were employed to produce the seeds crystals for both BLGA

and GDM used in the experiments.

E.2 Solubility Curves

The solubility curves used to determine the supersaturations of BLGA in water [3,52] and of GDM in a 10/90 wt-% mixture of propan-2-ol and water [153] are

$$c^*(T) = 3.37 \; \mathrm{e}^{(3.59 \times 10^{-2}T)} \tag{E.1}$$

and

$$c^*(T) = 64.9 \; \mathrm{e}^{(3.45 \times 10^{-2}T)} \tag{E.2}$$

respectively, where $c^*(T)$ is the solubility in $\mathrm{g\,kg^{-1}}$ on a per mass of solvent basis and T is the temperature in °C. The solubility curves within the temperature range of interest are shown in Figure E.1.

For all the experiments presented in Chapter 6, the supersaturation S at a given time t was computed as

$$S(t) = \frac{c_{\mathrm{filt}}(t)}{c^*\big(T(t)\big)} \tag{E.3}$$

where c^* is the solubility (see eqs E.1 and E.2) as a function of the current process temperature $T(t)$ and $c_{\mathrm{filt}}(t)$ is the low-pass filtered solute concentration estimate.

E.3 Experimental Setup

The experiments were performed in a 2 L glass jacketed stirred crystallizer. A ministat 230-CC3 thermostat (Huber, Offenburg, Germany) was used to control its temperature. The suspensions were stirred at a constant rate of 400 rpm using a 4-blade glass impeller of 60 mm diameter at
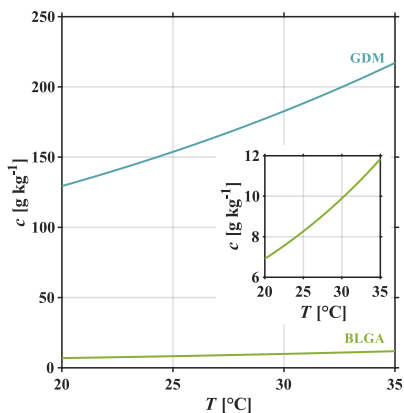
Figure E.1: Solubility curves of BLGA in water [3,52] (green solid line) and GDM in a 10/90 wt-% mixture of propan-2-ol and water [153] (blue solid line). The inset figure shows the solubility curve of BLGA in water with a narrower limit for the concentration axis.

an inclination of 45° (LaboTechSystems LTS AG, Reinach, Switzerland). The characterization of the solid phase was performed using the *ex situ* stereoscopic imaging device μ-DISCO (see Section 1.2).[32] An IKA Magic Lab equipped with the UTL module (IKA-Werke, Staufen im Breisgau, Germany) was the rotor-stator wet mill used in all the experiments. The suspension was pumped through the mill using a peristaltic pump (Ismatec, Wertheim, Germany) at a flow rate of $0.9\,\mathrm{L\,min^{-1}}$. The jacket temperature of the wet mill was regulated using a ministat 230-NR Pilot ONE thermostat (Huber, Offenburg, Germany). A schematic of the complete setup is shown in Figure E.2.

The suspension from the crystallizer was pumped to the μ-DISCO and in there through a transparent channel with a square cross section at a flow rate of $0.4\,\mathrm{L\,min^{-1}}$ and $0.1\,\mathrm{L\,min^{-1}}$ during the idle and the measurement phase, respectively. A total of 800 pairs of images were obtained using the stereoscopic imaging setup at a theoretical maximum frequency of 75 fps every 5 min (measurement phase). As an exception, in the case of a wet milling stage, the solid phase was characterized by the
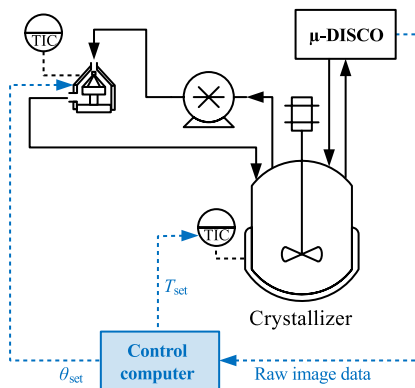
Figure E.2: Schematic of the experimental setup (crystallizer and recirculation loop including the wet mill) coupled with the stereoscopic imaging device (µ-DISCO) via a sampling loop. On the basis of the image data received from the µ-DISCO, the control computer calculates and provides set points for the rotor speed of the wet mill (θ_{set}) and for the temperature of the suspension in the crystallizer (T_{set}).

μ-DISCO every 10 min, because one full suspension pass through the wet mill[67] (roughly corresponding to running the mill for a duration of 102 s and also referred to as one wet milling step in Section 6.4.3) had to take place additionally between the measurements. The images thus obtained were processed on the fly using automated image analysis routines.[32] For the seed particle ensembles considered in Chapter 6, around 80 % of the detected particles were classified to be either of the needle-like or of the quasi-equant type. Each particle that fell into either of these two shape classes was approximated as a cylinder of length L_1 and width L_2 using the generic particle shape model proposed elsewhere.[23] After image acquisition, particle classification, and characterization, a binning protocol was applied to the set of characterized particles to generate online a two-dimensional particle size and shape distribution (PSSD) using a regular grid with 500 and 150 bins along the L_1 and the L_2 direction, respectively. This PSSD was used for calculating and controlling the average particle length during the growth and the milling stages. For plotting purposes, a regular grid with 120 and 40 bins along the L_1 and the L_2 direction, respectively, was used for improved visualization of the results presented in Chapter 6. Prior to using the average particle dimensions in the control algorithms and prior to presenting them in the plots, they were low-pass filtered as described previously (see also Section 3.5.5 and Appendix B.3).[65,66] During the dissolution stages, the feedback signal was a median-filtered version of the sum of all the estimated single particle volumes detected by the μ-DISCO for each sampling instant. This sum corresponds to the so-called total visual hull volume of all the detected particles (i.e., using all the five shape classes of the μ-DISCO), as described previously (see also Section 1.3).[40,68] Since the setup corresponds to a (closed) batch system, the change in the total visual hull volume was used for estimating the evolution of the solute concentration, as described elsewhere in detail (see also Section 1.3).[40] The estimated solid phase concentration was low-pass filtered, as described previously (see also Section 3.5.5),[65] before using it in the control algorithms and in eq E.3.

The image analysis routines[32] and the control algorithms for the milling and the dissolution stages described previously (see also Sections 4.3 and 5.5)[67,68] were implemented in a personal computer (control computer) running MATLAB.[140] The set point calculation of the

constant supersaturation controller (CSC, see, e.g., refs 123 and 124) was performed in the same computer by inverting eq E.3, i.e., by solving it for the temperature for given values of S and $c_{\text{filt}}(t)$. The interface between the control computer and the rotor-stator wet mill, as well as that between the computer and the peristaltic pump of the wet mill, was realized using an ATmega32U4 microcontroller (Atmel Corporation, San Jose, USA) running a custom firmware (not shown in Figure E.2). The output from the control computer running the control algorithms was either the rotor speed set point θ_{set} (in rpm) for the wet mill in case of a milling stage or the temperature set point T_{set} (in °C) for the thermostat of the crystallizer in case of a growth or a dissolution stage.

Darkfield micrographs were obtained using a Leica DM8000 M optical microscope (Leica Microsystems (Schweiz) AG, Heerbrugg, Switzerland) equipped with LED illumination and a 12.5 MP digital color camera with a CCD sensor at fivefold magnification.

E.4   Preparation of Seed Crystals

For the experiments with the compound BLGA, two different batches of seed particles were used. They are referred to as Seeds κ and Seeds λ. Initially, the BLGA seeds were obtained using a two-step process involving a pH-shift precipitation followed by a solvent-mediated transformation of the α polymorph to the β polymorph of L-glutamic acid (see also Appendix B.4). [66]

Seeds κ were obtained by dry-sieving (>63 μm) the particles obtained at the end of the two-step process. These crystals were then suspended in a saturated solution of BLGA in water at 29.9 °C and the suspension was heated to 33 °C at a rate of 0.4 °C h^{-1}. In order to recover the mass that was lost during the heating step and to grow the crystals to a larger size, the suspension was subsequently cooled down to 29.9 °C at a rate of 0.3 °C h^{-1}. After filtering off the solution, washing the crystals with acetone, and drying the washed crystals, Seeds κ were obtained.

Seeds λ were obtained by dry-sieving (63 μm-90 μm) the seeds obtained from the aforementioned two-step process. The crystals thus obtained were suspended in a saturated solution at 29.5 °C and this suspension was heated to 30.3 °C at a rate of 0.3 °C h^{-1}. Subsequently, the suspension was first crash cooled to 26.0 °C and then cooled to 25.5 °C at

Table E.1: The measured average length $\bar{L}_{1,v}$, width $\bar{L}_{2,v}$, and the measured broadness of the seed PSSD along the length direction $\sigma_{11,v}$ and along the width direction $\sigma_{22,v}$ for Seeds κ, Seeds λ, and Seeds ν.

Compound	Seeds	$\bar{L}_{1,v}$ [µm]	$\bar{L}_{2,v}$ [µm]	$\sigma_{11,v}$ [µm]	$\sigma_{22,v}$ [µm]
BLGA	κ	361	51	162	20
	λ	286	55	122	19
GDM	ν	356	57	149	25

a rate of $0.06\,°\mathrm{C\,h^{-1}}$. Upon reaching the final temperature, the solution was filtered off and the retained crystals were dried.

For the experiments with the compound GDM, a single batch of seed crystals, referred to as Seeds ν, was used. This batch of seed crystals corresponds to the products obtained at the end of an uncontrolled multistage process experiment (Experiment M3 in ref 153) comprising wet milling, dissolution, and growth steps.

The average characteristics of the populations of Seeds κ, Seeds λ, and Seeds ν are given in Table E.1 and the corresponding PSSDs are visualized in Figure E.3.

E.5 Protocol for the Multistage Process Experiments with BLGA

Seven controlled multistage process experiments were performed with the compound BLGA. Their most important characteristics are listed in Table E.2. The main phases of these experiments during which the multistage process controller was active are referred to as experiments κ_1, κ_2 and experiments λ_1 to λ_5. For all these experiments, saturated solutions of BLGA in water were prepared by adding an excess amount of purchased BLGA to water and letting the suspension equilibrate for a duration of at least 6 h at a temperature of 29.9 °C while stirring at 400 rpm. Afterward, the solution was filtered off and 2000.0 g of clear, saturated solution was loaded into the crystallizer. After inserting the sampling loop of the µ-DISCO and that of the wet mill into the crystallizer, the solution was cooled to 29.1 °C, corresponding to an initial
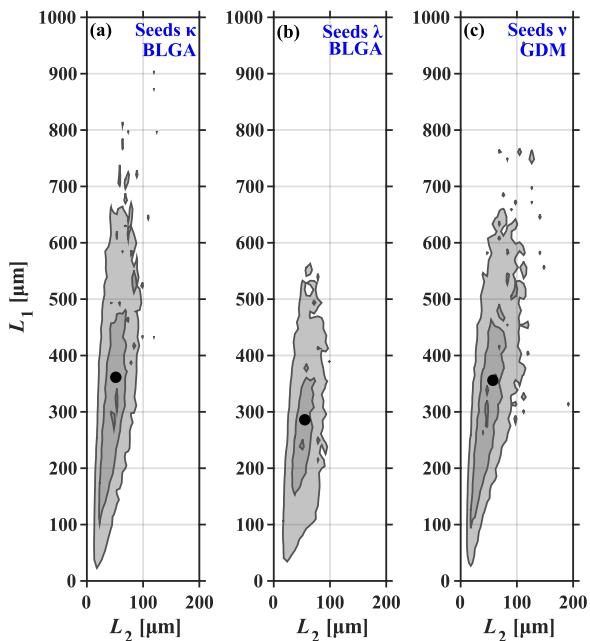
Figure E.3: PSSDs f_v (obtained using eq 6.3 and normalized by the maximum of each PSSD) of **(a)** Seeds κ and **(b)** Seeds λ of BLGA crystals, and of **(c)** Seeds ν of GDM crystals. The contour levels correspond to 0.1, 0.5, and 0.9 of each normalized PSSD. Along the L_1 direction, a regular grid with 120 bins and a spacing of 15 μm, 12 μm, and 13 μm was used for Seeds κ, Seeds λ, and Seeds ν, respectively. Along the L_2 direction, the corresponding grid spacing was 8 μm, 7 μm, and 7 μm using 40 bins. The solid circular markers indicate the average dimensions of the populations.

supersaturation of 1.03.

E.5.1 Experiments without Initial Growth Stage

After reaching the desired initial supersaturation, $0.40\,$g of Seeds κ was added. The subsequent experiment consisted of two phases, namely, of an initial idle phase and of a main experimental phase. The duration of the initial idle phase was $30\,$min, during which the suspension was kept at constant temperature and monitored and characterized using the µ-DISCO, but no process controller was active. After this idle phase, the multistage process controller was started to operate the main experimental phase. Either one (experiment κ_1) or two (experiment κ_2) cycles of wet milling, dissolution, and growth were performed using the stage control algorithms and the cycle logic described in Sections 6.2 and 6.3, respectively. The chosen parameters of the cycle logic are provided in Table E.2. Recall from Section 6.3 that ℓ^{ref} should correspond more or less to the average particle length in the seed population. It is worth noting that the initial measurement of the average particle length in each experiment can be different from the value of $\bar{L}_{1,\mathrm{v}}$ reported in Table E.1 due to measurement noise and due to random variations when sampling from a vial containing all the seed crystals. According to the values reported in Table E.2, the goal of the milling stage of the first cycle was to reduce the average particle length of the seed population from $\ell^{\mathrm{ref}} = 360.0\,$µm to $\ell_1^{\mathrm{m}} = 200.0\,$µm. To do so, the adaptive milling controller presented elsewhere (see also Section 4.3.6) was used with an initial wet mill rotor speed of $\theta_0 = 7500$ rpm and an upper limit of $\theta_{\mathrm{max}} = 12000$ rpm.[67] The subsequent first dissolution stage had to remove $1 - \xi = 20\,\%$ of the particle volume present at the beginning of this stage. The closed-loop mode of the particle volume controller presented previously (see also Section 5.5.1) was employed to do that,[68] with an initial supersaturation of $S_{\mathrm{init}} = 1.01$ approached during $t_{\mathrm{init}} = 20\,$min, a heating rate parameter of $\dot{T}_{\mathrm{HR}} = 0.15\,°\mathrm{C\,h}^{-1}$, and a final supersaturation of $S_{\mathrm{final}} = 1.10$. After dissolution, the first growth stage was initiated with the goal of growing the remaining particles to an average particle length of $\ell_1^{\mathrm{g}} = \omega\ell^{\mathrm{ref}} = 252.0\,$µm. This growth stage was operated by means of a CSC at $S = 1.16$. After reaching the target average length of the first growth stage, the suspension was heated to achieve a final supersaturation of $S = 1.05$. In the case of experiment κ_1, the

suspension was then filtered off and the product crystals were collected and dried over night.

For experiment κ_2, the second cycle started with a milling stage immediately after the first cycle had ended, using the same control algorithm, but operated at a constant temperature corresponding to a supersaturation of $S = 1.05$ instead of $S = 1.03$. The target average length for the milling controller was $\ell_2^{\mathrm{m}} = \omega \ell_1^{\mathrm{m}} = 140.0\,\mu\mathrm{m}$. The second dissolution stage was run in the same way as the first one. The subsequent growth stage was also run at a constant supersaturation of $S = 1.16$, but with a target average particle length of $\ell_2^{\mathrm{g}} = \omega^2 \ell^{\mathrm{ref}} = 176.4\,\mu\mathrm{m}$. After reaching the target average length of the second growth stage, the suspension was heated to achieve a final supersaturation of $S = 1.05$. Then, it was filtered off and the product crystals were collected and dried over night.

Even though a fixed set of cycle logic parameters has been used here, these can be potentially altered, which would obviously lead to different average characteristics of the final PSSD and to a different duration of the stages.

E.5.2 Experiments with Initial Growth Stage

After cooling the solution as described at the end of the initial paragraph of Appendix E.5, 0.40 g of Seeds λ was added to the solution. Then, a CSC phase was started to grow the seed crystals at a supersaturation of $S = 1.18$ to the different average particle lengths given in the column Init. growth of Table E.2. Afterward, the supersaturation was lowered to $S = 1.03$ and two cycles of the controlled multistage process were run in the same way as explained in Appendix E.5.1, but obviously using the Seeds λ crystals grown during the initial growth phase instead of using Seeds κ. Note that the parameter ℓ^{ref} of the cycle logic was set to 360 μm in all cases (despite the different targets of the preliminary growth phases) to ensure that the stage targets were the same for all these five experiments referred to as λ_1 to λ_5.

E.6 Protocol for the Multistage Process Experiments with GDM

Two controlled multistage process experiments were performed with the compound GDM. Their most important characteristics are listed in Ta-

Table E.2: List of all the controlled multistage process experiments, including the used compound (Comp.), the seed batch (Seeds), the experiment label (Exp.), the number of cycles (Cycles), the values of the four cycle logic parameters (ℓ^{ref}, ℓ_1^{m}, ω, and ξ), the $\bar{L}_{1,v}$ target of the initial growth stage, if there was any (Init. growth), and the section of the text where the experiment is discussed (Section).

Comp.	Seeds	Exp.	Cycles	ℓ^{ref} [μm]	ℓ_1^{m} [μm]	ω [–]	ξ [–]	Init. growth	Section
BLGA	κ	κ_1	1	360.0	200.0	0.7	0.8	-	Section 6.4.1
BLGA	κ	κ_2	2	360.0	200.0	0.7	0.8	-	Section 6.4.1
BLGA	λ	λ_1	2	360.0	200.0	0.7	0.8	to 340 μm	Section 6.4.2
BLGA	λ	λ_2	2	360.0	200.0	0.7	0.8	to 380 μm	Section 6.4.2
BLGA	λ	λ_3	2	360.0	200.0	0.7	0.8	to 420 μm	Section 6.4.2
BLGA	λ	λ_4	2	360.0	200.0	0.7	0.8	to 360 μm	Section 6.4.3
BLGA	λ	λ_5	2	360.0	200.0	0.7	0.8	to 360 μm	Section 6.4.3
GDM	ν	ν_1	2	360.0	200.0	0.7	0.8	-	Section 6.4.4
GDM	ν	ν_2	2	360.0	200.0	0.7	0.8	to 400 μm	Section 6.4.4

ble E.2. The main phases of these two experiments during which the multistage process controller was active are referred to as experiments ν_1 and ν_2. For both experiments, saturated solutions of GDM in a 10/90 wt-% mixture of propan-2-ol and water were prepared by adding an excess amount of purchased GDM to the mixture and letting the suspension equilibrate for a duration of at least 6 h at a temperature of 26.0 °C while stirring at 400 rpm. Afterward, the solution was filtered off and 2000.0 g of clear, saturated solution was loaded into the crystallizer. After inserting the sampling loop of the µ-DISCO and that of the wet mill into the crystallizer, the solution was cooled to 25.1 °C, corresponding to an initial supersaturation of 1.03.

E.6.1   Experiment without Initial Growth Stage

After cooling the clear solution, 0.30 g of Seeds ν was added. Similar to the experiments conducted using BLGA, the experiment consisted of a 30 min initial idle phase (suspension kept at constant temperature and characterized using the µ-DISCO) and of a main experimental phase with an active multistage process controller (experiment ν_1). Two cycles of wet milling, dissolution, and growth were performed using the stage control algorithms and the cycle logic described in Sections 6.2 and 6.3, respectively. The parameters of the cycle logic were the same as those for the BLGA experiments and they are listed in Table E.2. As already mentioned in Section 6.4.4, the individual stage controllers were operated with the same parameters as used for the BLGA experiments (see Appendix E.5.1), with a few exceptions. First, the heating rate parameter of the particle volume controller was reduced to a lower value of $\dot{T}_{HR} = 0.075$ °C h^{-1}. Also, the final supersaturation at the end of the dissolution stage was set to $S_{final} = 1.05$. Second, the CSC growth stages were operated at a relatively low supersaturation of $S = 1.05$. This supersaturation was chosen because of the high growth rate of GDM and because the compound was observed to nucleate significantly at supersaturations above 1.07 in the employed mixture of water and propan-2-ol. The third exception was that also the milling stage of the second cycle (and not only that of the first cycle) was operated at a supersaturation of $S = 1.03$ instead of $S = 1.05$.

After reaching the target average length at the end of the growth stage of the second cycle, the suspension was heated to achieve a final

supersaturation of $S = 1.03$. The suspension was then filtered and the product crystals were collected and dried over night.

E.6.2 Experiment with Initial Growth Stage

After cooling the solution, $0.30\,\mathrm{g}$ of Seeds ν was added. Then, a CSC phase was initiated to grow the seed crystals at $S = 1.05$ to an average particle length of $400\,\mathrm{\mu m}$ before starting experiment ν_2. Upon reaching the target, the controlled multistage process was run in the same way as explained in Appendix E.6.1 (see also the cycle logic parameters listed in Table E.2), but obviously starting from the crystals grown during the preliminary growth phase.

Curriculum Vitae

Stefan Bötschi

Born in Zürich, Switzerland
December 24$^{\text{th}}$, 1989

Education

06/2015 − 08/2019	**ETH Zurich**, Switzerland
	Doctoral studies at the Department of Mechanical and Process Engineering
02/2013 − 03/2015	**ETH Zurich**, Switzerland
	Master of Science ETH in Mechanical Engineering
09/2009 − 12/2012	**ETH Zurich**, Switzerland
	Bachelor of Science ETH in Mechanical Engineering
08/2002 − 09/2008	**Kantonsschule Oerlikon**, Switzerland
	Matura (university entrance diploma)

Professional Experience

09/2013 − 08/2014	**Siemens Schweiz AG**, Switzerland
	Working student position
08/2012 − 01/2013	**Siemens Schweiz AG**, Switzerland
	Internship
02/2011 − 06/2012	**ETH Zurich**, Switzerland
	Several student teaching assistant positions
10/2008 − 02/2009	**Rheinmetall Air Defence AG**, Switzerland
	Internship

List of Journal Publications

* = equal contribution

8. Bötschi, S.*; Rajagopalan, A. K.*; Rombaut, I.; Morari, M.; Mazzotti, M. From needle-like toward equant particles: A controlled crystal shape engineering pathway. *Comput. Chem. Eng.* **2019**, in press.

7. Bötschi, S.; Rajagopalan, A. K.; Morari, M.; Mazzotti, M. Feedback Control for the Size and Shape Evolution of Needle-like Crystals in Suspension. IV. Modeling and Control Dissolution. *Cryst. Growth Des.* **2019**, *19*, 4029–4043. DOI: 10.1021/acs.cgd.9b00445

6. Rajagopalan, A. K.; Bötschi, S.; Morari, M.; Mazzotti, M. Feedback Control for the Size and Shape Evolution of Needle-like Crystals in Suspension. III. Wet Milling. *Cryst. Growth Des.* **2019**, *19*, 2845–2861. DOI: 10.1021/acs.cgd.9b00080

5. Rajagopalan, A. K.; Bötschi, S.; Morari, M.; Mazzotti, M. Feedback Control for the Size and Shape Evolution of Needle-like Crystals in Suspension. II. Cooling Crystallization Experiments. *Cryst. Growth Des.* **2018**, *18*, 6185–6196. DOI: 10.1021/acs.cgd.8b01048

4. Bötschi, S.*; Rajagopalan, A. K.*; Morari, M.; Mazzotti, M. An Alternative Approach to Estimate Solute Concentration: Exploiting the Information Embedded in the Solid Phase. *J. Phys. Chem. Lett.* **2018**, *9*, 4210–4214. DOI: 10.1021/acs.jpclett.8b01998

3. Bötschi, S.; Rajagopalan, A. K.; Morari, M.; Mazzotti, M. Feedback Control for the Size and Shape Evolution of Needle-like Crystals in Suspension. I. Concepts and Simulation Studies. *Cryst. Growth Des.* **2018**, *18*, 4470–4483. DOI: 10.1021/acs.cgd.8b00473

2. Bötschi, S.; Ochsenbein, D. R.; Morari, M.; Mazzotti, M. Multi-Objective Path Planning for Single Crystal Size and Shape Modification. *Cryst. Growth Des.* **2017**, *17*, 4873–4886. DOI: 10.1021/acs.cgd.7b00837

1. Rajagopalan, A. K.; Schneeberger, J.; Salvatori, F.; Bötschi, S.; Ochsenbein, D. R.; Oswald, M. R.; Pollefeys, M.; Mazzotti, M. A comprehensive shape analysis pipeline for stereoscopic measurements of particulate populations in suspension. *Powder Technol.* **2017**, *321*, 479–493. DOI: 10.1016/j.powtec.2017.08.044

Zürich, 2019